Exclusive ρ^0 – Meson Electroproduction at HERMES

Machiel Kolstein

Cover: Photograph by Larissa Kolstein.

Exclusive ρ^0 – Meson Electroproduction at HERMES

Machiel Kolstein

The work described in this thesis is part of the research program of the ”Stichting voor Fundamenteel Onderzoek der Materie (FOM)”, which is financially supported by the ”Nederlandse Organisatie voor Wetenschappelijk Onderzoek (NWO)”.

VRIJE UNIVERSITEIT

Exclusive ρ^0 – Meson Electroproduction at HERMES

ACADEMISCH PROEFSCHRIFT

ter verkrijging van de graad van doctor aan
de Vrije Universiteit te Amsterdam,
op gezag van de rector magnificus
prof.dr. T. Sminia,
in het openbaar te verdedigen
ten overstaan van de promotiecommissie
natuurkunde en sterrenkunde
van de faculteit der exacte wetenschappen
op dinsdag 27 oktober 1998 om 13.45 uur
in het hoofdgebouw van de universiteit,
De Boelelaan 1105

door

Machiel Kolstein

geboren te Amsterdam

Promotor: prof.dr.ing J.F.J. van den Brand

If you understand, things are as they are.
If you do not understand, things are as they are.

old Zen saying

Contents

Chapter 1

Introduction

The fundamental theories in physics describing the behaviour and characteristics of matter are quantum field theories (QFT) which combine the special theory of relativity and quantum mechanics.

The combination of quantum field theory and the experimentally found characteristics of the various particles resulted in the formulation of the Standard Model. Here, two types of particles can be distinguished, i.e. those that build up matter and those that are associated with the exchange forces.

In the description of elementary particles quantum numbers play an important role. Particles can be characterised by their mass and lifetime, and quantum numbers such as electric charge, lepton number, baryon number, isospin and spin (the intrinsic angular momentum).

Of the particles that build up matter, 'leptons' do not interact by means of the strong force, while 'hadrons' do. In the second half of the 20th century it was shown that hadrons consisted of constituents referred to as quarks. Both leptons and quarks are 'fermions', i.e. particles with 1/2 integer spin. Leptons and quarks can be organised in families. The different types of quarks, $u, d,$ etc. are referred to as 'flavours'.

The force-mediating particles are 'bosons', i.e. integer spin particles. The electromagnetic force is mediated by photons, the weak nuclear force is mediated by Z and $W^{\pm}$ bosons, the exchange particles for the strong nuclear force are the gluons. The electromagnetic force couples to electrically charged particles. The weak force acts on all particles, but is highly suppressed at low Q^2 since its mediators have large mass. The strong force couples to yet another quantum number of elementary particles, referred to as 'colour'.

The part of the Standard Model, describing quark-quark interactions, by the exchange of gluons mediating the strong nuclear force, is called Quantum Chromo Dynamics (QCD). Since gluons carry colour they not only interact with quarks but with other gluons as well. This, together with the strength of the force they mediate, is believed to be the reason that quarks do not appear freely, which is referred to as 'confinement'. According to the string-fragmentation model, when a quark has sufficient kinetic energy, it moves away from the other quarks and potential energy will increase with growing distance until enough energy is present to create a new pair of a quark and anti-quark. In collisions with high momentum transfer, target hadrons will break up and new hadrons will be created as described by this string-fragmentation model.

The cross section for lepton-nucleon scattering is directly related to so-called structure functions which give the momentum and spin distribution of the quarks inside the nucleon. The spin independent structure functions for inclusive lepton–nucleon scattering are referred to as F_1 and F_2.

When a polarised lepton scatters from a polarised nucleon, the cross section is sensitive to the orientation of the lepton spin relative to the spin of the quarks inside the nucleon. The spin dependent structure functions for inclusive lepton–nucleon scattering are referred to as g_1 and g_2.

The Nucleon Spin Structure

Measurements of g_1 performed by a series of experiments indicated that the quark spins only contribute to a small fraction of the proton spin. This result is referred to as the 'EMC spin crisis'. This surprising result inspired the proposal of new experiments which could validate the earlier results and increase the accuracy of the measurements. Also, there was a growing interest in the contribution of quark spin to the neutron spin to test the Bjørken sum rule which constitutes a fundamental test of QCD.

HERMES is an experiment designed to scatter polarised electrons from polarised nucleons in order to study the nucleon spin structure. At HERMES different targets can be used; in 1995 data was taken mainly with a polarised ^{3}He gas target, in later years polarised hydrogen and polarised deuterium targets were used. Polarised ^{3}He gas effectively can be considered as a polarised neutron target. An important feature of the HERMES experiment is its excellent particle identification capabilities which allows for detailed studies of semi-inclusive physics, such as the flavour decomposition of the spin quark distributions.

The ρ^0 Vector Meson

Real and virtual photons can fluctuate into quark–antiquark pairs. The interaction of the quark–antiquark pair with the target permits it to fluctuate into a physical vector meson state (ρ^0, ω, ϕ, J/Ψ, ...). The interaction can be regarded phenomenologically either as the exchange of a Pomeron particle between a vector meson and the target (the basis of the vector meson dominance (VMD) model) or, at higher scattering energies, as the exchange of a gluon pair between a virtual quark–antiquark pair and the constituents of a nucleon in the target (perturbative QCD).

In the work presented here, ρ^0 meson production is studied. The dependence of the ρ^0 production cross section on the virtuality of the photon Q^2 and the invariant mass of the outgoing hadronic system W, is presented. This gives an indication of the accuracy of certain models in the kinematical region of the HERMES experiment, which lies between low energy and high energy experiments and might help to gain insight in the mechanisms that reign this transition region.

Moreover, angular distributions and their associated 'helicity-transfer' amplitudes are presented, which give more knowledge about the transfer of helicity of the virtual photon to the ρ^0 meson.

In future analyses, HERMES can take advantage of its polarised lepton beam and polarised gas target to study these helicity-transfer amplitudes in more detail than presented here.

Kinematically, the HERMES data cover a range in Q^2 and W not covered by other experiments.

Contents of this Thesis

The work presented here deals with data taken in 1995, which was the first year that the HERMES spectrometer was taken in commission. Since one of the main interests of the HERMES experiment is the study of the polarisation of the nucleon and its constituents, the theory of polarised structure functions will be explained in detail in chapter 2. The main subject of the work presented here, however, is ρ^0 production. Various theoretical models that describe ρ^0 meson production are presented in the second half of chapter 2.

The experimental set-up is described in chapter 3 and comprises the accelerator, the target and the HERMES spectrometer.

In order to decode and interpret the data, dedicated software packages are needed. An overview of HERMES -specific software is given in chapter 4. The algorithm that is used to calculate the efficiencies of the tracking chambers is explained in more detail.

In chapter 5, the particle identification scheme is outlined, quality requirements on the data are explained and the use of Monte Carlo is described.

In chapter 6, the results of the ρ^0 analysis are presented. The results are compared to theoretical models and a number of conclusions will be drawn.

Chapter 2

Physics at HERMES

HERMES is an internal target experiment with two important features: it uses a longitudinally polarised incoming lepton beam and a gas target which can be polarised parallel and anti-parallel with respect to the beam direction. This enables HERMES to perform spin-dependent measurements on the structure of nucleons via Deep Inelastic Scattering (DIS).

This chapter gives an overview of the kinematics and a discussion of the physics issues which can be accessed by the HERMES experiment.

2.1 Kinematics

Fig. 2.1 depicts the process where a lepton scatters from a nucleon via the exchange of a virtual photon. The four-vector of the incoming lepton is denoted by k, with E its energy in the HERMES laboratory frame; the four-vector of the scattered lepton is denoted by k', with E' its energy in the laboratory frame. The scattering angle is indicated by θ. The virtual photon has momentum $q = k - k'$. The momentum of the final hadronic state is denoted by $p' = (E_h, \vec{p'})$. Often the Lorentz invariant quantities Q^2, ν and W are used, where

$$Q^2 = -q_\mu q^\mu = -(k-k')^2 \stackrel{\text{lab}}{=} 4EE'\sin^2(\theta/2) > 0, \tag{2.1}$$

$$\nu = \frac{p \cdot q}{M} \stackrel{\text{lab}}{=} E - E', \tag{2.2}$$

$$W^2 = p'^2 \stackrel{\text{lab}}{=} M^2 + 2M\nu - Q^2, \tag{2.3}$$

with M the mass of the nucleon. In the laboratory frame, the momentum of the virtual photon can be written as $q = (\nu, \vec{q})$, with $\nu = E - E'$. The quantities Q^2 and ν completely constrain the kinematics of an inclusive event. In the analysis of DIS events two dimensionless variables, x and y, are used, where

$$x = \frac{Q^2}{2p \cdot q} \stackrel{\text{lab}}{=} \frac{Q^2}{2M\nu}, \tag{2.4}$$

$$y = \frac{p \cdot q}{p \cdot k} \stackrel{\text{lab}}{=} \frac{\nu}{E}. \tag{2.5}$$

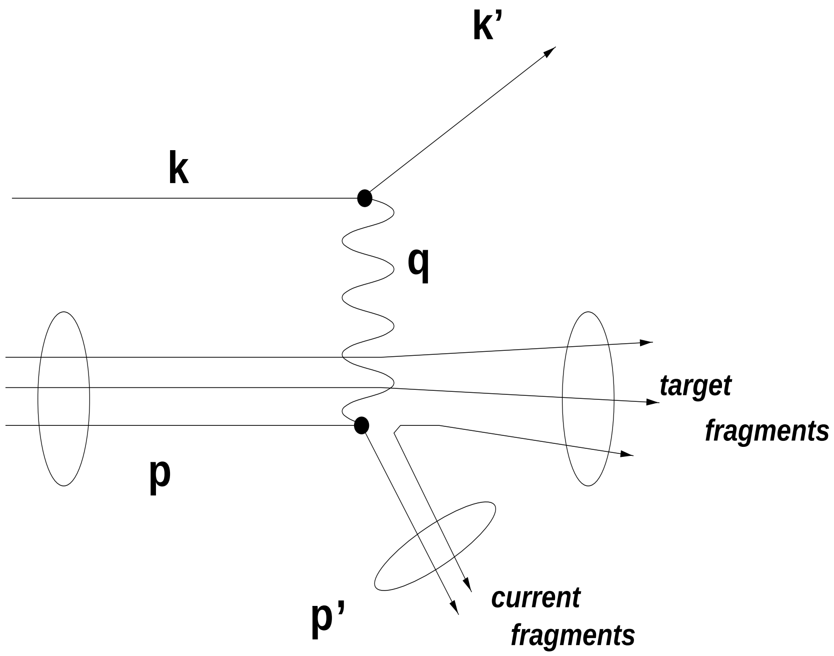

Figure 2.1: *Deep inelastic scattering of a lepton from a nucleon. In case of inclusive scattering, only the scattered lepton is detected. In case of semi-inclusive scattering also the final hadronic state of the current fragments is identified.*

Instead of using Q^2 and ν, one often employs Q^2 and x for a complete characterisation of the kinematics of a DIS event.

In semi-inclusive analyses the frame dependent variables z and x_F are used, with

$$z = \frac{E_h}{\nu} \tag{2.6}$$

and

$$x_F = \frac{p'_{||}}{W}, \tag{2.7}$$

where $p'_{||}$ is the component of $\vec{p}'$ parallel to the direction of the virtual photon and p' is calculated in the hadronic centre of mass frame, boosted with $\beta = |\overrightarrow{q}|/(\nu + M)$. The variable x_F can be used to separate current fragments and target fragments.

The acceptance of the HERMES spectrometer allows measurements in the kinematic range shown in Fig. 2.2. The line denoted by $W = 2$ GeV represents a cut made in the analysis to avoid the kinematic region where resonance production appears. The line denoted by $Q^2 = 1$ GeV^2 represents the general DIS cut. The line denoted by $y = 0.85$ represents a cut made in the analysis to avoid the kinematic region where large radiative corrections are necessary. The line denoted by $\theta = 220$ mrad indicates the limits of the detector acceptance.

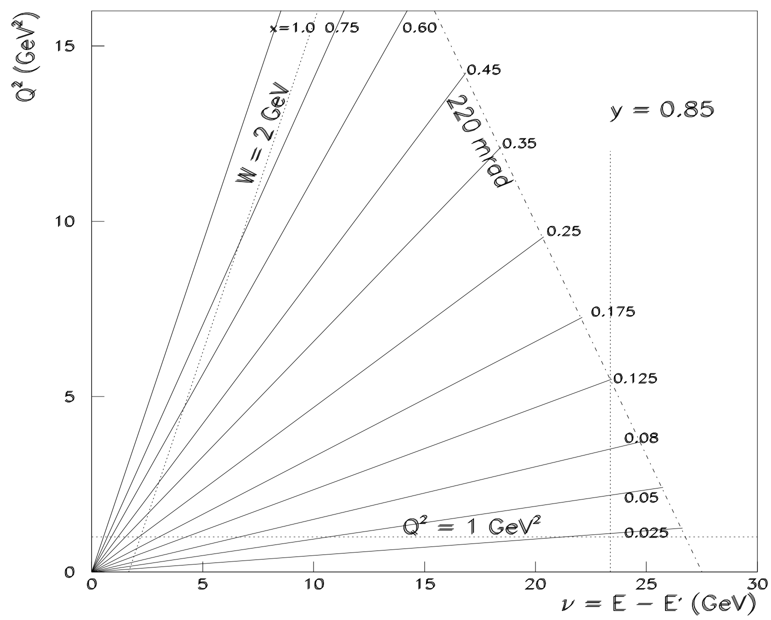

Figure 2.2: *The kinematic acceptance of* HERMES *for a beam energy of 27.5 GeV. For a given combination of Q^2 and ν, all other kinematic variables are fixed.*

2.2 Deep Inelastic Scattering

2.2.1 Cross Sections for DIS

In general for DIS events, in the one-photon exchange approximation, the cross section can be expressed in terms of the leptonic tensor $L_{\mu\nu}$ and the hadronic tensor $W_{\mu\nu}$ as

$$\frac{d^2\sigma}{dQ^2 d\nu} = \frac{4\pi\alpha^2}{Q^4 E^2} L_{\mu\nu} W^{\mu\nu}, \tag{2.8}$$

where $\alpha \approx \frac{1}{137}$ is the coupling constant of QED. The lepton tensor L is calculable directly from QED by using the Feynman rules and one finds (see Ref. [64]),

$$\begin{aligned} L_{\mu\nu} &= \frac{1}{2}\sum_{s'} \bar{u}(k',s')\gamma_\mu u(k,s)\bar{u}(k,s)\gamma_\nu u(k',s'), \\ &= \bar{u}(k')\gamma_\mu u(k,s)\bar{u}(k,s)\gamma_\nu u(k'), \\ &= 2[k_\mu k'_\nu + k_\nu k'_\mu - (k\cdot k' - m^2)g_{\mu\nu}] + 2i\epsilon_{\mu\nu\alpha\beta}S^\alpha(k-k')^\beta, \\ &= 2[k_\mu k'_\nu + k_\nu k'_\mu - \frac{1}{2}Q^2 g_{\mu\nu}] + 2i\epsilon_{\mu\nu\alpha\beta}S^\alpha(k-k')^\beta. \end{aligned} \tag{2.9}$$

The last term $2i\epsilon_{\mu\nu\alpha\beta}S^\alpha(k-k')^\beta$ represents the antisymmetric spin dependent part of the cross section, where S is the spinor of the incoming lepton given by

$$S^\alpha = \frac{1}{2}\bar{u}(k,s)\gamma^\alpha\gamma_5 u(k,s), \tag{2.10}$$

and $\epsilon_{\mu\nu\alpha\beta}$ is an element of the Levi-Cevita tensor.

The hadronic tensor, which describes the incoming and outgoing nucleons, cannot be expressed directly in fundamental fields of the incoming and outgoing fermions. Current conservation at the hadronic vertex, parity conservation and invariance under time reversal yields

$$\begin{aligned} W_{\mu\nu} &= (-g_{\mu\nu} + \frac{q_\mu q_\nu}{q^2})W_1(q^2,\nu) \\ &+ (p_\mu - \frac{p\cdot q}{q^2}q_\mu)(p_\nu - \frac{p\cdot q}{q^2}q_\nu)\frac{W_2(q^2,\nu)}{M^2} \\ &+ i\epsilon_{\mu\nu\alpha\beta}q^\alpha M S_N^\beta G_1(q^2,\nu) \\ &+ i\epsilon_{\mu\nu\alpha\beta}q^\alpha[(p\cdot q)S_N^\beta - (S_N\cdot q)p^\beta]\frac{G_2(q^2,\nu)}{M}. \end{aligned} \tag{2.11}$$

Here, S_N denotes the polarisation vector of the spin-1/2 target nucleon and W_1, W_2, G_1 and G_2 are scalar functions depending on Q^2 and ν which describe the electromagnetic structure of the target nucleon. When averaging over incoming lepton helicity states, the terms containing G_1 and G_2 vanish.

2.2.2 Unpolarised Structure Functions

In the unpolarised case, only the first two terms of Eq. (2.11) and the first term of Eq. (2.9) remain, resulting in an expression for the cross section as

$$\frac{d^2\sigma}{dQ^2 d\nu} = \frac{4\pi\alpha^2}{Q^4E^2}(W_2(Q^2,\nu)\cos^2\frac{\theta}{2} + 2W_1(Q^2,\nu)\sin^2\frac{\theta}{2}). \tag{2.12}$$

By introducing two dimensionless structure functions F_1 and F_2 with

$$F_1(x,Q^2) = MW_1(x,Q^2), \tag{2.13}$$
$$F_2(x,Q^2) = \nu W_2(x,Q^2), \tag{2.14}$$

one can write the unpolarised DIS cross section as

$$\frac{d^2\sigma}{dx dQ^2} = \frac{4\pi\alpha^2}{Q^4}\cdot[F_1(x,Q^2)\cdot y^2 + \frac{F_2(x,Q^2)}{x}\cdot(1-y-\frac{Mxy}{2E})]. \tag{2.15}$$

The unpolarised cross section can be related to the photon absorption cross section for transversely (σ_T) and longitudinally (σ_L) polarised photons by

$$\frac{d^2\sigma}{dx dQ^2} = \Gamma_T\left(\sigma_T(x,Q^2) + \epsilon\sigma_L(x,Q^2)\right). \tag{2.16}$$

Here, Γ_T is the flux of transversely polarised virtual photons, given by

$$\Gamma_T(x,Q^2) = \frac{\alpha E'}{4\pi^2 ME}\left(\frac{1}{x}-1\right)\frac{1}{1-\epsilon}. \tag{2.17}$$

In the two previous expressions ϵ is the virtual photon polarisation parameter which quantifies the degree of longitudinal polarisation of the virtual photons,

$$\epsilon = \frac{1-y}{1-y+y^2/2} \stackrel{\text{lab}}{=} \frac{1}{1+2(1+\nu^2/Q^2)\,\tan^2(\theta/2)}. \tag{2.18}$$

If one defines $R(x, Q^2) = \sigma_L/\sigma_T$, the ratio of the transversely and the longitudinally polarised virtual photon absorption cross sections, one can write R in terms of the unpolarised structure functions as

$$R(x, Q^2) = \frac{F_2(x, Q^2)}{2xF_1(x, Q^2)}\left(1 + \frac{4M^2x^2}{Q^2}\right) - 1. \tag{2.19}$$

Note that in order to extract R, not only x and Q^2, but also ϵ has to be varied.

The unpolarised two-fold differential cross section can be written as

$$\frac{d^2\sigma}{dxdQ^2} = \frac{4\pi\alpha^2}{xQ^4}F_2(Q^2, x)[(1 - y - \frac{Q^2}{4E^2}) + \frac{(y^2 + Q^2/E^2)}{2(1 + R(x, Q^2))}]. \tag{2.20}$$

2.2.3 Quark Parton Model

In the Quark Parton Model (QPM), one interprets structure functions in terms of an elastic scattering cross section of two point-like spin 1/2 fermions. The cross section for such a process can be expressed as

$$\frac{d\sigma}{d\Omega dE'} = \frac{4\alpha^2E'^2}{Q^4}\left(\cos^2\frac{\theta}{2} + \frac{Q^2}{2m^2}\sin^2\frac{\theta}{2}\right)\delta\left(\nu - \frac{Q^2}{2m}\right). \tag{2.21}$$

Under the assumption that the quarks in the nucleon at high Q^2 behave like free spin 1/2 particles, one can simplify W_1 and W_2 as

$$2mW_1(Q^2, \nu) = \frac{Q^2}{2m}\delta(\nu - \frac{Q^2}{2m}), \tag{2.22}$$

$$\nu W_2(Q^2, \nu) = \delta(\nu - \frac{Q^2}{2m}), \tag{2.23}$$

with m the mass of the struck parton (i.e. quark).

Hence, by using $x = Q^2/2m\nu$, W_1 and W_2 only depend on the dimensionless scaling variable x. Elastic scattering from a quark, with this definition of x, and by using the delta-functions of Eqs. (2.22, 2.23), would lead to $x = 1$.

Since the mass of the quark is not known, x is defined as $x = Q^2/2M\nu$ which can be interpreted as the fractional momentum of the struck quark in the infinite momentum frame. In the QPM one has

$$m_q^2 = (p'_q)^2 = (\xi p + q)^2,$$

with m_q the mass of the struck quark, p'_q the four-momentum of the struck quark and ξ the fraction of the total momentum of the nucleon carried by the struck quark. In the infinite momentum frame (often referred to as the Bjørken scaling limit, with $Q^2, \nu \to \infty$ so that $\xi^2 M^2/Q^2 \to 0$), one can rewrite this as

$$\begin{aligned}
& m_q^2 = 0 = \xi^2 M^2 + 2\xi M\nu + q^2 \\
\Longrightarrow \quad & \tfrac{\xi^2 M^2}{q^2} + 1 = \tfrac{-2\xi M\nu}{q^2}, \\
\Longrightarrow \quad & \xi = \tfrac{-q^2}{2M\nu}.
\end{aligned}$$

In this reference frame, the transverse momentum $P_T = 0$. Hence, x can be interpreted as the fraction of the total momentum of the nucleon carried by the struck quark, as long as $Q^2 \gg x^2 M^2$.

Under the assumption that lepton scattering from a nucleon can be described as elastic scattering from quarks with their momenta parallel to the momentum of the nucleon, at high Q^2 and ν, the unpolarised cross section of DIS can be expressed in terms of the structure functions $F_1(x)$ and $F_2(x)$

$$F_1(x) \;=\; MW_1(x) = \frac{1}{2}\sum_i e_i^2 f_i(x), \tag{2.24}$$

$$F_2(x) \;=\; \nu W_2(x) = \sum_i x e_i^2 f_i(x), \tag{2.25}$$

with $f_i(x)$ the probability of finding parton i with momentum fraction x in the nucleon. In the QPM, F_1 and F_2 are related through the so-called Callan-Gross relation as

$$F_2(x) = 2xF_1(x). \tag{2.26}$$

Deviations from the Parton Model

Note that the discussion presented above is only valid in the Bjørken scaling limit. In fact, Q^2 scaling violations occur which can be interpreted as an indication that with increasing Q^2 the probability to scatter from a parton with low momentum increases, as is illustrated by Fig. 2.3.

Hence, the more accurate description of partons, QCD, is required, where partons are associated with quarks and gluons, and the strong interaction between quarks and gluons is taken into account. The Q^2 dependence of the parton distribution functions are described by the GLAP equations, derived both by Altarelli and Parisi (see Ref. [12]) and by Gribov and Lipatov (see Ref. [65]).

2.2.4 Polarised Structure Functions

By measuring polarised structure functions, the difference of the cross sections of lepton scattering from nucleons with opposite nucleon spin projections can be studied. In the expression for the relative difference, the so-called cross section asymmetry, the unpolarised terms in Eqs. (2.9), (2.11) which appear in Eq. (2.8) cancel and only the spin-asymmetric terms remain after the contraction of the leptonic tensor L and the hadronic tensor W.

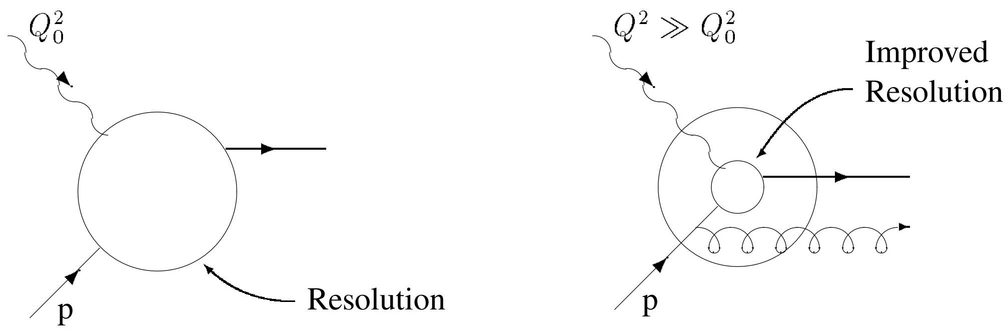

$\gamma^*(Q_0^2)$ probes $q(x)$

$\gamma^*(Q^2)$ resolves softer quarks inside $q(x)$

Figure 2.3: *Quark structure as probed by a virtual photon as Q^2 increases. At high values of Q^2 the probability to probe a quark at relatively low momentum increases.*

In the Bjørken scaling limit, as in the unpolarised case, one can rewrite G_1 and G_2 into the spin structure functions g_1 and g_2 as

$$M^2 \nu G_1(Q^2, \nu) \overset{\substack{Q^2 \to \infty \\ \nu \to \infty}}{=} g_1(x, Q^2), \tag{2.27}$$

$$M \nu^2 G_2(Q^2, \nu) \overset{\substack{Q^2 \to \infty \\ \nu \to \infty}}{=} g_2(x, Q^2). \tag{2.28}$$

The cross section difference for a longitudinally polarised beam incident on a parallel and antiparallel longitudinally polarised target is expressed as

$$\frac{d^2(\sigma^{\stackrel{\rightarrow}{\Leftarrow}} - \sigma^{\stackrel{\rightarrow}{\Rightarrow}})}{dx dy} = \frac{e^4}{2\pi Q^2} \left[(1 - \frac{y}{2} - \frac{y^2}{4} \frac{Q^2}{\nu^2}) g_1(x, Q^2) - \frac{y}{2} \frac{Q^2}{\nu^2} g_2(x, Q^2) \right]. \tag{2.29}$$

The expression for the measured asymmetry $A_{||}$ for a longitudinally polarised target and beam is

$$A_{||} = \frac{\sigma^{\stackrel{\rightarrow}{\Leftarrow}} - \sigma^{\stackrel{\rightarrow}{\Rightarrow}}}{\sigma^{\stackrel{\rightarrow}{\Leftarrow}} + \sigma^{\stackrel{\rightarrow}{\Rightarrow}}}. \tag{2.30}$$

The expression for the measured asymmetry $A_\perp$ for a transversely polarised target and longitudinally polarised beam becomes

$$A_\perp = \frac{\sigma^{\rightarrow\Uparrow} - \sigma^{\rightarrow\Downarrow}}{\sigma^{\rightarrow\Uparrow} + \sigma^{\rightarrow\Downarrow}}. \tag{2.31}$$

Since the polarisation of the virtual photon is not equal to the polarisation of the incoming lepton beam, the measured asymmetries have to be corrected for the polarisation transfer from the leptons to the virtual photon by using [46]

$$A_{\|} = D(A_1 + \eta A_2), \tag{2.32}$$
$$A_{\perp} = d(A_2 - \xi A_1), \tag{2.33}$$

with depolarisation factors given by

$$D = \frac{y(2-y)}{y^2 + 2(1-y)(1+R)}, \tag{2.34}$$
$$\eta = \frac{4\frac{Mx}{Q}(1-y)}{2-y}, \tag{2.35}$$
$$d = D\sqrt{\frac{2\epsilon}{1+\epsilon}}, \tag{2.36}$$
$$\xi = \eta\frac{1+\epsilon}{2\epsilon}. \tag{2.37}$$

Subsequentially, A_1 and A_2 can be related to g_1 and g_2 as

$$A_1 = \frac{g_1 - \gamma^2 g_2}{F_1}, \tag{2.38}$$
$$A_2 = \gamma\frac{g_1 + g_2}{F_1}, \tag{2.39}$$

where $\gamma = 2Mx/Q$.

Since γ^2 is small for the HERMES kinematics, the contribution from A_2 is small and g_1 can be approximated, using Eq.(2.19), by

$$g_1 \approx \frac{A_{\|}}{D} F_2 \frac{1}{2x} \frac{1+\gamma^2}{(1+R)}. \tag{2.40}$$

A simple depiction of the interpretation of an asymmetry measurement is shown in Fig. 2.4. In the naive parton model, one has scaling, i.e. $g_1(x, Q^2) = g_1(x)$, where the latter can be expressed as:

$$g_1(x) = \frac{1}{2}\sum_i e_i^2 (q_i^{\rightrightarrows}(x) - q_i^{\rightleftarrows}(x)), \tag{2.41}$$

with $q_i^{\rightrightarrows}(x)$ and $q_i^{\rightleftarrows}(x)$ the probabilities of finding parton i with momentum fraction x in the nucleon with the spin of the struck parton respectively parallel and antiparallel to the spin of the nucleon. Only interactions between quarks and gluons contribute to g_2, which is a measure of the amount of quark spin directed perpendicular to the nucleon spin. In the QPM, $g_2 = 0$.

HERMES was designed to measure g_1 of the nucleon by scattering a polarised lepton beam from polarised ^{1}H, ^{2}H and ^{3}He targets. In the start-up phase, HERMES carried out measurements with polarised ^{3}He and the polarised structure function of the neutron, g_1^n, has been

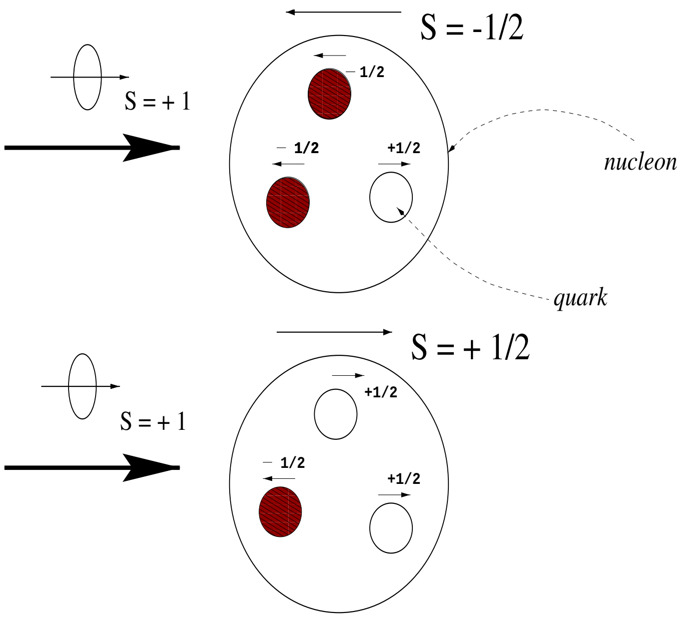

Figure 2.4: *Schematic representation of a photon interacting with quarks inside a nucleon. A photon with spin 1 can only interact with a spin 1/2 quark whose spin projection is antiparallel to the helicity of the photon (represented by the filled circles). The amount of quarks within the nucleon with an antiparallel spin is dependent on the polarisation state of the nucleon.*

extracted under the assumption that effectively the neutron in the ^{3}He nucleus is polarised. The experimental set-up employed for these measurements is described in chapter 3.

Fig. 2.5 shows data for g_1^n, as derived from using a polarised ^{3}He target, including the HERMES measurement performed in 1995. Fig. 2.6 shows the world data of the polarised structure function of the deuteron, g_1^d, and the neutron, g_1^n. Fig. 2.7 shows the world data of the polarised structure function of the proton, g_1^p. For a more detailed description of the extraction of g_1^n from HERMES data, see Ref. [32].

2.2.5 Sum Rules

One can arrive at a physical interpretation of the structure functions by studying their moments and by comparing those with predictions from theory. Moments of structure functions are integrals, defined as

$$\Gamma_n([F]) = \int dx\, x^{n-1} F(x, Q^2). \tag{2.42}$$

In DIS, a well-known example is the Gottfried sum rule [49] which is based on the assumption that the integral over the valence quark distributions has to equal the valence quark content of the nucleon. Hence

$$\int_0^1 dx\, u_v(x) = 2, \ \int_0^1 dx\, d_v(x) = 1. \tag{2.43}$$

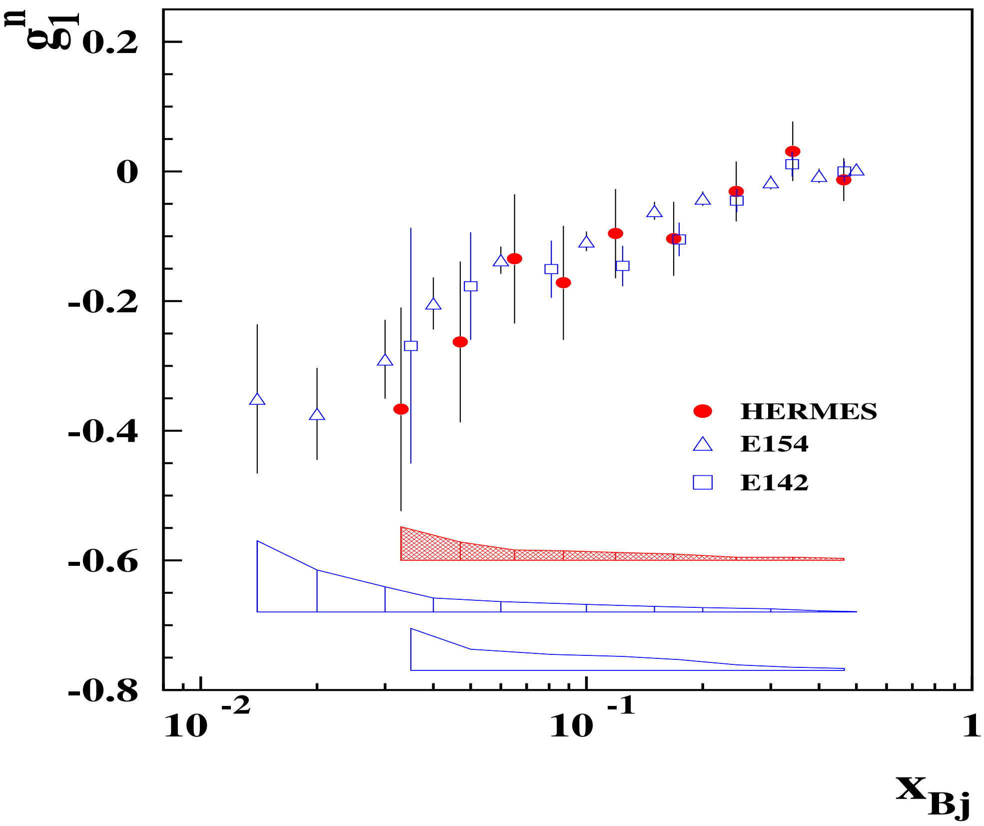

Figure 2.5: *Results for the spin structure function of the neutron, $g_1^n(x)$, determined by DIS from polarised ^{3}He. Data were obtained by the* HERMES *experiment (see Ref. [3]) at* DESY *and the* E-142 *experiment (see Ref. [13]) and the* E-154 *experiment (see Ref. [84]) at SLAC.*

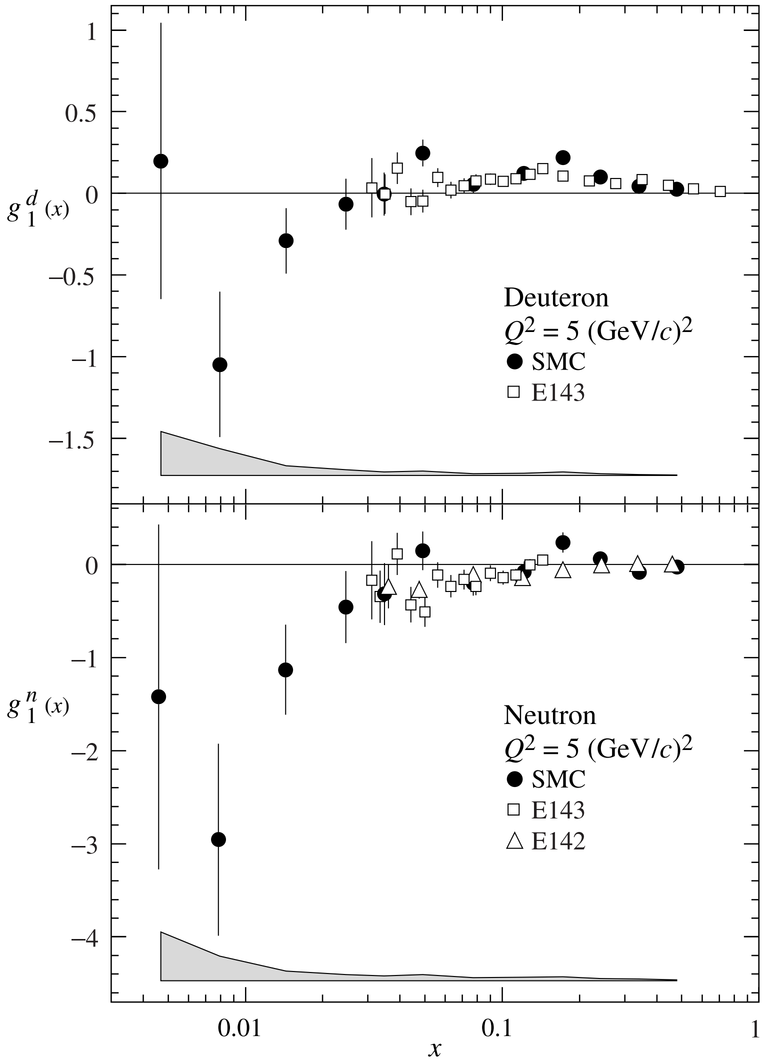

Figure 2.6: *World data on the structure functions $g_1^d(x)$ of the deuteron and $g_1^n(x)$ of the neutron [22] from deep-inelastic polarised electron scattering (E142, E143) and DIS muon scattering (SMC). All data are evolved to $Q^2 = 5\,\mathrm{GeV}^2$. The errors are statistical only, and as an example, the SMC systematic errors are indicated by the shaded area.*

With $u_v = u^{\mathrm{proton}} = d^{\mathrm{neutron}}$ and $d_v = d^{\mathrm{proton}} = u^{\mathrm{neutron}}$ according to isospin symmetry considerations. The Gottfried sum rule relates $F_2^p(x, Q^2)$ for the proton to $F_2^n(x, Q^2)$ for the neutron as

$$S_G = \int_0^1 \frac{dx}{x}(F_2^p(x, Q^2) - F_2^n(x, Q^2)) = \frac{1}{3}. \qquad (2.44)$$

Recent data from muon experiments at CERN [16] yield $S_G = 0.221 \pm 0.008$ (stat) ± 0.019 (syst) which indicates a violation of this sum rule.

This violation might be due to an asymmetry in the flavour distributions of the sea quarks, so

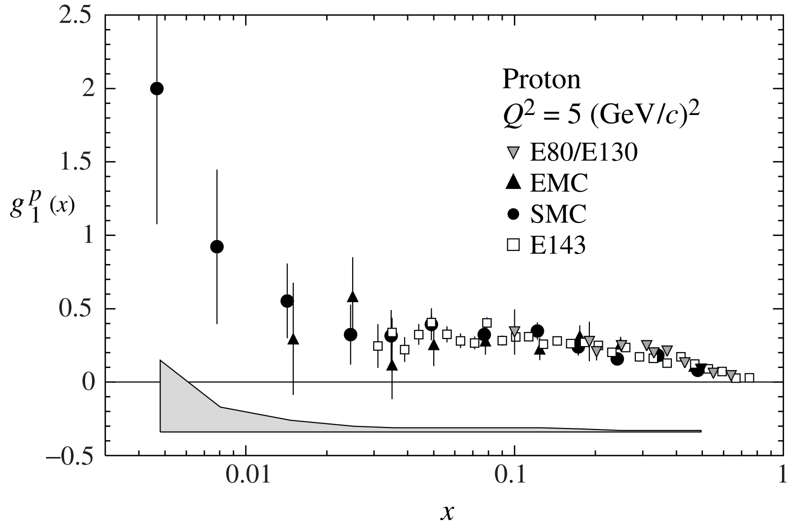

Figure 2.7: *World data on the structure function $g_1^p(x)$ of the proton [22] from deep-inelastic polarised electron scattering (E142, E143) and DIS muon scattering (SMC), at $Q^2 = 5\,\mathrm{GeV}^2$. The errors are statistical only, and as an example, the SMC systematic errors are indicated with the shaded area.*

that $\bar{u}(x) \neq \bar{d}(x)$.

From fundamental principles one can derive the Bjørken sum rule [30], which relates g_1^p of the proton to g_1^n of the neutron as

$$\int_0^1 dx(g_1^p(x,Q^2) - g_1^n(x,Q^2)) = \frac{1}{6}\left|\frac{g_A}{g_V}\right|(1 + \mathrm{QCD\ corrections}) = 0.21(1 + \mathrm{QCD\ corrections}). \tag{2.45}$$

The quantities g_A and g_V are the axial- and vector coupling constants in weak neutron β–decay. The QCD corrections are necessary to take into account the interactions of quarks with each other through the exchange of gluons and these couplings can be classified as powers of α_s. The QCD corrections to the Bjørken sum rule have been calculated to order α_s^3, and one has (see Ref. [51])

$$\int_0^1 dx(g_1^p(x,Q^2) - g_1^n(x,Q^2)) = \frac{1}{6}\left|\frac{g_A}{g_V}\right|\left[1 - \frac{\alpha_s(Q^2)}{\pi} - 3.5833\left(\frac{\alpha_s(Q^2)}{\pi}\right)^2 - 20.2153\left(\frac{\alpha_s(Q^2)}{\pi}\right)^3\right]. \tag{2.46}$$

At present, the Bjørken sum rule is known to be valid to an accuracy of 8 % based on data obtained in experiments performed at CERN (see Ref. [6]) and SLAC (see Ref. [13]).

A sum rule for $g_1(x)$ for the proton and the neutron separately is the Ellis-Jaffe sum rule. For this sum rule in addition to the assumptions made for the Bjørken sum rule, SU(3) flavour symmetry and an unpolarised strange sea is assumed. Theoretically, one finds (see Ref. [63]),

$$\Gamma_1^p = \int_0^1 dx\, g_1^p(x) = 0.185, \tag{2.47}$$

and

$$\Gamma_1^n = \int_0^1 dx\, g_1^n(x) = -0.024. \tag{2.48}$$

In 1987 the EMC published a result on the Ellis-Jaffe sum rule for the proton of $\Gamma_1^p = 0.126 \pm 0.010 \pm 0.015$ which constitutes a significant deviation from the predicted value (see Ref. [19]). Assuming the validity of the Bjørken sum rule this result implies that the asymmetry measured with polarised neutrons should be significantly negative over at least part of its x range. In addition, the result implies that a rather small fraction of the spin of the nucleon is carried by the spin of the quarks.

The result of the HERMES measurement of the Ellis-Jaffe sum rule for the neutron extracted from the 1995 data was $\Gamma_1^n = -0.037 \pm 0.013_{stat} \pm 0.005_{syst} \pm 0.006_{extrapol}$ [3, 32]. At SLAC and SMC similar values were measured.

At leading twist the only gauge invariant contributions are due to the non-singlet and singlet axial currents. The u, d and s wave functions transform according to SU(3) symmetry. The SU(3) group of transformations is generated by the unit matrix and eight 3×3 matrices. In the standard representation of this group, only the unit matrix a_0 and the two matrices with diagonal elements, a_3 and a_8 have eigenvectors. The first moment of g_1 can be written as

$$\Gamma_1^{p(n)} = \frac{C_1^S(Q^2)}{9} a_0 + \frac{C_1^{NS}(Q^2)}{12}(+(-)a_3) + \frac{1}{2}a_8, \tag{2.49}$$

where C_1^S and C_1^{NS} are the non-singlet and singlet coefficient functions respectively and a_0, a_3 and a_8 are the axial charge matrix elements which can be written as

$$\begin{aligned} a_0 &= a_u + a_d + a_s, \\ a_3 &= a_u - a_d \\ a_8 &= a_u + a_d - 2a_s. \end{aligned} \tag{2.50}$$

C_1^S has been computed to $\mathcal{O}(\alpha_s^2)$ and C_1^{NS} has been computed to $\mathcal{O}(\alpha_s^3)$. In the context of the QPM, the first moments of g_1 can be written as

$$\Gamma_1^p = \int_0^1 dx\, g_1^p(x) = \frac{1}{18}(4\Delta u + \Delta d + \Delta s), \tag{2.51}$$

and

$$\Gamma_1^n = \frac{1}{18}(\Delta u + 4\Delta d + \Delta s), \tag{2.52}$$

with $\Delta q \equiv \int_0^1 (q^+ - q^-)\, dx$ where $q^+(q^-)$ denotes the probability to find a quark with helicity parallel (antiparallel) to the nucleon spin. In the QPM, $a_f = \Delta f = \int_0^1 [q_f^\uparrow - q_f^\downarrow] dx$ and

$$\begin{aligned} a_0 &= \Delta\Sigma \\ a_3 &= F + D, \\ a_8 &= 3F - D, \end{aligned} \tag{2.53}$$

under the assumption of exact SU(3) symmetry for the axial flavour octet current. Here, F and D are quantities which are known from measurements of β decay of hyperons. In the QPM $a_0 = \Delta\Sigma$ represents the quark flavour singlet spin distribution which is associated with the intrinsic contribution of the quarks to the spin of the nucleon. Hence, by using

$$\Gamma_1^{p(n)} = \frac{C_1^S(Q^2)}{9}\Delta\Sigma + \frac{C_1^{NS}(Q^2)}{12}(+(-)(F+D)) + \frac{1}{2}(3F-D), \tag{2.54}$$

from the measurement of g_1 one can obtain a value for $\Delta\Sigma_q$ which represents the total spin carried by the quarks.

The total spin of the nucleon can be written as

$$\frac{1}{2} = \frac{1}{2}\Delta\Sigma_q + \Delta G + L_z, \tag{2.55}$$

with ΔG the amount of spin carried by the gluons, and L_z the contribution of orbital angular momentum of quarks and gluons to the nucleon spin.

Calculating $\Delta\Sigma_q^n$ from the earlier quoted value for Γ_1^n results in $\Delta\Sigma_q^n = 0.40 \pm 0.13$. Calculating $\Delta\Sigma_q^p$ from the earlier quoted value for Γ_1^p results in $\Delta\Sigma_q^p = 0.21 \pm 0.10$. Hence, some 30% of the nucleon spin is carried by the quark spins. Currently, plans for an upgrade of the HERMES detector are being studied, with the goal to measure J/Ψ and D^0 production to study the sensitivity to ΔG. With charm production, the lowest order DIS diagram, scattering from a single quark, is suppressed since presumably there is no significant charm content in the nucleon sea. The dominant process in this case is photon-gluon fusion, where a photon generates a $c\bar{c}$ pair, and one of these quarks couples to a gluon from the target. Either the charm quarks reunite to form a J/Ψ meson (hidden charm) or they separately form charmed hadrons like the D^0 (open charm).

2.2.6 Unpolarised (Semi-) Inclusive DIS

Semi-Inclusive Valence Quark Distributions

To obtain additional information about the flavour dependent quark distribution $f_{i/N}(x)$, the probability function f_i of a nucleon N, the hadronic final states of the current fragments have to be determined. One can measure the spin dependent cross section for different hadrons in the final state and use these data to derive the spin dependent flavour distributions.

The scattering process is depicted in Fig. 2.1, where the measured hadron is assumed to carry the flavour of the struck quark. The probability for a quark of flavour i to fragment into a hadron h is described by the fragmentation functions $D_i^h(z, Q^2)$. Assuming that scaling also holds for fragmentation functions, the semi-inclusive cross section is given by

$$\frac{1}{\sigma_{tot}}\frac{d\sigma_N^h(x,z)}{dz} = \frac{\sum_i e_i^2 f_{i/N}(x) D_i^h(z)}{\sum_i e_i^2 f_{i/N}(x)}. \tag{2.56}$$

This allows the determination of the valence quark distributions $u_v(x)$ and $d_v(x)$ (see Refs. [1] and [121]). Fig. 2.8 shows that within statistical errors the HERMES data for the valence quark ratio d_v/u_v agrees well with the EMC data both for a data sample containing all hadrons and for a data sample containing pions only. The fact that the hadron sample and the pion sample agree well with each other indicates that there is no large dilution of the hadron sample from target fragments. Both measurements indicate that at large x, the u quark dominates.

Asymmetries $A^\pi(x)$ can be extracted, for instance for the pion by using

$$A^\pi(x) = \frac{N_\uparrow^{\pi^+-\pi^-}(x) - N_\downarrow^{\pi^+-\pi^-}(x)}{N_\uparrow^{\pi^+-\pi^-}(x) + N_\downarrow^{\pi^+-\pi^-}(x)}. \tag{2.57}$$

The quantity $N_\uparrow^{\pi^+-\pi^-}$ is the difference between the number of leading (i.e. the hadrons with highest z) π^+ and π^- particles. Taking the difference of hadrons with opposite charge gets rid of all hadrons which are produced in pairs (e.g. resonances, vector meson production). The ratio suppresses the dependence on fragmentation functions. The up/down arrows denote parallel/antiparallel target polarisation.

Inclusive Unpolarised Structure Functions

Using data taken by HERMES in 1995 where the target gas was either hydrogen or deuterium, the ratio of F_2^n over F_2^p was extracted (see Ref. [1]). Under the assumption that the difference of the ratio of the longitudinal and transverse cross section, $R(Q^2, x)$, between hydrogen and deuterium is small, the structure function ratio F_2^d/F_2^p is proportional to the cross section ratio. Since the binding energy of deuterium is small compared to the energies involved in DIS, one can write $F_2^d = \frac{1}{2}(F_2^n + F_2^p)$ and hence

$$\frac{F_2^n}{F_2^p} = \frac{2F_2^d}{F_2^p} - 1. \tag{2.58}$$

In Fig. 2.9 one can see the agreement of HERMES data with the result of the NMC measurement (see Ref. [18]). When QCD effects are significant, structure functions are no longer expected to scale with Q^2. However, a similar Q^2 dependence is expected for the proton and the neutron with only small deviations due to the difference in quark composition. Therefore, the structure function ratio F_2^n/F_2^p should approximately scale. Measurements at CERN have confirmed this expectation. Since for small x the ratio is close to 1, one can draw the qualitative conclusion that in this x region the sea quarks (which are assumed to have similar distribution functions for the proton and the neutron) dominate.

2.3 Exclusive ρ^0 Production

2.3.1 Diffractive Physics

The term 'diffraction' is inherited from optical phenomena in physics. For example, when light of wavelength λ scatters from a black disk of radius R_0, then on a distant screen a diffraction

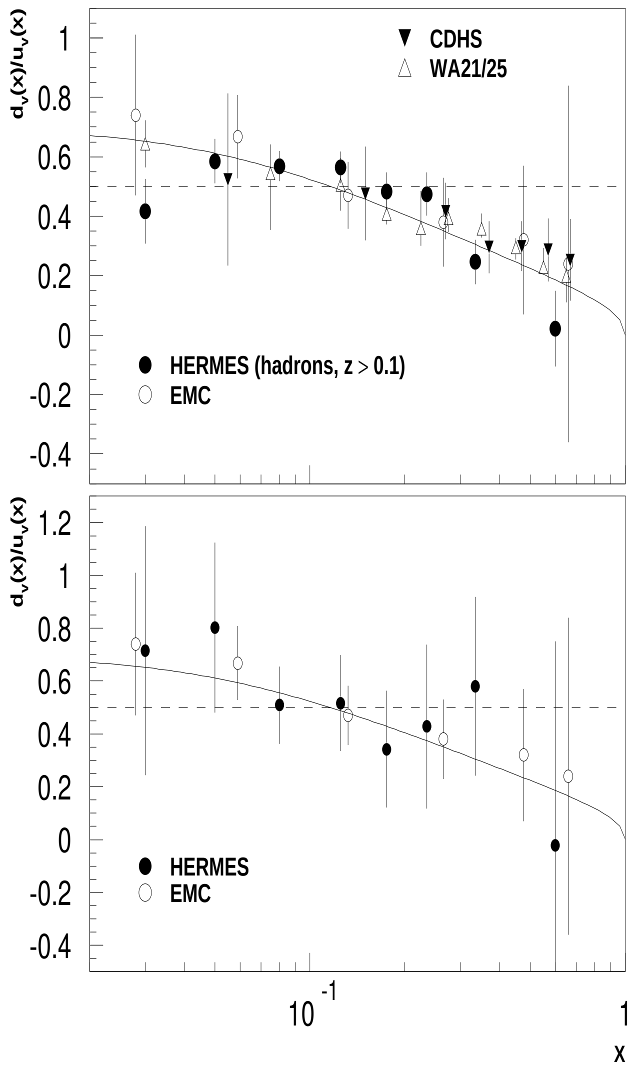

Figure 2.8: *Preliminary results for the valence quark distribution ratio d_v/u_v versus x from the* HERMES *experiment (see Ref. [1]) compared with the results of previous measurements at* CERN. *The upper plot shows the* HERMES *and* EMC *results using all hadrons. The triangles represent measurements from neutrino/anti neutrino experiments. The curve is based on the CTEQ3M (see Ref. [88]) parametrisation. The lower plots shows the same* EMC *data and CTEQ fit, but with* HERMES *data only using the pion sample. The dashed lines in both figures represent naive expectations from exact SU(6) symmetry.*

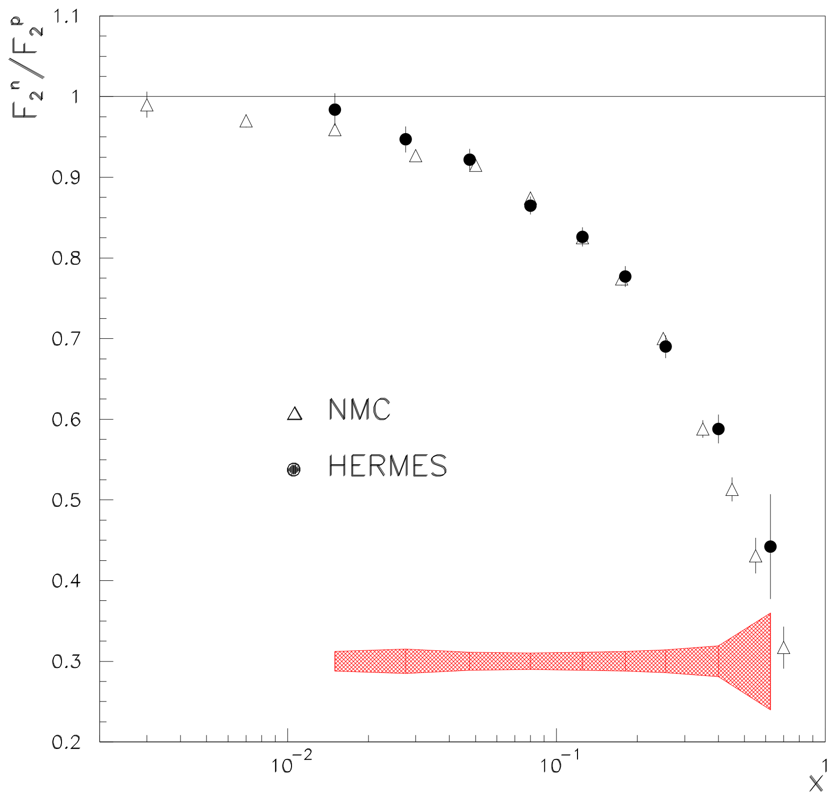

Figure 2.9: *The ratio F_2^n/F_2^p versus x from the* HERMES *experiment (see Ref. [1]), compared with data from a previous measurement at* CERN*. The grey area gives an upper bound of the systematic uncertainties.*

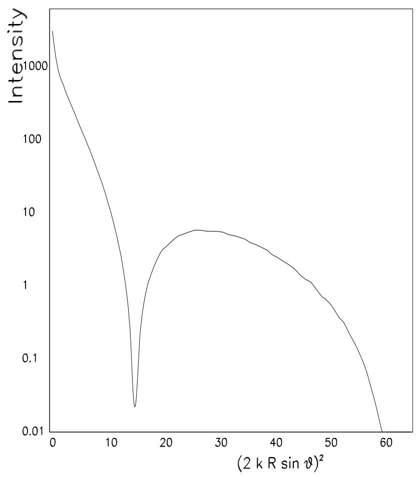

Figure 2.10: *Diffraction pattern of light scattered from a black disk showing the intensity versus four momentum transfer squared,* $4(R_0 k \sin(\theta))^2$.

pattern is produced, characterised by a large forward peak for scattering angle $\theta = 0$ and a series of symmetric minima and maxima, with the first minimum at $\theta_{min} \sim \pm\lambda/(2R_0)$. The intensity I as a function of the scattering angle is given as (see Ref. [15])

$$\frac{I(\theta)}{I(\theta = 0)} = \frac{[2J_1(x)]^2}{x^2} \sim 1 - \frac{R_0^2}{4} k^2 \sin(\theta)^2, \tag{2.59}$$

with $J_1(x)$ the Bessel function of the first order, $x = kR_0 \sin\theta$ and $k = 2\pi/\lambda$. Fig. 2.10 shows the dependence of the intensity on $(2kR_0 sin\theta)^2$, which is equivalent to the definition of the four momentum transfer squared, given below. In most textbooks only diffraction of one or more slits is discussed thoroughly. However, for scattering from a black disk we can use Babinet's principle (see pages 387 – 389 of Ref. [72]). According to Babinet's principle two complementary screens would produce exactly the same irradiance distributions. Two diffracting screens are said to be complementary when the transparent regions on one exactly correspond to opaque regions on the other.

In hadron–hadron scattering as depicted in Fig. 2.11, one has found a similar dependence of the cross section on the four momentum transfer squared, given by the Mandelstam variable $t = (p_1 - p_3)^2 \sim -(|\overrightarrow{p_1}|\theta)^2 < 0$. The approximation is valid when setting the masses equal to zero and keeping t small (i.e. $|\overrightarrow{p_1}| \sim |\overrightarrow{p_3}|$ and an opening angle close to zero). It was observed that

$$\frac{d\sigma}{dt} \sim \exp(bt) \sim 1 - b(|\overrightarrow{p_1}|\theta)^2, \tag{2.60}$$

with p_1 the incident proton momentum and b the impact parameter. In general, in scattering experiments, the impact parameter is defined as the distance from the centre of a nucleus to the location at which the interaction takes place and is related to the angular momentum l.

Fig. 2.12 gives an overview of the results of measurements of $d\sigma/dt$ for various proton–proton scattering experiments [66].

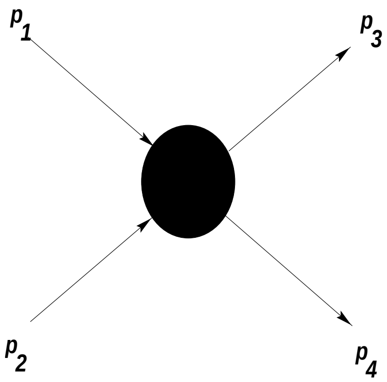

Figure 2.11: *Two-body reaction for hadron–hadron scattering with a two-body final state.*

It is observed that high-energy hadron-hadron interactions show the features of diffraction. In the case that the two outcoming hadrons emerge intact after the interaction, the diffractive reaction is called 'elastic'. When one of the hadrons is excited into a higher mass state with identical quantum numbers, the interaction is called single dissociative diffraction. Here, we will focus on single dissociative diffraction, in which the target nucleon emerges intact and the photon is excited to a ρ^0. Figure 2.13 depicts the process we are interested in.

2.3.2 Vector Meson Dominance

The physical state of the photon contains not only the bare state traditionally associated with the photon but also contributions from other bare states coupled to it. At high energies, the hadronic structure of the photon becomes apparent. Because the quantum numbers of the photon have to be conserved the quark-antiquark pairs into which it fluctuates can only combine to vector mesons where the spin is unity, such as the ρ^0 particle or the ω, ϕ or J/Ψ particles.

The Vector Meson Dominance (VMD) model expresses the photon-hadron scattering cross sections in terms of vector meson-hadron scattering cross sections. In 'VMD language' the photon fluctuates into a quark-antiquark pair which can be thought of as the superposition of various vector meson states V (ρ^0, ω, ϕ, J/Ψ).

In electroproduction one can express the virtual photoproduction cross sections $\sigma_T^{\gamma *,p}(Q^2, W)$ and $\sigma_L^{\gamma *,p}(Q^2, W)$ in terms of the real photoproduction ($Q^2 = 0$) as (see Ref. [23])

$$\sigma_T^{\gamma * p}(Q^2, W) = \sum_{V=\rho,\phi,\omega} \frac{e}{f_V} \left(\frac{m_V^2}{Q^2 + m_V^2} \right)^2 \sigma_T^{V,p}(W), \tag{2.61}$$

$$\sigma_L^{\gamma *,p}(Q^2, W) = \sum_{V=\rho,\phi,\omega} \frac{e}{f_V} \left(\frac{m_V^2}{Q^2 + m_V^2} \right)^2 \sigma_T^{V,p}(W) \frac{\xi^2 Q^2}{m_V^2}, \tag{2.62}$$

where e is the electromagnetic coupling constant, f_V measures the coupling of the vector meson to the photon and ξ^2 is an additional parameter related to R_ρ, given below. The total virtual

Figure 2.12: *Differential cross section for proton-proton elastic scattering versus four-momentum transfer squared for various incident proton momenta ([GeV/c]). As the energy increases, a classical diffraction pattern emerges. The plot is taken from Ref. [66].*

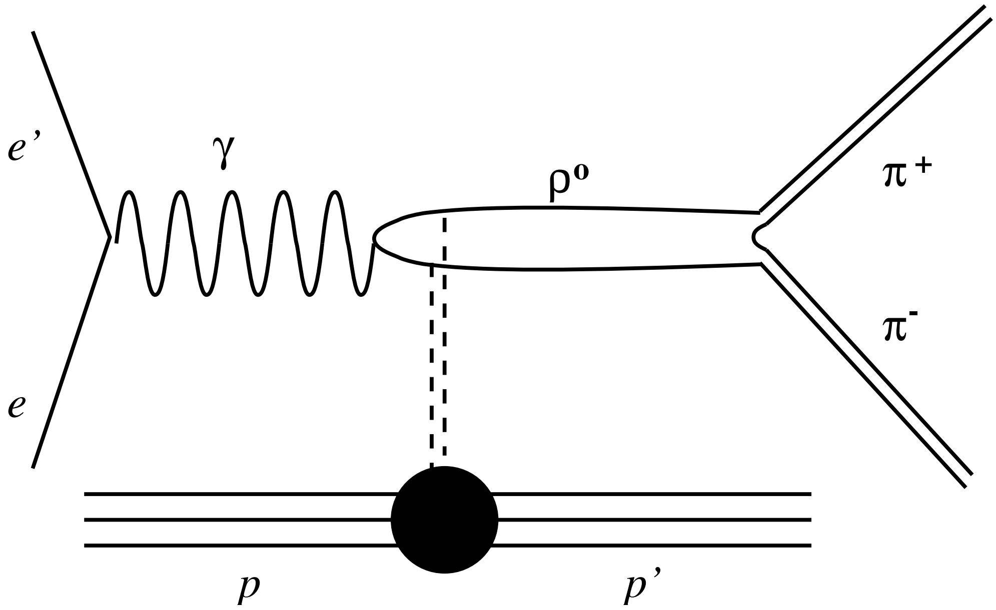

Figure 2.13: *Depiction of exclusive diffractive ρ^0 production.*

photoproduction cross section, for a given vector meson, is given by

$$\begin{aligned} \sigma^{V,p}(Q^2,W) &= \sigma_T^{V,p}(Q^2,W) + \epsilon\sigma_L^{V,p}(Q^2,W), \\ &= \sigma_T^{V,p}(W)\left(\frac{m_V^2}{Q^2+m_V^2}\right)^2(1+\epsilon R_\rho) \end{aligned} \tag{2.63}$$

with ϵ given in Eq. (2.18) and

$$R_\rho = \frac{\xi^2 Q^2}{m_V^2} = \frac{\sigma_L}{\sigma_T}, \tag{2.64}$$

the ratio of the ρ^0 production cross sections for longitudinally and transversely polarised photons. The ratio R_ρ should not be confused with R_{DIS} which gives the ratio of DIS cross sections for longitudinally and transversely polarised photons.

2.3.3 Regge Theory and the Pomeron

In the language of Regge theory (see Refs. [42] and [48]), hadron-hadron interactions occur by means of exchanging mesons which lie on a so-called Regge trajectory. An example [15] is the reaction $\pi^- p \to \pi^0 n$. In order to conserve all quantum numbers, only ρ, a_2 and ρ_3 mesons, characterised by the quantum numbers $J^P = 1^-, 2^+, 3^-$, can be exchanged in the t channel. The total transferred parity in the reaction is positive, and since the transferred parity equals $\Delta P = (-1)^J P$, only these mesons can be exchanged. Another Regge trajectory, with the π^0, b_1 and π_2 mesons on it, can be constructed where the parity exchange is negative. The latter is called unnatural parity exchange in the t–channel, whereas exchange of the ρ^0 , a_2 and ρ_3 mesons would be natural parity exchange in the t–channel. On page 46 this is discussed in more detail for the ρ^0 production process.

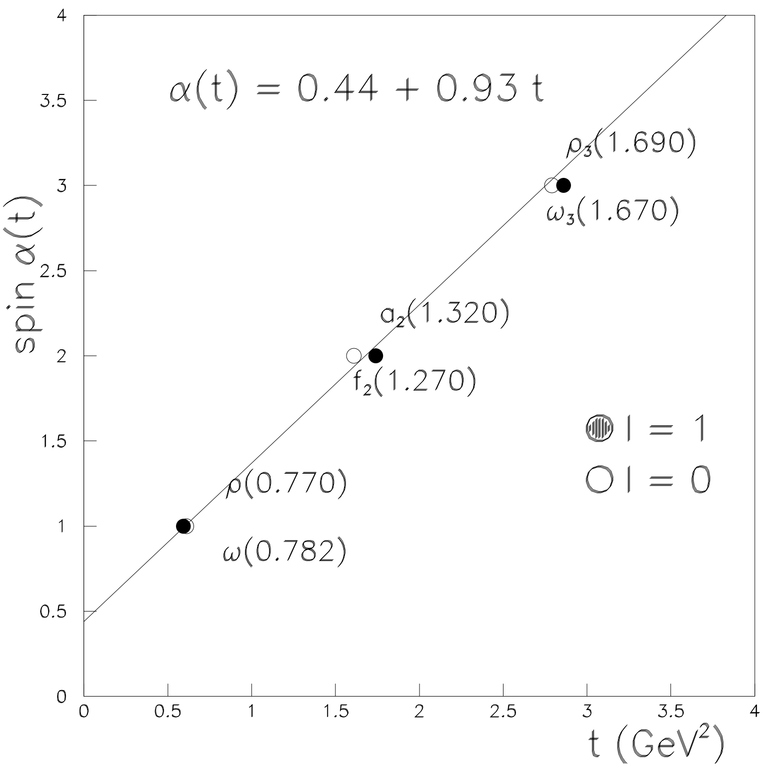

Figure 2.14: *Regge trajectory through mesons with isospin 1 (ρ, a_2, ρ_3) and with isospin 0 (ω, f_2, w^*). There is a clear relation between the mass squared and the spins of the particles. The values for the parameters $\alpha(0)$ and α' are taken from Ref. [48].*

According to Regge theory

$$\frac{d\sigma_{el}(s,t)}{dt} \sim \left(\frac{s}{s_0}\right)^{2\alpha(t)-2}, \tag{2.65}$$

at fixed t. The Mandelstam variable s represents the centre of mass energy squared. This dependence on s and t is typical of Regge theory. A derivation of this dependence from basic principles can be found e.g. in Refs. [71] and [81].

A so-called Regge trajectory can be drawn relating the masses squared and the spins of the exchanged mesons, as shown in Fig. 2.14. Using $\alpha(t) = \alpha(0) + \alpha' \cdot t$, the two parameters which define a Regge trajectory, the intercept $\alpha(0)$ and the slope α', appear in the cross section for the elastic interaction of hadrons which exchange a meson lying on that trajectory. One obtains

$$\frac{d\sigma_{el}(s,t)}{dt} \sim \left(\frac{s}{s_0}\right)^{2\alpha(0)-2} \exp(bt) \tag{2.66}$$

with $b = b_0 + 2\alpha' \ln(s/s_0)$. After integrating over t, one obtains

$$\sigma_{el} \sim \frac{1}{b}\left(\frac{s}{s_0}\right)^{2\alpha(0)-2}. \tag{2.67}$$

The optical theorem (see Refs. [62] and [92]) states that the total cross section can be written in terms of the imaginary part of the forward scattering amplitude, $\sigma_{tot} = \frac{4\pi}{k}\mathrm{Im}f(0)$ where $f(\theta)$ is the scattering amplitude and $k = 2\pi/\lambda$, the wavelength of the incident particle. The optical theorem follows from the fact that the total cross section is related to the part of the incident flux that is absorbed by the target. This absorption can only occur as a result of destructive interference, and the latter can only occur between the incident wave and the elastically scattered wave in the forward direction. Hence, the linear relation of the total cross section with the forward scattering amplitude.

Applying the optical theorem, the total cross section for diffractive hadron-hadron scattering can be written as

$$\sigma_{tot} \sim s^{\alpha(0)-1}, \tag{2.68}$$

where $s^{\alpha(0)-1}$ is proportional to the scattering amplitude.

For the Regge trajectories dealt with so far, the values for the intercepts $\alpha(0)$ are smaller than unity, which would lead to a decreasing total cross section with s. Nevertheless, a slow rise of the total hadron-hadron scattering cross sections with s is observed. This leads to the conclusion that an additional trajectory must be present with an intercept slightly larger than one. This trajectory is referred to as the Pomeron trajectory. In Ref. [48], a number of hadronic total cross sections were fitted to the sum of two powers as

$$\sigma_{tot} = X\left(\frac{s}{s_0}\right)^{\epsilon} + Y\left(\frac{s}{s_0}\right)^{-\eta} = \mathbb{P} + \mathbb{R}, \tag{2.69}$$

where the intercept of the Pomeron trajectory, $\alpha_{\mathbb{P}}(0)$, is given by $\epsilon = \alpha_{\mathbb{P}}(0) - 1 \approx 0.08$ and the intercept of the Regge trajectory, $\alpha_{\mathbb{R}}(0)$, is given by $\eta = |\alpha_{\mathbb{R}}(0) - 1| \approx 0.5$.

The slope of the Pomeron trajectory has been extracted as being approximately 0.25 GeV^{-2}. The Reggeon contribution to the total cross section dominates at low s, whereas at higher s, the Pomeron contribution sets in.

The above considerations lead to the following expressions for the contribution of Pomeron exchange to the hadron-hadron scattering cross sections, where the interaction is characterised by the exchange of a particle which lies on the Pomeron trajectory:

- A weak dependence of the cross section on the centre of mass energy squared $\sigma_{\mathbb{P}} \sim s^{0.08}$, at high s.
- An exponential t dependence given by

$$\frac{d\sigma_{el}}{dt} \sim \exp(bt). \tag{2.70}$$

An interesting feature of the exponential t dependence is the interpretation of the parameter $b = b_0 + 2\alpha'_{\mathbb{P}} \ln(s/s_0) \approx b_0 + 0.5 \ln(s/s_0)$. As the parameter b can be interpreted as a measure of the sizes of the two interacting hadrons by means of $b \propto R_1^2 + R_2^2$ (from Ref. [106]). One infers that with increasing energy, the size of the diffractive cone (i.e. the effective sizes of the two interacting hadrons) decreases; an effect which is referred to as 'shrinkage'.

The optical theorem states that the total photon - proton scattering cross section σ_{tot} is directly proportional to the scattering amplitude. In general, the cross section for a certain process equals the corresponding amplitude squared. Hence, the ρ^0 production cross section $\sigma_{\gamma^* p \to \rho^0 p}$, can be expressed as the square of a Reggeon term and a Pomeron term,

$$\sigma_{\gamma^* p \to \rho^0 p} \sim \left(A_{\mathbb{R}} \left(\frac{s}{s_0}\right)^{\Delta_{\mathbb{R}}} + A_{\mathbb{P}} \left(\frac{s}{s_0}\right)^{\Delta_{\mathbb{P}}} \right)^2, \tag{2.71}$$

with $\Delta = \alpha(0) - 1$. In Refs. [70] and [71] a model is given for the amplitudes $A_{\mathbb{R}}$ and $A_{\mathbb{P}}$ and the exponents $\Delta_{\mathbb{R}}$ and $\Delta_{\mathbb{P}}$. In chapter 6, this model is described in more detail and compared to our measurements of the ρ^0 production cross section.

2.3.4 Perturbative QCD

The VMD model describes diffractive interactions of the virtual photon at low and medium-high transverse momenta, which is referred to as 'soft' diffraction. In this kinematic region perturbative QCD (pQCD) cannot be applied since the coupling constant for the strong interaction $\alpha_s(Q^2)$ is too large and we cannot ignore the interactions of the current parton with spectator partons in its vicinity. At higher energies perturbative QCD (pQCD) comes into play. The basic difference with the phenomenological VMD model is that the quark-antiquark pair now couples to the nucleon through gluons. Fig. 2.15 depicts this quark-gluon coupling. These interactions can be calculated for high Q^2 in pQCD by using

$$\frac{d\sigma_{\lambda\lambda'}}{dt} = \frac{1}{16\pi s^2} \left|\mathcal{M}_{\lambda\lambda'}\right|^2, \tag{2.72}$$

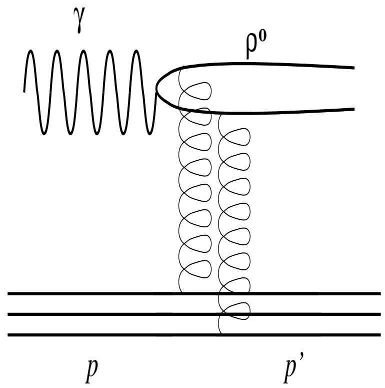

Figure 2.15: *A typical two-gluon exchange contribution to the amplitude $\mathcal{M}_{\lambda\lambda'}$ for $\gamma^* p \to Vp$.*

where λ is the helicity of the virtual photon and λ' is the helicity of the final-state vector meson.

The expression for the transition amplitude $\mathcal{M}_{\lambda\lambda'}$ can be extracted by writing it as a product of three subprocesses:

- The virtual photon fluctuates into a $q\bar{q}$ pair within a certain time τ_i.
- The $q\bar{q}$ pair scatters from the target nucleon through the exchange of two gluons.
- The $q\bar{q}$ pair exists for a certain time, $\tau_f \geq \tau_i$ before the final-state vector meson is formed.

This procedure as of yet can only be applied for longitudinally polarised vector mesons. In the case of transversely polarised vector mesons, the fluctuation of a photon to a $q\bar{q}$ pair is nonperturbative [34]. This is due to the fact that the terms for the coupling of the $q\bar{q}$ pair to the vector meson and the coupling of the photon to the $q\bar{q}$ pair do not converge for transversely polarised photons as they do for longitudinally polarised photons.

Refs. [34] and [59] give an expression for the cross section for electroproduction of longitudinally polarised vector mesons as

$$\frac{d\sigma^L_{\gamma^* N\to VN}}{dt}\rfloor_{t=0} = \frac{3\pi^3\Gamma_V m_V \alpha_s^2}{\alpha_{em} Q^6 N_c^2}\eta_V^2 \left|1 + i\frac{\pi}{2}\frac{d}{dlnx}xG(x,Q^2)\right|^2, \tag{2.73}$$

where Γ_V is the decay width for vector meson V, m_V is the mass of the vector meson, $\alpha_s = \alpha_s(Q^2)$ is the running coupling strength of the strong interaction, α_{em} is the electromagnetic coupling constant, $N_c = 3$ is the number of colours of the quark, η_V is defined in Ref. [34] as the inverse moment of the vector meson distribution amplitude and $G(x, Q^2)$ is the gluon distribution in the nucleon.

For the cross section of the electroproduction of transversely polarised vector mesons the authors of Ref. [34] predict a dependence of at least $1/Q^8$.

2.3.5 Electroproduction of Vector Mesons

The experiments E665, EMC, NMC, H1 and ZEUS have reported results for ρ^0 leptoproduction cross sections. The differential cross section describing ρ^0 production is given by

$$\frac{d\sigma}{d\phi\, dE'\, dQ^2\, dt\, dM_{\pi\pi}\, d\cos(\theta_{\pi\pi})\, d\phi_{\pi\pi}\, d\Phi_{ee}} = \Gamma_T \cdot \frac{d\sigma}{dt} \cdot W(\Phi_{ee}, \theta_{\pi\pi}, \phi_{\pi\pi}), \tag{2.74}$$

where $W(\Phi, \theta_{\pi\pi}, \phi_{\pi\pi})$ represents the angular distribution function. In this expression, E', Q^2 and ϕ arise from the lepton vertex, whereas Φ_{ee} and t define the vector meson production vertex and $M_{\pi\pi}, \theta_{\pi\pi}$ and $\phi_{\pi\pi}$ define the pion pair production vertex (i.e. the ρ^0 decay vertex).

The cross sections for electroproduction and virtual-photoproduction are related by

$$\frac{d\sigma}{d\Omega dE'} = \Gamma_T \sigma(\gamma^* p \to \rho^0 p) \tag{2.75}$$

with the expression for the transversely polarised photon flux (see Ref. [23]),

$$\Gamma_T = \Gamma_T(\Omega, E') = \frac{\alpha}{4\pi^2} \left(\frac{W^2 - M_p^2}{2M_p} \right) \frac{1}{Q^2} \frac{E'}{E} \frac{2}{1-\epsilon}. \tag{2.76}$$

It is useful to express the cross section as a differential in Q^2 and W,

$$\frac{d\sigma}{dQ^2 dW} = \int_0^{2\pi} d\phi \frac{d\cos\theta}{dQ^2} \frac{dE'}{dW} \frac{d\sigma}{d\Omega dE'} = 2\pi \frac{1}{2EE'} \frac{W}{M_p} \Gamma_T(\Omega, E') \sigma(\gamma^* p \to \rho^0 p) \tag{2.77}$$

and hence define $\Gamma_T(Q^2, W)$ as

$$\Gamma_T(Q^2, W) = \frac{\alpha}{2\pi} \frac{W}{M_p} \left(\frac{W^2 - M_p^2}{2M_p} \right) \frac{1}{Q^2} \frac{1}{E^2} \frac{1}{1-\epsilon}, \tag{2.78}$$

and

$$\frac{d\sigma}{dQ^2 dW} = \Gamma_T(Q^2, W) \sigma(\gamma^* p \to \rho^0 p). \tag{2.79}$$

The total virtual photoproduction cross section can be written as $\sigma(\gamma^* p \to \rho^0 p) = \sigma_T + \epsilon\sigma_L$, as shown in Eq. (2.63).

In reporting cross sections, only the virtual photoproduction cross sections are given, since the photon flux factor Γ_T is already known and does not convey new information.

Fig. 2.16 shows the ρ^0 virtual photoproduction cross section as measured by various experiments.

2.3.6 Mass Spectrum of the ρ^0 Particle

Due to the lack of rigorous theoretical understanding of the ρ^0 invariant mass spectrum a number of phenomenological fits are used to account for the non-resonant background and the $\rho^0 - \omega$

Figure 2.16: *Cross section results for the reaction $\gamma^* p \to \rho^0 p$ versus Q^2 measured by various experiments. The results are taken from Ref. [8]. The dashed curve is a prediction by Pichowski et al. [101, 102]. The dotted curve is a prediction by Nemchik et al. [94]. The solid curve represents the result of fitting Eqs. (2.63) and (2.64) to the* E665 *data points.*

interference. Non-resonant background is caused by reactions which produce two pions with opposite charge without a vector meson having been involved.

Breit-Wigner Lineshape

The basic line shape for the ρ^0 is expressed by a relativistic p-wave Breit-Wigner function for a spin-1 object decaying into two spin-0 objects (see Refs. [77] and [115]),

$$\frac{d\sigma}{dM_{\pi\pi}} = \frac{M_{\pi\pi} m_\rho \Gamma_\rho}{(M_{\pi\pi}^2 - m_\rho^2)^2 + m_\rho^2 \Gamma_\rho^2} \text{ with, } \Gamma_\rho = \Gamma_0 \left(\frac{\sqrt{M_{\pi\pi}^2 - 4m_\pi^2}}{\sqrt{m_\rho^2 - 4m_\pi^2}} \right)^3 \frac{m_\rho}{M_{\pi\pi}}, \tag{2.80}$$

where $M_{\pi\pi}$ is the invariant mass of the pion pair.

Skewed Breit-Wigner Lineshape (Ref. [108])

An additional Ross-Stodolsky skewing term can be applied to the Breit-Wigner function to account for non-resonant background,

$$\frac{d\sigma}{dM_{\pi\pi}} = \frac{d\sigma}{dM_{\pi\pi}}\rfloor_{Breit\,Wigner} \left(\frac{m_\rho}{M_{\pi\pi}}\right)^{n_{\mathrm{skew}}}. \tag{2.81}$$

Söding Method (Ref. [117])

The Söding method involves the superposition of the Breit Wigner shape and an additional interference term plus a background term to account for non-resonant background,

$$\frac{d\sigma}{dM_{\pi\pi}} = A_{\mathrm{bw}} \frac{d\sigma}{dM_{\pi\pi}} \rfloor_{Breit\,Wigner} + A_{\mathrm{sod}} I(M_{\pi\pi}) + A_{\mathrm{background}}, \tag{2.82}$$

where A_{bw} is the contribution of the Breit-Wigner lineshape A_{sod} is the contribution of the Söding lineshape, $A_{\mathrm{background}}$ is the background term and

$$I(M_{\pi\pi}) = \frac{m_\rho^2 - M_{\pi\pi}^2}{(M_{\pi\pi}^2 - m_\rho^2)^2 + m_\rho^2\,\Gamma_\rho^2}. \tag{2.83}$$

$\rho - \omega$ Interference

In addition to the non-resonant background one has to account for $\rho - \omega$ interference. The ω has a 2.2 % probability to decay into a $\pi^+\pi^-$ pair (see Ref. [98]). This interference distorts the shape of the mass spectrum in the region of the ρ^0 particle. This effect can be taken into account by adding a term for the ω contribution to the ρ^0 propagator appearing in the expression for the pion-pair production amplitude. In Refs. [24] and [29] expressions are given for the distribution function, including an additional skewing term to account for non-resonant background with a shape given by

$$\begin{aligned} \frac{d\sigma}{dt\,dm}\Big|_{t=0} &= \frac{d\sigma}{dt}\Big|_{t=0} \frac{2}{\pi}\, m\, m_\rho\, \Gamma_\rho\, (\frac{m_\rho}{m})^n \cdot \\ &\left| \frac{1}{m^2 - m_\rho^2 + i m_\rho\,\Gamma_\rho} + \frac{\xi e^{i\alpha}}{m^2 - m_\omega^2 + i m_\omega\,\Gamma_\omega} \right|^2 + W(m), \end{aligned} \tag{2.84}$$

where Γ_ρ is a function of $m = M_{\pi\pi}$ as for the Breit-Wigner and the Söding lineshapes. We can rewrite the above in a different form by using

$$A_\rho \equiv m^2 - m_\rho^2\ ;\ \ A_\omega \equiv m^2 - m_\omega^2. \tag{2.85}$$

One then obtains after squaring the interference terms,

$$\frac{d\sigma}{dt\,dm}\Big|_{t=0} = \frac{d\sigma}{dt}\Big|_{t=0} \frac{2}{\pi} m\, m_\rho\, \Gamma_\rho \left(\frac{m_\rho}{m}\right)^n \left(\frac{t_1 + t_2 + t_3 + t_4}{n_1 + n_2 + n_3 + n_4}\right) + W(m), \tag{2.86}$$

with

$$\begin{aligned} t_1 &= A_\omega^2 + m_\omega^2\,\Gamma_\omega^2 \\ t_2 &= \xi^2 (A_\rho^2 + m_\rho^2\,\Gamma_\rho^2) \\ t_3 &= 2A_\omega\,\xi(A_\rho \cos(\alpha) + m_\rho\,\Gamma_\rho\,\sin(\alpha)) \\ t_4 &= 2m_\omega\,\Gamma_\omega\,\xi(A_\rho\,\sin(\alpha) + m_\rho\,\Gamma_\rho\,\cos(\alpha)) \\ n_1 &= A_\rho^2\,A_\omega^2 \\ n_2 &= m_\rho^2\,\Gamma_\rho^2\,m_\omega^2\,\Gamma_\omega^2 \\ n_3 &= A_\rho^2\,m_\omega^2\,\Gamma_\omega^2 \\ n_4 &= A_\omega^2\,m_\rho^2\,\Gamma_\rho^2. \end{aligned} \tag{2.87}$$

Figure 2.17: *Fit through the data points in the invariant mass spectrum, measured at Daresbury for the reaction $\gamma + C \rightarrow \pi^+ + \pi^- + C$. The solid curve is the fit with $\rho - \omega$ interference taken into account, the dashed curve shows the same fit without the interference.*

The measured values for the free parameters are (see Ref. [29]) given as $m_\rho = 0.768$ GeV$/c^2$, $\Gamma_{\rho,0} = 0.146$ GeV$/c^2$, $m_\omega = 0.783$ GeV$/c^2$, $\xi = 0.0097$, $\alpha = 104.0°$.

Note that $\Gamma_\omega = 8.43$ MeV [98] is the full width of the ω meson.

Fig. 2.17 shows the fitted mass spectrum, for the data obtained at Daresbury (see Ref. [29]).

2.4 Angular Distributions

2.4.1 Density Matrices

In order to facilitate the interpretation of density matrices, which build up the frame work needed to relate angular distributions to polarisation states of the ρ^0 , here a brief summary is given of some of the relevant quantum-mechanical principles, most importantly the mathematical object referred to as a density matrix.

Quantum-mechanical states are described by superpositions of states,

$$|\psi> = \sum_{i=1}^{N} a_i |\phi_i>, \tag{2.88}$$

with $a_i \in \mathbb{C}$ and $|\phi_i>$ denoting all possible orthogonal states in which the particle can be found at a measurement. The probability to find a quantum mechanical system in one of its possible states is given by $|a_i|^2$. Hence, the probability of observing a certain event is determined by taking the square of the sum of a number of quantum-mechanical amplitudes describing all possible ways this event can occur.

In descriptions of measurements one most often deals with numerous observations instead of one single measurement and hence for most practical purposes it is more convenient to deal with an expression for the statistical mixture of all possible states. This mixture of states is called a density matrix. In quantum-mechanical notation, a density matrix is defined as

$$\begin{aligned} \mathbf{D} &= |\psi><\psi| \qquad (2.89) \\ &= a_1^* a_1 |\phi_1><\phi_1| + a_1^* a_2 |\phi_1><\phi_2| + a_2^* a_1 |\phi_2><\phi_1| + a_2^* a_2 |\phi_2><\phi_2| + \ldots\ldots \end{aligned}$$

Here $|\psi><\psi|$ can be represented by a matrix, constructed out of the bases $|\phi_i><\phi_j|$ and the factors $a_i^* a_j$ are the matrix elements.

For example, the angular momentum part of a particle with spin 1/2 can be described by a superposition of two orthogonal states,

$$|\psi>= a_1|\uparrow> +a_2|\downarrow> . \qquad (2.90)$$

The polarisation density matrix ρ takes the form

$$\rho = \begin{pmatrix} |a_1|^2 & a_1 a_2^* \\ a_1^* a_2 & |a_2|^2 \end{pmatrix} . \qquad (2.91)$$

To represent a measurement performed on the mixture of states represented by the density matrix, a density operator (a projector) is used. For instance, when one wants to measure whether the spin is parallel or anti parallel with respect to a particular direction, the density operator is represented by

$$\mathbf{E} = |\uparrow><\uparrow| \qquad (2.92)$$

The probability P of finding the system in an upward spin state is then obtained by taking the trace of the matrix product of ρ and $\mathbf{E}$,

$$P = \mathrm{trace}(\rho\mathbf{E}) = a_1^2| <\uparrow|\uparrow> |^2. \qquad (2.93)$$

In the following, we will deal with the polarisation density matrix of the ρ^0 particle.

2.4.2 Polarisation Density-Matrix Elements

The ρ^0 polarisation density matrix can be constructed in three steps. Since the ρ^0 particle has the same quantum numbers as the photon and since a polarisation density matrix is basically a summation over all possible polarisation states of all incoming and outgoing particles, one can start by writing down a polarisation density matrix for the photon.

The differential cross section for vector meson electroproduction reads

$$\frac{d\sigma_{eN\to eNV}}{dE' d\Omega_l d\Phi dt} = \frac{1}{(2\pi)^5} \frac{E'}{E} \frac{m^2}{4(\nu^2 + Q^2)^{\frac{1}{2}}} \frac{1}{Q^4} \frac{1}{4} \sum_{\text{lepton spins}} |\mathcal{M}|^2, \tag{2.94}$$

where

$$\sum_{\text{lepton spins}} |\mathcal{M}|^2 = \sum_{\text{lepton spins}} L_{\mu\nu} T^{\mu\nu},^{1} \tag{2.95}$$

where $L_{\mu\nu}$ is the sum of an unpolarised leptonic part and a polarised part, $L_{\mu\nu} = \tilde{L}_{\mu\nu} + \tilde{M}_{\mu\nu}$. $\tilde{L}_{\mu\nu}$ are elements of the leptonic tensor and can be expressed as

$$\tilde{L}_{\mu\nu} = \sum_{\text{el.spins}} m^2 < l_2 | j_\mu^{el} | l_1 >< l_2 | j_\nu^{el} | l_1 >^* \tag{2.96}$$

$$= m^2 \mathrm{Tr} \left(\frac{l_2 + m}{2m} \gamma_\mu \frac{l_1 + m}{2m} \gamma_\nu \right), \tag{2.97}$$

where l_1 and l_2 are the spinors for the incoming and outgoing lepton, respectively, j_μ^{el} is the electromagnetic current operator and γ_μ is the Dirac–matrix.

The tensor $\tilde{L}$ can be rewritten in a coordinate system where $\vec{q}$ is parallel to the z-axis and l_1 and l_2 lie in the $x - z$ plane. The tensor $\tilde{L}$ describes the photon spin states with transverse (x, y), longitudinal (z) and scalar (0) components. Under a Lorentz transformation, the longitudinal and the scaler components transform into each other, hence $\tilde{L}$ can be rewritten into a 3×3 tensor L'. Subsequently, a rotation around the z-axis with an angle Φ is applied,

$$L_{\lambda\lambda'} = U_{\lambda\mu} L'_{\mu\nu} U^{-1}_{\nu\lambda'}, \tag{2.98}$$

where λ labels the photon spin states and hence for convenience $\lambda, \lambda' = -1, 0, 1$.

The resulting 3×3 tensor L contains elements $L_{\lambda\lambda'} = f(\epsilon, \delta_m, \Phi)$, where ϵ is already given in Eq. (2.18) and where $\delta_m = \frac{2m^2}{Q^2}(1 - \epsilon)$.

In the same way as we dealt with $\tilde{L}$, we can deal with $\tilde{M}$ to get a 3×3 tensor M with elements $\tilde{M}_{\lambda\lambda'} = f(\epsilon, \Phi, \mathbf{P})$, where $\mathbf{P}$ is the lepton polarisation four–vector of the incoming lepton beam.

We can now construct a photon density matrix $\rho(\gamma)$ by means of

$$\rho(\gamma)_{\lambda\lambda'} = \frac{1 - \epsilon}{Q^2} L_{\lambda\lambda'} + M_{\lambda\lambda'}. \tag{2.99}$$

Subsequently, we can decompose the density matrix into an orthogonal set of nine matrices,

$$\rho(\gamma) = \frac{1}{2} \sum_{\alpha=0}^{8} \Pi_\alpha \Sigma^\alpha, \tag{2.100}$$

[1]Here, the convention of Ref. [111] is followed. Often, also $\sum_{\text{lepton spins}} |\mathcal{M}|^2 = \frac{e^4}{Q^4} \sum_{\text{lepton spins}} L_{\mu\nu} T^{\mu\nu}$ can be found.

where Σ is a set of nine orthogonal matrices and Π is a vector with $\Pi_\alpha = f(\epsilon, \delta_m, \Phi, \mathbf{P})$.

Until now we dealt with the lepton vertex only. In order to arrive at a cross section for vector meson production we can either use Eq. (2.94) or we can use an expression in 'density matrix language',

$$\frac{d\sigma}{dt d\Phi} = \frac{1}{2}\mathrm{Tr}(T\rho(\gamma)T^\dagger), \tag{2.101}$$

where T is a tensor containing helicity amplitudes, as defined by Jacob and Wick [79]. The helicity amplitudes are defined by

$$T_{\lambda_V \lambda_{N'} \lambda_\gamma \lambda_N} =< \lambda_V \lambda_{N'} | j_{\lambda_\gamma} | \lambda_N > . \tag{2.102}$$

Often one sums over the polarisation directions of the target λ_N with respect to the incoming virtual photon.

Hence, the expression for the vector meson density matrix becomes $\rho(V) = \frac{1}{2}T\rho(\gamma)T^\dagger$. We can decompose $\rho(V)$ by using

$$\rho(V) = \sum_{\alpha=0}^{8} \Pi_\alpha \rho^\alpha, \tag{2.103}$$

where $\Pi_\alpha = f(\epsilon, \delta_m, \Phi, \mathbf{P}, R)$ is known. $R_\rho = \sigma_L/\sigma_T$ is the ratio of the ρ^0 production cross sections for longitudinally and transversely polarised photons. The matrices ρ^α are defined by

$$\rho^\alpha_{\lambda_V \lambda'_V} = \frac{1}{2N_\alpha} \sum_{\lambda_{N'} \lambda_N \lambda_\gamma \lambda'_\gamma} T_{\lambda_V \lambda_{N'} \lambda_\gamma \lambda_N} \Sigma_{\lambda_\gamma \lambda'_\gamma} T^*_{\lambda'_V \lambda_{N'} \lambda'_\gamma \lambda_N}. \tag{2.104}$$

The $\Sigma_{\lambda_\gamma \lambda'_\gamma}$ matrix elements are completely determined by the kinematics of the scattered electron, expressed by Φ_{ee} and ϵ and the longitudinal polarisation of the beam. The $T_{\lambda_V \lambda_{N'} \lambda_\gamma \lambda_N}$ matrix elements (after summing over nucleon helicities $\lambda_{N'}, \lambda_N$) describe the transfer of helicity of the photon state to the ρ^0 meson state. Although the results presented here are still based on summing over nucleon helicities, note that at HERMES it is not necessary to do this since the polarisation states of the nucleon are known. Analysis on angular distributions for different nucleon polarisation states is in progress.

Next, we have to include the ρ^0 decay vertex in the description as well. Since we do not measure the ρ^0 particle directly, but its decay products, the $\pi^\pm$ pair, we need to use the Wigner–d functions in addition. The ρ^0 particle has spin 1, and hence the total angular momentum of a ρ^0 particle at rest is $J = L + S = 1$. Since the total angular momentum has to be conserved, the final hadronic state still has $J = 1$. When expressing the wave function for the final state as $\psi = \psi_{\vec{r}}(\pi_1\pi_2) \cdot \chi_S(\pi_1\pi_2)$ where $\psi_{\vec{r}}$ denotes the space wave function and χ_S denotes the spin wave function, then χ_S is symmetric because the spin of pions, $S = 0$. Since $\psi_{\vec{r}}(\pi_1\pi_2) = (-1)^L\psi_{\vec{r}}(\pi_2\pi_1)$ and $L = 1$ because of conservation of total angular momentum, $\psi_{\vec{r}}$ is anti symmetric. For this reason, a ρ^0 particle cannot decay into a π^0 pair since $\psi_{\vec{r}}(\pi^0\pi^0)$ must be symmetric according to Bose statistics for two identical bosons. The space wave function can be expressed as $\psi_{\vec{r}} = \psi(r)Y_l^m(\theta, \phi)$.

In general a Wigner-D operator $\mathcal{D}^{(j)}_{mm'}(R)$ is defined as the amplitude for a rotated state to be found in quantum state $|j, m' >$ when the original unrotated state was labeled with $|j, m >$. In our case, we can write

$$\begin{aligned} \mathcal{D}^{(j)}_{mm'}(R) &= \mathcal{D}^{S_V}_{\lambda_V \lambda_{\pi+}}(\phi, \theta - \phi) \\ &= \mathcal{D}^{1}_{\lambda_V 0}(\phi, \theta, -\phi), \end{aligned} \tag{2.105}$$

with

$$D^1_{10}(\phi_{\pi\pi}, \theta_{\pi\pi}, -\phi_{\pi\pi}) = -\mathrm{e}^{-i\phi_{\pi\pi}}(\frac{1}{\sqrt{2}}) \sin\theta_{\pi\pi} \tag{2.106}$$

$$D^1_{00}(\phi_{\pi\pi}, \theta_{\pi\pi}, -\phi_{\pi\pi}) = \cos\theta_{\pi\pi} \tag{2.107}$$

$$D^1_{-10}(\phi_{\pi\pi}, \theta_{\pi\pi}, -\phi_{\pi\pi}) = \mathrm{e}^{i\phi_{\pi\pi}}(\frac{1}{\sqrt{2}}) \sin\theta_{\pi\pi}, \tag{2.108}$$

and $\theta_{\pi\pi}$ and $\phi_{\pi\pi}$ the opening angle and the azimuthal angle of the π^+ particle in the ρ^0 centre of mass frame.

We can now write down the vector meson decay angular distribution function in terms of the density matrix,

$$W(\theta_{\pi\pi}, \phi_{\pi\pi}, \Phi) = \frac{3}{4\pi} \sum_{\lambda\lambda'} D^1_{\lambda 0}(\phi_{\pi\pi}, \theta_{\pi\pi}, -\phi_{\pi\pi})^* \rho(V)_{\lambda\lambda'} D^1_{\lambda' 0}(\phi_{\pi\pi}, \theta_{\pi\pi}, -\phi_{\pi\pi}). \tag{2.109}$$

Again, we can decompose $W(\theta, \phi, \Phi)$ into

$$\begin{aligned} W(\theta_{\pi\pi}, \phi_{\pi\pi}, \Phi) &= \sum_{\alpha=0}^{8} \Pi_\alpha W^\alpha, \\ &= \frac{3}{4\pi} \sum_{\lambda\lambda'} D^1_{\lambda 0}(\phi_{\pi\pi}, \theta_{\pi\pi}, -\phi_{\pi\pi})^* \left(\sum_{\alpha=0}^{8} \Pi_\alpha \rho^\alpha_{\lambda\lambda'}(V) \right) D^1_{\lambda' 0}(\phi_{\pi\pi}, \theta_{\pi\pi}, -\phi_{\pi\pi}). \end{aligned} \tag{2.110}$$

Each of the nine independent 3×3 matrices $\rho^\alpha_{\lambda\lambda'}$ represents a different polarisation state [26]: $\alpha = 0 - 2$ represent transverse polarisation and $\alpha = 3$ represents production by the component of circular polarisation. Production by longitudinally polarised photons is given by $\alpha = 4$. The remaining matrices $\alpha = 5$—8 are attributed to longitudinal-transverse interference. For unpolarised leptons only $\rho^{5,6}_{ij}$ contribute. With longitudinal lepton polarisation, there can be additional L-T interference given by $\rho^{7,8}_{ij}$, due to the *circular* component of virtual photon polarisation.

One way to separate the contributions of longitudinal and transverse ρ^0 particles would be by using the Rosenbluth L/T separation, which takes advantage of the fact that at fixed Q^2, the transverse contribution to the cross section will be varying with opening angle θ. Measuring the cross section at different values of θ at fixed Q^2 (i.e. at varying values for the energy of the incident beam), would separate the longitudinal and transverse contributions. Since at

HERMES the beam energy is fixed, it is not possible to do an L/T separation at constant Q^2 and W and hence, one measures the linear combinations

$$r_{ik}^{04} = \frac{\rho_{ik}^{0} + \epsilon R_\rho \rho_{ik}^{4}}{1+\epsilon R_\rho}, \tag{2.111}$$

$$r_{ik}^{\alpha} = \frac{\rho_{ik}^{\alpha}}{1+\epsilon R_\rho}, \quad \alpha = (1,2,3), \tag{2.112}$$

$$r_{ik}^{\alpha} = \sqrt{R_\rho}\frac{\rho_{ik}^{\alpha}}{1+\epsilon R_\rho}, \quad \alpha = (5,6,7,8), \tag{2.113}$$

where R_ρ is the ratio of ρ^0 production cross sections for longitudinally and transversely polarised photons. Since for DIS events the photon should be transversely polarised (i.e. in the $|1, \pm 1 >$ states) in order to scatter from quarks with spin 1/2, R_{DIS} will be close to zero. With exclusive, diffractive ρ^0 production, the photon scatters from the nucleon or nucleus by exchanging a spin 0 object while helicity is conserved at the photon – vector meson vertex and hence both longitudinally and transversely polarised photons can take part.

The angular distribution function $W(\theta_{\pi\pi}, \phi_{\pi\pi}, \Phi)$ can be expressed as

$$W(\cos\theta_{\pi\pi}, \phi_{\pi\pi}, \Phi) = W^{\text{unpol.}}(\cos\theta_{\pi\pi}, \phi_{\pi\pi}, \Phi) + W^{\text{long.pol.}}(\cos\theta_{\pi\pi}, \phi_{\pi\pi}, \Phi), \tag{2.114}$$

with

$$\begin{aligned}
W^{\text{unpol.}} = {} & \frac{3}{4\pi}\Big[\,\frac{1}{2}(1-r_{00}^{04}) + \frac{1}{2}(3r_{00}^{04}-1)\cos^2\theta_{\pi\pi} \\
& -\sqrt{2}\mathrm{Re}\, r_{10}^{04}\sin 2\theta_{\pi\pi}\cos\phi_{\pi\pi} - r_{1-1}^{04}\sin^2\theta_{\pi\pi}\cos 2\phi_{\pi\pi} \\
& -\epsilon\cos 2\Phi(r_{11}^{1}\sin^2\theta_{\pi\pi} + r_{00}^{1}\cos^2\theta_{\pi\pi} \\
& \quad -\sqrt{2}\mathrm{Re}\, r_{10}^{1}\sin 2\theta_{\pi\pi}\cos\phi_{\pi\pi} - r_{1-1}^{1}\sin^2\theta_{\pi\pi}\cos 2\phi_{\pi\pi}) \\
& -\epsilon\sin 2\Phi\left(\sqrt{2}\mathrm{Im}\, r_{10}^{2}\sin 2\theta_{\pi\pi}\sin\phi_{\pi\pi}\right. \\
& \quad \left. +\mathrm{Im}\, r_{1-1}^{2}\sin^2\theta_{\pi\pi}\sin 2\phi_{\pi\pi}\right) \\
& +\sqrt{2\epsilon(1+\epsilon)}\cos\Phi(r_{11}^{5}\sin^2\theta_{\pi\pi} + r_{00}^{5}\cos^2\theta_{\pi\pi} \\
& \quad -\sqrt{2}\mathrm{Re}\, r_{10}^{5}\sin 2\theta_{\pi\pi}\cos\phi_{\pi\pi} - r_{1-1}^{5}\sin^2\theta_{\pi\pi}\cos 2\phi_{\pi\pi} \\
& +\sqrt{2\epsilon(1+\epsilon)}\sin\Phi\left(\sqrt{2}\mathrm{Im}\, r_{10}^{6}\sin 2\theta_{\pi\pi}\sin\phi_{\pi\pi} + \mathrm{Im}\, r_{1-1}^{6}\sin^2\theta_{\pi\pi}\sin 2\phi_{\pi\pi}\right)\Big],
\end{aligned} \tag{2.115}$$

and,

$$\begin{aligned}
W^{\text{long.pol.}} = {} & \frac{3}{4\pi}\mathbf{P}\Big[\sqrt{1-\epsilon^2} \\
& \left(\sqrt{2}\mathrm{Im}\, r_{10}^{3}\sin 2\theta_{\pi\pi}\sin\phi_{\pi\pi} + \mathrm{Im}\, r_{1-1}^{3}\sin^2\theta_{\pi\pi}\sin 2\phi_{\pi\pi}\right) \\
& +\sqrt{2\epsilon(1-\epsilon)}\cos\Phi\left(\sqrt{2}\mathrm{Im}\, r_{10}^{7}\sin 2\theta_{\pi\pi}\sin\phi_{\pi\pi} + \mathrm{Im}\, r_{1-1}^{7}\sin^2\theta_{\pi\pi}\sin 2\phi_{\pi\pi}\right) \\
& +\sqrt{2\epsilon(1-\epsilon)}\sin\Phi\times \\
& \quad (r_{11}^{8}\sin^2\theta_{\pi\pi} + r_{00}^{8}\cos^2\theta_{\pi\pi} \\
& \quad -\sqrt{2}\mathrm{Re}\, r_{10}^{8}\sin 2\theta_{\pi\pi}\cos\phi_{\pi\pi} - r_{1-1}^{8}\sin^2\theta_{\pi\pi}\cos 2\phi_{\pi\pi})\Big],
\end{aligned} \tag{2.116}$$

with $Q^2 \gg m_e^2$.

After integrating $W(\cos\theta_{\pi\pi}, \phi_{\pi\pi}, \Phi)$ over $\phi_{\pi\pi}$ and Φ we obtain

$$W(\cos\theta_{\pi\pi}) = \frac{3}{4}\left[1 - r_{00}^{04} + (3r_{00}^{04} - 1)\cos^2(\theta_{\pi\pi})\right]. \tag{2.117}$$

The matrix element r_{00}^{04} is related to the longitudinal polarisation of the ρ^0 particle. For purely longitudinally polarised ρ^0 particles, one has $r_{00}^{04} = 1$, whereas for completely transversely polarised ρ^0 particles, one has $r_{00}^{04} = 0$.

After integrating $W(\cos\theta_{\pi\pi}, \phi_{\pi\pi}, \Phi)$ over $\cos\theta_{\pi\pi}$ and Φ we obtain

$$W(\phi_{\pi\pi}) = \frac{1}{2\pi}\left[1 - 2r_{1-1}^{04}\cos 2\phi_{\pi\pi} + P_b\sqrt{1-\epsilon^2}\mathrm{Im}r_{1-1}^{3}\sin 2\phi_{\pi\pi}\right]. \tag{2.118}$$

After integrating $W(\cos\theta_{\pi\pi}, \phi_{\pi\pi}, \Phi)$ over $\cos\theta_{\pi\pi}$ and $\phi_{\pi\pi}$ we obtain

$$W(\Phi) = \frac{1}{2\pi}\left[1 - \epsilon\cos 2\Phi\mathrm{Tr}(r^1) + \sqrt{2\epsilon(1+\epsilon)}\cos\Phi\mathrm{Tr}(r^5) + P_b\sqrt{2\epsilon(1-\epsilon)}\sin\Phi\mathrm{Tr}(r^8)\right]. \tag{2.119}$$

Under the assumption of s-channel helicity conservation (SCHC) [111], one can extract the ratio of the ρ^0 production cross sections for longitudinally and transversely polarised photons without having to do an L/T separation, by

$$R_\rho \equiv \frac{\sigma_L}{\sigma_T} = \frac{1}{\epsilon}\frac{r_{00}^{04}}{1 - r_{00}^{04}}, \tag{2.120}$$

which can be interpreted simply as the ratio of the number of longitudinally polarised ρ^0 mesons (r_{00}^{04}) to the number of transversely polarised ρ^0 mesons ($1 - r_{00}^{04}$) divided by the flux of longitudinally polarised photons normalised to the flux of transversely polarised photons (ϵ). Hence, SCHC states that the helicity of the photon is transferred completely to the vector meson.

The angles ϕ and Φ can be combined into a single angle $\psi = \phi_{\pi\pi} - \Phi$. After integrating W over $\cos\theta$ one obtains

$$W(\psi) = \frac{1}{2\pi}\left[1 + 2\epsilon r_{1-1}^{1}\cos 2\psi\right]. \tag{2.121}$$

Within the model of SCHC, r_{1-1}^1 is the linear polarisation of the ρ^0 meson. If in addition to SCHC one assumes natural parity exchange in the t-channel, then the following relationship has to hold

$$r_{1-1}^1 = \frac{1}{2}(1 - r_{00}^{04}). \tag{2.122}$$

Assuming SCHC, with $\Psi = \phi_{\pi\pi} - \Phi_{ee}$ Eq. (2.114) can also be reduced to

$$W(\cos\theta, \psi) = \frac{3}{4\pi}\left[\frac{1}{2}(1 - r_{00}^{04}) + \frac{1}{2}(3r_{00}^{04} - 1)\cos^2\theta + \epsilon r_{1-1}^1\sin^2\theta\cos 2\psi \right.$$
$$\left. +2\sqrt{\epsilon(1+\epsilon)}\mathrm{Re}(r_{10}^5)\sin 2\theta\cos\psi + 2P_b\sqrt{\epsilon(1+\epsilon)}\mathrm{Re}(r_{10}^8)\sin 2\theta\sin\psi\right]. \tag{2.123}$$

Using

$$\mathrm{Re}(r^5_{10}) = -\frac{1}{2}\sqrt{R/2}\cos\delta/(1+\epsilon R) \tag{2.124}$$

$$\mathrm{Re}(r^8_{10}) = \frac{1}{2}\sqrt{R/2}\sin\delta/(1+\epsilon R) \tag{2.125}$$

where δ is the phase difference between the transverse and the longitudinal amplitudes, one obtains

$$\begin{aligned} W(\cos\theta,\psi) = {} & \frac{1}{1+\epsilon R}\frac{3}{8\pi} \\ & [\,\sin^2\theta(1+\epsilon\cos 2\psi) + 2\epsilon R_\rho\cos^2\theta - \sqrt{2\epsilon(1+\epsilon)R}\cos\delta\sin 2\theta\cos\psi \\ & +P\sqrt{2\epsilon(1+\epsilon)R}\sin\delta\sin 2\theta\sin\psi\,]\,. \end{aligned} \tag{2.126}$$

Fig. 2.18 depicts the process of diffractive ρ^0 production. The quantum numbers of the ρ^0 meson are the same as those of the photon. Under the assumption of SCHC the helicity of the ρ^0 meson is the same as of the photon too and hence no angular momentum is transferred from the target to the ρ^0 meson. If one assumes that no quantum numbers are exchanged from the target to the ρ^0 meson ($L = 0$), then the parity of the exchanged particle, the pomeron, is equal to

$$P_{\mathbb{P}} = \epsilon_{\mathbb{P}}(-1)^L, \tag{2.127}$$

where $\epsilon_{\mathbb{P}}$ is the intrinsic parity of the pomeron. In order for the ρ^0 meson to have the same parity as the photon, with $P_{\rho^0} = P_\gamma \times P_{\mathbb{P}}$, it is required that $P_{\mathbb{P}} = 1$. Natural parity exchange in the t-channel is defined (see Ref. [112]) as $P = (-1)^L$, and hence ρ^0 production is assumed to proceed via natural parity exchange in the t-channel.

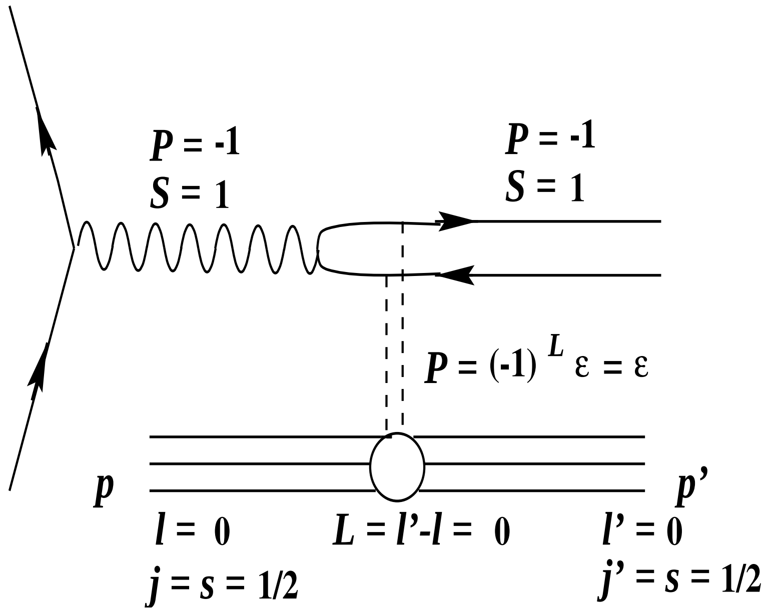

Figure 2.18: *Schematic representation of transfer of parity and spin in diffractive ρ^0 production.*

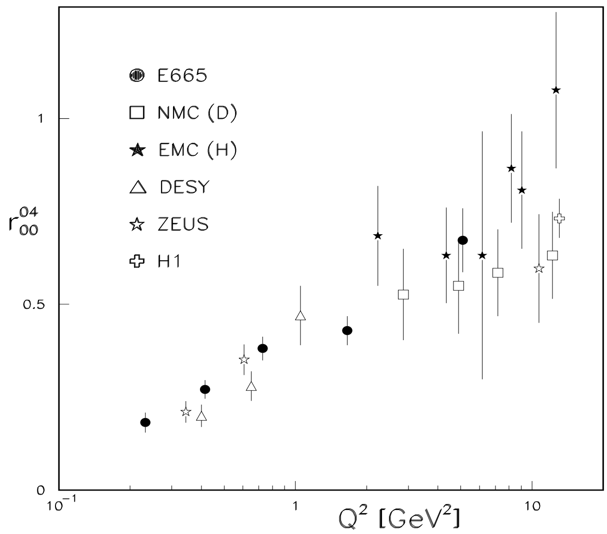

Figure 2.19: *The spin density matrix element r^{04}_{00} as a function of Q^2. The data are taken from Ref. [8].*

Figs. 2.19 and 2.21 show the world data for r^{04}_{00} and r^1_{1-1}. Fig. 2.20 shows data from measurements of R_ρ based on measurements of r^{04}_{00}. Fig. 2.22 shows r^1_{1-1} as determined from the E665 measurement of r^{04}_{00}, assuming SCHC compared with the direct measurement of r^1_{1-1}.

2.4.3 ρ^0 Decay and Production Angles

Next, the various angles are given in terms of momenta, using the definitions from Ref. [80]. The notation for the various three-vectors is consistent with the notations in the rest of this thesis, with $\hat{\rho}$, $\hat{q}$, $\hat{p}$, $\hat{p}'$, $\hat{\pi}$, $\hat{k}$, and $\hat{k}'$ denoting the unit vectors along the momenta of the ρ^0, virtual photon, incident nucleon, outgoing nucleon, pion, incident lepton and outgoing lepton, respectively. By convention, the π^+ is used in these definitions.

In Fig. 2.23 the angles are indicated.

The decay angles $\theta_{\pi\pi}$ and $\phi_{\pi\pi}$ are defined in the ρ^0 rest frame, where $\hat{z}$ (in a right-handed coordinate frame) is pointing in the direction of the ρ^0 meson.

$$\cos(\theta_{\pi\pi}) = (\hat{\rho} \cdot \hat{\pi}^+), \tag{2.128}$$

$$\cos(\phi_{\pi\pi}) = \frac{(\hat{q} \times \hat{\rho}) \cdot (\hat{\rho} \times \hat{\pi})}{|\hat{q} \times \hat{\rho}| \cdot |\hat{\rho} \times \hat{\pi}|}, \tag{2.129}$$

$$\sin(\phi_{\pi\pi}) = \frac{-[(\hat{q} \times \hat{\rho}) \times \hat{\rho}] \cdot (\hat{\rho} \times \hat{\pi})}{|(\hat{q} \times \hat{\rho}) \times \hat{\rho}| \cdot |\hat{\rho} \times \hat{\pi}|}. \tag{2.130}$$

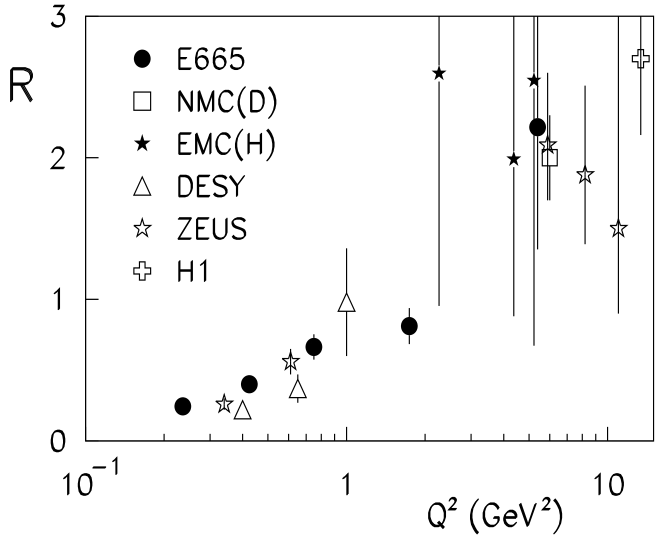

Figure 2.20: *Measurements of R as a function of Q^2 based on measurements of r^{04}_{00} and assuming SCHC. The data are taken from Ref. [8].*

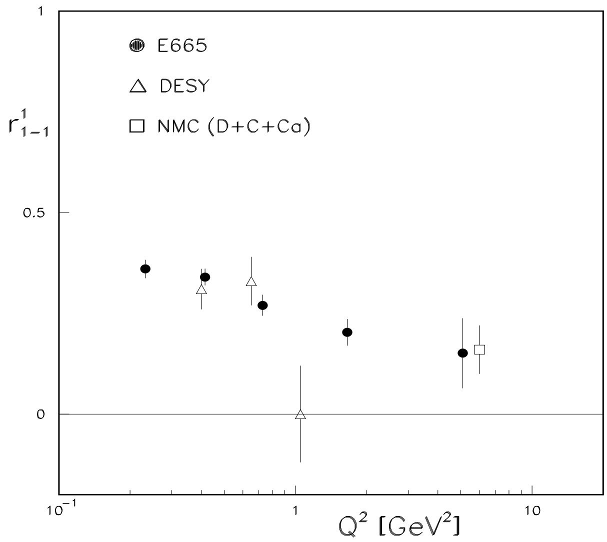

Figure 2.21: *The spin density matrix element r^1_{1-1} as a function of Q^2. Shown is r^1_{1-1} from the fit to the Ψ distribution. The data are taken from Ref. [8].*

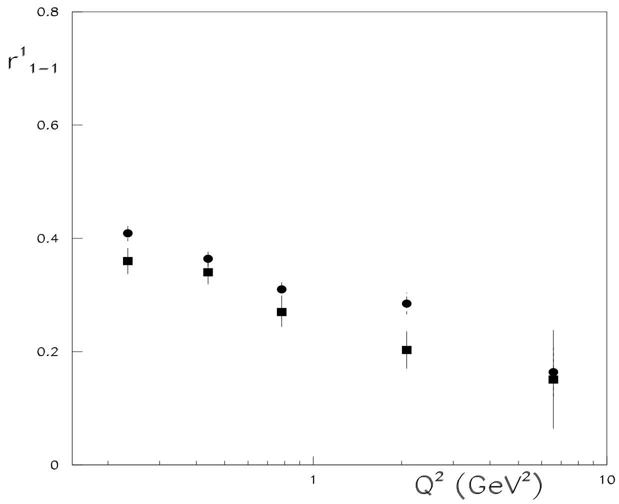

Figure 2.22: *The spin density matrix element r^1_{1-1} as a function of Q^2. Shown is r^1_{1-1} from the fit to the Ψ distribution (squares) and r^1_{1-1} as determined from the* E665 *measurement of r^{04}_{00}, assuming SCHC (circles). The data are taken from Ref. [8].*

The production plane angle Φ_{ee} is defined in the hadron centre of mass frame (i.e. boosted with W).

$$\cos(\Phi_{ee}) = \frac{(\hat{q} \times -\hat{p}') \cdot (\hat{e} \times \hat{e}')}{|\hat{q} \times -\hat{p}'| \cdot |\hat{e} \times \hat{e}'|}, \tag{2.131}$$

$$\sin(\Phi_{ee}) = \frac{[(\hat{q} \times -\hat{p}') \times (\hat{e} \times \hat{e}')] \cdot \hat{q}}{|\hat{q} \times -\hat{p}'| \cdot |\hat{e} \times \hat{e}'|}. \tag{2.132}$$

One can rewrite $\phi_{\pi\pi}$ and Φ_{ee} by using $\psi = \phi_{\pi\pi} - \Phi_{ee}$.

2.5 Summary

In this chapter, the cross section and angular distributions associated with ρ^0 production have been addressed. This thesis will discuss measurements performed at HERMES and present the data taken in 1995. The data will be compared to the results of other experiments and to various theoretical predictions that have been discussed in this chapter.

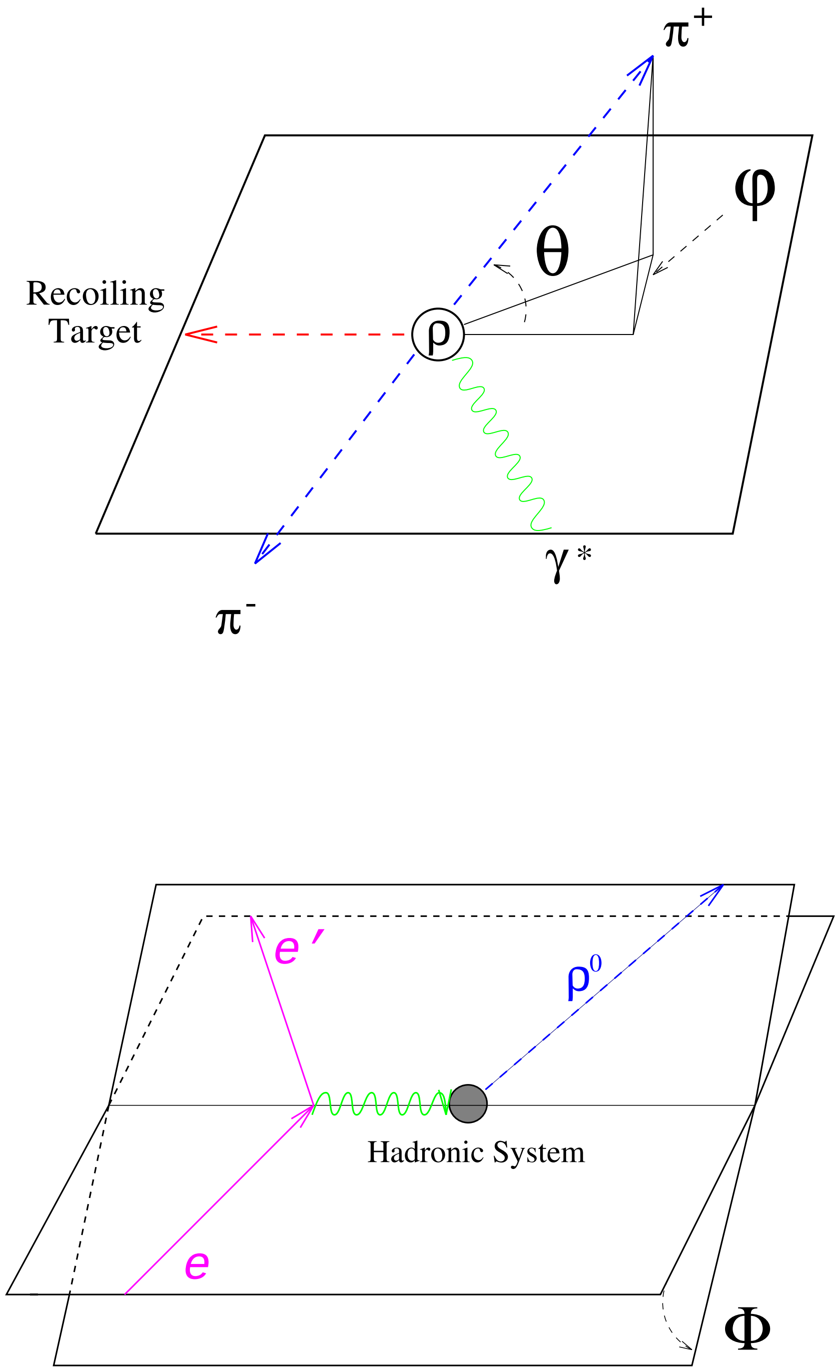

Figure 2.23: *Overview of the definition of the decay angles $\theta_{\pi\pi}$ and $\phi_{\pi\pi}$ (top) and the production plane angle Φ_{ee} (bottom).*

Chapter 3

The HERMES Experiment at HERA

3.1 Introduction

The HERMES experiment is designed to study the spin structure of the nucleon by means of measuring asymmetries for inclusive and semi-inclusive processes. It uses spin-dependent scattering of polarised positrons from polarised internal gas targets in the HERA storage ring at DESY. At the HERA accelerator facility polarised positrons are accelerated up to 27.5 GeV and protons are accelerated up to 820 GeV.
In table 3.1 the parameters of the HERA collider are summarised. In 1995, three experiments actively used HERA (HERA-B was not active yet), as depicted in Fig. 3.1.
In the ZEUS en H1 experiments data from positron-proton beam collisions are collected. The

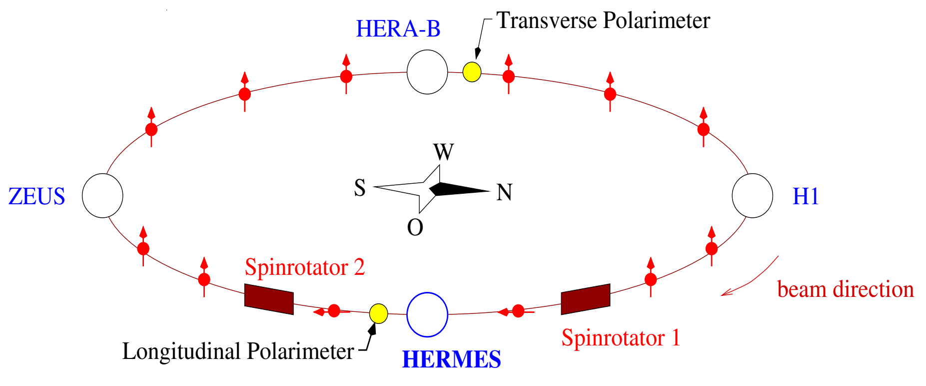

Figure 3.1: *The* HERA *ring and the locations of the* ZEUS*,* H1*,* HERA-B *and* HERMES *experiments.*

HERMES experiment only uses the positron beam and measures the results of collisions of this beam with a polarised gas. In 1996 the first test set up of the HERA-B experiment was installed. HERA-B will study collisions of protons in the beam halo with target wires and is scheduled to start taking data in 1998.

The HERMES spectrometer comprises a dipole magnet together with chambers for track reconstruction and detectors for particle identification. In this chapter the beam, target and spectrometer are described in more detail.

Table 3.1: *The 1995 operating values of the proton-positron collider* HERA *at* DESY.

	Positron	Proton
Nominal energy	27.5 GeV	820 GeV
Centre of mass energy	300 GeV	
Maximum momentum transfer	90,200 $\mathrm{GeV}^2/\mathrm{c}^2$	
Luminosity	$1.5 \cdot 10^{31}\mathrm{cm}^{-2}\mathrm{s}^{-1}$	
Polarisation time	25 min	
Number of interaction points	3	
Crossing angle	0	
Circumference	6336 m	
Time between crossing	96 ns	
Energy range	10–33 GeV	300–820 GeV
Relative energy spread$(\Delta E/E)$	10^{-3}	10^{-4}
Injection energy	12 GeV	40 GeV
Average beam current	30 mA	160 mA
Particles per bunch	3.65 x 10^{10}	10^{11}
Number of bunch buckets	220	220
Maximum number of bunches	210	210
Beam size at crossing σ_x	0.26 mm	0.29 mm
Beam size at crossing σ_y	0.07 mm	0.07 mm
Beam size at crossing σ_z	11 mm	0.8 mm

3.2 Polarised Beam and Polarimetry

In order to measure the polarised structure functions, a longitudinally polarised lepton beam is required. Due to the Sokolov-Ternov effect (see Ref. [78] and Ref. [116]), the circularly accelerated positrons become transversely polarised.

For initially unpolarised electrons of charge e, mass m, energy $E = \gamma mc^2$ (with γ the Lorentz factor) in uniform circular motion with radius ρ, the exponential rise of the transverse polarisation with time can be expressed as

$$P(t) = P_{ST} \cdot (1 - \exp^{-t/\tau_P}),$$

where the maximum polarisation is

$$P_{ST} = frac85\sqrt{3} = 0.9238, \quad (3.1)$$

and the characteristic time is

$$\tau_P = \left[\frac{5\sqrt{3}}{8} \frac{e^2\hbar\gamma^5}{m^2c^2\rho^3} \right]^{-1}. \quad (3.2)$$

The polarisation is perpendicular to both velocity and acceleration, that is, along the direction of the magnetic field of the bending magnets. Positrons are polarised parallel to the magnetic field, electrons antiparallel. The polarisation of the electrons can also be written as

$$P = \frac{N^{\uparrow} - N^{\downarrow}}{N^{\uparrow} + N^{\downarrow}},$$

where $N^{\uparrow}(N^{\downarrow})$ is the number of electrons with the spin parallel (antiparallel) to the magnetic field.

The probability for spin-flip radiation by the circularly accelerated electrons or positrons is

$$w = \frac{5\sqrt{3}}{16}\frac{e^2\hbar\gamma^5}{m^2c^2\rho^3}\left[1 - \frac{2}{9}(\vec{\zeta}\cdot\hat{\beta})^2 + \frac{8\sqrt{3}}{15}\vec{\zeta}\cdot(\hat{\beta}\times\hat{\beta}')\right], \tag{3.3}$$

where $\vec{\zeta}$ is the initial spin direction in the electron's rest frame and $\hat{\beta}$ and $\hat{\beta}'$ are unit vectors in the directions of the velocity and acceleration, respectively.

Defining $w^{\uparrow\downarrow}$ as the probability for synchrotron photon emission from an electron causing a parallel to antiparallel spin-flip in the transverse direction and $w^{\downarrow\uparrow}$ as the probability for a spin-flip in the opposite direction, one can extract from Eq. (3.3) that

$$w^{\uparrow\downarrow} = \frac{0.962}{\tau_P} \text{ ; and } w^{\downarrow\uparrow} = \frac{0.038}{\tau_P},$$

with $r_e = e^2/4\pi\epsilon_0 m_e c^2$ the classical electron radius. At HERA, one has $\gamma = E/m_e = 53800$ and the average bending radius $\rho = 707\text{m}$, giving the following probabilities for an electron to change its spin orientation

$$w^{\uparrow\downarrow} = \frac{1}{38.5\,\text{min}} \;;\; w^{\downarrow\uparrow} = \frac{1}{16.2\,\text{h}}. \tag{3.4}$$

The process that causes the self-polarisation is rare compared to the ordinary (non-flip) synchrotron radiation. The ratio of radiated powers is

$$\frac{\mathcal{P}_{\text{spin-flip}}}{\mathcal{P}_{\text{non-flip}}} = 3\left(\frac{\hbar\gamma^2}{mc\rho}\right)^2\left(1 \pm \frac{35\sqrt{3}}{64}\right), \tag{3.5}$$

where the sign depends on the initial spin state of the particle.

The high degree of maximum polarisation P_{ST} is possible because of the large difference in the spin-flip rates given in Eq. (3.4).

Figure 3.1 shows the positions of the spin rotators that are installed upstream and downstream of the interaction point. Spin rotators consist of vertical and horizontal dipole magnets which, by means of a succession of rotations, cause the direction of the spin to be longitudinal without affecting the position and slope of the beam. The spin rotator upstream of the experiment rotates the transverse polarisation of the positron into longitudinal polarisation. The spin rotator downstream of the experiment rotates the longitudinal polarisation of the positron back into the transverse direction, ensuring that the positrons remain polarised throughout the storage ring. HERA is the first electron storage ring which achieved longitudinal polarisation. Figure 3.2 shows a rise-time curve indicating the build-up of polarisation during a luminosity run.

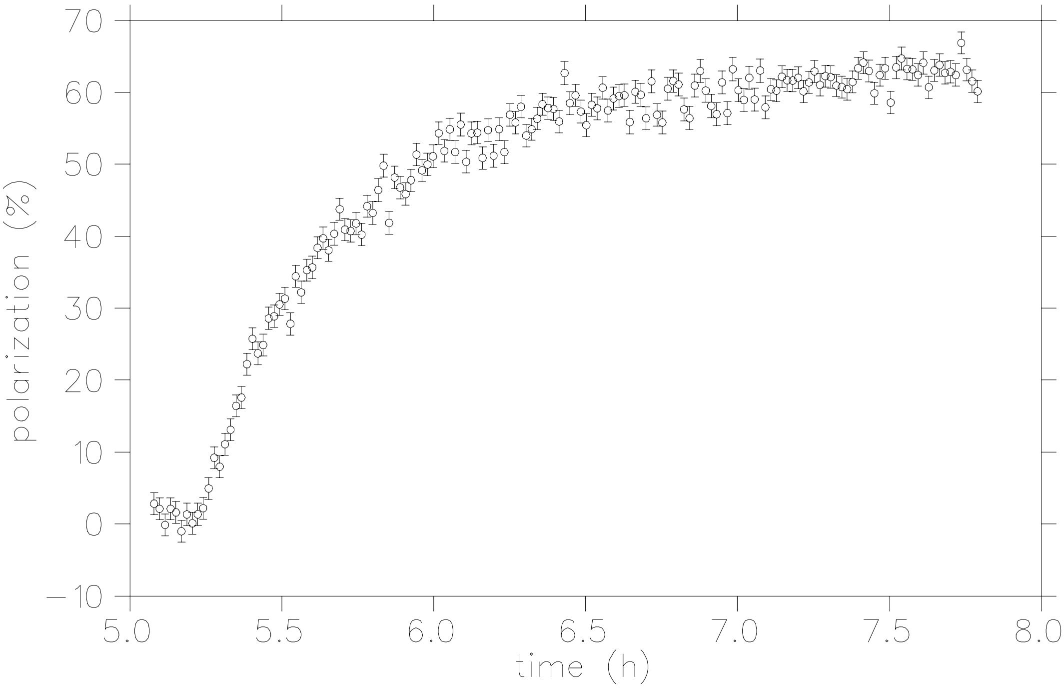

Figure 3.2: *Rise-time curve of electron beam polarisation as measured in 1995 with the transverse polarimeter.*

3.2.1 Transverse Polarimeter

In 1995 transverse polarisation in the ring was measured using a laser backscattering polarimeter. Since the loss of polarisation due to the spin-rotators is expected to be negligible [45], one can safely assume the transverse polarisation in the ring to be equal to the longitudinal polarisation in the region of the HERMES experiment. The degree of polarisation has to be the same everywhere in the ring due to the statistical equilibrium of polarisation and depolarisation effects which cannot be different at different locations in the ring. The direction of polarisation is ensured both by the precision of the spin rotators which is at the permill level (hence, within a few permill the rotation is 90°), and by the requirement that the transverse polarisation in the ring should be exactly vertical in order not to destroy all polarisation by depolarisation effects.

For transverse polarimetry one takes advantage of the fact that the cross section for Compton scattering of polarised laser light from a polarised lepton beam contains a term which is depending on both the lepton beam polarisation and the circular polarisation of the incident photons. In the rest frame of the initial electron, Compton scattering of a polarised photon and a polarised lepton is given as (see Ref. [46]),

$$\frac{d\sigma}{d\Omega}(\vec{S},\vec{P}) = \Sigma_0 + \Sigma_1(S_1) + \Sigma_2(S_3,\vec{P})$$

where Σ_0 represents the unpolarised part of the cross section, $\Sigma_1(S_1)$ represents the contribution from linear polarised light and depends on the polarisation of the laser light only and $\Sigma_2(S_3,\vec{P})$

represents the contribution from circular polarised light and depends on the polarisation of both the laser light and the positron beam. $\vec{S}$ describes the polarisation of the laser light and $\vec{P}$ represents the polarisation vector of the lepton beam. If the laser light is circularly polarised, then the intensity of the backscattered photons is distributed asymmetrical with respect to the azimuthal scattering angle ϕ. The magnitude of this asymmetry is proportional to the transverse polarisation of the lepton beam.

The backscattered photons are detected in a tungsten scintillator sandwich calorimeter, consisting of four segments, a left, right, upper and lower half. For the determination of the polarisation, one measures the counting rate asymmetry that results from a comparison of the upper two segments and the lower two segments of the calorimeter as

$$\eta = \frac{E_U - E_D}{E_U + E_D},$$

with E_U and E_D the fraction of the total energy of a shower deposited in the upper and lower half of the calorimeter respectively. The variable η is a measure of the transverse polarisation of the lepton beam. The equalisation of the calorimeter segments is monitored by using

$$R = \frac{E_U + E_D}{E_L + E_R}$$

which should equal unity in an ideal detector.

At the location of the calorimeter, the mean of the vertical photon coordinate shifts by typically 150 μm between the two laser helicity states. This assumes a positron beam polarisation of 50 % and Compton photon energies between 5.5 and 11.1 GeV, which is typical. The corresponding angular shift is about 2.5 μrad [114].

3.3 HERMES **Polarised Internal Target**

HERMES uses a polarised internal target system consisting of a polarised gas source, storage cell, holding field magnets (Fig. 3.3) and several polarimeters. A more detailed description can be found in Ref. [99] and [105]. The advantage of using an internal storage cell target is the increase of the luminosity by more than two orders of magnitude compared to that of a free atomic beam. The advantage of using pure gas targets is the high degree of polarisation which can be obtained without any dilution due to the presence of non-polarised nuclei. At HERMES, the target polarisation was reversed every ten minutes in order to minimise systematic uncertainties.

The limiting factor on the target density of internal targets is their effect on the beam life-time. At HERMES the upper limit for the allowed target density is $3.5 \cdot 10^{14}\,\mathrm{atoms/cm^2}$ for ^{3}He. Pumping stations are installed upstream and downstream of the target cell to pump out the target gas and maintain an ultrahigh vacuum in the beam pipe.

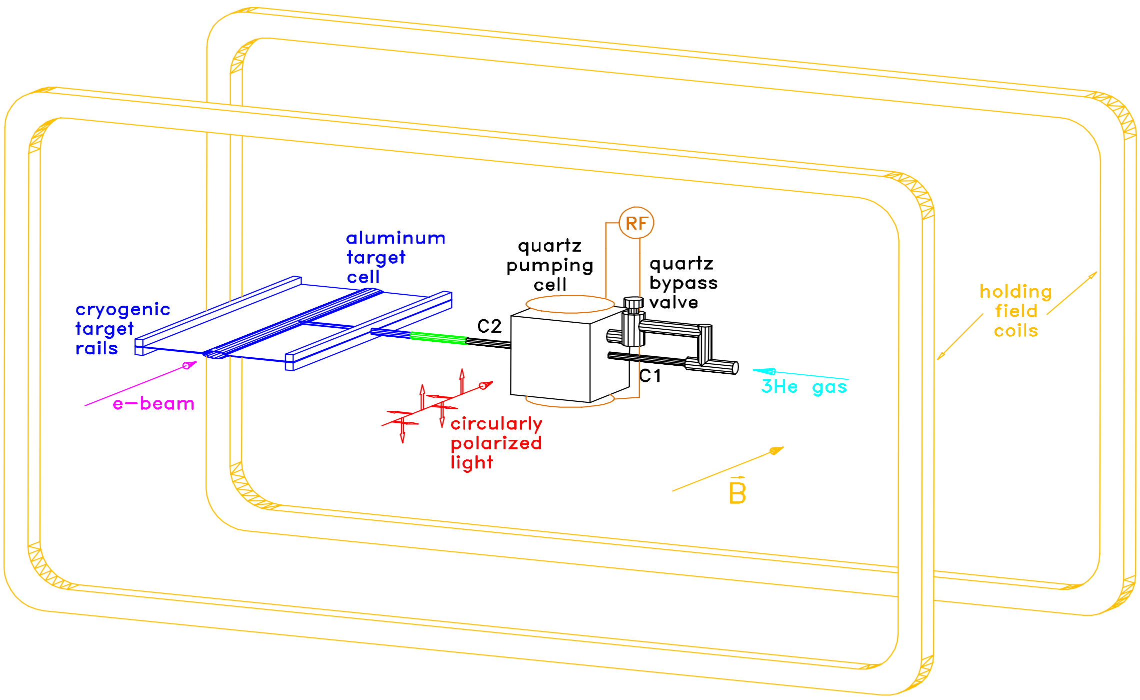

Figure 3.3: *Overview of the ^{3}He target. The unpolarised ^{3}He gas is injected into the quartz pumping cell, where the ^{3}He atoms become polarised through metastability exchange by optical pumping with circularly polarised 1083 nm radiation incident on the pumping cell. The polarised ^{3}He atoms flow to a cryogenic open-ended storage cell through which the* HERA *positron beam passes. Also indicated are the target holding-field coils, necessary to determine the axis of polarisation.*

3.3.1 Polarised ^{3}He

In 1995 data were taken with polarised ^{3}He, except for a few days in which unpolarised hydrogen and deuterium targets were used. ^{3}He is polarised by means of metastability-exchange optical pumping [110]. Fig. 3.4 shows a schematic overview of the relevant energy levels of the ^{3}He atom. ^{3}He gas is fed into a pumping cell in which a weak radio frequency discharge excites a small fraction ($\sim 10^{-6}$) of the ^{3}He atoms to the long-lived 2^3S_1 metastable state with a life time in the order of 1 millisecond [105]. Circularly polarised light incident upon the sample, together with an applied weak magnetic field allows to excite transitions between 2^3S_1 and 2^3P_0 states. The total angular momentum of the polarised photons is thus transferred to the metastable atoms which become polarised. By selecting right-handed circularly polarised laser light (with $\Delta m = +1$) only particular 2^3P_0 states will be pumped. The 2^3P_0 states will decay back to the 2^3S_1 states and because of the selection of right-handed incident laser light the 2^3S_1 state with $m = +3/2$ will be enhanced.

Transfer of polarisation to the ground-state atoms is achieved through metastability exchange collisions by

$$^3\overrightarrow{\mathrm{He}}(2^3S_1) +^3 \mathrm{He}(1^1S_0) \rightarrow^3 \overrightarrow{\mathrm{He}}(1^1S_0) +^3 \mathrm{He}(2^3S_1).$$

In these collisions the electron clouds of the metastable atom $^3\vec{\mathrm{He}}(2^3S_1)$ (with a polarised electron cloud and a polarised nucleus) and a ground-state atom $^3\mathrm{He}(1^1S_0)$ (with an unpolarised electron cloud and an unpolarised nucleus) effectively exchange, resulting in a metastable atom with unpolarised nucleus $^3\mathrm{He}(2^3S_1)$ and a ground-state atom with polarised nucleus $^3\vec{\mathrm{He}}(1^1S_0)$. The nucleus of the metastable atom gets polarised again by means of the mechanism described above. The polarised nucleus of the ground state $^3\vec{\mathrm{He}}(1^1S_0)$ remains polarised.

3.3.2 The Storage Cell.

The HERMES storage cell is a 125 μm thick aluminium tube of length 400 mm with an elliptical cross section of 30 $\times$ 10 mm^2. There are no entrance and exit windows on the storage cell and therefore interaction of the positron beam with the cell material is avoided. The cell is constructed in such a way that the atoms experience a high number of wall bounces before they leave the storage cell, thus increasing the probability of interactions with the beam. The resulting target density is approximately triangular in shape as shown in Fig. 3.5. Meshes of 125 μm thick titanium in the target chamber along the beam direction avoid wake field excitations which otherwise would heat up the storage cell.

To avoid excessive synchrotron radiation rates in the cell as well as scattered synchrotron photons into the spectrometer, three collimator systems are installed upstream of the experiment. Two collimators can be opened and closed in either the horizontal or the vertical direction; the third collimator has a fixed aperture. In the HERMES test experiment, performed in 1994, it was shown that these collimators adequately decrease the background rates due to synchrotron radiation without affecting the life time of the beam [1].

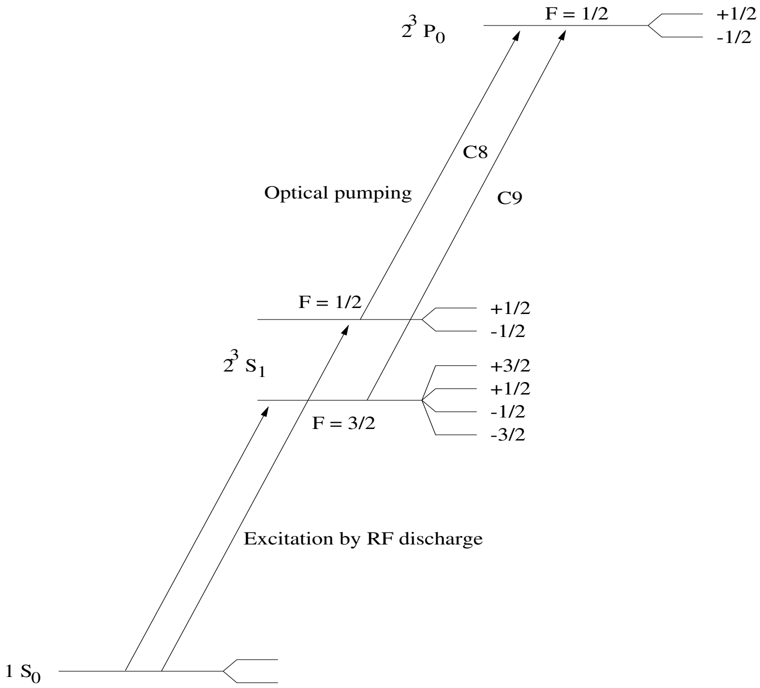

Figure 3.4: *The energy levels of* ^{3}He. *The* ^{3}He *gas is brought to the metastable* 2^3S_1 *state via a weak radio-frequency discharge.*

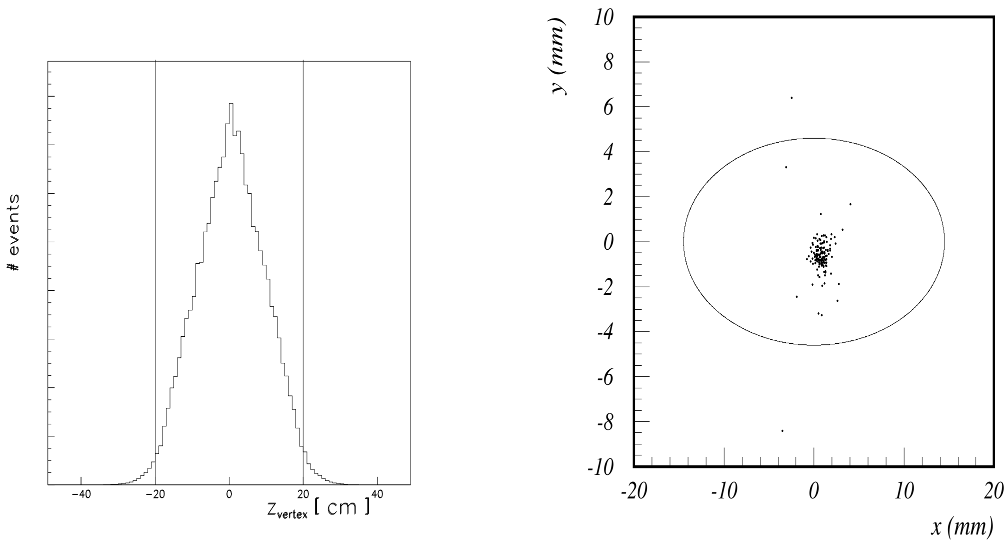

Figure 3.5: *Left: Number of events versus primary vertex position. The two vertical lines mark the size of the target cell. Right: Number of events in the* $x - y$ *plane at the centre of the target-cell. The drawn ellipse indicates the size of the storage cell.*

3.3.3 Target Polarimetry

To determine the polarisation of the atoms in the pumping cell, the degree of circular polarisation in the $3^1D_2 \rightarrow 2^1P_1$ 667 nm transition, emitted in the discharge of the ^{3}He gas sample, is measured. This transition occurs coincidentally as a result of the radio frequency excitation of the ^{3}He gas. The emitted light from the pumping cell passes through a rotating quarter-wave plate, a linear polariser, a 667 nm filter and is detected by a photomultiplier tube. The relation between the measured amount of relative intensity of left- and right-handed circularly polarised photons and the degree of nuclear polarisation was calibrated at an earlier stage [90]. One expects a negligible loss of polarisation after the gas is emitted into the storage cell.

A measurement of the polarisation of the ^{3}He gas inside the target cell is provided by the Target Optical Monitor (TOM) (see Ref. [103]). The Coulomb interaction of the beam with the polarised gas will excite the atoms in the internal gas target into 4^1D states. The photon emission rate from the atomic levels is proportional to the product of target thickness and beam current, so it is a measure of the luminosity for H, D, or ^{3}He targets. Thus the TOM can provide a useful relative luminosity monitor of the two different target spin states (i.e., relative changes in luminosity will be detected by the TOM). In the case of ^{3}He, the polarisation of the nuclei is transferred to the electrons in the atoms, which, on relaxation, emit circular polarised light and thus the polarisation of the nucleus can be determined by measuring the circular polarisation of the emitted atomic photons.

The optical photons from the target are reflected by a polished aluminium plate, placed upstream of the target cell. The photons are reflected through a quartz vacuum window, pass through a focused lens and then reflect off a second mirror into a two inch phototube.

Fig. 3.6 shows the target polarisation determined by the TOM and by the pumping cell polarimeter. Although the lack of statistics does not allow using the TOM for an absolute measurement of the polarisation, the TOM provided a means to cross-check the sign and order of magnitude of the target polarisation as measured by the pumping cell polarimeter.

3.4 HERMES spectrometer

In Fig. 3.7, an overview of the HERMES spectrometer is shown. The HERMES coordinate system is right handed, with the z axis along the beam direction, the x axis pointing towards the centre of HERA and the y axis pointing upwards. The geometrical acceptance is 40 mrad $\leq |\theta_y| \leq$ 140 mrad and $|\theta_x| \leq 170$ mrad.

The upper and lower half of the spectrometer consist of similar detectors. The dipole magnet divides the spectrometer into a front and a back region. The magnet, with a magnetic field integral of $\int Bdl = 1.4$ Tm, is used for momentum determination. Tracking chambers are installed in the front and in the back region. In the front region are the Vertex Chambers (VC), using the novel technique of Micro Strip Gas Counters (MSGC), and the Front Chambers (FC) which are multi-wire drift chambers. The VCs and FCs are used to determine partial tracks

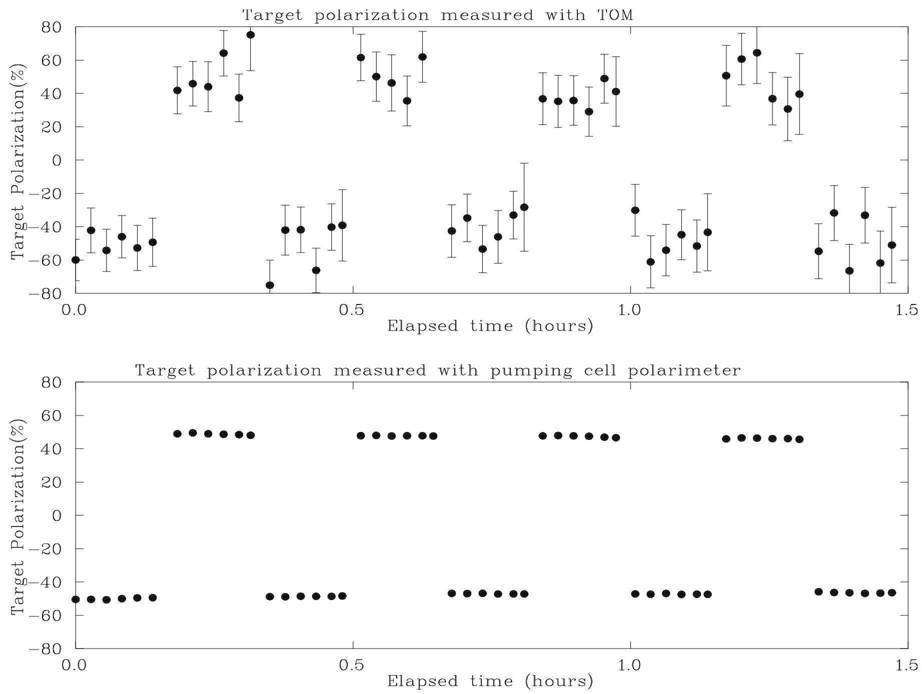

Figure 3.6: *Measurement of the target polarisation determined by the TOM and by the pumping cell polarimeter versus time (hours).*

in the front region. In the back region are the Back Chambers (BC) which are also multi-wire drift chambers. The BCs are used to determine partial tracks in the back region. Multi-wire proportional chambers, the Magnet Chambers (MC), are installed in the magnet region to resolve track ambiguities when combining the partial tracks of the front and the back region. The most important characteristics of the VCs, FCs, MCs and BCs are summarised in Table 3.2.

For particle identification as well as for providing the main triggers, an electromagnetic calorimeter, two rows of scintillation hodoscopes and a Čerenkov detector are installed. A transition radiation detector (TRD) is used in addition for electron (positron) identification.

The various components of the HERMES spectrometer are described in further detail in the following sections.

3.4.1 Multi-Wire Drift Chambers

The chambers FC1, FC2, BC1, BC2, BC3, and BC4 are conventional horizontal drift chambers. They comprise planes of alternating anode and cathode wires between a pair of cathode foils. The cathode wires and foils are at negative high voltages and the anode sense wires are at ground potential. The chambers are assembled as modules consisting of six such planes in three coordinate doublets (UU', XX' and VV'). The wires are directed vertically for the X planes and at angles of $\pm 30^o$ to the vertical for the U and the V planes. The X', U', and V'

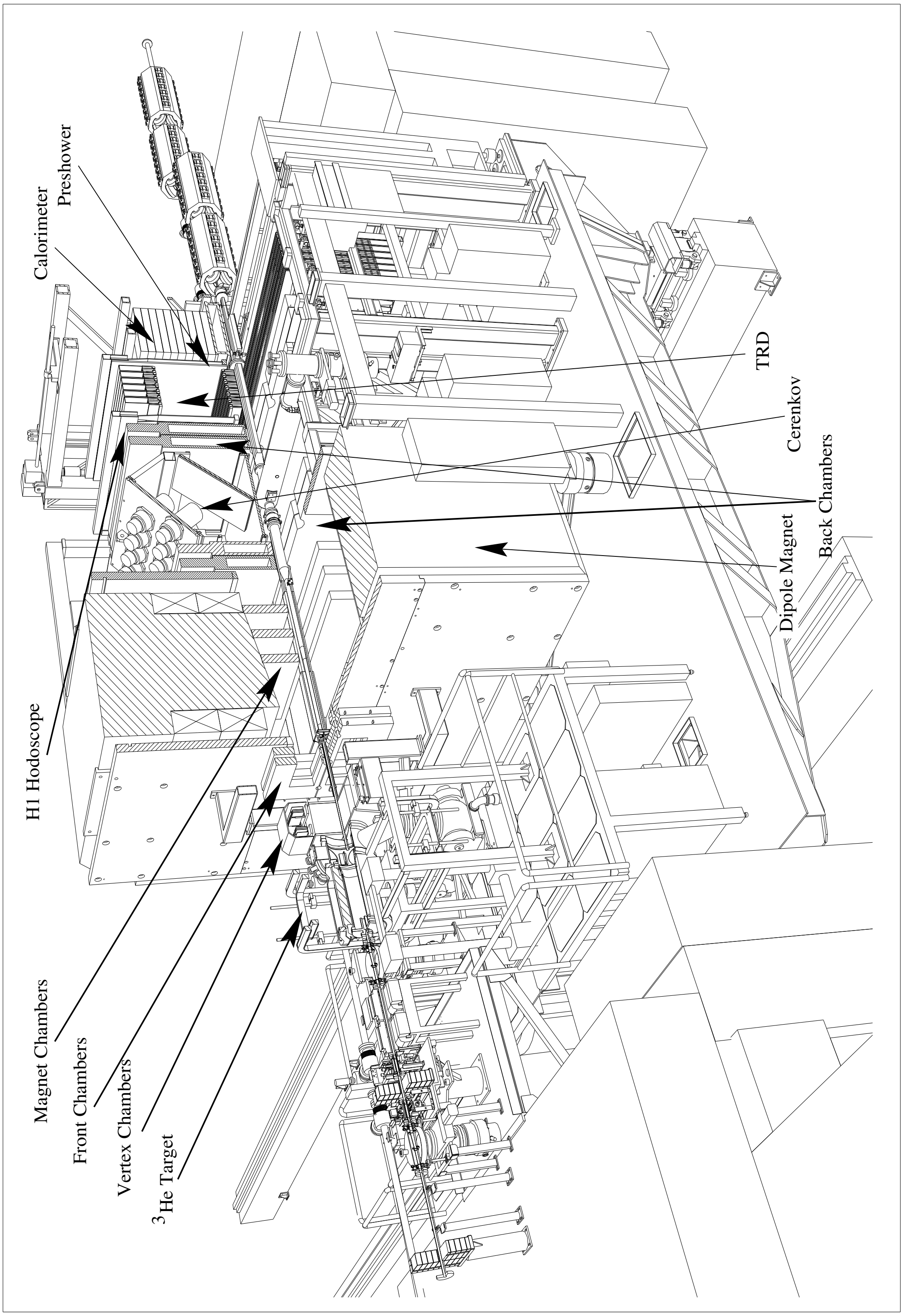

Figure 3.7: *Overview of the* HERMES *spectrometer, showing the target, tracking chambers, particle identification detectors and magnet.*

Table 3.2: *Characteristics of the tracking chambers.*

	Vertex	Front	Magnet	Back
name	VC1 VC2	FC1 FC2	MC1 MC2 MC3	BC1/2 BC3/4
z-pos (mm)	727 972	1526 1637	2655 3060 3423	4150 5900
active hor. (mm)	420 420	680 680	996 1216 1424	1888 2890
active ver. (mm)	137 145	220 220	263 306 347	520 710
type	micro strip gas	drift	proportional	drift
cell size	193 μm	7 mm	2 mm	15 mm
gas types	$\mathrm{DME/Ne}$	$\mathrm{Ar/CF_4/CO_2}$	$\mathrm{Ar/CF_4/CO_2}$	$\mathrm{Ar/CF_4/CO_2}$
gas mixture	50/50 %	90/5/5 %	65/30/5 %	90/5/5 %
nom. resolution	45 – 56 μm	150 μm	460 – 570 μm	150 μm
rad. length / mod.	0.8 %	0.20 %	0.29 %	0.26 %
num. of modules	1 1	1 1	1 1 1	2 2
module config.	VUX XVU	UU'XX'VV'	UXV	UU'XX'VV'
# planes / mod.	3 3	6 6	3 3 3	6 6
# wires (X planes)	1674 2046	96 96	496 608 720	120 192
„ „ (U, V planes)	2170 2170	96 96	512 608 720	118 186
readout	digital (APC)	TDC	digital (PCOS)	TDC

planes are staggered with respect to their partners by half the cell size in order to resolve left-right ambiguities.

The front drift chambers FC1 and FC2 consist above and below the beam of one module of six planes each. Hence, in total the front chambers have twelve sense planes. The FC chambers have a drift cell size of 7 mm.

The back drift chambers BC1, BC2, BC3 and BC4 consist above and below the beam of one module of six planes each. Hence, in total the back chambers have twenty–four sense planes. The BC chambers have a drift cell size of 15 mm. A more detailed description of the FCs and the BCs can be found in Ref. [2] and in Ref. [28], respectively.

3.4.2 Multi-Wire Proportional Chambers

The proportional chambers MC1, MC2, and MC3 are located in the magnet region and are intended to help resolve multiple tracks in case of high multiplicity events. In addition they are used for the momentum analysis of low-energy tracks which are bent out of the detector acceptance in the back region. Each chamber consists of three submodules U, X, and V and each submodule comprises an anode plane at ground potential and two cathode planes with a common negative high voltage.

3.4.3 Micro-Strip Gas Counters.

The VCs use the novel technique of micro-strip gas chambers (MSGC). They consist of two times two modules. Each vertex chamber module VC1 and VC2 consists above and below the beam of a U, V, and X plane. Compared to traditional drift chambers there are a number of differences which characterise a MSGC [32]. The size of the drift cells of a MSGC is considerably smaller. Charged particles will travel away from the cathode plane at the front of the cell, through the cell volume which is filled with a particular gas, towards the substrate plane. The substrate is covered with anode and cathode strips, causing electrons to drift towards the anodes and positive ions towards the cathodes. In the vicinity of the anode, gas multiplication occurs. In Fig. 3.8 the principle of an MSGC is depicted. Currently the VCs at HERMES, with active

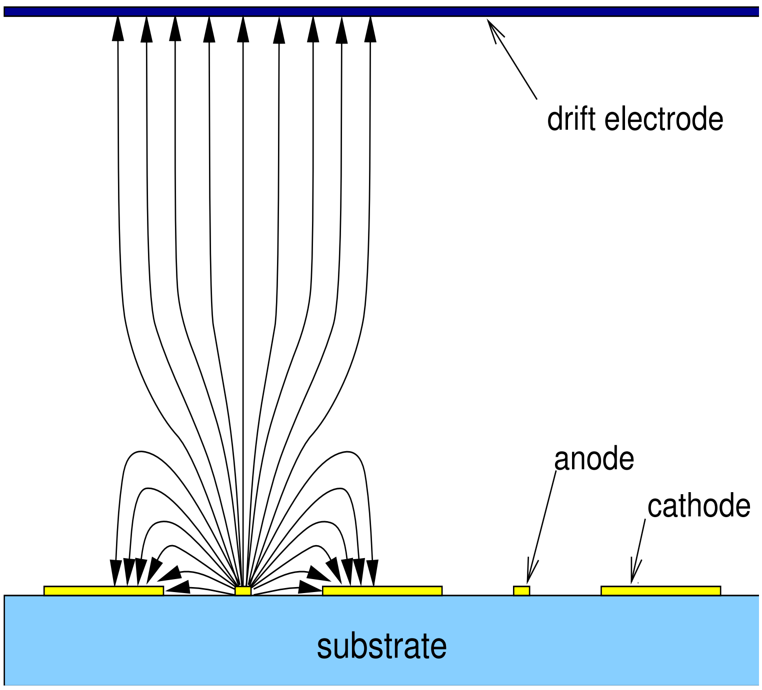

Figure 3.8: *Principle of operation of a micro-strip gas counter, showing the geometry and electrical field lines. (Picture taken from [91].)*

areas of $420 \times 137\,\mathrm{mm}^2$ (VC1) and $420 \times 145\,\mathrm{mm}^2$ (VC2), and a number of strips per plane in the order of 2000, are the largest application of the MSGC technique in the world. The U and V planes consist of 5 substrates of 434 anode strips each. The X planes consist of three substrates of 558 anode strips each. The cell size in the z direction is 3 mm. The anode strips are 7 μm wide and the cathode strips are 90 μm wide. The distance between two anode strips is 193 μm. The drift gas in the chamber is a mixture of 50 % Ne and 50 % DME.

The design of the HERMES VC is shown in Fig. 3.9. The two outer substrates of the X planes are tilted at an angle of $\pm 6.93^o$ with respect to the $x - y$ plane, the centre wing is perpendicular to the z axis. The tilted angle in the X planes is introduced to keep the angle of incidence of

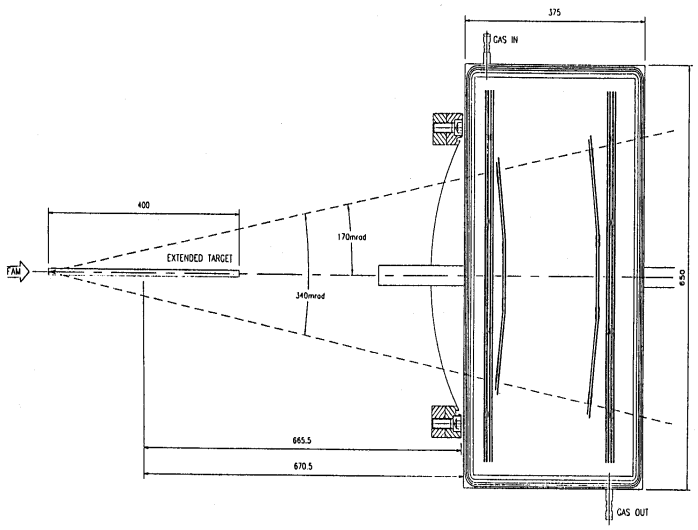

Figure 3.9: *Top view of the VC. The 6 planes are arranged in a UVX and XVU sequence, respectively. The horizontal and vertical angular acceptance are given by 40 mrad* $\leq$ $\mid \theta_{vert} \mid \leq$ *140 mrad and* $\mid \theta_{hori} \mid \leq$ *170 mrad.*

scattered particles originating from the target with respect to the detector planes below 72 mrad to avoid loss of position resolution for large scattering angles. The substrates consist of a thin plate (200 μm) of borosilicate glass D263 covered by a thin resistive layer made of a nickel-chromium alloy and an aluminium layer of 1 μm. The minimised thickness of the glass layer ensures a minimal amount of radiation lengths in the VC of 0.8 % [31].

3.5 Detectors for Particle Identification

The detectors which are used for PID purposes are the hodoscopes, Čerenkov counter, Transition Radiation Detector (TRD) and calorimeter.

3.5.1 Hodoscopes

The hodoscopes consist of two rows of 42 scintillator modules, 1 cm thick and 9.3 $\times$ 91 cm^2 in the $x - y$ plane, both in the top half and the bottom half of the spectrometer. The modules are made of BC-412 scintillator material from Bicron Co., a fast scintillator with large attenuation length (300 - 400 cm). The scintillation light is detected by 5.2 cm diameter Thorn EMI 9954 photomultiplier tubes. The modules are staggered to provide maximum efficiency with 2 - 3 mm of overlap between each unit. The first row (H1) is located directly behind the BCs. The second row (H2) is located behind the Čerenkov detector, in front of the calorimeter. The second row of hodoscopes is often referred to as the ‘Preshower’, because of the 11 mm thick layer of lead in front of it. This causes electrons, positrons and photons to start showering before entering the calorimeter, thus increasing the electron/pion separation.

3.5.2 Čerenkov Counter

Both the top and bottom half of the Čerenkov detector consists of an array of 2×10 mirrors at the backside of a volume filled, in 1995, with pure nitrogen gas. Particles with relativistic velocities β that exceed the velocity of light in N_2 will emit Čerenkov light, which will be reflected in the mirrors onto an array of 5” RCA 14-stage Quantacon photomultipliers. For a given momentum, the detection of Čerenkov radiation indicates that the particle mass is below a certain value. Depending on the gas mixture used in the detector, there will be a limit $\gamma_{threshold}$ to the Lorentz factor γ of the particle which can still be detected. The momentum threshold for a certain particle type is given by $p_{threshold} = \beta_{threshold} \times \gamma_{threshold} \times m_{particle}$, with $\beta = \sqrt{1 - 1/\gamma^2}$. The threshold velocity is related to the index of refraction of the gas by means of the relation $\beta_{threshold} = 1/n$.

For the 1995 data N_2 gas was used, resulting in momentum thresholds of 6 GeV, 16 GeV and 38 GeV for pions, kaons and protons, respectively. Hence, if the other PID detectors indicate that a particular particle was *not* an electron and the momentum is in the range 6 - 16 GeV, then the particle can be identified as a pion.

3.5.3 Transition Radiation Detector

The TRD is based on the detection of transition radiation. When an electrically charged particle with a relativistic velocity crosses a dielectric boundary, it will produce X rays. The energy spectrum of the emitted X rays is depending on the Lorentz factor γ which allows for a better particle identification compared to more conventional PID detectors which use a dependency on the relativistic velocity β. The energy of the produced photons is typically in the range 2 - 15 keV for particles with $\gamma > 1000$. For positrons the Lorentz factor will differ ($\gamma > 1000$) from that for hadrons ($\gamma < 300$).

The TRD consists of six consecutive modules. Each module is composed of a radiator in which the radiation is produced followed by the radiation detector in which the radiation is detected. The radiator consists of a gas–mixture (90% Xe, 10% CH_4), in which polypropylene fibres are stacked in a random fashion. The radiation occurs at the boundaries of the fibres and the surrounding gas. The radiation detector in each module is a wire-chamber, filled with Xe gas, comprising 256 wires with a wire spacing of 1.27 cm. An extensive description of the TRD can be found in Ref. [53].

3.5.4 Electromagnetic Calorimeter

The electromagnetic calorimeter is designed to measure the energies of incoming electrons, positrons and photons. An overview of the calorimeter is given in Fig. 3.10. At energies in the GeV range photons will produce electron-positron pairs by pair–production, whereas electrons and positrons will radiate photons by brehmstrahlung in the calorimeter material. An increasing number of photons, electrons and positrons will be produced with decreasing average energies. Eventually, the leptons with lower energies produce Čerenkov light which is detected by 3" Philips XP3461 photomultipliers. The amount of photons reaching the photomultipliers at the end of the lead glass counters is in first order proportional to the energy of the incoming electrons or positrons. Hadrons or heavier leptons will not deposit all their energy in the calorimeter. Comparing the energy as measured in the calorimeter with the momentum determined from tracking enables separation of hadrons and electrons (positrons).

To relate the amount of photons detected with the photomultipliers to the energy of the incoming particle, calibration tests were performed, both at a DESY test beam and a CERN test beam. The characteristic parameters of these test beams are given in table 3.3. The results of these tests are described below.

Table 3.3: *Test beam parameters.*

	CERN	DESY
test beam	SPS X1	N21
particle	e	e
	π	
intensity $[sec^{-1}]$	$10^3 - 10^2$	10
	$10^4 - 10^2$	
$\Delta p/p$	$\pm 0.3\%$	$\pm 4\%$
P_{max} [GeV]	80	6

The calorimeter consists of 840 lead glass blocks (42 columns of 10 rows in both the top and the bottom half of the detector) of $9 \times 9 \times 50$ cm^3 size. Because of the potentially high radiation levels present in the HERA environment, radiation-resistant lead glass - type F101 is used. The parameters of F101 lead glass are summarised in Table 3.4. The counters are supported by two inner frames. To prevent radiation damage of the lead glass, both frames can be vertically moved away from the beam pipe by 50 cm during beam injection and beam dump. The lead glass blocks are wrapped in aluminised mylar foil of 50 μm thickness and the front and rear ends were covered with tedlar foil of 150 μm thickness to provide light isolation. The cathode windows of the photomultipliers are glued to the rear ends of the lead glass blocks with silicon glue (SILGARD 184) with refraction index 1.41. The photomultiplier tubes are surrounded by a 1.5 mm thick μ-metal shield to decrease the influence of magnetic fields on the photomultipliers.

Table 3.4: *Characteristics of the radiation resistant F101 lead glass used for the* HERMES *electromagnetic calorimeter.*

Chemical composition	(weight %)
Pb_3O_4	± 51.23
SiO_2	± 41.53
K_2O	± 7.0
Ce	± 0.2
Radiation length	2.78 cm
Density	3.86 g/cm^3
Index of Refraction	1.65

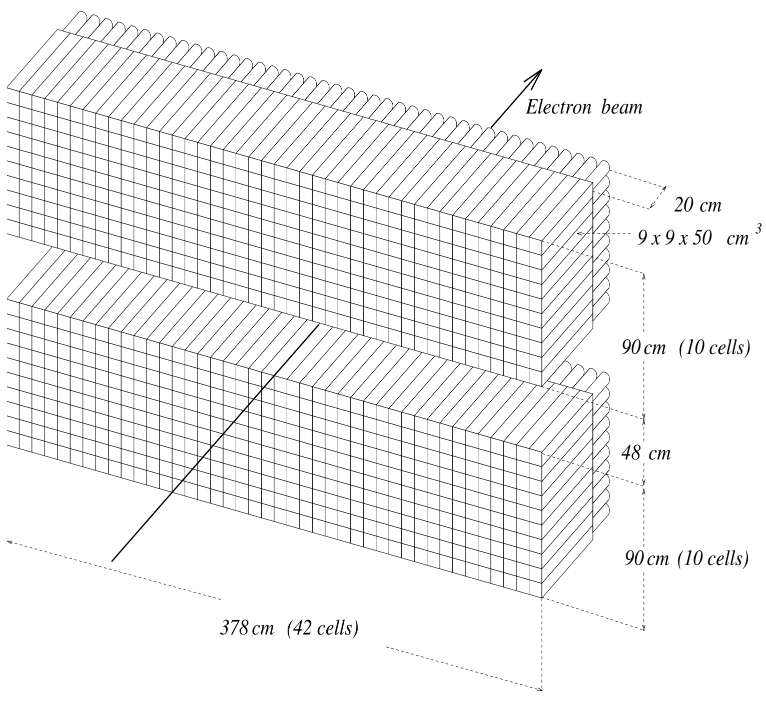

Figure 3.10: *Overview of the geometry of the electromagnetic calorimeter. The lead glass blocks are stacked in a fly's eye configuration.*

3.5.5 Calibration of the Calorimeter

In 1994, calibration tests were performed by using test beams at DESY and CERN. A detailed description of these tests and their conclusions can be found in [21], [54] and [55]. At DESY, all calorimeter blocks were equalised, using a 3 GeV electron beam to calibrate the response of the calorimeter together with the preshower set-up and the ADCs as used in the actual experiment. Two reference counters were continuously placed in the test area to monitor gain shifts due to temperature changes which afterwards were corrected for, when determining the gain curve of each individual lead glass block.

At CERN additional tests were carried out on a random sample of 60 blocks in order to study their response for various beam parameters (energy up to 30 GeV, incoming angle and particle type). Also the effect of the preshower in front of the lead glass was studied.

Fig. 3.11 shows the linearity of the response of the calorimeter versus the energy of the electrons incident at a $90°$ angle with respect to the front of the calorimeter. The figure shows the data points and the fitted function $E = \Sigma_{i=1}^{9} C_i \cdot (A_i - P_i)$, with C_i the calibration constant for block i and A_i the number of ADC counts and P_i the pedestal value. The response is summed over an array of 3×3 blocks; the impact point of the beam was positioned at the centre of the centre block of this array.

Fig. 3.12 shows the distribution of the difference between the position of an impact point measured by the calorimeter and the impact point as estimated by tracking. The resolution of the position reconstruction is about 0.7 cm.

Fig. 3.13 shows the lateral spread of the shower as a function of the impact point for the 3 GeV electron beam. The sum of the deposited energy in two adjacent blocks varies with less than 2 $\%$. Moreover, it was found that for incident angles within the acceptance of the HERMES spectrometer, the variation of the response is less than 1 $\%$ for the central block in a 3×3 array. The leakage of the shower into adjacent blocks can be used to optimise the position determination of incoming photon tracks in the experiment. This is especially important for reconstructing π^0s, which can be used as an additional tool in the offline analysis of the HERMES data to fine-tune and monitor the calibration constants of the calorimeter blocks.

Fig. 3.14 shows the energy resolution $\Delta E/E$ as a function of the energy of the incoming electron beam, directed at the centre of a 3×3 array of blocks. The energy is measured by summing over all nine blocks and taking into account the energy loss due to the presence of the preshower. The dotted curve is a fit to the data of the form $\Delta E/E[\%] = A/\sqrt{E\,[GeV]} + B$. The obtained values for A and B are 5.1 ± 1.1 and 1.5 ± 0.5, respectively.

Fig. 3.15 shows the pion/electron rejection factors for different energies of incoming pion and electron test beams. The particular threshold for $E/|\vec{p}|$ choosen to obtain these factors correspond to a 95% electron efficiency. The rejection factors can be slightly improved by reducing the cluster size from a 3×3 array to a cluster formed by blocks less than half the block-size away from the impact point which effectively makes a cut on the lateral spread of the showers, which in the case of pions tend to be bigger than in the case of leptons or photons.

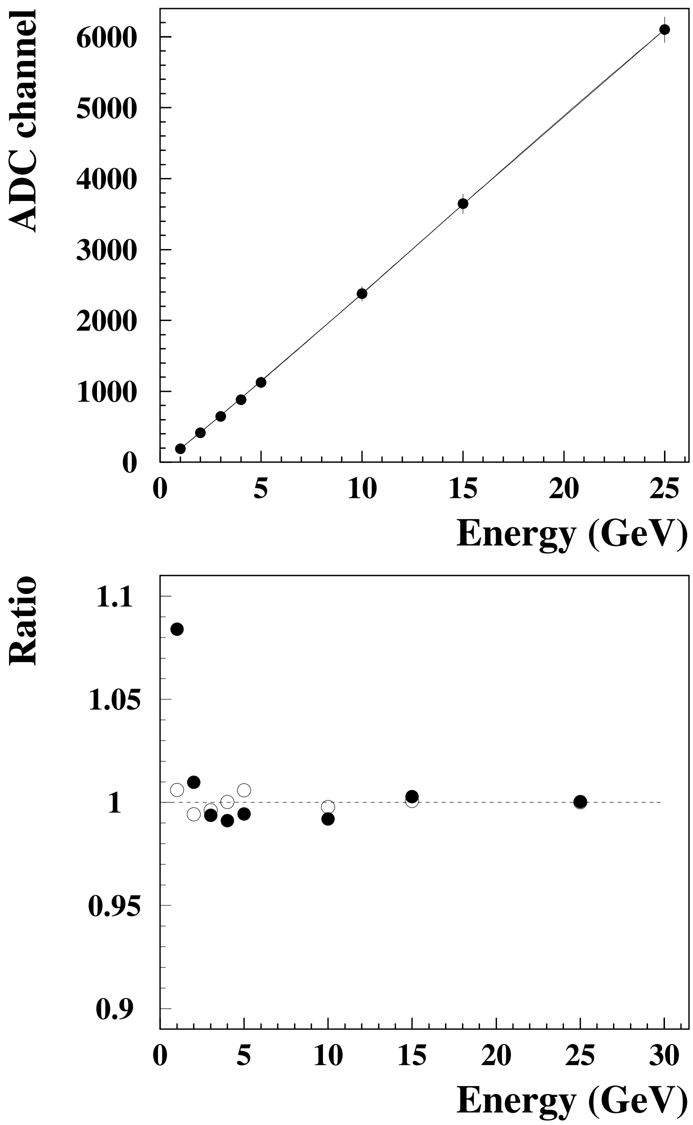

Figure 3.11: *The top figure shows the calorimeter response versus incident energy. The solid line is a linear fit to the data. The bottom figure shows the ratio between the linear fit and the data (filled circles) and the ratio between a cubic fit and the data (open circles).*

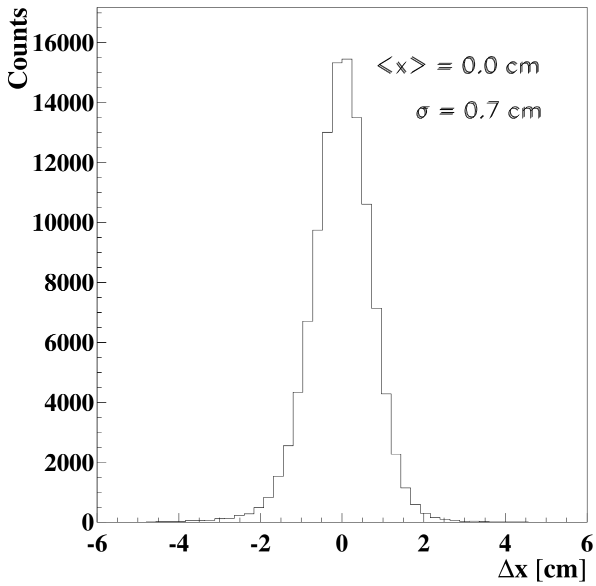

Figure 3.12: *Distribution of the difference between the position of an impact point measured by the calorimeter and the impact point as estimated by tracking.*

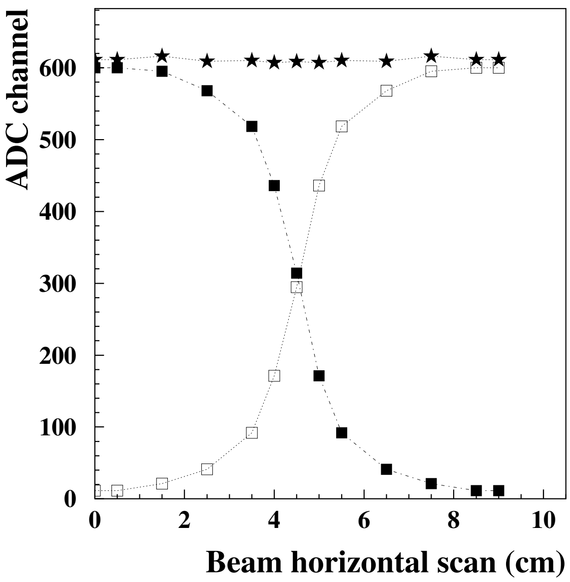

Figure 3.13: *Response of the calorimeter as a function of the lateral position of the impact point. The positions 0 and 9 cm correspond to the centers of two adjacent blocks. The solid and open squares correspond to the responses of the two adjacent blocks separately, the stars correspond to the sum of the responses of the two blocks.*

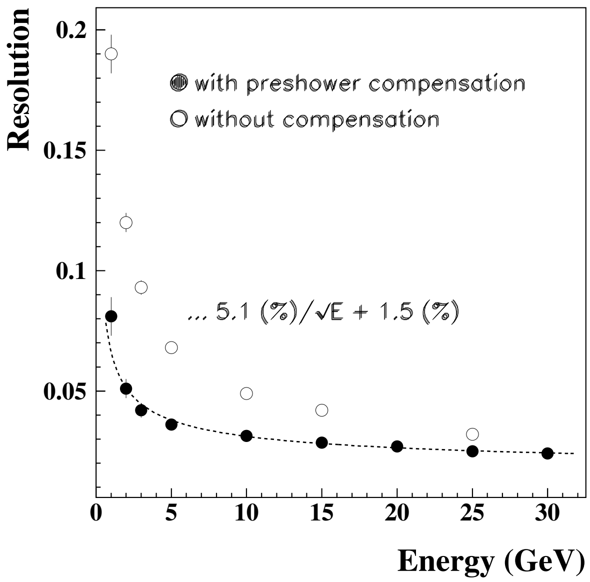

Figure 3.14: *Energy resolution of a* 3×3 *array of calorimeter blocks as a function of incoming electron energy.*

3.6 Measurement of Luminosity

The luminosity can be established by measuring rates of a process of which the theoretical cross section is well understood. Determination of the luminosity is essential to normalise data which are taken under different circumstances (e.g. different target spin states, different target gases, etc.) as well as for a determination of absolute cross sections. In addition, by measuring the luminosity one can monitor fluctuations in the target density and beam current. In the case that HERA accelerates electrons, the rates of Møller scattering (i.e. electrons scattering from target electrons) are measured; in the case that HERA operates with positrons, the rates of Bhabha scattering (i.e. positrons scattering from target electrons) are measured.

The HERMES luminosity monitor consists of two modules, located in the aperture in between the two calorimeter halves, at the left and right hand side of the beam pipe, 30 mm away from the beam axis. Each module consists of an array of $3 \times 4\,\mathrm{NaBi(WO_4)}$ crystals, each having a size of $22 \times 22 \times 200\,\mathrm{mm}^3$. The coincidence rate of e^+e^- or e^-e^- particles is measured to determine the luminosity.

For absolute cross sections, the precise acceptance of the luminosity monitor should be known. For comparison of different data sets, only knowledge of the relative change in luminosity during the different periods is necessary.

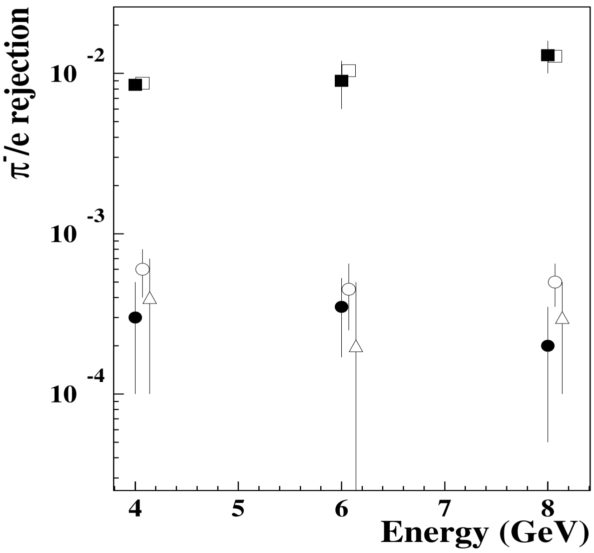

Figure 3.15: *Pion/electron rejection factor as a function of incoming energy, using a cut corresponding to a 95% electron efficiency. Filled and open symbols correspond to data and Monte Carlo predictions respectively. The circles correspond to the combined use of the preshower and calorimeter, the squares correspond to using the calorimeter only. The triangles represent the pion/electron rejection factor when using a reduced cluster size instead of the* 3×3 *cluster. Instead, only counters at a distance less or equal than half the counter size away from the track impact point are taken into account.*

3.7 HERMES Trigger.

For most analyses, the trigger has to select events in which the scattered positron was in the detector acceptance. The main "physics trigger" for HERMES required a four-fold coincidence between the two hodoscope arrays (H1 and H2), the calorimeter and the bunch crossing time provided by the accelerator RF system (the "HERA clock"). The purpose of this trigger is to require that the positron bunch passed the target at the right time, that both hodoscopes fired (the threshold is set below the minimum ionising signal) and that a shower with a energy above 3.5 GeV was recorded in one of the segments of the calorimeter. In Fig. 3.16 is shown the formation of the segments, consisting of two adjacent columns. When either in the top half or the bottom half of the detector these requirements were met, the event was written to tape.

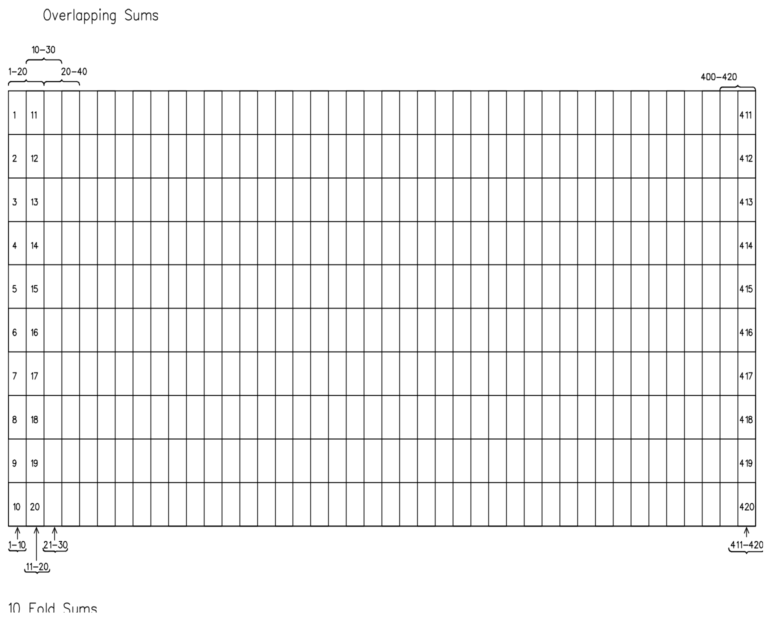

Figure 3.16: *Formation of segment sums in the calorimeter. The responses of two adjacent columns are summed. The segments overlap.*

In 1995 it was found that a large number of proton showers generated by the HERA proton beam also satisfied the trigger requirements. Compared to about 35 positron triggers and 35 pion-induced triggers per second, typically 20 to 100 proton triggers were observed with the standard ^{3}He target operation and a positron beam current of about 30 mA. To reduce proton background in the physics trigger an additional scintillator in the front region (H0) was installed. The timing information of H0 together with the timing information of H1 and H2 eliminates the proton induced triggers by using the time of flight between the front and rear scintillators. In 1995, events which were selected because of proton induced triggers were removed from the data samples using the tracking information.

3.8 Additional Monitoring Components

There are a number of components used to monitor the proton beam and the gain shifts in the detectors.

- A Gain Monitor System (GMS) is used to monitor gradual shifts or sudden jumps in the gains of the photo-multipliers of the Čerenkov detector, hodoscopes, calorimeter and luminosity monitor. A dye laser operating at 500 nm sends light pulses of different intensity through light guiding glass fibres to all photomultipliers of the aforementioned detectors and additionally to a reference photodiode. The various intensities are produced by a rotating wheel with several attenuation filters. The gain of the photodiode is known to be stable and is used to monitor relative changes in the various photomultipliers.

- The P-Veto counters are scintillators located behind the calorimeter. They measure rates in coincidence with the proton bunch crossing time thus monitoring the amount of proton background. During data taking, these scintillators are mainly used for monitoring the position and slope of the proton beam to ensure an environment which allows operation of wire chambers and TRD.

- Tuning Scintillators. In 1996, additional small scintillators were installed in the front region of the experiment, close to the beam pipe. They are used for tuning the positron beam position and slope before switching on the wire chambers and the rest of the detector.

Chapter 4

HERMES Software and ACE

4.1 HERMES Software

For the analysis of the data a number of software programs which have been written specifically for HERMES are used. The tasks performed by these programs are described below. All these programs are using databases which rely upon the software package called ADAMO [58], which ensures a transparent interpretation of data in the form of related entity sets, called ADAMO tables. The files which contain these ADAMO tables are called GAFs, Generic Adamo Files. Two tools for accessing the data stored in ADAMO format were developed at HERMES. The Dad package [124] ensures a fast I/O of ADAMO tables between the various programs and between large databases and programs. The PinK package [5] enables graphical display of the contents of the databases.

The main programs in the HERMES software chain are:

- HDC [82]. The Hermes DeCoder translates the raw data in EPIO [40] format into physics-interpretable quantities in ADAMO format.
- HMC [47]. The Hermes Monte Carlo takes care both of generating events of a particular physics signature (DIS, Møller, BhaBha) and of the tracking of the resulting event through the HERMES spectrometer, simulated by an adapted version of GEANT. It is also possible to generate so-called "user-events" in a private code and give the resulting four-vectors as input to HMC, which will track the event through the simulated spectrometer.
- HRC [126]. The Hermes ReConstruction program reconstructs tracks using either HMC or HDC events as input. It also calculates the various variables used in the PID scheme, using the information of the PID detectors.
- ACE calculates unbiased (i.e. absolute) efficiencies of the various tracking chambers, by using tracks that are calculated by HRC. A more detailed description of ACE can be found in section 4.3 of this chapter or in the manual on the World Wide Web [85].

- HEP [56] and Hanna [61]. These are two packages that can be used for reading, manipulating, and combining data in ADAMO format originating from various sources.

4.1.1 Data Production

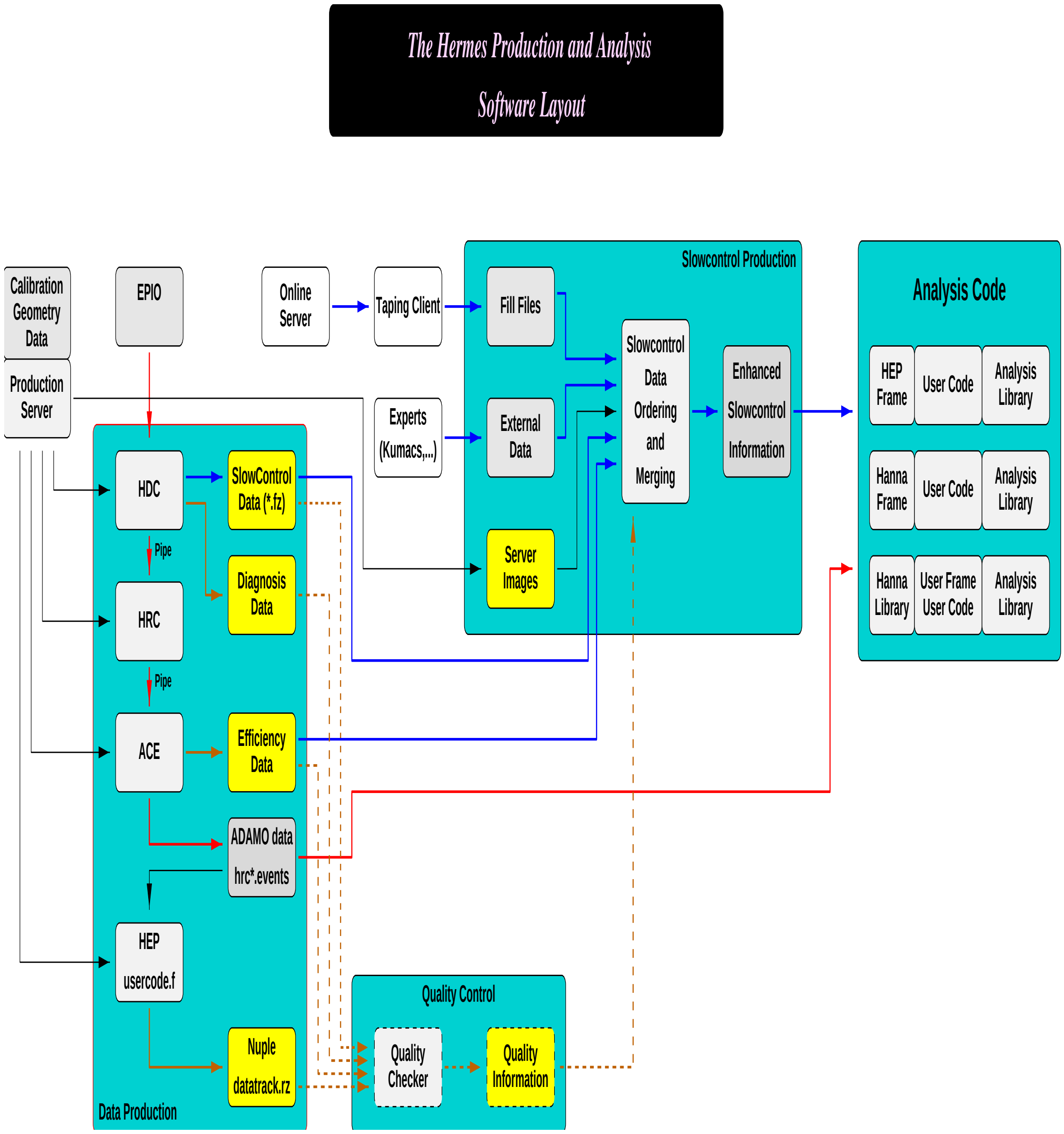

Figure 4.1: *Overview of the* HERMES *data analysis chain showing the various software packages reading, processing and writing particular parts of the data. The picture is taken from Ref. [60].*

In Fig. 4.1 an overview of the HERMES data analysis chain is shown. The raw data in EPIO format is decoded by HRC into physical quantities (energy deposition in calorimeter, drift times in the wire chambers, etc.). The output of HDC is read by HRC which determines tracks by using the hit patterns of the tracking chambers and furthermore calculates PID information. ACE uses the output of HRC to calculate efficiencies of the tracking chambers. The main tracking information as calculated by HRC is stored in a GAF. Also the slow-control information and efficiencies are written to ADAMO GAF files. Slow-control information is partly processed by HDC, and partly by online monitoring programs. Slow-control information gets updated every ten seconds, and each new period of ten seconds, a so-called "burst", is labelled with a burst number. Programs, based on the analysis packages Hanna or HEP are used to combine the information stored in the various ADAMO files and to synchronise the data with the slow-control information.

4.2 HRC and Track Reconstruction

The HERMES track reconstruction program HRC ([125], [126]) reconstructs partial tracks in the front and the back region of the spectrometer. Subsequentially, taking the bending of trajectories of charged particles in the magnet region into account, partial tracks are combined and the momentum is determined from the curvature of the resulting complete track. HRC uses a tree-search algorithm for the reconstruction of partial tracks and a look-up table for the momentum determination of the tracks. Fig. 4.2 shows the top view of an event with three particles, two with negative and one with positive charge, traversing the tracking chambers.

The tree-search algorithm is based on pattern recognition by using look-up tables consisting of hit patterns. The first step in constructing a partial track is by constructing "treelines" out of the hits of the U, X and V planes separately. These treelines are combined into partial tracks. For each treeline, the tree-search algorithm is applied. All detector planes which are used for constructing a particular type of treeline are assigned an artificially reduced resolution. Starting from a resolution equal to half the width of the detector plane, in each successive step the resolution is increased by a half.

At each level of artificially reduced resolution HRC looks for a hit pattern out of the set of possible hit patterns with the current resolution which matches the event hit pattern of the detector planes under study (see Fig. 4.3). All possible hit patterns are stored in a data base at the initialisation phase. The number of possible hit patterns with the full resolution at the final iteration step is in the order of 100,000,000. In order to reduce the look-up time and the memory space needed for the database, only unique hit patterns are stored. Starting from a "mother" hit pattern at a certain level of artificial reduced resolution, only a small number (4 to 8) of "daughter" hit patterns at the subsequential level are possible. If a daughter hit pattern is identical to the mother hit pattern, then the daughter is linked to the mother and the "granddaughters" are identical to the original daughters of the previous iteration step. This "fractal-like" hierarchy reduces the number of basic hit patterns which have to be stored in the data base to about 50,000.

The treelines are combined into partial tracks, by using a least-square fit. The tree-search algorithm is not applied to the X detector planes in the front region because of the tilted X planes of

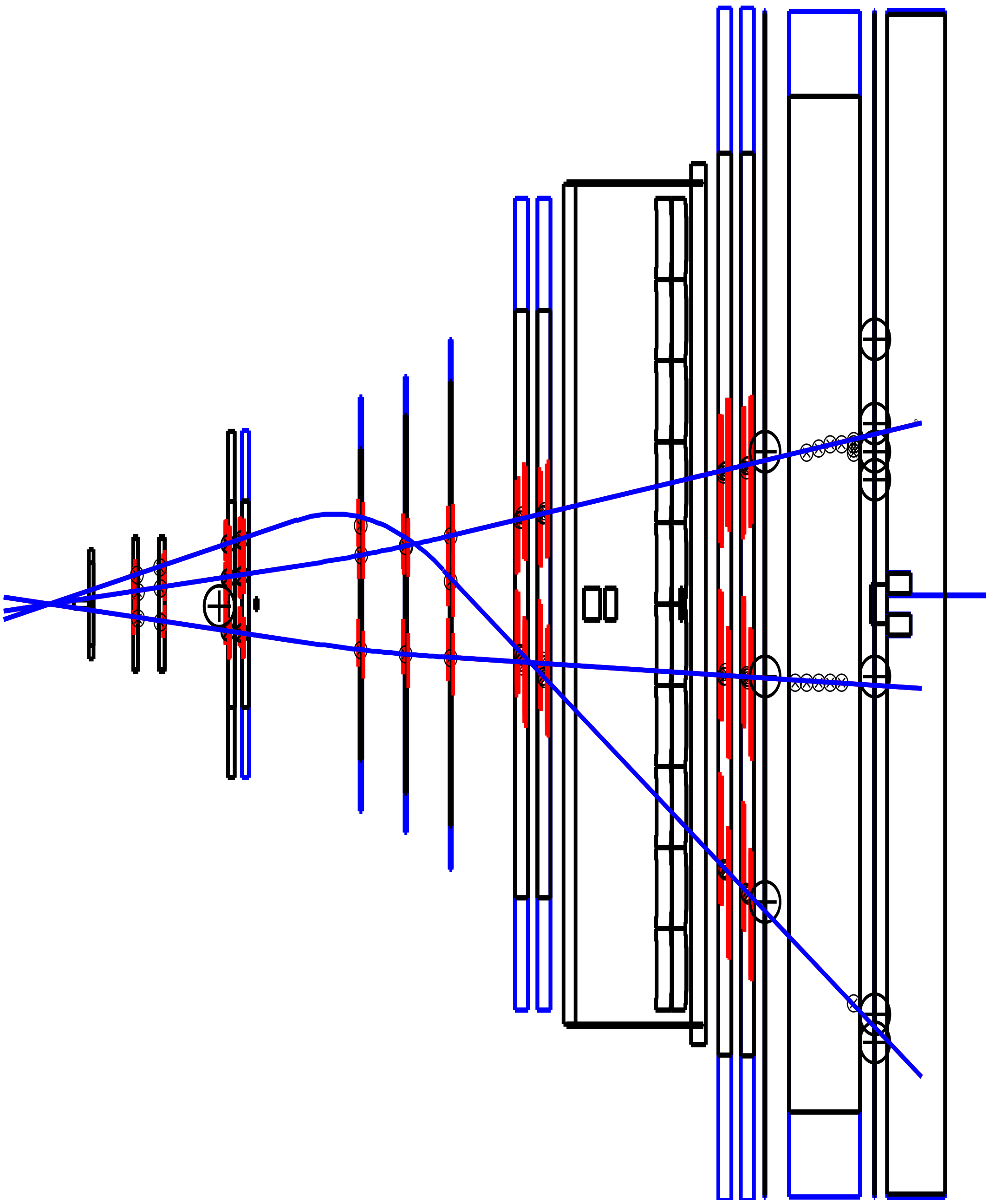

Figure 4.2: *Event display: top view of an event with three tracks, reconstructed by* HRC.

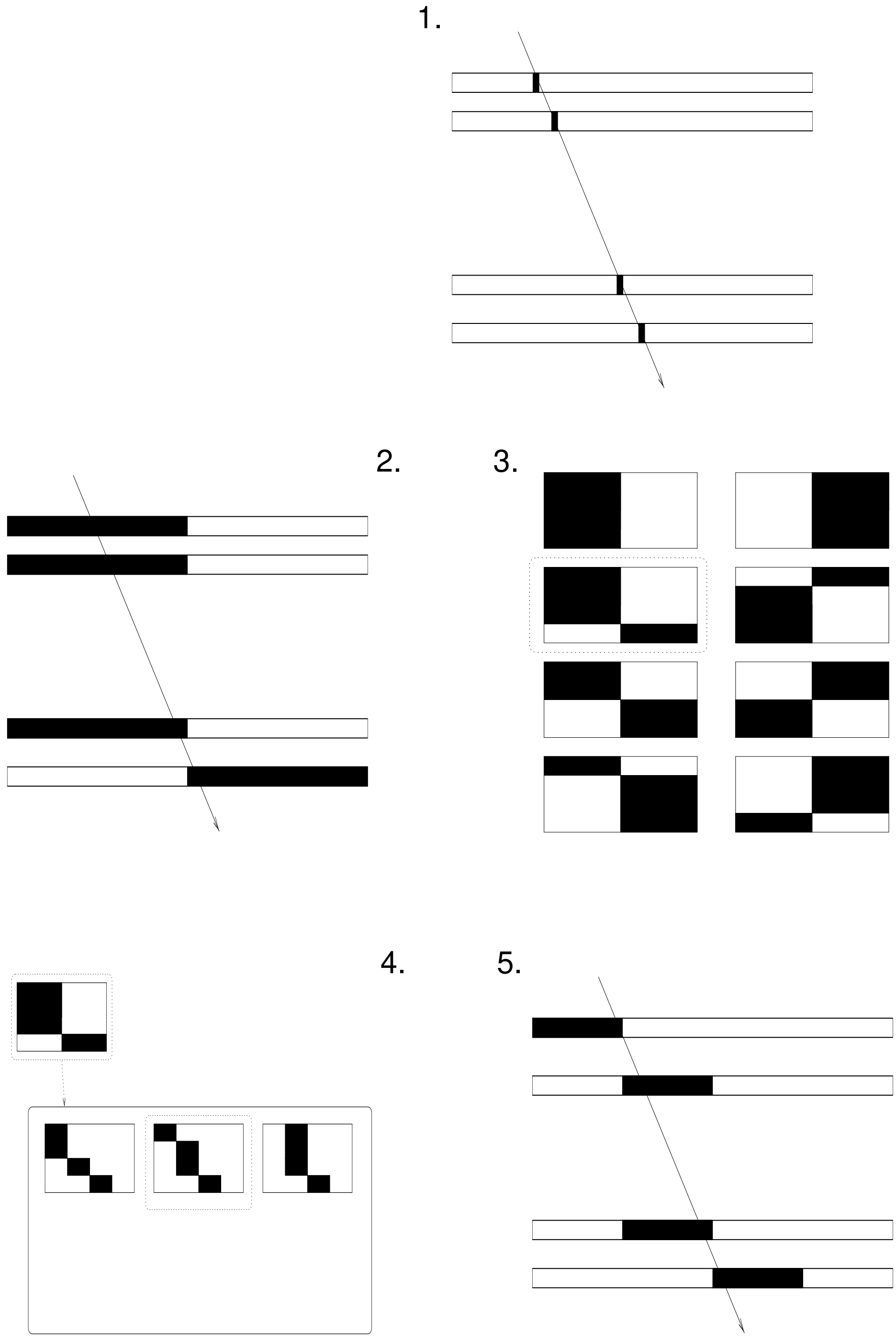

Figure 4.3: *The tree-search algorithm. The first figure shows a track causing hits in four planes. The second figure shows a hit pattern for the first step of the tree-search algorithm, with maximum reduced resolution.* HRC *looks for the matching hit pattern in its database highlighted in the third figure. The fourth figure shows a few of the "daughters" of the matching hit pattern. The daughters have a resolution twice as good as their mother. The fifth figure shows the matching daughter hit pattern.*

the VC which do not fulfill the symmetry of the hit patterns in the database. Instead the hits of the X planes in the front region are used for modifying the slope of the partial track constructed out of the U and V treelines. In the back region the partial tracks are constructed out of U, V and X treelines. The slope and position of the front partial track and the horizontal slope of the back partial track are used as input for the momentum look-up table. This method avoids time consuming tracking through the magnetic field on an event by event basis. The resolution of the table is chosen such that, after interpolating the input variables, the precision of the track momentum is better than $\Delta p/p = 0.5\,\%$.

1995 was the first year in which HERMES took data. The VC performance was not optimal due to a delay in the production of the readout chips. This caused lower efficiencies for the VC. Hence, HRC provided the option to make tracks by using the FC and BC chambers only, without taking the VC chambers into account. The front-back matching of partial tracks is done as in the case when the VCs are used, except with somewhat larger tolerances. Then, for all matching pairs of partial tracks, the match point at the centre of the magnet defined by the back partial track is used to refine the front partial track. Thus the front partial track is adjusted by using the presumably higher quality information of the back partial track. Also a third track reconstruction method in HRC was developed which only partly uses the VC chambers. This so-called "hybrid" method constructs tracks as in the case when the VC chambers are not used at all. Subsequentially, an additional requirement on the number of hits in the VCs within the defined road width around the track impact point is used to increase the reliability of the accepted tracks.

In the next section, ACE will be described. ACE calculates efficiencies by using tracks as calculated by HRC. To avoid a biased efficiency determination, ACE needs to take into account the track requirements which are made in HRC. Requirements are made on the following variables,

- The number of hits within the road width (the resolution of the lowest level hit pattern) of a partial track.
- The number of hits within the road width of a treeline.
- The number of hits in the VC within the road width of a partial track (when the VC chambers are used in the track reconstruction).
- The number of hits in a U, V, and X plane per module within the road width of each treeline.

4.3 ACE

4.3.1 ACE Efficiencies

ACE calculates the efficiencies of the tracking chambers by using tracks as calculated by HRC.

The efficiency η for a particular plane $plane_i$ is defined as

$$\eta(plane(i)) = \frac{\#tracks\,with\,hit\,in\,plane(i)}{total\,\#\,of\,tracks\,in\,plane(i)} \equiv \frac{N_{sucs}}{N_{ents}} \qquad (4.1)$$

There are two different types of efficiencies which ACE calculates, identified with "software efficiency" and "hardware efficiency".

The software efficiency only considers hits which were inside the road width corresponding to the road width used by HRC around the impact point of the track. The software efficiencies can be used to calculate the overall tracking efficiency, i.e. the absolute efficiency with which HRC finds tracks.

The hardware efficiencies are calculated by means of looking for hits in a wider region of a particular plane. For the wire chambers, ACE looks for a hit at either the closest or the second closest wire with respect to the track impact point. For the VCs, ACE looks for the next $\pm\, n$ strips around the track-impact point with n a number which can be chosen. This is mainly intended for debugging purposes, since a road width of several strips would introduce too much noise and background signals to result in a meaningful efficiency.

4.3.2 Avoiding Bias

The requirements that HRC imposes on a track would introduce a bias to the calculation of efficiencies, in case these requirements are not taken properly into account. The following example illustrates this.

Suppose that out of a total number of four planes, for each track HRC requires a minimum of three planes to have a hit. Suppose that the four planes would have efficiencies of $60\%, 60\%, 60\%$, and 1%. The following hit patterns would be accepted by HRC, with their associated probabilities.

$$\begin{array}{|l|}\hline 1110 \rightarrow (0.6)^3 \cdot 0.99 \\ 1101 \rightarrow (0.6)^2 \cdot 0.4 \cdot 0.01 \\ 1011 \rightarrow (0.6)^2 \cdot 0.4 \cdot 0.01 \\ 0111 \rightarrow (0.6)^2 \cdot 0.4 \cdot 0.01 \\ 1111 \rightarrow (0.6)^3 \cdot 0.01 \\ \hline \end{array}$$

If Eq. (4.1) would be used to calculate the efficiency of plane 1, 2 or 3, this would lead to $N_{ents} \propto 1.02$ and $N_{sucs} \propto 1.01333...$ which then would result in an efficiency of 99%. For plane 4 one would obtain an efficiency of 2.9%. Hence, efficiencies would be overestimated.

In order to avoid such a biased result when calculating the efficiency of a certain plane, one should only use events in which at least three planes had a hit (according to the requirements of HRC) without counting the plane under study. For plane 1, this leads to (only taking the hit patterns 0111 and 1111 into account) $N_{ents} \propto (0.6)^2 \cdot 0.01$ and $N_{sucs} \propto (0.6)^3 \cdot 0.01$, hence giving an efficiency of 60%. For plane 4 one should ignore all hit patterns except 1110 and 1111, resulting in an efficiency of 1%.

Since there are four types of requirements made in HRC on valid tracks, there are four sources of bias which ACE has to avoid when calculating efficiencies. The four requirements on tracks are:

- For each partial track, the total number of hits has to be larger than a certain number. This introduces *Bias 1*.
- For each treeline, the total number of hits has to be larger than a certain number. This introduces *Bias 2*.
- For each partial track in the front region of the detector, the total number of hits of the VC has to be larger than a certain number. This introduces *Bias 3*.
- For each treeline, at least one plane per module has to have a hit. This introduces *Bias 4*.

For each plane separately, ACE has to determine whether a certain track is allowed to contribute to the calculation of the efficiency for this particular plane. This has the consequence that in general for a certain track, the quantity N_{ents} will not be the same for different planes.

ACE deals with *Bias 1*, *Bias 2*, and *Bias 3* as follows: when the number of hits belonging to a track is equal to the number required by HRC, then the track is only used for planes that did *not* have a hit. For planes that *did* have a hit, the track is *not* used (since in the latter case the track would not have been found when the plane would not have been there. Consequently, including the track for this particular plane would result in an overestimate of the efficiency). When the number of hits is larger than required, the track is usable for all planes. Obviously, *Bias 3* is relevant only when the track reconstruction method used information of the VC chambers (i.e. the standard track reconstruction method or the hybrid method).

In case of *Bias 4*, bias is avoided in a slightly different way. For a particular plane, a track is only accepted when the “partner-plane” had a hit. A “partner-plane” is the plane with the same slope (U, V or X), from the same module as the plane which is studied.

An easy way to check this procedure is by means of adding up all possible permutations of firing and not firing planes resulting in tracks accepted by HRC. This was done in the simple example at the beginning of this section. Each plane has a certain efficiency ϵ_i. Each possible permutation of N_{planes} planes can be weighted with ϵ_i for each plane i with a hit and with $(1 - \epsilon_j)$ for each plane j without a hit. The sum of all these permutations gives the number of weighted trials, N^k_{ents}. Note that the number of entries N^k_{ents} depends on the plane number k. The number of successful trials N^k_{sucs} for a certain plane k should be composed out of the expression for N^k_{ents} in such a way that

$$\eta_k = \frac{N^k_{sucs}(\epsilon_1, ..., \epsilon_N)}{N^k_{ents}(\epsilon_1, ..., \epsilon_N)} = \epsilon_k. \tag{4.2}$$

This leads to the set of rules as described above for dealing with the various sources of bias.

4.3.3 Global efficiencies

Plane efficiencies can be combined into global efficiencies, i.e. efficiencies which reflect the total tracking efficiency. One will obtain four global efficiencies for the HERMES spectrometer: the front upper half and lower half, and the back upper half and lower half. In order to calculate these efficiencies correctly, one has to take into account the parameters used by HRC in its algorithm for finding tracks. These parameters are needed to establish all possible combinations of firing planes and not firing planes which would result in tracks which would be accepted by HRC. The total sum of all possible permutations N_{perms} will in general be larger than N^k_{ents} of the previous section for any plane k. The total absolute efficiency for finding a partial track in a particular half of the spectrometer is determined by adding the probabilities (i.e. the combined software plane efficiencies) for all possible permutations.

4.3.4 Calculating Errors with ACE

As a first approach, one can use the binomial distribution to calculate errors for the measured efficiencies. For the binomial distribution, the number of trials is denoted as n and the number of successes is denoted as r, where r and n are integers. Hence, the efficiency can be defined as: $p = r/n$. The standard deviation of r, σ_r is

$$\sigma_r = \sqrt{np(1-p)}.$$

Using $\sigma_p^2 = \sigma_r^2/n^2$ gives

$$\sigma_p = \sqrt{p(1-p)/n}, \tag{4.3}$$

for the standard deviation of the measured efficiency p.

The above expression for σ_p is only approximately correct, and only for large n and p not close to 0 or 1. When $p = 0$ or $p = 1$, one obtains $\sigma_p = 0$, independent of n. Obviously this is not correct. The expression $\sigma_p^2 = \sigma_r^2/n^2$ is based on the assumption that n is not a stochastic variable. For large n this is a valid approximation; for lower values of n, another error calculation should be used.

The correct way to calculate errors for efficiencies is by using the F–distribution ([36], [104], [109]). This method is based on the idea of hypothesis testing. When after a certain total number of trials n, the number of successes is r, one can postulate that the binomial probability governing each trial is $p_0 = r/n$. Now, one can test the hypothesis for the real probability, $H_0 : p = p_0$. For large n, the test statistic can be approximated by the normal approximation to the binomial distribution. For smaller n, binomial tables should be used. To avoid using those, one can use the F-test which is valid for all n.

The F–distribution has three parameters: ν_1, ν_2, and α. The parameter α denotes the confidence level with which one determines the lower and upper confidence region for the measured efficiency p.

The relation between the binomial distribution and the F–distribution is as follows (see Ref. [36]). For the binomial distribution, the confidence limits are defined as

$$P\{r \geq r_0 | p = p_l\} = 1 - \alpha_2, \tag{4.4}$$
$$P\{r \leq r_0 | p = p_h\} = \alpha_1, \tag{4.5}$$

where $\alpha_1 + \alpha_2 = 1$. Eq. (4.4) can be written as

$$\begin{aligned} 1 - P\{r \geq r_0 | p = p_l\} &= P\{r < r_0 | p = p_l\} \\ &= P\{r \leq r_0 - 1 | p = p_l\} = \alpha_2. \end{aligned} \tag{4.6}$$

In general, the following is always true for a stochastic variable x from a binomially distributed sample,

$$P\{x \leq x_0\} = \sum_{j=0}^{x_0} \binom{n}{j} p^j (1-p)^{n-j} = G(p, a = x_0, b = n - x_0 + 1), \tag{4.7}$$

with G being the Beta distribution evaluated at p,

$$G(p, a, b) = \frac{(a+b-1)!}{a!b!} p^{a-1} (1-p)^{b-1}. \tag{4.8}$$

However, since tables for the Beta distribution are not easily available, it is more convenient to convert to the F–distribution ([89]). When a random variable Y follows the Beta distribution, the variable X follows the $F(\alpha; \nu_1, \nu_2)$–distribution, using

$$X = \frac{\nu_2}{\nu_1} \left(\frac{1-Y}{Y} \right), \tag{4.9}$$

with parameters $\nu_1 = 2a$ and $\nu_2 = 2b$.

Hence,

$$P\{x \leq x_0\} = \sum_{j=0}^{x_0} \binom{n}{j} p^j (1-p)^{n-j} = 1 - P\left\{ F < \frac{n - x_0}{x_0 + 1} \frac{p}{1-p} \right\}, \tag{4.10}$$

where F is a random variable from the F–distribution with degrees of freedom $\nu_1 = 2(x_0 + 1)$ and $\nu_2 = 2(n - x_0)$.

Applying this to Eq. (4.5) one obtains

$$\alpha_1 = 1 - P\left\{ F < \frac{n - r_0}{r_0 + 1} \frac{p_h}{1 - p_h} \right\}, \tag{4.11}$$

and thus, we have to look in the F–distribution table for the $1 - \alpha_1$ point, denoted as $F_{\nu_1;\nu_2;1-\alpha_1}$. Hence,

$$\frac{n - r_0}{r_0 + 1} \frac{p_h}{1 - p_h} = F_{\nu_1;\nu_2;1-\alpha_1}, \tag{4.12}$$

and thus,

$$p_h = \frac{(r_0+1)F_{\nu_1;\nu_2;1-\alpha_1}}{n - r_0 + (r_0+1)F_{\nu_1;\nu_2;1-\alpha_1}}, \tag{4.13}$$

where $\nu_1 = 2(r_0+1)$ and $\nu_2 = 2(n-r_0)$. In the same way, Eq. (4.6) can be solved for p_l, using

$$F_{\mu_1;\mu_2;1-\alpha_2} = \frac{1}{F_{\mu_2;\mu_1;\alpha_2}}, \tag{4.14}$$

resulting in

$$p_l = \frac{r_0}{r_0 + (n-r_0+1)F_{\nu_1;\nu_2;\alpha_2}}, \tag{4.15}$$

where $\nu_1 = 2(n-r_0+1)$ and $\nu_2 = 2r_0$.

The parameter $\alpha = 1-\alpha_1 = \alpha_2$ now denotes the confidence level with which one determines the lower and upper confidence region for the measured efficiency p. Hence,

$$\begin{aligned}
\nu_{1,l} &= 2(n-r+1) \qquad \text{(lower level)}, && (4.16)\\
\nu_{2,l} &= 2r \qquad \text{(lower level)}, && (4.17)\\
\nu_{1,h} &= 2(r+1) \qquad \text{(upper level)}, && (4.18)\\
\nu_{2,h} &= 2(n-r) \qquad \text{(upper level)}, && (4.19)
\end{aligned}$$

and the expression for the lower and upper confidence values for p becomes

$$\frac{r}{r+(n-r+1)F_{\nu_{1,l};\nu_{2,l};\alpha}} \leq p \leq \frac{(r+1)F_{\nu_{1,h};\nu_{2,h};\alpha}}{(n-r)+(r+1)F_{\nu_{1,h};\nu_{2,h};\alpha}}. \tag{4.20}$$

For the calculation of these errors, a library function was made which calculates the efficiency and the upper and lower confidence value with a confidence level of $\alpha = 97.5\%$. The library function is an adapted version of the "stattab package" developed by the Department of Biomathematics of the University of Texas M. D. Anderson Cancer Center [118].

The difference between the two methods of calculating errors is shown in Fig. 4.4.

4.4 ACE Output.

4.4.1 Monte Carlo Tests.

To test that the efficiencies calculated by ACE are absolute efficiencies (i.e. that they can be used for an absolute normalisation of the data, e.g. for the calculation of total cross sections) and to test that they are method independent (i.e. not depending on the steering parameters used in HRC), a number of tests were performed, by using Monte Carlo data. Fig. 4.5 shows the efficiencies as calculated by ACE. They are compared with the actual efficiencies used in the generation of the Monte Carlo data and with the results of a more time consuming way to calculate efficiencies.

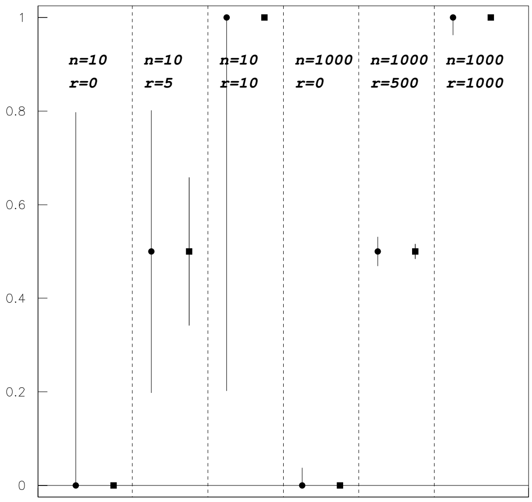

Figure 4.4: *Example picture of the difference between confidence intervals calculated by means of the F–distribution (circles) and confidence intervals calculated by means of the binomial approximation (squares). When $r = 0$ or $r = n$, using the F–distribution will still give (asymmetrical) confidence intervals for the efficiency.*

In the more time consuming way, two detector planes, one in the bottom half, one in the top half of the detector, are not used by HRC. ACE looks for hits in those detector planes close to the impact points of the tracks as calculated by HRC. No bias needs to be avoided, since the tracks were made without using the detector planes under study. The method is time consuming because both HRC and ACE have to run for all planes separately. Nevertheless, for checking the "fast" output of ACE the method is useful.

The efficiencies are in good agreement with each other, demonstrating that ACE efficiencies are absolute efficiencies.

4.4.2 Efficiencies for the 1995 Data.

Fig. 4.6 shows the software efficiencies of the FC and the BC detector planes, as calculated by ACE. The tracks were calculated by HRC without using information of the VC chambers. Fig. 4.7 shows the software efficiencies for one (top figure) and two (bottom figure) detector planes of the VC. The top figure shows efficiencies during a run. The plane reaches full efficiency 5 minutes after switching on the high voltage at the beginning of a new fill. The bottom figure shows that the efficiencies of the VC over a period of months remain stable.

Fig. 4.8 shows the software efficiencies for the FC and BC for various runs for the two different directions of the target polarisation. The differences between the efficiencies for the two different polarisation states per run are statistical. The differences of the efficiencies of BC planes 93 – 98 (corresponding to the planes of the lower half of the BC3 module) when comparing runs 3014, 3015 with runs 5010, 5013 are due to a change in high voltage in this

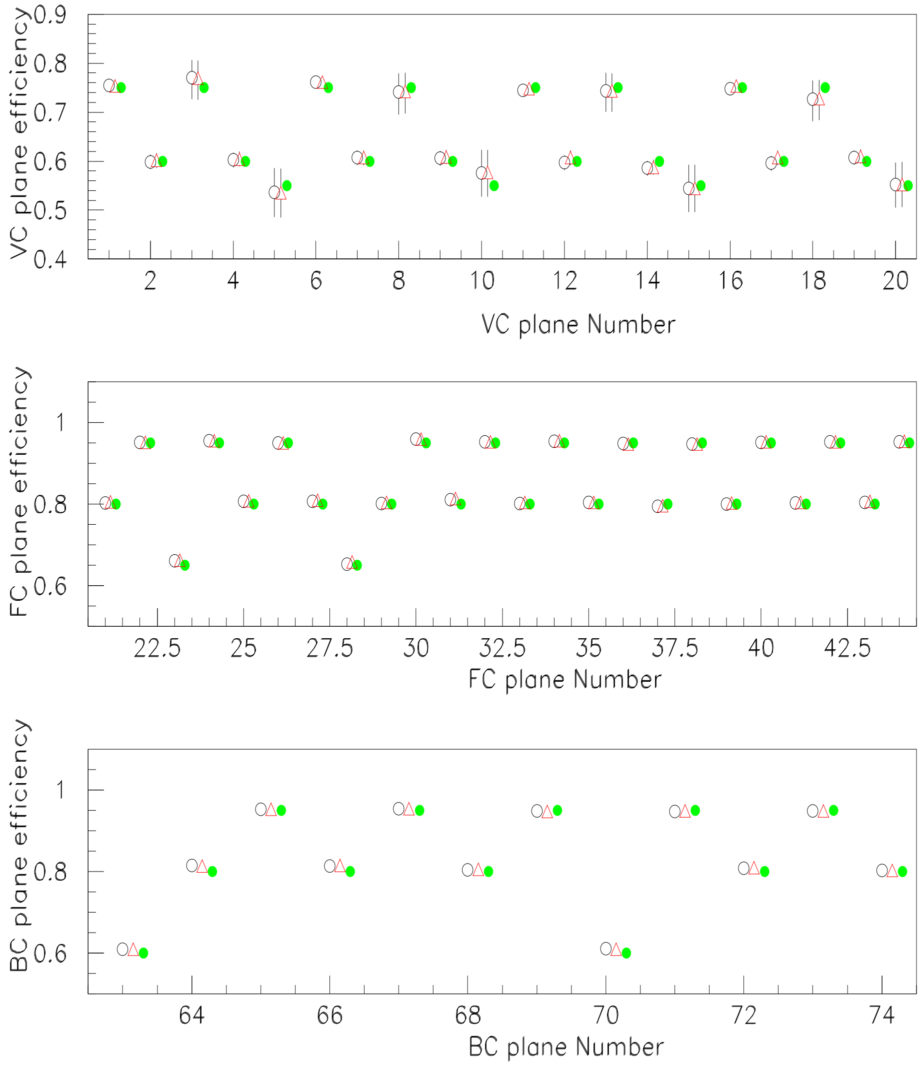

Figure 4.5: *Results of* ACE *for calculating efficiencies for Monte Carlo events. The filled circles represent the artificially applied efficiencies which were used in the generation of the data. The open circles represent the software efficiencies as calculated by* ACE. *The triangles represent the efficiencies calculated in the time consuming way by using a road width equal to the road width used by* HRC. *The efficiencies are in good agreement with each other, demonstrating that* ACE *efficiencies are absolute efficiencies.*

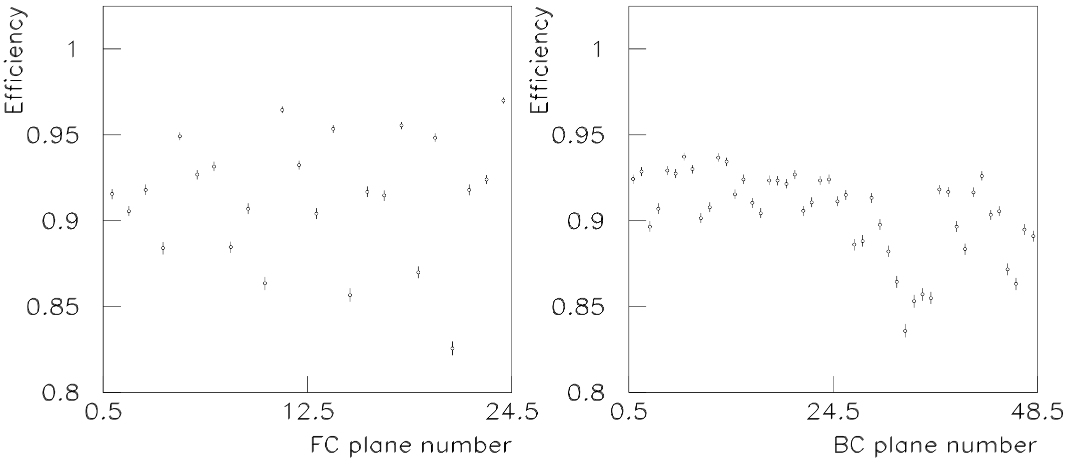

Figure 4.6: *Software efficiencies for the FC and BC detector planes for run 3360.*

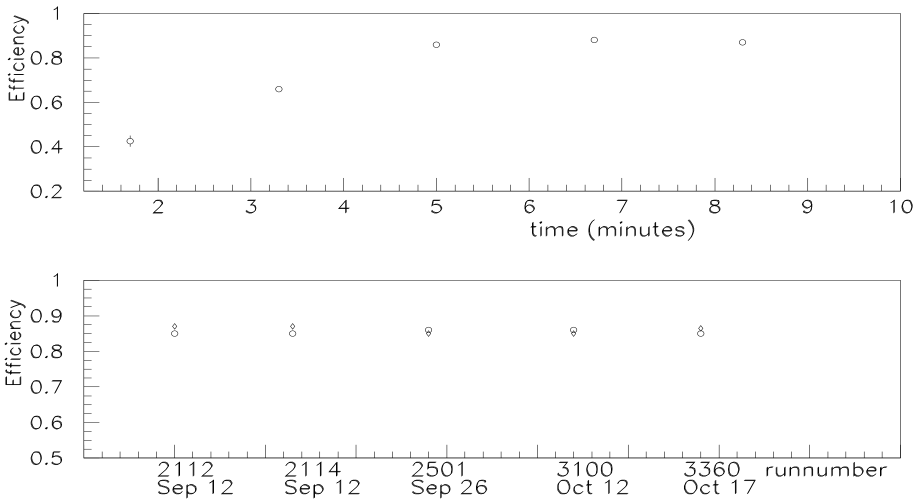

Figure 4.7: *The top figure shows efficiencies for one VC plane versus time during the first minutes of a fill. The bottom figure shows efficiencies per run for two VC planes. Over a period of a month, the efficiencies remain constant.*

module [87].

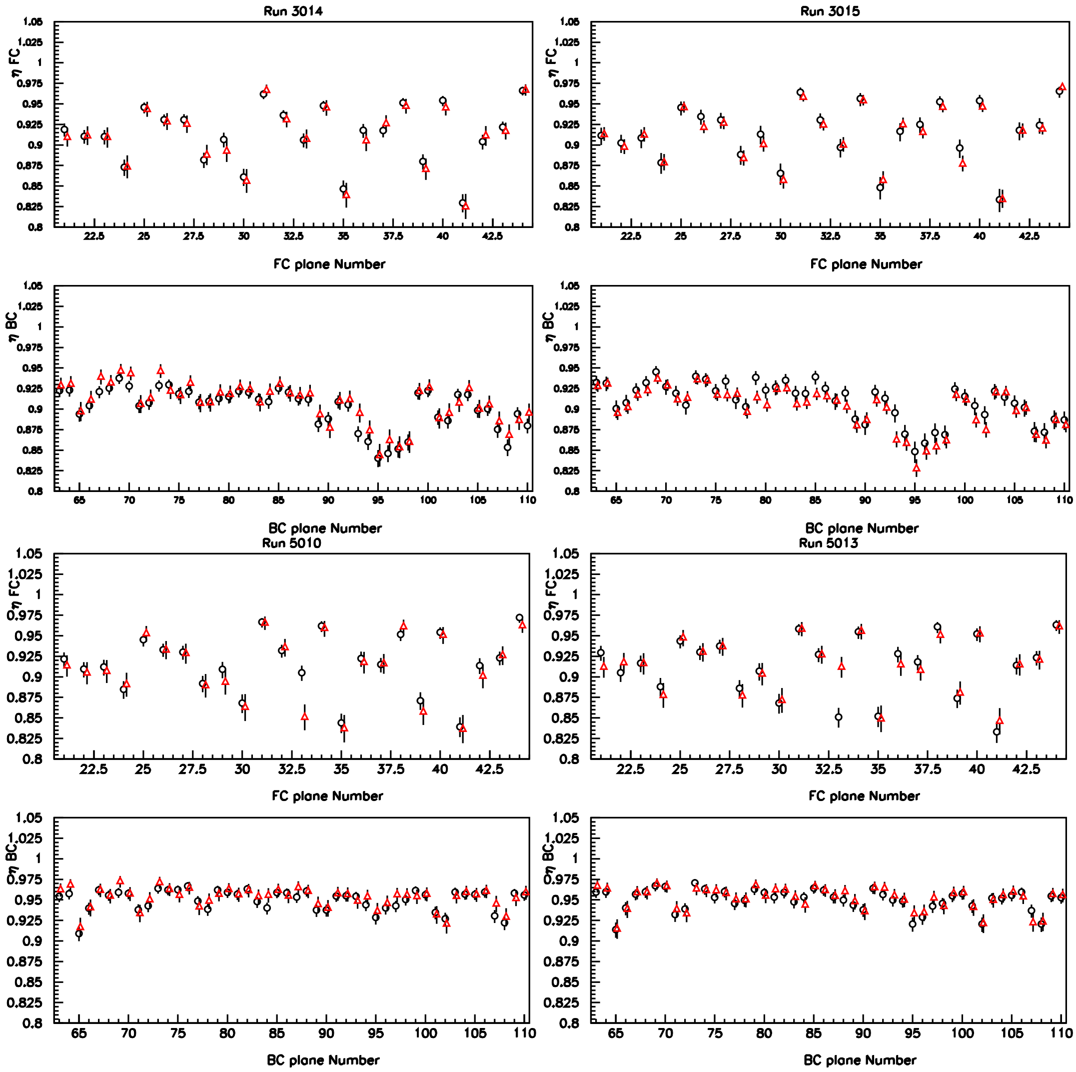

Figure 4.8: ACE *efficiencies for various runs. In each figure, the efficiencies are calculated for the two directions of target polarisation separately. The squares correspond to a measurement with the target polarisation direction parallel to the beam polarisation, the triangles to an anti-parallel measurement.*

Chapter 5

Data Analysis

5.1 Particle Identification Scheme

In order to select tracks according to particle type, the information of the PID detectors is used. For the 1995 data, due to the gas mixture and threshold settings in the Čerenkov counter, only a distinction can be made between electrons (or positrons) and hadrons. At HERMES most of the hadrons are pions [52]. Additional techniques (e.g. time of flight information by using the TDC readout of the hodoscopes) can be used for certain momenta to distinguish between pions, protons or kaons. For the analysis of ρ^0 electroproduction, the possible proton and kaon background is effectively removed with the cuts described in section 6.1.

Generally, in the analysis of HERMES data there are two ways in which the responses of the PID detectors are combined to distinguish between electrons/positrons and hadrons.

The first method is by using so-called "straight cuts". Fig. 5.1 shows the response of the calorimeter, preshower, Čerenkov counter and TRD for the relevant range of energies for both hadrons and positrons. In each of these spectra, a cut can be made to separate positrons from hadrons.

The other method to establish the particle type is more complicated and is explained in detail in Ref. [53]. The method is based on Bayes theorem [9] and uses the following definitions.

- C_i, the actual cause of an event (e.g. C_1 denotes that an electron entered a certain detector whereas C_2 denotes that a hadron entered a certain detector).
- E_i, the response of a certain detector, (i.e. E_i corresponds to a certain bin in the range of possible responses of a certain detector).
- $\mathcal{P}(C_i)$, the probability that a certain event C_i will happen.
- $\mathcal{P}(E_k|C_i)$, the probability that, given that a certain event of type C_i occurred (i.e. a certain particle type entered the detector), the detector will respond with E_k.

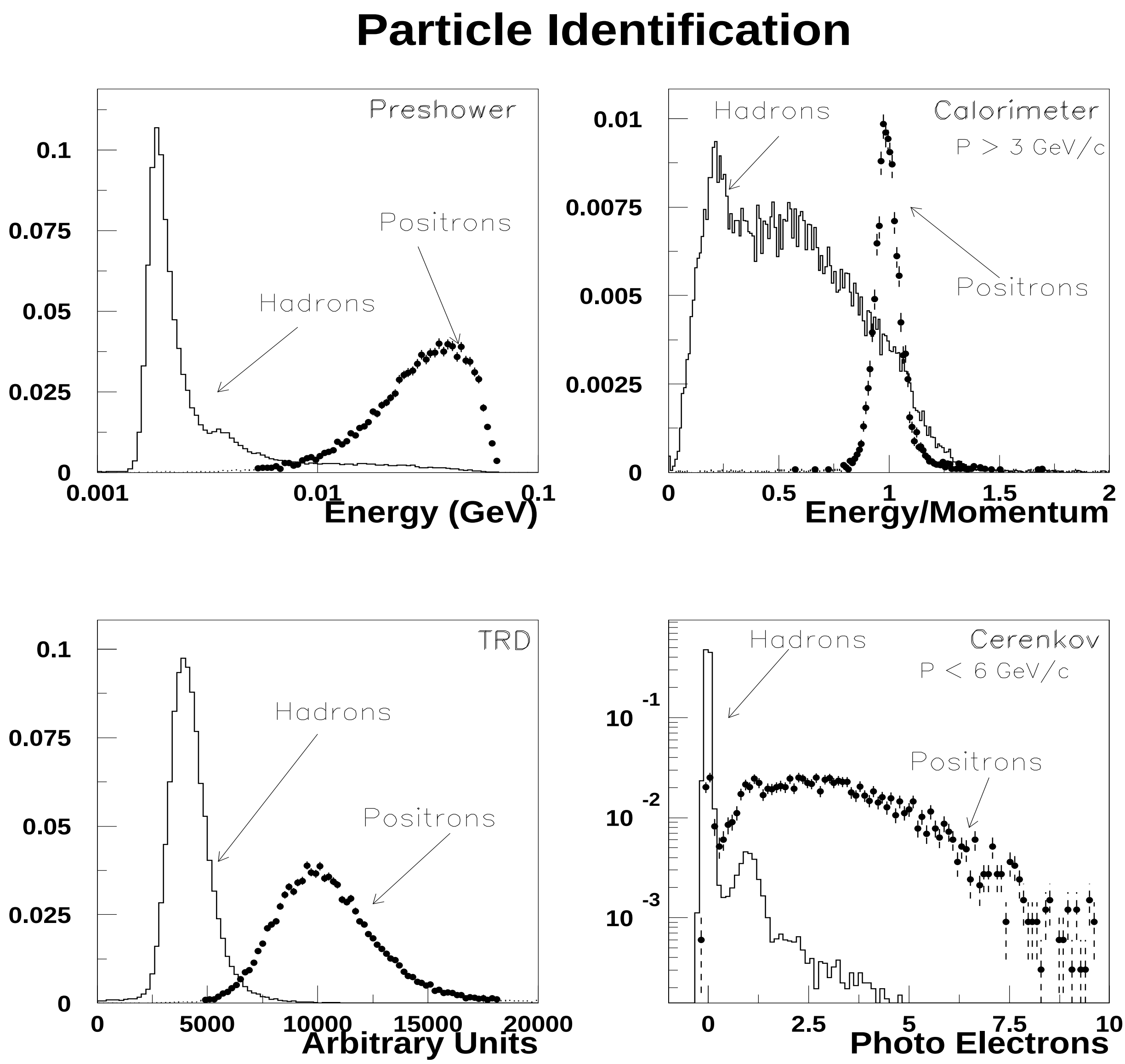

Figure 5.1: *Responses of the four PID detectors for hadrons and positrons. The tracks were selected by applying straight cuts to all PID detectors except to the one under study.*

- $\mathcal{P}(C_i|E_k)$, the probability that, given that a certain detector responded with E_k, the event which caused this event was of type C_i.

Bayes theorem [9] states that

$$\mathcal{P}(C_i|E_k) = \frac{\mathcal{P}(E_k|C_i)\mathcal{P}(C_i)}{\sum_{l=1}^{n_c} \mathcal{P}(E_k|C_l)\mathcal{P}(C_l)}, \tag{5.1}$$

where n_c denotes the number of particle types to be distinguished. Ultimately, one wants to know the chance that a measured detector response E_k was caused by an incoming particle of the type C_i, denoted by $\mathcal{P}(C_i|E_k)$. In order to be able to do this, the normalised incoming fluxes for the various particle types (in this case, electrons or hadrons), i.e. the chances that the various causes C_i will occur, denoted by $\mathcal{P}(C_i)$, have to be known. The final probability $\mathcal{P}(C_i|E_k)$ can be used to define an unconditional likelihood for the hypothesis that the incoming particle was of a certain type. Hence

$$\mathcal{L}^e_{det} = \frac{\mathcal{P}^e_{det}}{\mathcal{P}^e_{det} + \mathcal{P}^h_{det}}, \tag{5.2}$$

where $\mathcal{L}^e_{det}$ denotes the likelyhood that the incoming particle was an electron or positron. The probabilities $\mathcal{P}^e_{det}$ and $\mathcal{P}^h_{det}$ are the conditional probabilities on the left-hand side of Eq. (5.1).

The whole scheme depends on an iteration of unfolding data with respect to particle type, by using Monte Carlo models to describe $\mathcal{P}(E_k|C_i)$ in order to estimate the normalised fluxes $\mathcal{P}(C_i)$. The iteration procedure is as follows:

1. Choose an initial distribution of $P_0(C)$. When this would be the true distribution, the number of observed events of a certain particle type would be $n_0(C_i) = \mathcal{P}_0(C_i)N_{obs}$, with N_{obs} the total number of observed events.

2. By using Bayes theorem (see Eq. (5.1)), one can derive $\mathcal{P}_0(C_i|E_k)$ from $\mathcal{P}(E_k|C_i)$ (the Monte Carlo model of the detector) and $P_0(C)$.

3. Summing over all energy bins, a new estimate of observed events $n_1(C_i)$ of a certain particle type C_i can be derived by using $n_1(C_i) = \sum_{k=1}^{N_e} n(E_k)\mathcal{P}(C_i|E_k)$, where $n(E_k)$, the number of events in bin k, is taken from the data.

4. Subsequently, a new value for the normalised flux can be estimated by using $\mathcal{P}_1(C_i) = \frac{n_1(C_i)}{\sum_{i=1}^{N_C} n_1(C_i)}$.

5. The two distributions $n_0(C_i)$ and $n_1(C_i)$ are compared. When χ^2 is not minimal yet, $n_0(C_i)$ is replaced with $n_1(C_i)$, and $\mathcal{P}_0(C_i)$ with $\mathcal{P}_1(C_i)$.

This iteration is repeated until χ^2 is minimised.

For each PID detector at HERMES, likelihood functions $\mathcal{L}^e_{det}$ and $\mathcal{L}^h_{det}$ can be derived, as in Eq. (5.2). The likelihood functions of the calorimeter, preshower, and Čerenkov detector are combined into one number, the so-called quantity “PID3” given by

$$\mathrm{PID3} =^{10} \log\left(\frac{\mathcal{L}_e^{\mathrm{Pre}}\mathcal{L}_e^{\mathrm{Cal}}\mathcal{L}_e^{\mathrm{\check{C}er}}}{\mathcal{L}_h^{\mathrm{Pre}}\mathcal{L}_h^{\mathrm{Cal}}\mathcal{L}_h^{\mathrm{\check{C}er}}}\right). \tag{5.3}$$

Fig. 5.2 shows the value of PID3 for both positron events (shaded grey) and hadron events (shaded black). Since for the TRD no calibration of signal versus probability was available at the time of the analysis, the TRD was used by plotting its signal versus PID3 (or PID2 on occasions that the Čerenkov could not be used). Fig. 5.3 shows the TRD signal versus PID3 for positron and hadron events.

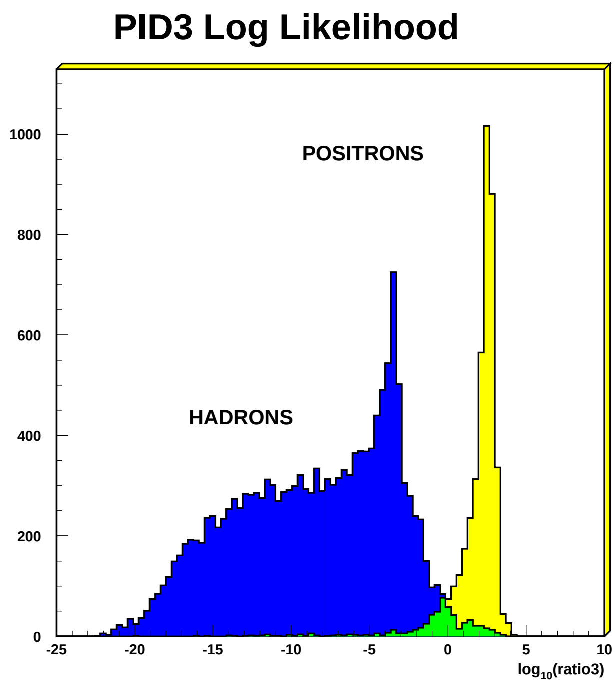

Figure 5.2: *PID3 log-likelihood function of the three particle ID detectors, calorimeter, preshower and Čerenkov for both positron events (shaded grey) and hadron events (shaded black).*

5.2 Data Quality

When watching a film in a cinema, events and situations out of a three-dimensional world are represented by a two-dimensional projection with a finite pixel resolution on a screen of a few square meters. Moreover, in some cinemas there will be a disturbing break halfway in the film, forcing the spectator to switch off his senses for fifteen minutes in order not to distort the recorded impressions.

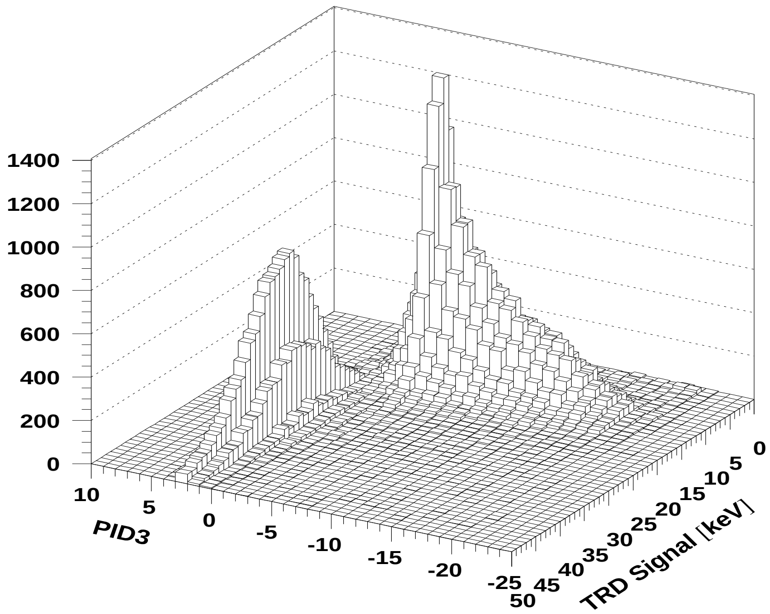

Figure 5.3: *Three-dimensional plot of the TRD signal versus the PID3 log-likelihood ratio for positron and hadron events.*

One could interpret a measurement in a physics experiment with a projection of nature onto a setup of detectors. In order to extract any physics from such measurements, one has to deduce the laws of nature from the projected measurement. This implies applying both a correction to take the limited size of the detectors into account (this is called “acceptance correction”, which is dealt with in detail in section 6.2.2) and applying cuts and corrections to take the finite resolutions and occasional failures of the detectors into account. This section deals with the various methods to select those data in which the detectors and the monitors of the characteristics of the beam and target were working in a reliable way. Some of these selection criteria will depend on the kind of physics one wants to obtain from the data.

5.2.1 General Data Quality Analysis

The general data quality procedure for HERMES data is based on the data quality analysis done for the extraction of g_1^n. The g_1^n data selection is divided into three levels:

- Run selection. For this the information of the HERMES log-book and information from the beam polarisation and the target polarisation and state was used to define a list of potentially good runs. For the ρ^0 analysis only the log-book information is of relevance.

- Burst selection. A burst-by-burst analysis, using various criteria, was used to determine the performance of the experiment on a finer time scale. (For the definition of what is a burst, see page 77.)

- Track selection. The track selection is dependent on the physics one intends to extract from the data. For the g_1^n analysis one is interested in tracks of scattered positrons. For the ρ^0 analysis, the track selection is discussed in chapter 6.

The burst selection was based on a number of criteria which are applied to the top and the bottom half of the spectrometer separately. The following sections describe the burst cuts in more detail.

Beam Criteria

There are a number of characteristics of the beam which need to be monitored and which are given below.

- *Current of the beam.* When the positron beam at DESY has just been injected, the current is at maximum value. During the time that this beam is stored, the current is gradually decreasing until it is so small that background events have similar or higher rates than physics events and the contribution to the total integrated luminosity is negligible. At this point the beam is "dumped" and a new fill is injected. The luminosity of the experiment is proportional to the integrated beam current. During a data-taking fill, the current is monitored and written to tape for later analysis. Fig. 5.4 shows the typical shape of the decreasing current during a fill. The cut on the beam current is given by $8\,\mathrm{mA} < \mathrm{I} < 32\,\mathrm{mA}$.

- *Polarisation of the beam.* Depending on whether the beam polarisation is of consequence for a particular measurement, this quantity is taken into account. For most of the analysis dealing with exclusive ρ^0 production, this quantity is of no relevance. For the g_1^n analysis, data with unrealistically high polarisation values are rejected as well as data with polarisation values too small to add significantly to any polarisation dependent measurement. Also data where the polarimeter did not work reliably are rejected.

- *Beam slope and position.* The beam slope and position can influence the yields and background conditions. They are monitored during data taking to ensure optimal measuring conditions for HERMES (i.e. low background rates and no tripping detectors).

Target Criteria

There are a number of characteristics of the target which need to be monitored and which are given below.

- *Target density.* The luminosity of the experiment is proportional to the target density which is supposed to be stable. This can be verified in two ways by either looking at the ratio of counts of the luminosity monitor and the current or directly at the monitor of the

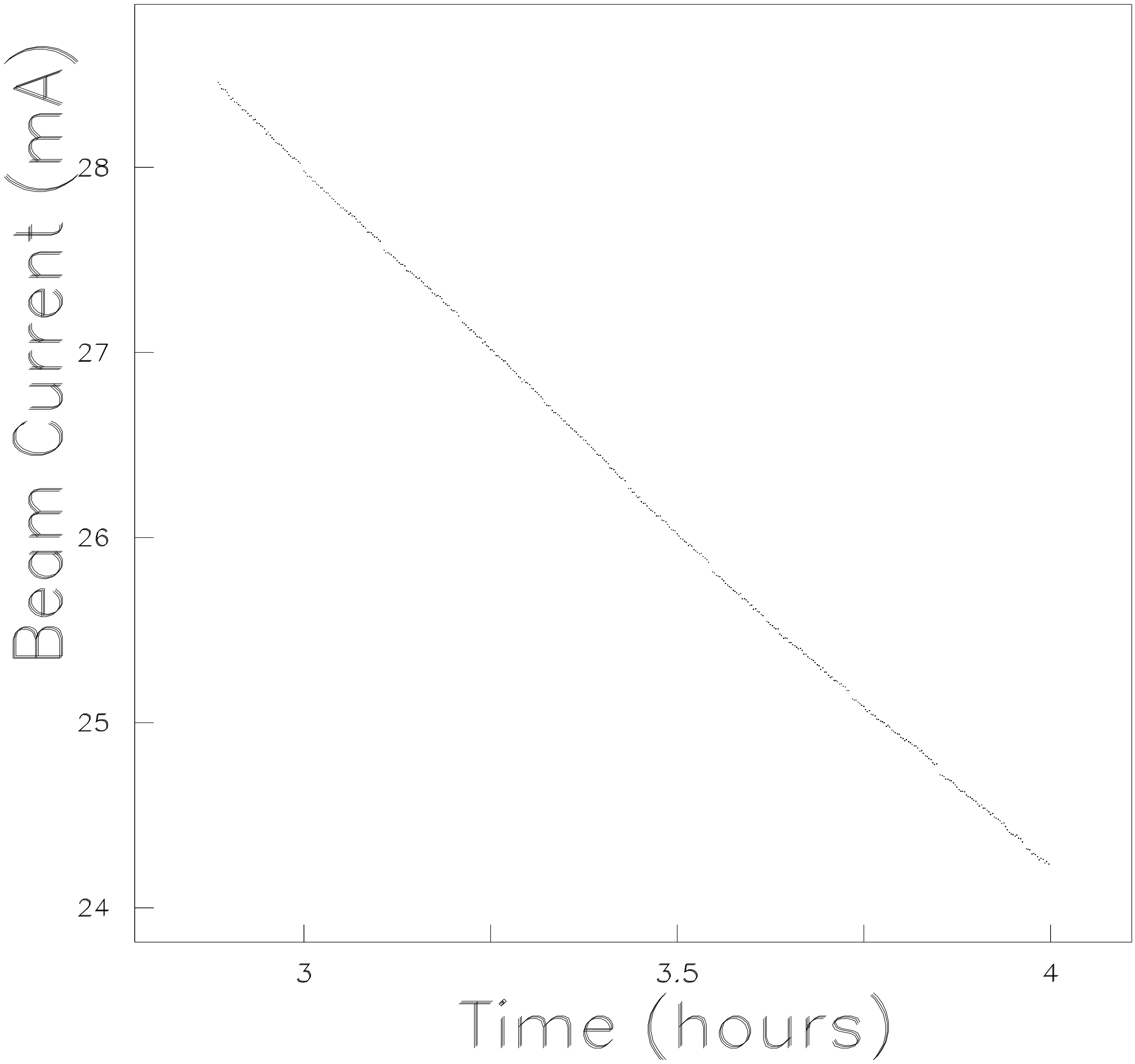

Figure 5.4: *Decrease of beam current during a typical fill of* HERA *positrons during 1995. The sudden jumps in beam current are caused by changes in the beam parameters (slopes and positions) which are required during a fill in order to minimise background rates.*

target density. A direct monitoring of the target density is done by using the information from the target gas feed system which gives the gas flow rate into the storage cell, together with the temperature inside the storage cell [1]. Since the number of counts measured by the luminosity monitor is dependent only on the beam current and the target density, the ratio of the measured luminosity and the beam current will indicate changes in the target density as well. The cut on the target density is given by

* $0.85 \cdot 10^{15} < n < 1.4 \cdot 10^{15}$ ([nucleons/cm^2]).

- *Target polarisation.* Depending on whether the target polarisation is of consequence for a particular measurement, this quantity is taken into account. For most of the analysis dealing with exclusive ρ^0 production this quantity is of no relevance.

Dead Time of the Data Acquisition

In the acquisition of data after a trigger signal has occurred, new incoming data is rejected while the signals from the various detectors are read out by the DAQ and written to tape. That means that during a certain amount of time, typically in the order of 400 microseconds, no other triggered events are accepted [37]. This time period is referred to as "dead time". A relative measure of the dead time is the ratio of the number of generated triggers and the number of accepted triggers (both counted by a scaler). Often, the so-called "live time" is used, which is the inverse of the dead time and is, by definition, not smaller than 0 or larger than 1. This information is part of the slow-control data stream and is updated for every new burst. Besides cuts on the live time, also cuts on the burst length are applied in the data selection:

- Reject in each run: first 3 bursts.
- Reject in each run: last burst.
- Live time: 50 % $<$ T$_{live}$ $<$ 100 %.
- Burst length: 9 sec $\leq$ T$_{burst}$ $\leq$ 11 sec

Luminosity

The luminosity measurement is used for both relative and absolute normalisation of the data. Because of the changing beam current and the relatively long time of ten seconds in between polarisation reversals, asymmetry measurements have to be normalised with the luminosity. For the ρ^0 analysis, the luminosity measurement is used to normalise the data on ^{3}He, deuterium and hydrogen for the nuclear transparency measurement and the data on ^{3}He for the absolute cross section. In the g_1^n data selection cuts are made on both the luminosity monitor rates and on the ratio of luminosity rates and the product of target density and beam current.

- Luminosity monitor rate: 40 Hz $< R_{lumi} <$ 210 Hz.
- Ratio ([cm$^2\cdot$ s / mA $\cdot$ nucleons]) $5 \cdot 10^{-15} < R_{lumi}/(n \cdot I) < 7.2 \cdot^{-15}$

Tracking Efficiencies

The quality of the tracking chambers is controlled by cuts on the tracking efficiencies as calculated by ACE. To ensure that trips are reliably identified and that no bursts are accepted in which halfway some tracking chambers suffered from a HV trip, the burst before a burst failing the efficiency cuts is rejected as well.

- Tracking efficiency for forward partial tracks: $80\% < \epsilon_{front} < 100\%$
- Tracking efficiency for back partial tracks: $94\% < \epsilon_{front} < 100\%$
- For each burst failing the cuts above, also the previous burst is rejected.

PID Quality Checks

The performance of the PID detectors influence the trigger efficiency and the reliability of the particle identification. For the preshower and the calorimeter the GMS information can only be used on a run-by-run basis since statistics of the GMS measurements are insufficient to allow for a burst-by-burst estimate of the detector qualities. The number of bad modules is calculated by comparing the average gain of the module, as determined by the GMS, and the nominal gain value. For the inner thirty modules of both the top and the bottom half of the calorimeter and preshower stronger cuts are applied than for the outer modules. For the calorimeter, bad modules are defined as having a gain not within 10 % of the nominal value, for the preshower, bad modules have a gain not within 20 % of the nominal value.

For H1, the first row of hodoscopes, and for the preshower, the number of scaler counts per burst for each module is required to be larger than zero. For the Čerenkov counter, an efficiency is calculated from the number of positron tracks recognised by the Čerenkov detector divided by the total number of positron tracks as determined by the preshower and the calorimeter. As for the GMS information, this method can only be performed on a run-by-run basis in order to have sufficient statistics. Similarly, the TRD data quality checks are performed on a run-by-run basis. For each TRD module it was checked that the high voltage was set at the proper value and checks were made on the TRD responses. Based on this information it was determined whether the TRD was usable for a particular run or not.

After establishing for each PID detector how many bad modules were present, a number of requirements are made for a run to be accepted:

- number of bad modules in top inner calorimeter (GMS): $N \leq 3$
- number of bad modules in bottom inner calorimeter (GMS): $N \leq 4$
- number of bad modules in outer calorimeter (GMS): $N \leq 8$
- number of bad modules in inner preshower (GMS): $N \leq 1$

- number of bad modules in outer preshower (GMS): $N \leq 5$
- number of bad modules in top H1 (scaler): $N \leq 1$
- number of bad modules in bottom H1 (scaler): $N = 0$
- number of bad modules in top preshower (scaler): $N = 0$
- number of bad modules in bottom preshower (scaler): $N = 0$
- Čerenkov efficiency: $\epsilon > 92\%$ or TRD usable.

When during a fill the overall data quality was unstable, bursts in this unstable period were rejected. Runs where the burst quality criteria indicated only a small fraction of good bursts or where good bursts and bad bursts alternated frequently were rejected. A gap is defined as the number of times the burst quality changes from good to bad between two good periods.

- maximum fraction of gaps per run: $\frac{n_{gaps}}{n_{bursts}} < 0.10$
- minimum fraction of good bursts per run: $\frac{n_{goodbursts}}{n_{bursts}} > 0.40$
- minimum number of good bursts per fill:
  $n_{goodbursts,top} > 100$ (per run)
  $n_{goodbursts,bottom} > 100$ (per run)

Table 5.1 gives an overview of the number of bursts which are removed from the data sample.

Table 5.1: *Effect of the various data quality cuts applied on the total amount of 1995 data. Eventually about 2.5 million DIS events were left.*

	top	bottom
total number of bursts	125196	125196
total number of bad bursts	53852 (43.0 %)	48927 (39.1 %)
total number of good bursts	71344 (57.0 %)	76269 (60.9 %)

5.3 ρ^0 Monte Carlo

Monte Carlo programs are meant to simulate both physics and detector environments in such a way that the kinematics of the resulting simulated events match with the kinematics of the events from data. The Monte Carlo events are used for example for acceptance corrections (see section 6.2.2), rates and background predictions and verification of analysis algorithms.

In chapter 4 the Hermes Monte Carlo HMC was mentioned. This program can be used with several different physics generators, each simulating particular physics processes (e.g. Møller scattering, DIS, Bhabha scattering). Besides the physics generators which are already part of this package, HMC can also read event kinematics from an ADAMO GAF file, created by an independent physics generator. Subsequently, HMC will track these events through the various HERMES detectors, simulating their resolutions and efficiencies. A dedicated physics generator was written for the ρ^0 analysis [97] (the so-called ρ^0 Monte Carlo, RMC), which was adapted to write the kinematics of the three outgoing tracks (the scattered positron and the two decay products of the ρ^0 , two pions with opposite charge) into an ADAMO GAF.

The tracking of events through the HERMES spectrometer and magnet requires a large amount of CPU time. Also, the output files of HMC occupy a large fraction of disk space, partly because it is stored in ADAMO format and partly because of the large amount of detailed information in its output. For these reasons, often studies were performed based on the output of RMC directly. A relatively simple simulation of the HERMES geometry and magnetic field was implemented in RMC for this goal. The sections below describe various items involved in RMC.

5.3.1 Theoretical Model of the Cross Section

In RMC, events are generated according to a model for the process $ep \longrightarrow e'p'\pi^+\pi^-$ with π^+, π^- the decay products of the ρ^0 particle. Under particular assumptions, which will be dealt with below, the complete cross section can be written as in Eq. (2.74).

The process $ep \longrightarrow e'p'\pi^+\pi^-$ is assumed to proceed through ρ^0 production and one can distinguish between the ρ^0 production and decay mechanisms, $ep \longrightarrow e'p\ \rho^0$ and $\rho^0 \longrightarrow \pi^+, \pi^-$, respectively. The ρ^0 decay mechanism involves $M_{\pi\pi}, \cos(\theta_{\pi\pi})$ and Ψ. These are mainly important for studies of the shape of the distributions of these variables, and their “hit-or-miss” curves (see section 5.3.3) are normalised to one. In other words, the events are generated according to a distribution in these variables, but the total number of events is not influenced by this.

The ρ^0 production mechanism is assumed to be comprised of an overall electroproduction cross section $ep \longrightarrow e\gamma p'$, followed by photoproduction $\gamma p \longrightarrow \rho^0\ p'$. The lepton scattering process is defined by the variables Q^2 and E'. The photoproduction process is the process which is not yet accurately known in theory and hence the most interesting process to measure. It is described in terms of Q^2, E', t and ϕ_V. The variables t and ϕ_V are again distributed only according to their expected shape.

The total amount of events is expected to depend on the modelled cross section dependence on Q^2, ϕ and E', or after rewriting, on Q^2, ϕ and W. To obtain an absolute number for the expected rates, one has to normalise with the “monte-carlo luminosity”, as explained in section 5.3.3.

The expression for the photoproduction process in RMC is given by

$$\sigma_0(Q^2 = 0) = \frac{A_\gamma 2M_p}{W^2 - M_p^2} + B_\gamma, \tag{5.4}$$

with $A_\gamma = 29.4\,\mu$b $\cdot$ GeV and $B_\gamma = 9.5\,\mu$b, determined by a fit to data from Ref. [39]. The Q^2

dependence is simulated according to:

$$\sigma_0(Q^2) = \frac{1}{(1 + Q^2/m_{\rho_0}^2)^2} \cdot \sigma_0(Q^2 = 0), \tag{5.5}$$

based on results of Ref. [23].

The events have to be generated according to the leptoproduction cross section. This is done using the expressions from Ref. [23]. The events were generated with free variables Q^2, E' and ϕ according to

$$\begin{aligned}\frac{d\sigma}{dQ^2dE'd\phi} &= \frac{d\sigma}{d\cos(\theta)dE'd\phi}\frac{d\cos(\theta)}{dQ^2} \\ &= \frac{d\sigma}{d\cos(\theta)dE'd\phi}\frac{1}{2EE'} \\ &= \frac{1}{2EE'}\Gamma_T(Q^2, E')\sigma_0(Q^2),\end{aligned} \tag{5.6}$$

with Γ_T the photon flux factor,

$$\Gamma_T(\cos(\theta), \phi, E') = \frac{\alpha}{2\pi^2}\frac{(W^2 - M_p^2)}{2M_p}\frac{1}{Q^2}\frac{E'}{E}\frac{1}{1-\epsilon}, \tag{5.7}$$

which is equivalent to Eq. (2.78), with ϵ given by Eq. (2.18).

For the variables which are generated according to a normalised shape function, the following expressions were used. The invariant mass $M_{\pi\pi}$ was generated according to a skewed [108], relativistic Breit-Wigner shape [23],

$$F(M_{\pi\pi}) \propto \frac{M_{\pi\pi}\Gamma_M}{(M_{\pi\pi}^2 - m_\rho^2)^2 + m_\rho^2\Gamma_M^2}(\frac{m_\rho}{M_{\pi\pi}})^{n_{skew}}. \tag{5.8}$$

In this equation, $n_{skew} = 3.18$ and Γ_M is the energy dependent width of the invariant mass peak [77],

$$\Gamma_M = \Gamma_0(\frac{\pi^*}{\pi_0^*})^3\frac{m_\rho}{M_{\pi\pi}}, \tag{5.9}$$

$$\pi^* = \sqrt{M_{\pi\pi}^2 - 4m_\pi^2}/2 \tag{5.10}$$

$$\pi_0^* = \sqrt{M_\rho^2 - 4m_\pi^2}/2 \tag{5.11}$$

where $\Gamma_0 = 0.1507$ GeV and $m_\rho = 0.7699$ GeV taken from the particle data book [98].

The variable t' is related to the Mandelstam invariant t according to $t' = t - t_0$ where t_0 is the value for t in case the three vector of the ρ^0 particle would be parallel to the direction of the virtual photon. The variable t_0 is Lorentz invariant and it can be calculated in the hadron centre of mass frame [98],

$$t_0 = (E_{\gamma,cm} - E_{\rho,cm})^2 - (|p_{\gamma,cm}| - |p_{\rho,cm}|)^2. \tag{5.12}$$

The hadron centre of mass quantities can be easily derived by using the Mandelstam variable $W = (p_\gamma + p_{proton})^2$ and

$$\begin{aligned} E_{\gamma,cm} &= \frac{W^2 - Q^2 - m^2_{proton}}{2W}, && (5.13) \\ E_{\rho,cm} &= \frac{W^2 + M^2_{\pi\pi} - M^2_x}{2W}, && (5.14) \\ |p_{\gamma,cm}| &= \sqrt{E^2_{\gamma,cm} + Q^2}, && (5.15) \\ |p_{\rho,cm}| &= \sqrt{E^2_{\rho,cm} - M^2_{\pi\pi}}, && (5.16) \\ & && (5.17) \end{aligned}$$

where M_x is the invariant mass of the outgoing proton, $M_x^2 = p'_{proton,\mu} \cdot p'^{\nu}_{proton}$. Events are distributed in t' with probabilities proportional to

$$F(t') \propto \exp^{b_N \cdot t'}, \quad t' < 0, \tag{5.18}$$

where $b_N = 6$ GeV^{-2}, again based on Ref. [23].

The decay and production angles $\cos(\theta_{\pi\pi})$, $\phi_{\pi\pi}$ and Φ_{ee} are generated assuming s-channel helicity conservation (SCHC) and natural parity exchange in the t-channel ([80] and [111]). Using these assumptions, one can define $\Psi = \phi_{\pi\pi} - \Phi_{ee}$. Using Ref. [23], one obtains:

$$\begin{aligned} W(\cos\theta_{\pi\pi}, \Psi) \quad \propto & \qquad\qquad (5.19) \\ & 2\epsilon R \cos^2\theta_{\pi\pi} + \sin^2\theta_{\pi\pi}(1 + \epsilon\cos 2\Psi) - \sqrt{2\epsilon R(1+\epsilon)}\cos\delta \sin 2\theta_{\pi\pi}\cos\Psi. \end{aligned}$$

with, assuming again SCHC, $R = \frac{1}{\epsilon}\frac{r^{04}_{00}}{1 - r^{04}_{00}}$ where, using Ref. [113], $r^{04}_{00} = r_{ampl}\,(Q^2)^{r_{exp}}$ with $r_{ampl} = 0.28015$ and $r_{exp} = 0.45080$.

5.3.2 Simulation of Geometry and Magnetic Field

When the kinematics of the scattered positron and the two pions have been determined, the space-vector elements are compared with the x and y coordinates of two rectangles representing the HERMES geometrical acceptance given in table 5.2.

Table 5.2: *Coordinates of* HERMES *geometrical acceptance, defining the minimum and maximum slopes of tracks which can be detected by the* HERMES *detector.*

Quantity	Description	Value
$\|x_{min}\|/z$	minimum slope in x	0.0
$\|y_{min}\|/z$	minimum slope in y	0.040
$\|x_{max}\|/z$	maximum slope in x	0.170
$\|y_{max}\|/z$	maximum slope in y	0.140

For the simulation of the HERMES magnetic field [25, 26], the acceptance for particles with momenta lower than 4 GeV, i.e. the distribution of particle momentum versus the opening angle in the x-plane, was modelled according to

$$|p_{\pi^\pm}| = \frac{(Z_{\rm calo} - Z_{\rm magnet}) \int \boldsymbol{B} \cdot \boldsymbol{dl}}{W_{\rm calo} + Z_{\rm calo}\frac{dX}{dZ}}, \tag{5.20}$$

with $Z_{\rm calo}$, $Z_{\rm magnet}$, $W_{\rm calo}$ and $\int \boldsymbol{B} \cdot \boldsymbol{dl}$ given in table 5.3.

The values used in the model are compared with the nominal values which were presented in the original HERMES proposal [73]. The meaning of Eq. (5.20) is explained in Fig. 5.5. The projection of Eq. (5.20) onto a data scatter plot (Fig. 5.6) shows that the measured acceptance is in excellent agreement with the model. One can now apply the requirement to the Monte Carlo events that all hadrons should have momenta larger than those given by Eq. (5.20). Scattered positrons will automatically fulfill this requirement since they are always required to have momentum larger than 3.5 GeV (simulating the data trigger threshold in the calorimeter). Of all generated events, the events for which the three tracks pass the geometrical and magnetic field cuts will be referred to as "accepted events".

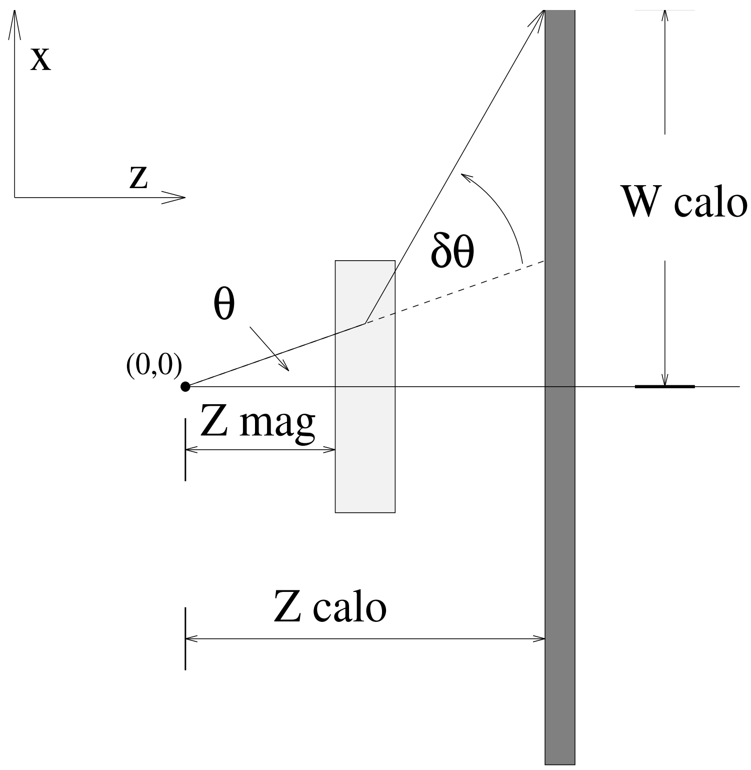

Figure 5.5: *Schematic outline of the modeling of the magnetic field geometry used in* RMC. *A particle with initial slope $dX/dZ = \tan\theta$ is propagated to the centre of the magnet, bent by an angle $\delta\theta = \tan^{-1} p^{-1} \cdot (0.40\,\mathrm{GeV/c})$, and then propagated to the calorimeter face.*

Table 5.3: *Parameters used in the definition of the low-momentum acceptance of the* RMC.

Quantity	Description	Nominal Value (TDR)	Adjusted Value
Z_{mag}	Magnet Centre (z)	2725 mm	2725 mm
Z_{calo}	Calorimeter Position (z)	7200 mm	7200 mm
W_{calo}	Calorimeter half-width	1800 mm	1800 mm
$\int \boldsymbol{B} \cdot \boldsymbol{dl}$	Field Integral	1.5 T·m= 0.45 GeV/c	0.40 GeV/c

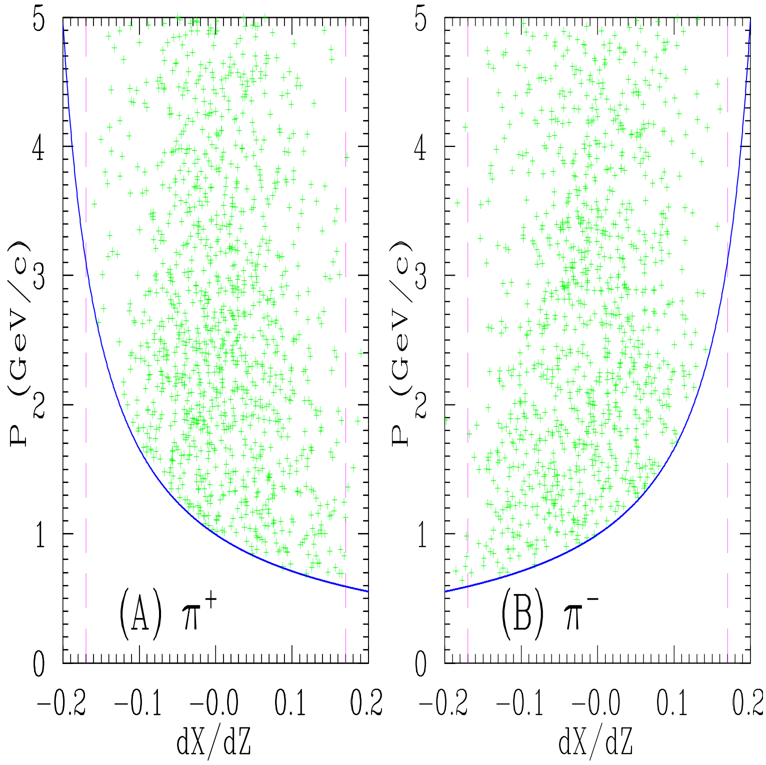

Figure 5.6: *The scatter plot shows particle momentum versus the horizontal slope, for both positive (A) and negative (B) momentum pions from the sample of ρ^0 events. The dashed lines represent the opening angle acceptance of $\pm 170\,\mathrm{mrad}$. The solid curve is given by Eq. (5.20), showing that the low-momentum acceptance is well understood.*

5.3.3 Monte Carlo Techniques.

RMC, as most Monte Carlo programs, uses the "hit-or-miss" method to generate events with kinematics distributed according to a certain shape. An extensive description of statistical methods in data analysis can be found in Ref. [93]. The method compares the output of a uniform distributed random function $R[p_{min}, p_{max}]$ with output values in the range p_{min}, p_{max}, with a distribution function $f(x)$ with the required shape. The algorithm proceeds as follows,

1. $x_i = R[x_{min}, x_{max}]$
2. $y_i = R[y_{min}, y_{max}]$
3. "hit" if $y_i < f(x_i)$ and "miss" if $y_i > f(x_i)$

In case of a "miss", a next pair x_i, y_i will be generated, in case of a "hit", the event is used as a real physics event in the rest of the program. The distribution of events with respect to x will have the shape $f(x)$ as depicted in Fig. 5.7.

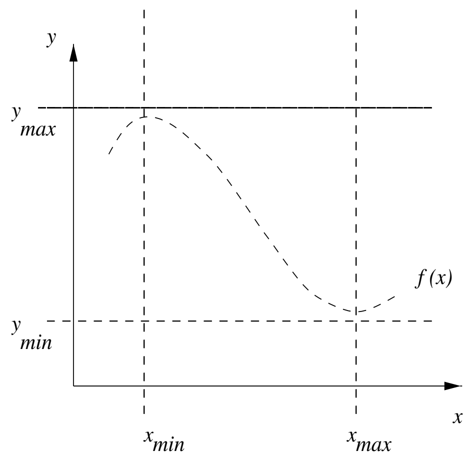

Figure 5.7: *The "hit or miss" method. Events are generated with a uniform distribution over a range x_{min}, x_{max} in y_{min}, y_{max}. When a certain point x_i, y_i is below the curve $f(x_i)$ the event is used, ensuring that the final sample of generated events are distributed according to $f(x)$.*

RMC can also be used for predicting rates as a function of Q^2, ϕ or E' when the proper normalisation is taken into account. Also, when different event samples generated by RMC are to be compared, an absolute normalisation is necessary. In order to convert the number of events to a cross section, a so-called Monte Carlo luminosity L_{mc} is used. In the example given above, $f(x)$ represents the shape of the cross section as a function of x, where y_{max} is the maximum cross section, $y_{min} = 0$, and L_{mc} is given by

$$L_{mc} = \frac{n_{kin}}{y_{max}(x_{max} - x_{min})}, \tag{5.21}$$

with n_{kin} the total number of "hits" and "misses".

Hence, in RMC, the luminosity is given by

$$L_{mc} = \frac{n_{kin}}{\sigma_{max}(\phi_{max} - \phi_{min})(Q^2_{max} - Q^2_{min})(E'_{max} - E'_{min})}. \tag{5.22}$$

As long as σ_{max} is always larger than $\sigma(Q^2, E', \phi)$, its actual value is not relevant. Nevertheless, for speed considerations one should keep σ_{max} as small as possible.

One obtains the cross section by dividing the number of events with L_{mc}.

Chapter 6

Results

6.1 Selection of Exclusive Diffractive ρ^0 Events

Events from exclusive, diffractive ρ^0 production are selected in two steps. First a '3-track-sample' of events where only the scattered positron and two hadrons with opposite charge are detected in the spectrometer is extracted from the data. Additionally, the following cuts are made,

- $W^2 > 4$ GeV^2, excludes background events from nucleon resonance excitation,
- $\nu > 9$ GeV, excludes low energy background,
- $y = \nu/E_{\text{beam}} < 0.85$, to minimise radiative corrections.

A number of subsequent cuts is applied to this data sample to select exclusive, diffractive events around the ρ^0 mass peak, using

- $\Delta E < 0.6$ GeV.
  ΔE is a measure for the difference in the invariant mass of the incoming nucleon and the outgoing undetected hadronic system,
  $$\Delta E = (M_x^2 - M_p^2)/2M_p, \tag{6.1}$$
  with M_p the proton mass and M_x the invariant mass of the undetected hadronic system.
- $-t' < 0.4$ GeV^2.
  $-t'$ is a measure of the transverse momentum of the ρ^0 meson with respect to the photon, as explained on page 102.
- $0.6 < M_{\pi\pi} < 1$ GeV$/c^2$.
  $M_{\pi\pi}$ is the invariant mass calculated by using the four vectors of the two detected hadrons, where the two hadrons are assumed to be pions,
  $$M_{\pi\pi}^2 = (p_{\pi^+} + p_{\pi^-})^2. \tag{6.2}$$

- $M_{KK} > 1.04$ GeV$/c^2$.
  M_{KK} is the invariant mass calculated by using the four vectors of the two detected hadrons, where the two hadrons are assumed to be kaons. This eliminates most of the $\phi \rightarrow K^+K^-$ background. The ϕ has a mass of 1.02 GeV/c^2 and a width of 4.4 MeV/c^2 (see Ref. [98]). For a ρ^0 meson, if one would insert the kaon mass instead of the pion mass into Eq. (6.2), one would end up with an invariant mass which would be about 1.22 GeV/c^2. Because of the rather large full width of the ρ particle, a conservative lower limit of 1.04 GeV/c^2 is chosen.

In Fig. 6.1 the invariant mass spectrum of the ρ^0 particle is shown, after applying the various cuts. The final spectrum is not corrected for the limited geometric acceptance of the HERMES spectrometer which explains the slight bump on the left hand side of the peak. This will be explained in further detail in section 6.1.1.

Additionally, a number of 'fiducial' cuts are required [95]. These ensure that no anomalies in the data set occur and hence possible significant systematic errors are avoided. Positrons and hadrons are subjected to a cut on the opening angle in the $z - y$ plane, $|\theta_y| > 0.04$ mrad. In addition, the efficiency for identifying positrons drops near the calorimeter edges, so positrons should also be subject to fiducial cuts on calorimeter position by requiring $|X(\mathrm{calo})| < 175\,\mathrm{cm}$ and $|Y(\mathrm{calo})| > 30\,\mathrm{cm}$.

Furthermore, the following cuts on the track vertex positions are applied. The distance of the z–position of the positron track to the centre of the target cell should be less than 18 cm. The distance of the z–position of the positron track to the z–position of either one of the hadron tracks should be less than 20 cm. The minimal distance to the beam of the positron track should be less than 0.2 cm. The minimal distance to the beam of either one of the hadron tracks should be less than 2 cm.

6.1.1 Invariant Mass Spectrum

After subtracting DIS background (see section 6.2.1) and applying an acceptance correction the mass spectrum was fitted with a number of different fitting functions. The method of background subtraction is described in section 6.2.1. For the acceptance correction, the ratio of the generated and the accepted sample of Monte Carlo events in each bin of the mass spectrum was used. Fig. 6.2 shows the invariant mass spectrum before and after applying the acceptance correction. Because of the limited HERMES acceptance only a fraction of the total events will be detected. The enhancement of events at the left hand side of the peak is due to a larger acceptance for events with small pion opening angles. However, close to the production threshold of twice the pion mass the cross section decreases rapidly. The combination of these two effects results in the 'bump' observed in the uncorrected invariant mass spectrum.

Fig. 6.3 shows the fit results for the skewed Breit-Wigner function (see Eq. (2.81)) and the Söding fitting function (see Eq. (2.82)). The basic fitting function is the relativistic Breit-Wigner p-wave function. The skewing factor and/or the Söding interference term were devised

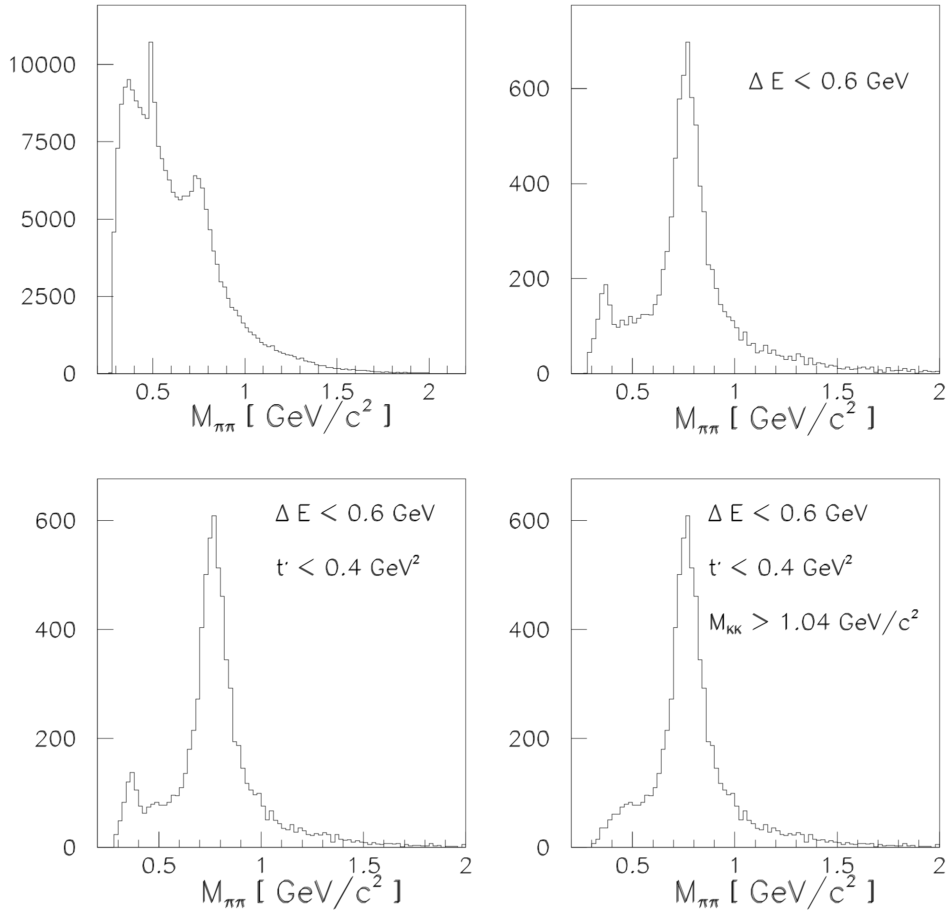

Figure 6.1: *The $\pi^+\pi^-$ invariant mass spectrum in a window of $M_{\pi\pi} < 2$ GeV/c^2. The top left plot shows all events with only three tracks as explained in the text, and after applying cuts on y, ν and W. The top right plot is obtained by applying an additional cut on ΔE. The bottom left plot is obtained by applying an additional cut on $-t'$. The bottom right plot is obtained by applying an additional cut on M_{KK}.*

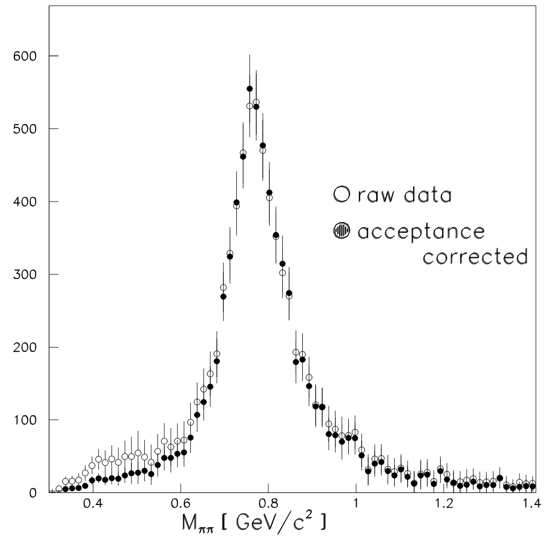

Figure 6.2: *Invariant mass spectrum before (open circles) and after (filled circles) applying the acceptance correction.*

to correct for non-resonant background. Fig. 6.4 shows the fitting results when fitting to the $\rho - \omega$ interference shape (see Eq. (2.84)).

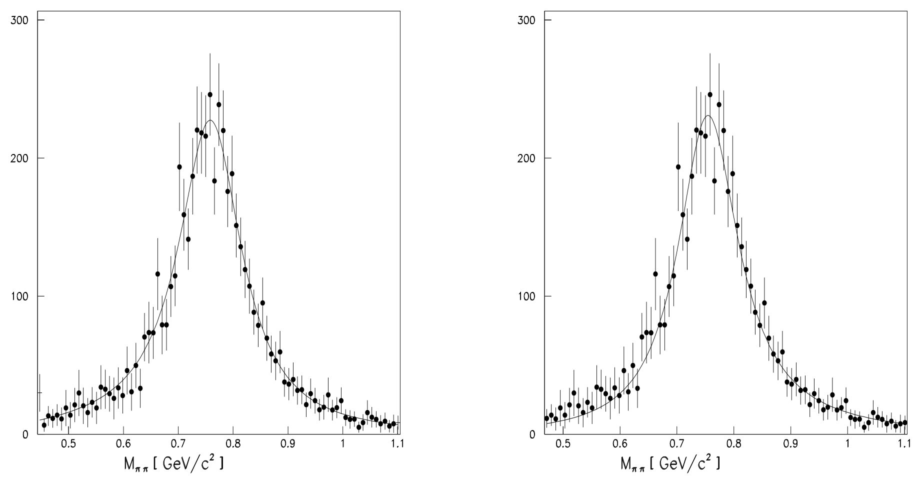

Figure 6.3: *Invariant mass spectrum fitted with a skewed Breit-Wigner function (left panel) and with the Söding function (right panel).*

The parameters of the various fits are shown in Table 6.1. The results agree well with the parameters from Ref [98], where $M_{\rho^0} = 0.770$ GeV/c^2, $\Gamma_{\rho^0} = 0.151$ GeV/c^2, $M_\omega = 0.782$ GeV/c^2 and $\Gamma_\omega = 8.4$ MeV/c^2.

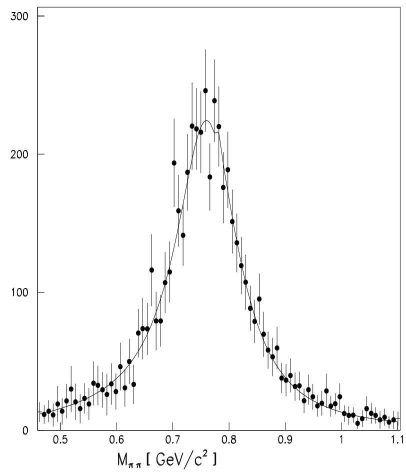

Figure 6.4: *Invariant mass spectrum fitted with a skewed Breit-Wigner shape, where also the interference with the ω – meson is taken into account.*

Table 6.1: *Fit results on the invariant mass spectrum for the skewed Breit-Wigner shape (left column), the Söding method (middle column), and for the skewed ρ^0 –ω interference shape (right column).*

	Breit-Wigner	Söding	ρ^0 –ω interference
M_{ρ^0} [GeV/c^2]	0.773 ± 0.001	0.766 ± 0.003	0.775 ± 0.001
Γ_{ρ^0} [GeV/c^2]	0.146 ± 0.003	0.135 ± 0.006	0.140 ± 0.02
M_ω [GeV/c^2]			0.782 ± 0.001
Γ_ω [GeV/c^2]			0.008 ± 0.0003
n_{skew}	3.0 ± 0.02		3.2 ± 0.15
A_{bw}		31.2 ± 1.0	
A_{sod}		3.8 ± 0.3	
$A_{\mathrm{background}}$		-5.4 ± 0.6	
α			$0.8 \pm 0.1\,\mathrm{rad} = 46^\circ \pm 6^\circ$
ξ			0.0015 ± 0.005
χ^2	0.38	0.52	0.36

6.1.2 Distribution of Transverse Momentum

The data sample presented here only comprises data which were recorded during 1995 with a polarised ^{3}He gas target. When comparing the HERMES cross section to data obtained by other experiments, the nuclear effects should be accounted for. One feature of scattering from a nuclear target is that one can distinguish between coherent scattering from the entire nucleus and incoherent scattering from individual nucleons. In our comparison to other experiments we will be mainly interested in incoherent scattering.

In Fig. 6.5 the $-t'$ distribution is shown. In diffractive scattering, the slope of this distribution can be associated with the transverse size of the two scattering objects, in our case the ρ^0 particle and the nucleus or nucleon. Clearly one can observe that the slope in Fig. 6.5 is the sum of the two separate contributions of coherent and incoherent scattering. At low absolute values for $-t'$ less energy is transferred between target and the ρ^0 particle and hence here the scattering will be mainly coherent. At higher values of $-t'$ incoherent scattering will set in.

The distribution in Fig. 6.5 is fitted to the shape

$$f(-t') = A\left(\frac{\sigma_{coh}}{\sigma_{incoh}}\, B_{coh}\, e^{-B_{coh}t'} + B_{inc}\, e^{-B_{inc}t'}\right), \tag{6.3}$$

where B_{coh} denotes the slope in case of coherent scattering and B_{inc} denotes the slope in case of incoherent scattering. The fit function contains four free parameters, A, B_{inc}, B_{coh} and $\frac{\sigma_{\mathrm{coh}}}{\sigma_{\mathrm{inc}}}$. The fit results are given in Table 6.2.

Table 6.2: *Fit results for the $-t'$ distribution.*

$\frac{\sigma_{\mathrm{coherent}}}{\sigma_{\mathrm{incoherent}}}$	0.49 ± 0.28
B_{coherent}	24.1 ± 7.3 GeV^{-2}
$B_{\mathrm{incoherent}}$	5.9 ± 1.3 GeV^{-2}
χ^2	1.1

As stated earlier, the impact parameter B can be related to the radii of the scattering particles, $B = R_1^2 + R_2^2$. In our case, these will be the radii of the ρ^0 meson and either the nucleon in case of incoherent scattering or the nucleus in case of coherent scattering. The relation between the aforementioned radii and measurable electromagnetic radii is given by $< r^2 >= 3R^2$ (see Ref. [106]). Hence, since the radius of the ρ^0 meson is much smaller than the radius of the nucleon or the nucleus, one obtains for incoherent scattering $B \simeq 1/3 < r_N^2 >$, with r_N the radius of a nucleon, and for coherent scattering $B \simeq 1/3 < r_A^2 >$, with r_A the radius of a nucleus. Using the values from Table 6.2, one obtains for the measured radii, $r_N = 0.84 \pm 0.09$ fm and $r_A = 1.68 \pm 0.25$ fm. These values are in good agreement with results from other measurements, $r_N = 0.85$ fm and $r_A = 1.98$ fm [123].

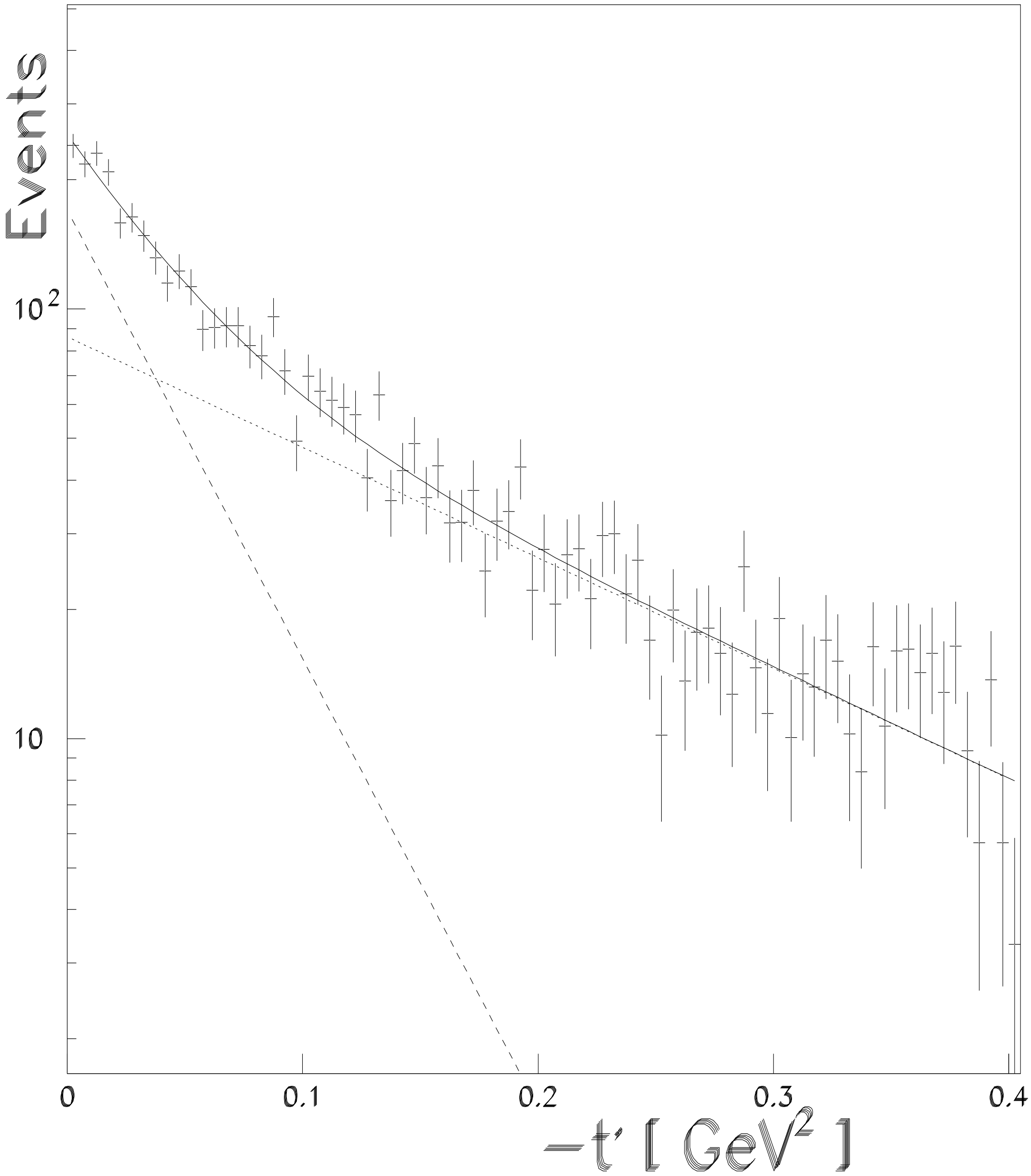

Figure 6.5: *The $-t'$ distribution for the 1995* HERMES ${}^3\vec{\mathrm{He}}(\vec{e}, e'\pi^+\pi^-)$ *data. The curve shows the fit to the data with the function of Eq. (6.3). Clearly, one can observe that the slope is the sum of contributions of coherent (dashed curve) and incoherent scattering (dotted curve). The results of the fit are given in Table 6.2.*

6.2 Cross Section

The main ingredients needed for the extraction of the cross section are the background subtraction, the acceptance correction and the normalisation. As explained below, the conversion from the number of electroproduction events to a photoproduction cross section either explicitly or implicitly involves the acceptance correction.

6.2.1 Background Subtraction

The amount of DIS events which fulfil the requirements made to select ρ^0 events is small compared to the total amount of DIS events. This means that a vast number of DIS events have to be generated in order to have a large enough sample of DIS events which pass the ρ^0 selection requirements to have an estimate of the amount of background events. Unfortunately, both time and disk space considerations did not allow for using HMC to estimate the amount of DIS background.

Instead, an alternative method for subtracting background was used. In Fig. 6.6 ΔE is plotted versus $-t'$ for the event sample. The scatter plot is divided into four regions. Exclusive, diffractive ρ^0 particles are located in region I, at low ΔE and low $-t'$. The event sample in this region will also contain DIS events, which comprise the background of the exclusive, diffractive ρ^0 sample. Under the assumption that the $-t'$ dependence of background DIS events does not depend on ΔE, one can relate the number of background DIS events in region I to region IV, by comparing the number of events in region II and III. Fig. 6.7 shows that this assumption is valid. Regions III and IV will contain DIS events only and hence the number of background events in region I, B_I can be approximated by using

$$B_I = N_{IV} \cdot \frac{N_{II}}{N_{III}},$$

where N_i denote the number of events in region i. Hence, the number of ρ^0 events will be $N_{\rho^0} = N_I - B_I$.

6.2.2 Acceptance Correction

The number of generated events and accepted events obtained with our Monte Carlo program were used to estimate the ratio of the measured cross section of events with tracks within the HERMES geometric acceptance to the total cross section.

There are two different methods to correct for the limited geometric acceptance of the HERMES spectrometer where either explicitly or implicitly each event is divided by the photon flux factor to obtain the virtual photoproduction cross section.

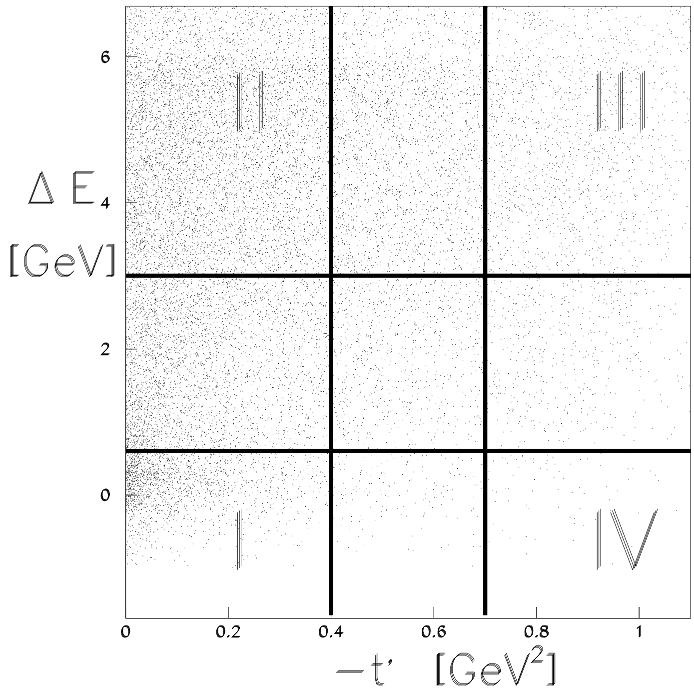

Figure 6.6: *Scatter plot of* $^3He(e, e'h^+h^-)$ *events for* ΔE *versus* $-t'$*. Region I contains the events selected by the cuts described in section 6.1.*

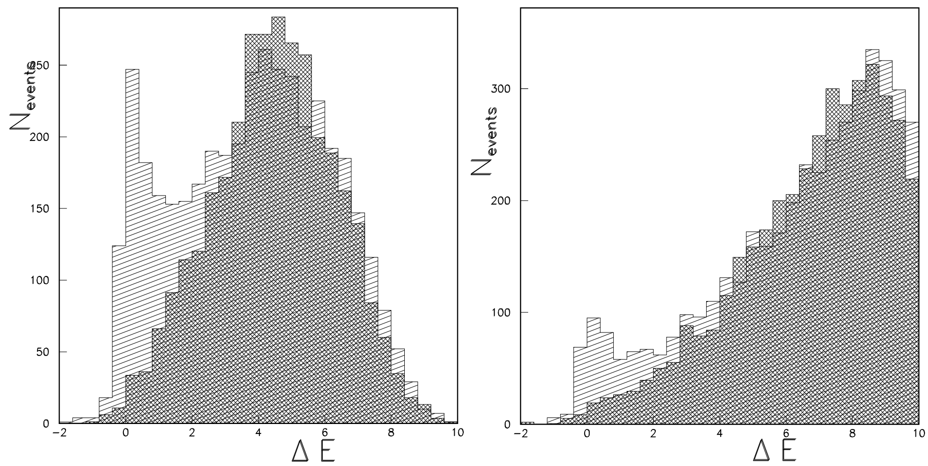

Figure 6.7: ΔE *distribution for regions I and II (shaded) and the projected* ΔE *distribution for regions III and IV (double shaded) showing that the shape of the distribution of background events is similar for both* $4 < W < 5.25$ *GeV (left) and* $5.25 < W < 6.5$ *GeV (right).*

Explicit Weighing with Photon Flux

The total number of events $N_{\rho^0}(\Delta Q^2, \Delta W)$ in a certain bin $(\Delta Q^2, \Delta W)$ is proportional to the electroproduction cross section, $\frac{d\sigma}{dQ^2 dW}$. Cross sections for ρ^0 production are most often published in the form of a virtual photoproduction cross section since the photon flux emitted by the scattering lepton is already known. Using the relation given in Eq. (2.75), all events should be normalised by the corresponding value for the flux of transverse photons, Γ_T.

When summing over all ρ^0 events in bin $(\Delta Q^2, \Delta W)$ and normalising each event by $\Gamma_T(Q^2, W)$, one obtains

$$\sum_{i=1}^{N_{\rho^0}(\Delta Q^2, \Delta W)} \frac{1}{\Gamma_T(Q^2, W)} = \mathcal{L} \int_{\Delta Q^2} \int_{\Delta W} \frac{1}{\Gamma_T(Q^2, W)} \frac{d\sigma}{dQ^2 dW} dQ^2 dW, \tag{6.4}$$

where

$$\frac{d\sigma}{dQ^2 dW} = \frac{d\sigma}{dQ^2 d\nu} \frac{d\nu}{dW}. \tag{6.5}$$

Using Eq. (2.75), one can rewrite Eq. (6.4) into

$$\sum_{i=1}^{N_{\rho^0}(\Delta Q^2, \Delta W)} \frac{1}{\Gamma_T(Q^2, W)} = \mathcal{L} \int_{\Delta Q^2} \int_{\Delta W} \sigma(\gamma^* p \to \rho^0 p) \frac{W}{M_p} dQ^2 dW. \tag{6.6}$$

Assuming that $\sigma(\gamma^* p \to \rho^0 p)$ varies slowly in a certain bin $(\Delta Q^2, \Delta W)$, this expression becomes

$$\sum_{i=1}^{N_{\rho^0}(\Delta Q^2, \Delta W)} \frac{1}{\Gamma_T(Q^2, W)} = \mathcal{L} \frac{1}{2M_p} (W_{max}^2 - W_{min}^2) \Delta Q^2 \sigma(\gamma^* p \to \rho^0 p). \tag{6.7}$$

Hence

$$\sigma_{(\gamma^* p \to \rho^0 p)}(Q^2, W) = \frac{1}{\mathcal{L}} \frac{2M_p}{(W_{max}^2 - W_{min}^2)} \frac{1}{\Delta Q^2} \sum_{i=1}^{N_{\rho^0}(\Delta Q^2, \Delta W)} \frac{1}{\Gamma_T(Q^2, W)}. \tag{6.8}$$

Weighing the events from the data sample and the sample of generated and accepted Monte Carlo events with their photon fluxes gives σ_{data}, $\sigma_{\text{generated}}$ and σ_{accepted} which can be combined to give the final result for the total cross section, given by

$$\sigma_{(\gamma^* p \to \rho^0 p)}(Q^2, W) = \sigma_{\text{data}}(Q^2, W) \frac{\sigma_{\text{generated}}(Q^2, W)}{\sigma_{\text{accepted}}(Q^2, W)}. \tag{6.9}$$

Implicit Weighing with Photon Flux

When the distribution of accepted Monte Carlo events looks similar to the distribution of the data, there is no need to weigh explicitly with the photon flux factor.

Summing over all ρ^0 events in the data sample and the sample of accepted Monte Carlo events, one obtains respectively, $N_{\rm data}$ and $N_{\rm accepted}$, with

$$N_{{\rm data},(ep\to e'\rho^0 p)}(Q^2,W) \sim \frac{d\sigma}{dQ^2dW} = \frac{1}{\mathcal{L}_{\rm tot}} \cdot \frac{N_{\rho^0}(\Delta Q^2,\Delta W)}{\tau_{\rm live}\cdot \eta^3_{\rm ACE}\cdot Res(\rho^0)\cdot Acc(\rho^0)}, \qquad (6.10)$$

and

$$N_{{\rm accepted},(ep\to e'\rho^0 p)}(Q^2,W) \sim \frac{d\sigma}{dQ^2dW} = \frac{M_{\rho^0}(\Delta Q^2,\Delta W)}{(\mathcal{L}_{\rm tot})_{\rm MC}\cdot \eta^3_{\rm MC}\cdot Res(\rho^0)\cdot Acc(\rho^0)}. \qquad (6.11)$$

Here, both $N_{\rm data}$ and $N_{\rm accepted}$ are the number of counts resulting from *electroproduction* of exclusive ρ^0 particles $(ep \to e'\rho^0 p')$ and $\tau_{\rm live}$ is the DAQ live time, and $\eta_{\rm ACE}$, $\eta_{\rm MC}$ is the ACE efficiency per run per track for the data and the Monte Carlo, respectively. $Res(\rho^0)$ accounts for all additional reconstruction effects (multiple scattering, secondaries, detector frames, HRC tracking cuts, smearing), and $Acc(\rho^0)$ is the geometrical acceptance for ρ^0 events. The values $N_{\rho^0}(\Delta Q^2,\Delta W)$ and $M_{\rho^0}(\Delta Q^2,\Delta W)$ denote the number of events in bin ($\Delta Q^2,\Delta W$) from the data and the sample of accepted Monte Carlo events, respectively. Also, $(\mathcal{L}_{\rm tot})_{\rm MC}$ is the total luminosity used in the Monte Carlo (in order to convert the number of counts to a cross section).

The final result for the total virtual photoproduction cross section can now be given by

$$\sigma_{(\gamma^* p\to\rho^0 p)}(Q^2,W) = \frac{N_{\rm data}}{N_{\rm accepted}} \cdot \sigma_{{\rm generated}(\gamma^* p\to\rho^0 p)}(Q^2,W). \qquad (6.12)$$

The outcome of both methods are compared in Fig. 6.12.

6.2.3 Absolute Normalisation

The HERMES measurement of F_2^n was based on a detailed analysis which produced a calibration factor based on normalising data to DIS rates. The calibration factor was derived by extracting the number of DIS positrons and comparing this number to a theoretical prediction for the DIS cross section convoluted with the HERMES geometrical acceptance [35].

This will give for $\mathcal{L}_{\rm tot}$

$$\mathcal{L}_{\rm tot} = \frac{N_{\rm DIS}}{\sigma_{\rm DIS,hermes}\cdot Res({\rm DIS})\cdot \tau_{\rm live}\cdot \eta_{\rm ACE}} \qquad (6.13)$$

where $Res({\rm DIS}) = 0.84$ represents all additional reconstruction effects for DIS events and $\sigma_{\rm DIS,hermes} = 0.056\,\mu$b represents the average DIS cross section for scattering into the HERMES acceptance ([35, 38]).

Hence, rewriting Eq. (6.12), one obtains for the final result

$$\sigma(\gamma^* p \to \rho^0 p) = \sum_{i=1}^{N(\rho^0)} \frac{(\mathcal{L}_{\rm tot})_{\rm MC}\,\eta^3_{\rm MC}}{\sum_{i=1}^{M(\rho^0)}\rfloor_{cuts}} \cdot \frac{\sigma_{\rm DIS,accepted}\,Res({\rm DIS})}{\sum_{i=1}^{N({\rm DIS})}\eta^2_{\rm ACE}} \cdot \sigma_{\rm generated}. \qquad (6.14)$$

In this equation, the cuts on the ρ^0 data sample and Monte Carlo sample have been described in section 6.1. The same PID criteria and data quality cuts are applied to the ρ data sample and the DIS data sample.

6.2.4 Correction Factors

In section 6.1 the selection cuts were summarised. These cuts will result in excluding a certain fraction of valid exclusive, diffractive ρ^0 events. Generally, this is corrected for by the division of the data spectrum by the spectrum of accepted Monte Carlo events. However, some effects are not properly simulated in the Monte Carlo and therefore these have to be corrected for separately.

I. Correction On t' Cuts

In order to ensure the selection of incoherent scattering events, a lower limit to $-t'$ is applied. In Fig. 6.5 one can see that, in the HERMES data, at about $-t' = 0.04$ GeV^2 incoherent scattering starts to dominate. Nevertheless, at $-t' > 0.04$ GeV^2 there is still a contribution from coherent scattering events. The Monte Carlo only simulates scattering from a nucleon, hence, the accepted Monte Carlo spectrum will not contain this contamination.

The contribution of coherent scattering in the data is Q^2 dependent and has to be corrected for. In Fig. 6.8 one can see the result of fitting the shape of Eq. (6.3) to the $-t'$ data spectrum for different Q^2 bins.

The slopes for the coherent and the incoherent part of the cross section are kept constant so that the only free parameter is the ratio of the coherent and incoherent cross section. For various Q^2 bins, ($[0.1;1]$ GeV^2, $[1;2]$ GeV^2, and, $[2;5]$ GeV^2), this ratio is determined. Table 6.3 summarises the results of the fits.

Table 6.3: *Fit results for the $-t'$ distribution for various Q^2 bins.*

Q^2 range	$[0.1;1]$ GeV^2	$[1;2]$ GeV^2	$[2;5]$ GeV^2
$\frac{\sigma_{\text{coherent}}}{\sigma_{\text{incoherent}}}$	0.81 ± 0.08	0.55 ± 0.06	0.35 ± 0.07
χ^2	1.2	0.8	0.9

By keeping the correction factor f_t fixed for all Q^2 bins, with

$$f_t = \frac{\int_{-t'=t_{lowercut}}^{t_{uppercut}} \frac{\sigma_{coh}}{\sigma_{incoh}} B_{coh}\, e^{-B_{coh}t'} + B_{inc}\, e^{-B_{inc}t'}}{\int_{-t'=t_{lowercut}}^{t_{uppercut}} B_{inc}\, e^{-B_{inc}t'}} = 1.03, \tag{6.15}$$

for each Q^2 bin a different $t_{lowercut}$ can be obtained.

In the end the cross section is corrected by $\sigma^* = \sigma/1.03$

II. Correction On ΔE Cut

In section 6.1 we introduced a cut on the ΔE spectrum to select exclusive events. The upper limit to the value of ΔE cuts away some valid exclusive ρ^0 events. Figure 6.9 shows how the

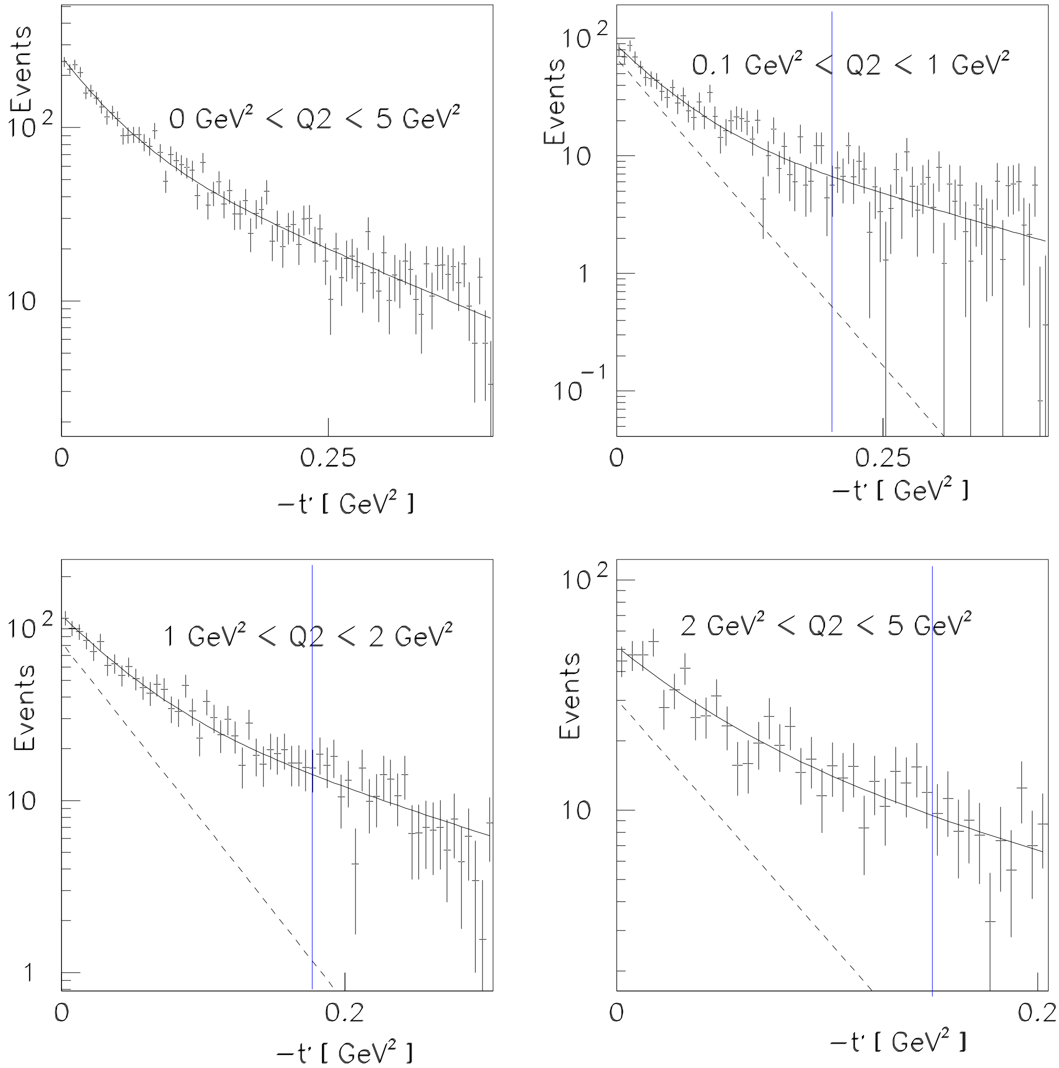

Figure 6.8: *Slopes of the $-t'$ distribution for the 1995* HERMES $^3\vec{\mathrm{He}}(\vec{e}, e'\pi^+\pi^-)$ *data for different Q^2 bins. The slopes are the sum of contributions of coherent (dashed curve) and incoherent scattering. The vertical lines represent the lower cut on $-t'$ in order to keep the contamination of coherent scattering events fixed at 3 %.*

Table 6.4: *Gaussian fit results for the ΔE distribution.*

Amplitude	134.5 ± 5
Mean	0.30 ± 0.02 GeV
Standard Deviation	0.41 ± 0.02 GeV
χ^2	0.9

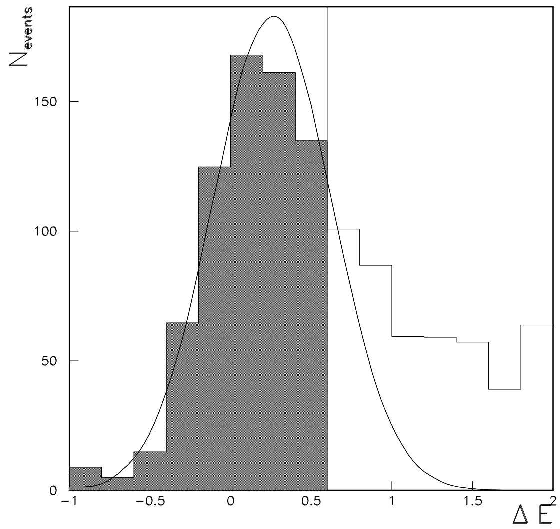

Figure 6.9: *The ΔE distribution is used to select exclusive events. The peak in region 1 (shaded area) is fitted to a Gaussian shape. The ratio of the total number of events under the Gaussian fit to the number of events inside region 1 provides the correction factor $f_{\Delta E}$.*

Gaussian peak of the exclusive ρ^0 events is partly cut away due to the cut at $\Delta E = 0.6$ GeV. The fit results are summarised in Table 6.4. The Monte Carlo does not produce a ΔE peak similar to that observed in the data. Hence, the loss of ρ^0 events in the data sample and the Monte Carlo sample, due to the ΔE cut, has to be corrected for separately.

For the data, using the Gaussian function as fitted to the exclusive peak, one can obtain a correction factor by dividing the total number of events by the number of events with $\Delta E < 0.6$ GeV. Also for the Monte Carlo, the total number of events is divided by the number of events with $\Delta E < 0.6$ GeV. The total correction is the ratio of those two ratios,

$$f_{\Delta E} = \left.\frac{\mathrm{total}\ \#\ \mathrm{events}}{\mathrm{cut\ fraction}}\right\rfloor_{\mathrm{data}} \Big/ \left.\frac{\mathrm{total}\ \#\ \mathrm{events}}{\mathrm{cut\ fraction}}\right\rfloor_{\mathrm{MonteCarlo}} = 1.27/1.37 = 0.93, \tag{6.16}$$

$$\sigma^* = \sigma \cdot f_{\Delta E}. \tag{6.17}$$

III. Nuclear Transparency

The data presented here were taken with a ^{3}He gas target. At low Q^2 the ratio of incoherent ρ^0 production on ^{3}He to incoherent ρ^0 production on a hydrogen target will be smaller than unity. This ratio is called the nuclear transparency and is given by

$$T_A \equiv \frac{\sigma_A}{A \cdot \sigma_H}. \tag{6.18}$$

It is shown that T_A is depending on the coherence length l_{coh},

$$l_{coh} = \frac{2\nu}{Q^2 + m_\rho^2}, \tag{6.19}$$

and hence on both Q^2 and W. Using the data taken from 1995 through 1997 on a hydrogen target, the nuclear transparency of ^{3}He can be extracted (see Refs. [4] and [96]). The result of the measurement of $T_{^3\mathrm{He}}$ is shown in Fig. 6.10.

The final result for the cross section $\sigma_{(\gamma p\to\rho^0 p),(^3\mathrm{He})}$ can be corrected for the nuclear transparency effect by means of

$$\sigma_{(\gamma p\to\rho^0 p)}(Q^2, W) = \frac{\sigma_{(\gamma p\to\rho^0 p),(^3\mathrm{He})}(Q^2, W)}{T_{^3\mathrm{He}}(\langle l_{coh}\rangle)}, \tag{6.20}$$

using the calculation of Kopeliovich et al. to obtain $T_{^3\mathrm{He}}$ for each l_{coh} bin. Table 6.5 gives $\langle l_{coh}\rangle$ for each Q^2 and W bin.

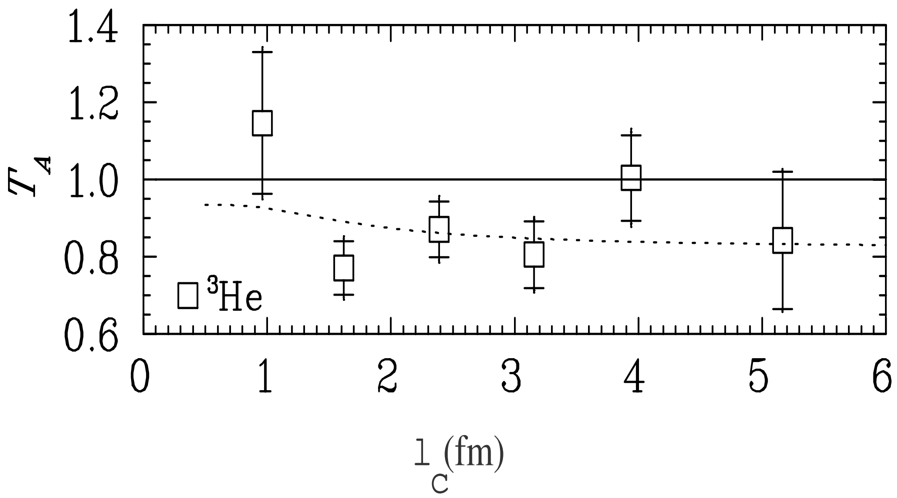

Figure 6.10: *Measured l_{coh} dependence of the nuclear transparency $T_{^3\mathrm{He}}$. The inner error bars are statistical and the outer error bars include the systematic uncertainty. The additional uncertainty in overall normalisation of $\pm$ 6 % is not shown. The dotted curve represents a calculation by Kopeliovich et al. (see Refs. [4] and [96]).*

IV. Radiative Corrections

Due to a limited energy resolution in the detection of the scattered positron and the contributions of processes other than the one we are interested in to the total cross section, the observed cross section will be an underestimate of the real one-photon exchange cross section σ_0. Fig 6.11 shows some of the Feynman diagrams contributing to the total measured cross section. The relevant physics cross section is obtained by applying electromagnetic radiative corrections to the experimentally observed cross section.

Table 6.5: *Average values of l_{coh} in fm, for each Q^2 and W bin.*

$< Q^2 >$ [GeV^2]	$4 < W < 5.25$ GeV	$5.25 < W < 6.5$ GeV
0.75	3.3	4.7
1.33	2.5	3.5
2.33	1.7	2.5
4.30	1.2	1.5

A study was done to calculate the radiative correction for exclusive ρ^0 production for values of Q^2, ν and ΔE corresponding to the HERMES environment [10]. The correction was calculated for various Q^2 bins and proved to be constant in the complete Q^2 range for which a cross section was estimated. The final cross section was corrected by

$$\sigma_0 = \sigma_{\mathrm{observed}}/f_{\mathrm{RC}} \tag{6.21}$$

where f_{RC} is the radiative correction which was established to be 0.80.

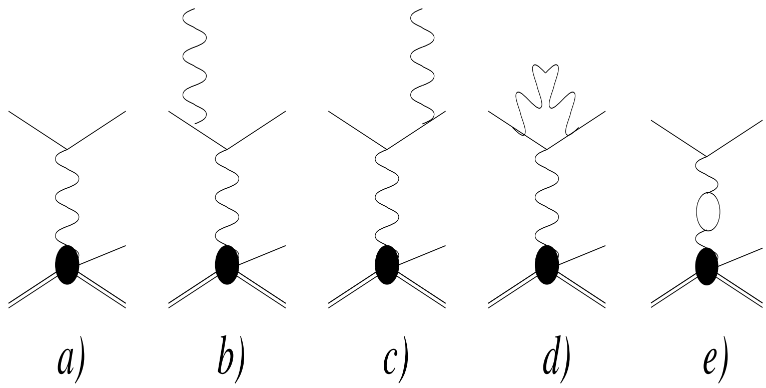

Figure 6.11: *Feynman diagrams for the radiative correction cross sections b), c), d) and e) contributing to the one-photon exchange cross section σ_0 depicted by diagram a).*

6.2.5 Results

After extracting the cross section by using the implicit weighing method, described above, and normalising to DIS rates, one obtains the cross section for each Q^2 and W bin, where the correction factors have to be applied by using

$$\sigma_{(\gamma^* p \to \rho^0 p)}(Q^2, W) = \sigma_{\mathrm{uncorrected},(\gamma^* p \to \rho^0 p)}(Q^2, W) \frac{1}{f_{t'}} f_{\Delta E} \frac{1}{f_{\mathrm{RC}}} \frac{1}{T_{^3\mathrm{He}}(Q^2, W)}. \tag{6.22}$$

In Fig. 6.12 is shown that the implicit and explicit weighing methods agree. Moreover, the use of the implicit weighing method is justified by the observed agreement of the various kinematic

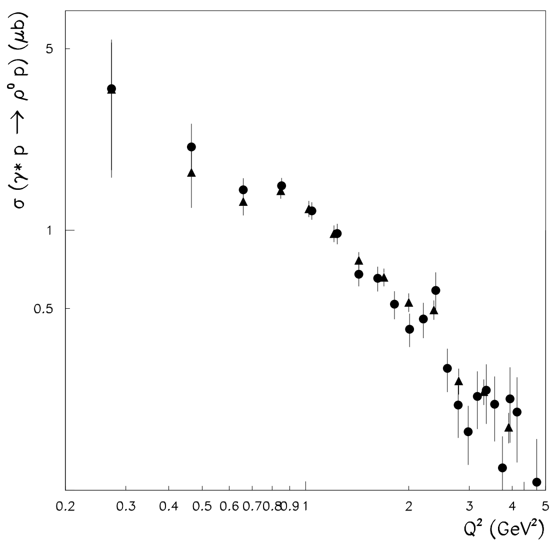

Figure 6.12: *The virtual photoproduction cross section for all W and with a fixed lower limit to $-t'$. Both the results obtained with the explicit weighing method (circles) and the implicit weighing method (triangles) are presented.*

distributions in the data sample compared to the accepted Monte Carlo sample as shown in Figs. 6.13 and 6.14.

The average values of Q^2, W or any other variable V in a certain bin are given by

$$< V >= \frac{\int_{\Delta Q^2, \Delta W} V \frac{d\sigma}{dQ^2 dW} dQ^2 dW}{\int_{\Delta Q^2, \Delta W} \frac{d\sigma}{dQ^2 dW} dQ^2 dW}. \tag{6.23}$$

In Tables 6.6 and 6.7 the final results for the virtual photoproduction ρ^0 cross section at HERMES are given for four Q^2 bins and 2 W bins and four Q^2 bins and 1 W bin respectively. In Fig. 6.15 the radiative corrected virtual photoproduction ρ^0 cross section versus Q^2 is shown for the two different W bins. In Fig. 6.16 the radiative corrected nuclear–transparency-corrected virtual photoproduction ρ^0 cross section versus Q^2 is shown for the two different W bins. The cross sections are fitted to the function

$$\sigma(Q^2) = \sigma(Q^2 = 0\,\mathrm{GeV}^2) \cdot \left(\frac{m_\rho^2}{Q^2 + m_\rho^2}\right)^2 \cdot (1 + \epsilon R_\rho), \tag{6.24}$$

where $R_\rho = \frac{\xi^2 Q^2}{m_\rho^2}$. Free parameters in this fit were $\sigma(Q^2 = 0\,\mathrm{GeV}^2)$ and ξ^2. We obtained $\sigma(Q^2 = 0\,\mathrm{GeV}^2) = 17.5 \pm 1.2\,\mu$b and $\xi^2 = -0.05 \pm 0.02$ (4 GeV $< W < 5.25$ GeV) and $\sigma(Q^2 = 0\,\mathrm{GeV}^2) = 11.4 \pm 1.6\,\mu$b and $\xi^2 = -0.09 \pm 0.04$ (5.25 GeV $< W < 6.5$ GeV). The χ^2/degrees of freedom was 0.8 for both fits. The E665 experiment obtained $\sigma(Q^2 = 0\,\mathrm{GeV}^2) = 10.3 \pm 0.3\,\mu$b and $\xi^2 = -0.04 \pm 0.02$ for $W \approx 15$ GeV (see Ref. [8]). Despite the excellent fit to the data, the slightly negative value for ξ^2 (and hence the slightly negative value for R_ρ) does not allow an interpretation of R_ρ as the ratio σ_L/σ_T.

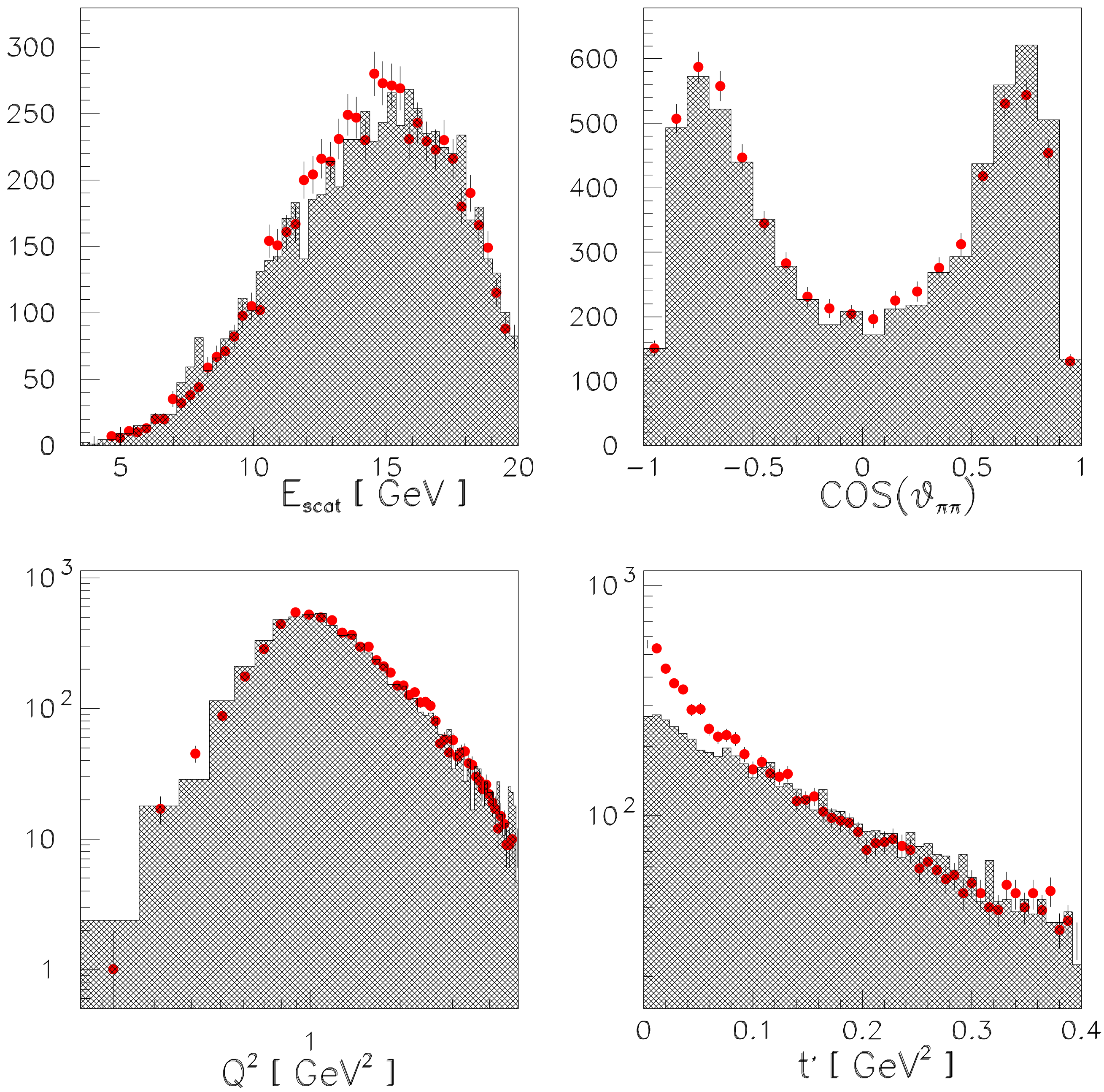

Figure 6.13: *Comparison of data (circles) and accepted Monte Carlo events (histogram) for distributions of scattered positron energy, decay angle $\cos\theta_{\pi\pi}$, virtual photon mass Q^2 and $-t'$. Note that the $-t'$ slope of the data has a coherent component for small $-t'$ which is not included in the Monte Carlo simulation.*

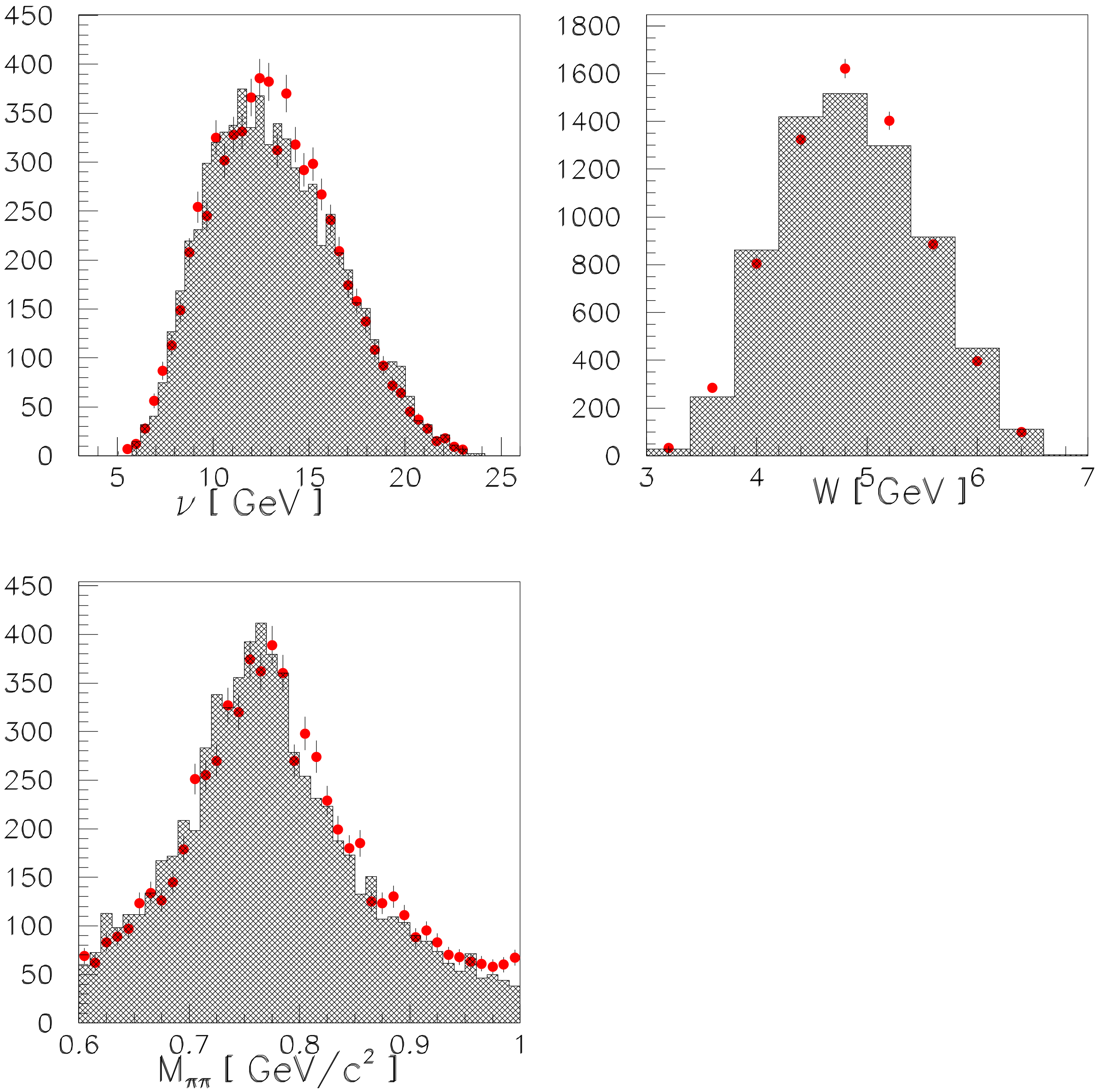

Figure 6.14: *Comparison of data (circles) and accepted Monte Carlo events (histogram) for distributions of virtual photon energy, hadron center of mass W and the invariant mass of the pion pair $M_{\pi\pi}$.*

Table 6.6: *The cross section $\sigma_{(\gamma^* p \to \rho^0 p)}(Q^2, W)$ for all Q^2 and W bins. For each Q^2 bin, the first, second and third row give, respectively, the uncorrected cross section, the cross section corrected for radiative effects, and the cross section additionally corrected for the nuclear transparency.*

comment	range in Q^2	$\sigma_{(\gamma^* p \to \rho^0 p)}(\mu\text{b})$			
	[GeV^2]	$< Q^2 >$ [GeV^2]	$4 < W < 5.25$ $< W >= 4.6$ [GeV]	$< Q^2 >$ [GeV^2]	$5.25 < W < 6.5$ $< W >= 5.8$ [GeV]
uncorrected	0.56 - 1.0	0.75	2.27 ± 0.19 μb	0.76	1.36 ± 0.19 μb
rad. corr.			2.77 ± 0.22 μb		1.66 ± 0.24 μb
rad. corr. and T_A corr.			3.26 ± 0.32 μb		2.00 ± 0.39 μb
uncorrected	1.0 - 1.78	1.33	1.01 ± 0.05 μb	1.33	0.59 ± 0.09 μb
rad. corr.			1.23 ± 0.07 μb		0.73 ± 0.11 μb
rad. corr. and T_A corr.			1.43 ± 0.12 μb		0.87 ± 0.15 μb
uncorrected	1.78 - 3.16	2.33	0.37 ± 0.03 μb	2.33	0.17 ± 0.04 μb
rad. corr.			0.46 ± 0.04 μb		0.20 ± 0.05 μb
rad. corr. and T_A corr.			0.51 ± 0.07 μb		0.24 ± 0.06 μb
uncorrected	3.16 - 5.62	4.05	0.15 ± 0.02 μb	4.37	0.07 ± 0.03 μb
rad. corr.			0.18 ± 0.02 μb		0.08 ± 0.03 μb
rad. corr. and T_A corr.			0.19 ± 0.03 μb		0.09 ± 0.03 μb

In Fig. 6.17 the virtual photoproduction ρ^0 cross section versus W is shown. In this figure, the E665 data are extrapolated to our Q^2 values. The measurements at E665 (see Ref. [8]), were carried out at $< Q^2 >= 0.61, 1.84$ and 5.69 GeV^2. Using Eqs. (2.63) and (2.64), the cross sections can be extrapolated to the HERMES values where $< Q^2 >= 0.75, 1.33, 2.32$ and 4.3 GeV^2. Their values for $\xi^2, < \epsilon >$ and $\sigma(Q^2 = 0\,\mathrm{GeV}^2)$ are taken from the fit by the E665 collaboration as reported in Ref. [8]. In Fig. 6.18 the cross section is shown for one W bin, with $4.75 < W < 6.5$ GeV.

6.2.6 Systematic Uncertainties

There are a number of sources of systematic uncertainties, which are itemised below.

The three main sources of systematic uncertainties are the background subtraction, the uncertainty in the description of the HERMES geometric acceptance by the Monte Carlo, and the acceptance correction itself. In the following, the cross section is calculated while varying

Table 6.7: *The cross section* $\sigma_{(\gamma^* p \to \rho^0 p)}(Q^2, W)$ *for all* Q^2 *bins and* $4.75 < W < 6.5$ *GeV. For each* Q^2 *bin, the first, second and third row give, respectively, the uncorrected cross section, the cross section corrected for radiative effects, and the cross section additionally corrected for the nuclear transparency.*

comment	range in Q^2	$\sigma_{(\gamma^* p \to \rho^0 p)}(\mu\text{b})$	
	[GeV^2]	$< Q^2 >$ [GeV^2]	$4.75 < W < 6.5$ $< W >= 5.625$ [GeV]
uncorrected	0.56 - 1.0	0.75	1.65 $\pm$ 0.14 μb
rad. corr.			2.01 $\pm$ 0.17 μb
rad. corr. and T_A corr.			2.40 $\pm$ 0.20 μb
uncorrected	1.0 - 1.78	1.33	0.80 $\pm$ 0.06 μb
rad. corr.			0.97 $\pm$ 0.07 μb
rad. corr. and T_A corr.			1.13 $\pm$ 0.10 μb
uncorrected	1.78 - 3.16	2.33	0.28 $\pm$ 0.03 μb
rad. corr.			0.34 $\pm$ 0.03 μb
rad. corr. and T_A corr.			0.39 $\pm$ 0.04 μb
uncorrected	3.16 - 5.62	4.25	0.12 $\pm$ 0.02 μb
rad. corr.			0.15 $\pm$ 0.02 μb
rad. corr. and T_A corr.			0.17 $\pm$ 0.03 μb

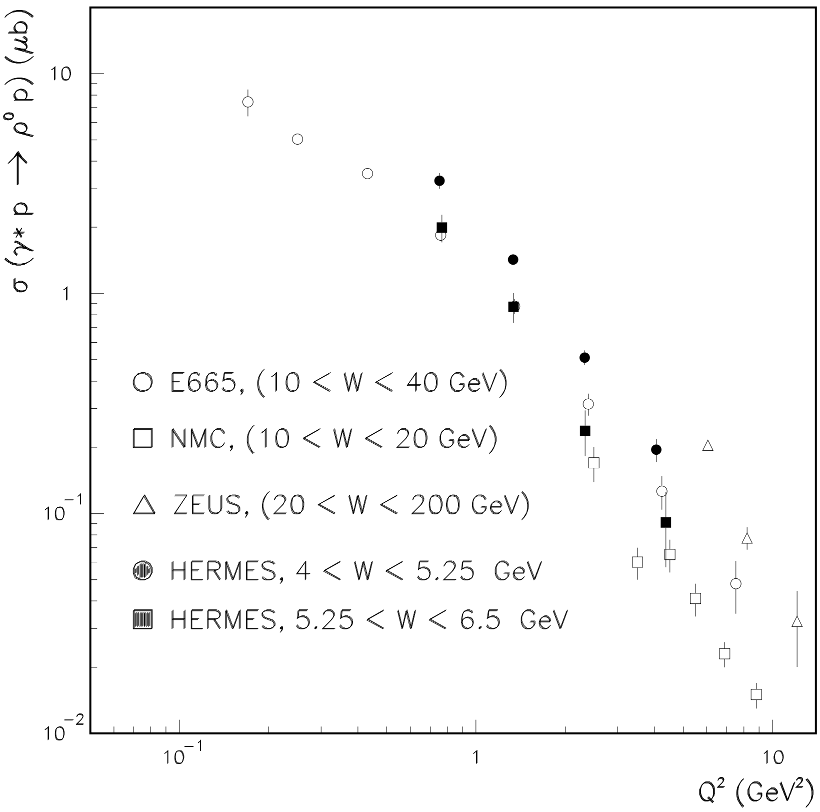

Figure 6.15: *The radiative corrected virtual photoproduction cross section for ρ^0 production versus Q^2 for $4 < W < 5.25$ GeV (circles) and $5.25 < W < 6.5$ GeV (squares).*

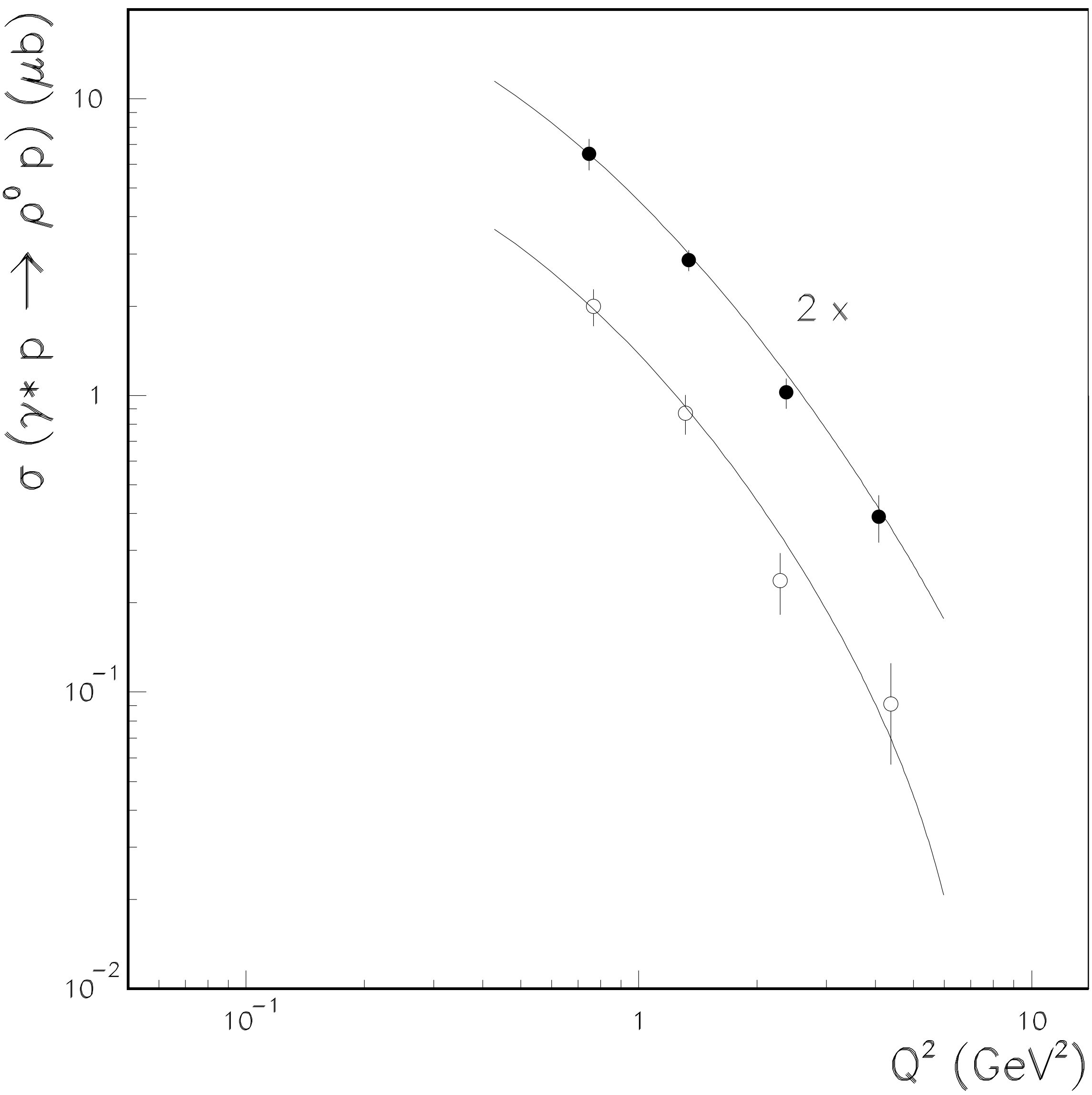

Figure 6.16: *The virtual photoproduction cross section for ρ^0 production versus Q^2 for $4 < W < 5.25$ GeV (top) and $5.25 < W < 6.5$ GeV (bottom). The data for $4 < W < 5.25$ GeV is artificially multiplied with a factor two for convenience. The data are corrected for radiative effects and losses due to nuclear transparency. The results were fitted with the function of Eq. (6.24). For the free parameters we obtained $\sigma(Q^2 = 0\,\mathrm{GeV}^2) = 20.8 \pm 2.5\,\mu\mathrm{b}$ and $\xi^2 = -0.07 \pm 0.03$ and $\sigma(Q^2 = 0\,\mathrm{GeV}^2) = 11.7 \pm 2.0\,\mu\mathrm{b}$ and $\xi^2 = -0.08 \pm 0.04$.*

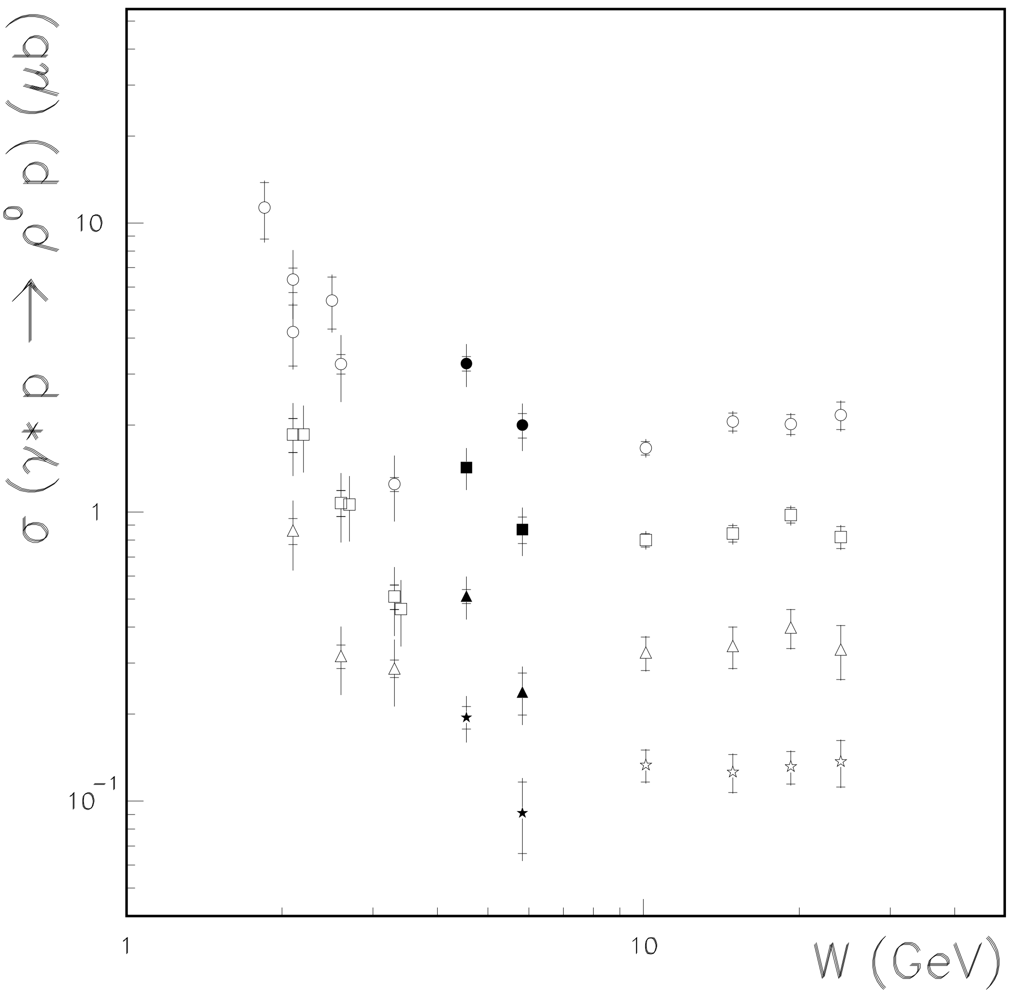

Figure 6.17: *The virtual photoproduction cross section for ρ^0 production versus W. The solid symbols represent the* HERMES *data. The solid circles, solid squares, solid triangles and solid stars denote* HERMES *data with an average Q^2 of 0.75 GeV^2, 1.33 GeV^2, 2.32 GeV^2, and 4.3 GeV^2, respectively. The open symbols on the left of the* HERMES *data represent data taken at* DESY *(see Ref. [80]) and data taken at* Cornell *(see Ref. [39]), extrapolated to the Q^2 values of* HERMES *as explained in the text on page 128. The open symbols on the right of the* HERMES *data represent measurements done by the* E665 *experiment (see Ref. [8]), extrapolated to the Q^2 values of* HERMES.

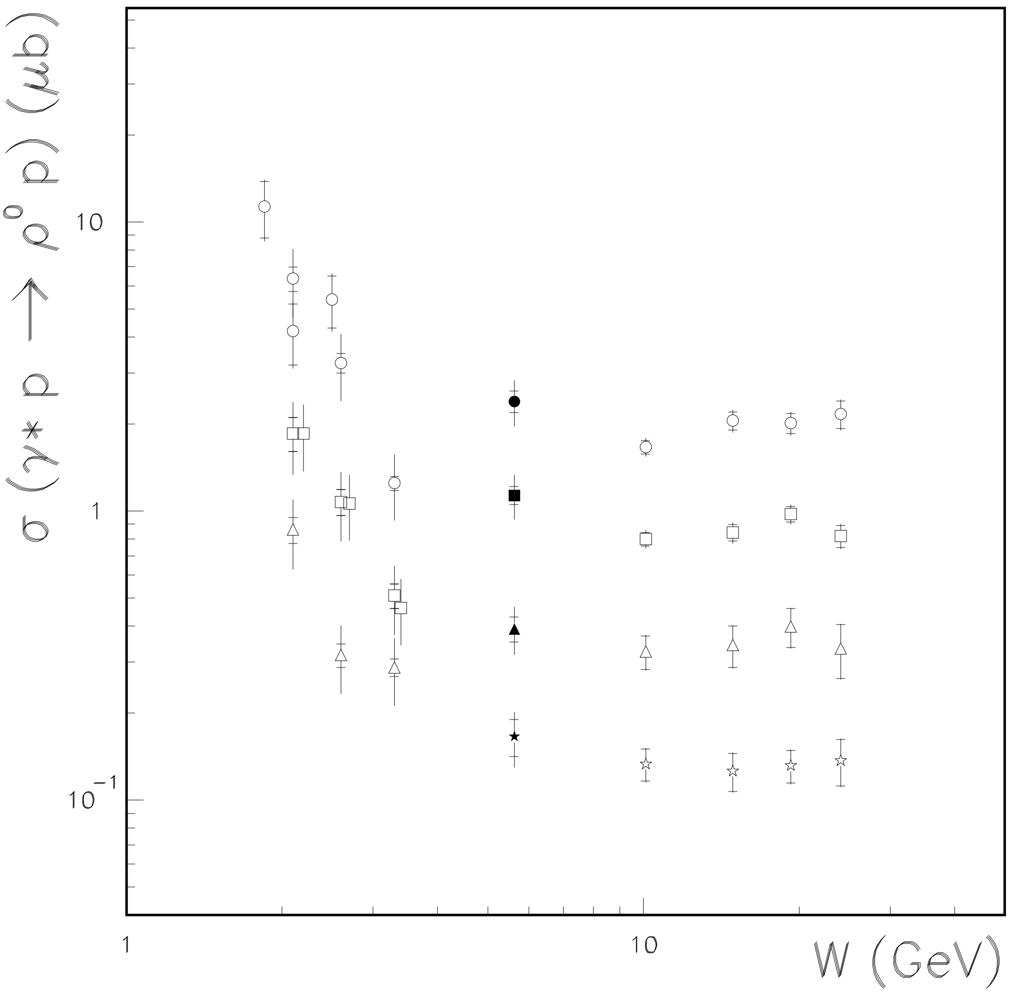

Figure 6.18: *The virtual photoproduction cross section for ρ^0 production versus W. The solid symbols combine the* HERMES *data in a single W bin for each Q^2 bin. See Fig. 6.17 for the explanation of all symbols.*

several of the analysis parameters. The systematic uncertainty $\zeta_{\rm syst}$ is then evaluated by using

$$\zeta_{\rm syst} = \frac{\sigma_{\rm alternative} - \sigma_{\rm default}}{\sigma_{\rm default}} = \frac{\delta_{\rm syst}}{\sigma_{\rm default}}, \tag{6.25}$$

where $\sigma_{\rm default}$ is the estimated cross section using the default analysis and $\sigma_{\rm alternative}$ is the estimated cross section using alternative analysis parameters. This method may lead to an overestimate of the systematic uncertainty, because statistical fluctuations enter the variation of the cross section as well. In Table 6.9 the main contributions to the systematic uncertainties are shown. The statistical uncertainty $\zeta_{\rm stat}$ defined by

$$\zeta_{\rm stat} = \frac{\delta_{\rm stat}}{\sigma_{\rm default}}, \tag{6.26}$$

where $\delta_{\rm stat}$ is the statistical error on the estimated cross section, is included to show the statistical accuracy of the evaluation of the systematic uncertainty as depicted in Fig. 6.19.

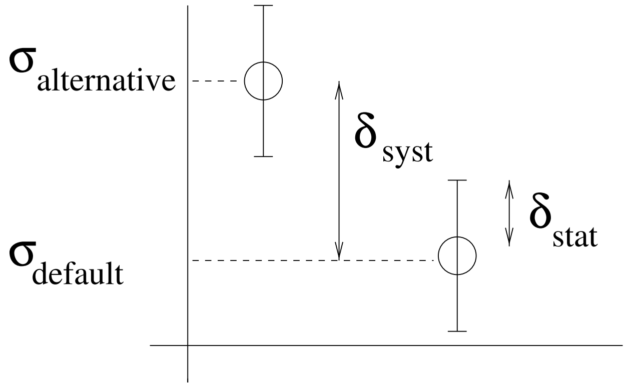

Figure 6.19: *Depiction of systematic and statistical errors $\delta_{\rm syst}$ and $\delta_{\rm stat}$, as defined in Eqs. (6.25) and (6.26).*

- **Background Subtraction**
  The background subtraction hinges on the assumption that the shape of the ΔE distribution of DIS events does not depend on $-t'$, i.e. that the ratio of DIS events in region I to region II equals the ratio of DIS events in region III to region IV. This assumption is not completely valid and this will introduce a contribution to the systematic uncertainty. Convoluted in this contribution is the systematic uncertainty due to the assumption that the ρ^0 peak in the ΔE distribution is Gaussian. This contribution to the systematic uncertainty was estimated by varying the sizes of the various regions I, II, III and IV, while observing the effect on the final result. Region I and IV where divided in subregions A ($-2 < \Delta E < 0.1$ GeV) and B ($0.1 < \Delta E < 0.6$ GeV). For both subregions, the cross sections were calculated and corrected for the amount of data cut away by using the additionally estimated values for $f_{\Delta E;\, A/B}$ so that these cross sections could be compared to the result of the standard analysis.

- **Geometric Acceptance**
  The quality of our analysis largely depends on the accuracy of the Monte Carlo description of the HERMES geometry. When the uncertainty in this description is known, it can be used to estimate the corresponding systematic uncertainty. Analysis of the alignment of the detectors indicated an uncertainty in the alignment of the bottom half of the spectrometer of about 1.8 mrad. The cross section was calculated twice where the geometric description of the bottom detector was shifted by 1.8 mrad both towards and away from the beam. All the usual cuts of the standard analysis are applied to these samples too, including the lower cut on the opening angle $\|\theta\| < 40$ mrad. Hence, from the sample where the detector is moved towards the beampipe, effectively more events are cut away and the deviation from the standard result will be large. The effect of moving the detector further away from the beampipe is small.

- **Acceptance Correction**
  One can split up the data in two subsamples. The difference between these subsamples should not be Q^2 or W dependent, to avoid a bias and overestimate of the systematic uncertainty. These subsamples should be chosen in such a way that they only differ in a certain geometrical variable which does not depend on Q^2 or W. To estimate the systematic uncertainty due to the acceptance correction, we investigated the variation of the cross section when selecting events only with $\cos\theta_{\pi\pi} < 0$ or with $\cos\theta_{\pi\pi} > 0$. Here, $\cos\theta_{\pi\pi}$ is calculated in the hadron center of mass frame, as explained in further detail in section 6.3. The spectrum of events versus $\cos\theta_{\pi\pi}$ is symmetrical with respect to $\cos\theta_{\pi\pi} = 0$.

- **Double Dissociative Diffraction**
  In Fig. 6.20 single and double dissociative diffractive ρ^0 production is depicted. As it is only the single dissociative signal we are interested in, we need to correct for the double dissociative background. The amount of this background depends on the resolution of the experiment, i.e. how well we can, by using ΔE, distinguish an event in which the nucleon did not break up from one in which it did.

  It has been found that the contamination of the double diffractive dissociation in electroproduction of the ρ^0 particle at large Q^2 can be as large as ~ 20 % (see Ref. [75]). This means that the HERMES results presented here might be an overestimate of the actual cross section.

  Measurements of diffractive pp scattering have suggested that the shape of the double dissociative background could be described by (see Ref. [8])

$$\frac{d\sigma}{dM_x^2} = \begin{cases} c\frac{M_x^2-(M_p+m_\pi)^2}{1.8\mathrm{GeV}^2-(M_p+m_\pi)^2} & M_x^2 < 1.8\mathrm{GeV}^2 \\ c & M_x^2 \geq 1.8\mathrm{GeV}^2, \end{cases} \tag{6.27}$$

  where c is a constant. This leads to a ΔE spectrum as shown in Fig. 6.21. The distribution of ΔE in a diffractive process should be independent of the type of scattering particle.

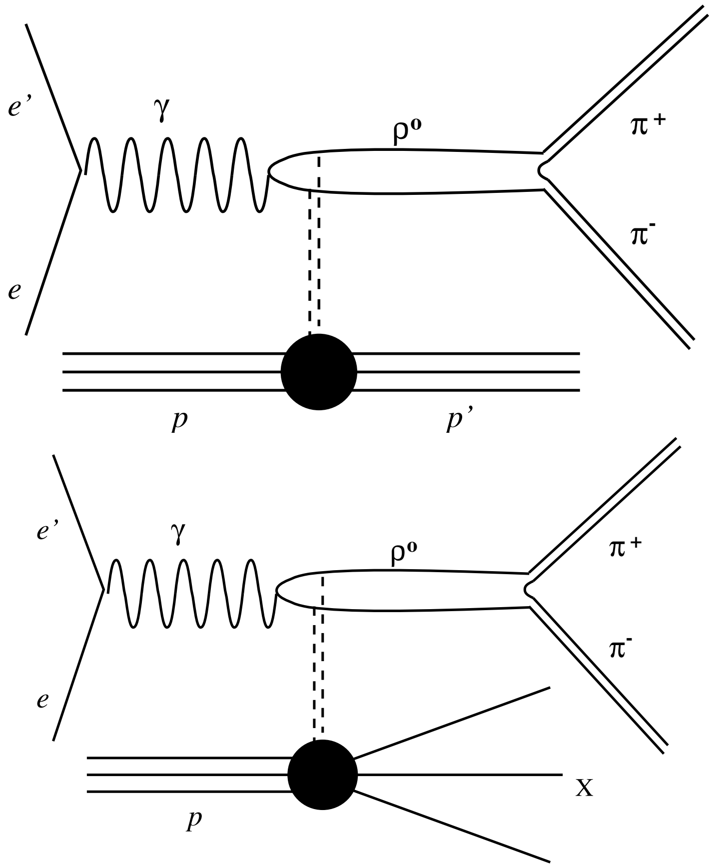

Figure 6.20: *Schematic representation of single (top) and double (bottom) dissociative diffractive ρ^0 production.*

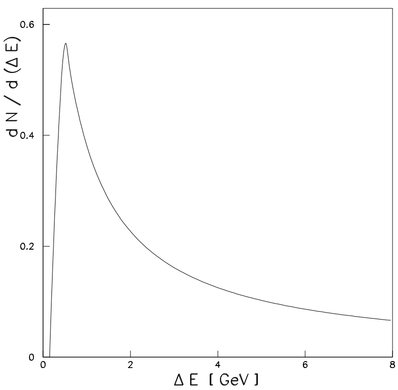

Figure 6.21: *Spectrum of double dissociative background versus ΔE.*

Estimates for the double dissociative contamination quoted in Ref. [8], are of the order of 20 % up to 37 %. However, the resolution at the E665 measurement is worse than at HERMES. In Fig. 6.22 one can see, respectively, the parametrisations of E665 data and HERMES data versus ΔE. For both spectra, the assumed shape for the double dissociative contamination is shown as well, assuming a contamination of 37 % to the data sample. From Fig. 6.22 it can be seen that the E665 resolution in ΔE does not allow the cut, $\Delta E < 0.6$ GeV whereas at HERMES this cut can be made. After applying this cut, the ratio of selected double dissociative events to all selected events varies from 2.7 % to 5.3 %, assuming a total contamination of 20 % and 37 % respectively. One should note that here a 100 % detector acceptance is assumed. A realistic simulation of the detector acceptance would further decrease the contamination of double dissociative background events.

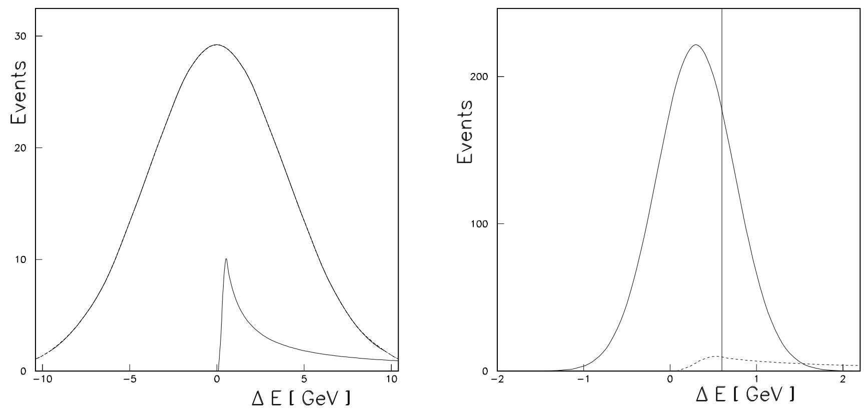

Figure 6.22: *Representation of* E665*(left) and* HERMES*(right) data versus ΔE. The dotted curves indicate the double dissociative background. The vertical line in the right hand plot represents the $\Delta E < 0.6$ GeV cut.*

In the future, the double dissociative background should be estimated more precisely by doing a thorough Monte Carlo study. For now, instead of subtracting the double dissociative background, its contribution to the systematic uncertainty is taken into account. This contribution is estimated to be at maximum 5 %, as explained above.

- **Correction Factors**
  In addition, the correction factors are a source of systematic uncertainties.
  - $f_{t'}$**:** the values for B_{coh} and B_{inc} obtained from the fit have an uncertainty. Using the extreme values for these variables, one can refit the $-t'$ spectrum for the three Q^2 ranges. This will result in different values for $\sigma_{coh}/\sigma_{incoh}$. Keeping the values for t_{lowcut} fixed at the originally obtained values, one obtains an estimate for the variation for the correction factor $f_t = 1.03$.

An additional systematic uncertainty is introduced by the relatively wide Q^2 ranges. This uncertainty is determined by the difference of f_t between two neighbouring ranges.
The total systematic uncertainty is estimated to be 1.5%.

- **ΔE:** the fitted values of the parameters from the Gaussian distribution function over the exclusive ΔE peak have an uncertainty. One can obtain the spread in $f_{\Delta E}$ by determining the number of events for the Gaussian function by using the limiting values for the fit parameters.

- **$T_{^3\mathrm{He}}(Q^2, W)$:** the correction for losses due to nuclear transparency have to be taken into account.

- **f_{RC}:** there is a systematic uncertainty in the correction for radiative effects.

Table 6.8 summarises the contributions of the correction factors to the total systematic uncertainty.

Table 6.8: *Overview of systematic uncertainties for the virtual photoproduction cross section due to the uncertainties in the various correction factors.*

Ingredient	Denoted As	Value	Variation
Coherent Contamination Correction	$f_{t'}$	1.03	1.5 %
Delta E Cut loss	$f_{\Delta E}$	0.93	1 %
Nuclear Transparency	$T_{^3\mathrm{He}}$		6 %
Radiative Correction	f_{RC}	0.80	1.5 %
Total			8 %

The various contributions to the total systematic uncertainty are summarised in Table 6.9.

6.2.7 Q^2 Dependence of the Cross Section

VMD Predictions for Q^2 Dependence

The fit to the cross section versus Q^2 as discussed on page 125 showed that the shape of the Q^2 dependence, as predicted by the VMD model, given in Eq. (6.24) describes the data well. However, the slightly negative value obtained for the free fit parameter ξ (and hence for R_ρ) shows that R_ρ from this fit cannot be interpreted as the ratio σ_L/σ_T. To obtain the ratio $R_\rho = \sigma_L/\sigma_T$ the results of the analysis of the angular distributions are used, as explained in the second half of this chapter.

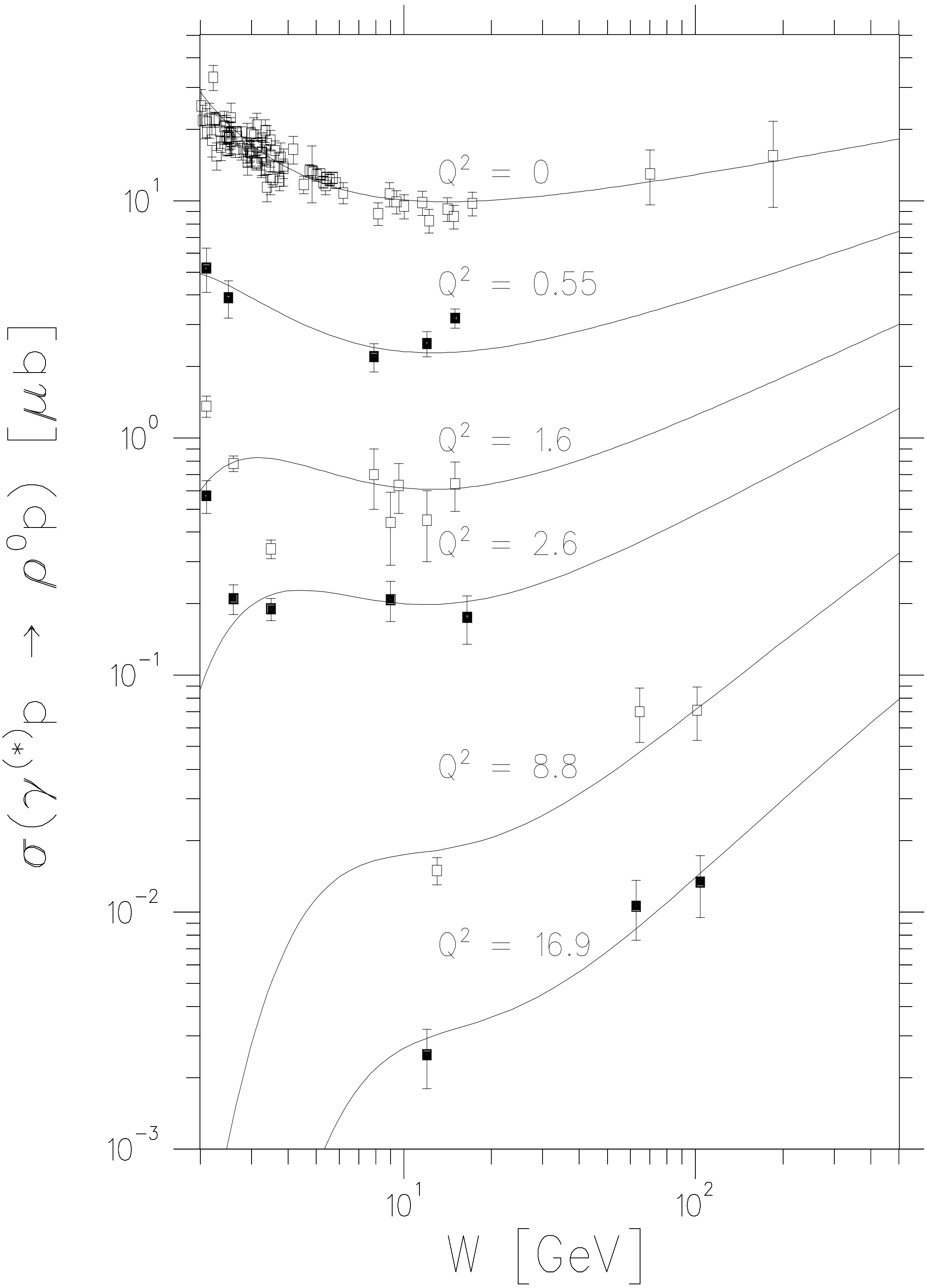

Figure 6.23: *The virtual photoproduction ρ^0 cross sections for several values of Q^2 in GeV^2. The* HERMES *data are not included. The curves are predictions from Ref. [70] from which this plot was taken.*

Table 6.9: *The main contributions to the systematic uncertainties. The significance of the statistical uncertainty is explained in the text.*

contribution	systematic uncertainty	statistical uncertainty
$4 < W < 5.25$ GeV		
geometry	– 0.7 % ; + 10 %	± 3 %
acc. corr.	– 4 % ; + 4 %	± 6 %
backg. subtr.	– 5 % ; + 10 %	± 6 %
double diss.	±5 %	
corr. factors	±6 %	
total	– 10 % ; + 17 %	
$5.25 < W < 6.5$ GeV		
geometry	– 0.7 % ; + 10 %	± 4 %
acc. corr.	– 10 % ; + 10 %	± 7 %
backg. subtr.	– 8 % ; + 12 %	± 7 %
double diss.	±5 %	
corr. factors	±6 %	
total	– 15 % ; + 20 %	

6.2.8 W Dependence of the Cross Section

Looking at the world data (see Figs. 6.17 and 6.23) we observe, starting from low W and going to higher values for W, for the cross section

- $2 < W < 4$ GeV: decrease with W at least for $Q^2 < 4$ GeV^2.
- $4 < W < 7$ GeV: a region covered by the HERMES kinematics.
- $9 < W < 19$ GeV: no significant dependence on W. This is the region covered by the E665 kinematics.
- $20 < W < 200$ GeV: slow increase with W. This is where ZEUS and H1 data are available.

The HERMES kinematics cover a region in Q^2 and W where no other experiments have measured before. Figs. 6.17 and 6.18 show at lower values of W, the measurements performed at Cornell (see Ref. [39]) and, at lowest Q^2, at DESY (see Ref. [80]) and at higher values of W the measurement performed by the E665 collaboration. Whereas the HERMES data for our highest W bin, with $5.25 < W < 6.5$ GeV, agree with the E665 data within the error, indicating no W dependence of the cross section in this kinematical region, our data in our lowest W bin, with $4 < W < 5.25$ GeV disagree with the highest W data points of the measurement performed at Cornell.

Although the agreement between data and Monte Carlo in Fig. 6.14 is reasonable, the observed W dependence is stronger than simulated by the Monte Carlo generator. This W dependence can be expressed by the ratio $r(W) = N_{\text{events}}(W\,\text{bin1})/N_{\text{events}}(W\,\text{bin2})$.
For the generated cross section $\sigma_{\text{generated}}$, the ratio is $r = 1.11$. Systematic effects which potentially could give rise to an artificial dependence in W, with $r_{\text{data}}(W) > r_{\text{accepted}}(W)$, were studied. Defining $R_W = r_{\text{data}}/r_{\text{accepted}}$, Table 6.10 summarises the systematic deviations of R_W due to various sources. Clearly, these ingredients are not enough to explain the observed $R_W \sim 2$.

For the background subtraction, we already showed the point-to-point systematic uncertainty. This could give rise to an artificial W dependence of 15 %. The variation in R_W due to varying the fiducial cuts (e.g. the cut on the y projection of the opening angle θ_y) is of the order of 10 % and reflects the systematic uncertainty in geometric acceptance. Instead of estimating the lower cut on $-t'$ for different Q^2 bins, it can be estimated as a function of W. This influences the result by about 3 %.

The last entry in Table 6.10, "Acceptance in W", denotes the effect of binning the data in two W bins with $4.5 < W < 5.25$ GeV and $5.25 < W < 6$ GeV instead of $4 < W < 5.25$ GeV and $5.25 < W < 6$ GeV. This was done to avoid possible acceptance effects at the edges of the HERMES acceptance. The effect, however, is small, which can also be seen from Fig. 6.24 which shows the data for all Q^2, and four different W bins, $4 < W < 4.625$ GeV, $4.625 < W < 5.25$ GeV, $5.25 < W < 5.875$ GeV and $5.875 < W < 6.5$ GeV. Clearly, the observed W dependence is not limited to the outer bins in W.

Since the observed W dependence cannot be explained by the systematic uncertainties of the analysis, we conclude that this W dependence is not an artefact[1].

Table 6.10: *Potential sources of an artificial W dependence of the cross section.*

	δR_W
Background subtraction	15 %
Fiducial cuts	10 %
Lower $-t'$ cut	3 %
Acceptance in W	3 %

A Parametrisation from Ref. [70]

On page 31 and beyond, the vector meson dominance model was discussed, using the Regge model to explain the s and t dependence of the cross section. In Refs. [70, 71], a model for the parameters used in Eq.(2.71) is given.

[1] Items to be investigated in the future include both the use of a different Monte Carlo generator in an attempt to simulate a stronger W dependence and the use of the Monte Carlo program for the background subtraction.

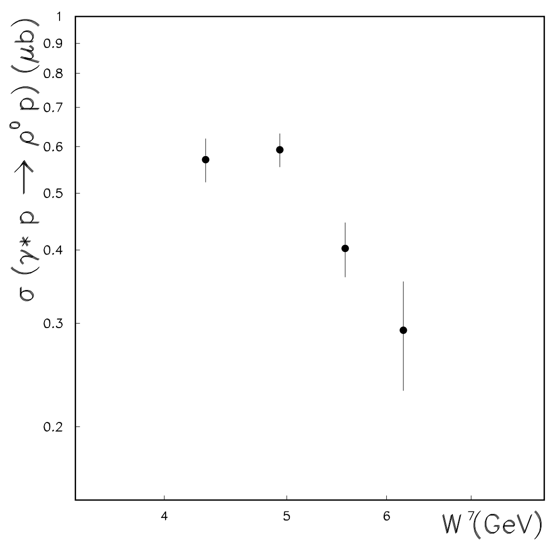

Figure 6.24: *The virtual photoproduction cross section for ρ^0 production versus W with $4 < W < 6.5$ GeV with four bins in W combined for all Q^2.*

For the Pomeron part of the cross section, the following is derived. After integrating Eq. (2.66) over t, one obtains

$$\sigma_{\mathbb{P}}(s) \sim \frac{(s)^{2(\alpha_{\mathbb{P}}(0)-1)}}{2b_0 + 2\alpha'_{\mathbb{P}} \ln(s/s_0)}, \tag{6.28}$$

with the Mandelstam variable $s = W^2$. Here, b_0 is written as R^2, with $R^2 = R_p^2 + R_\rho^2(Q^2)$, where

$$\begin{aligned} R_\rho^2 &= \frac{R_{0\rho}^2 m_\rho^2}{m_\rho^2 + Q^2}, \\ R_p^2 &= 2\,\mathrm{GeV}^{-2}, \\ R_{0\rho}^2 &= 1\,\mathrm{GeV}^{-2}. \end{aligned} \tag{6.29}$$

In Refs. [70, 71] the intercept $\alpha(0)$ is written as a function of Q^2, with

$$\frac{d\sigma_{\mathbb{P}}}{dt} = \mathcal{F}(Q^2, m_V^2) \left(\frac{s}{s_0}\right)^{2\Delta_{\mathbb{P}}(Q^2)} \exp(\Lambda(s)t), \tag{6.30}$$

where $\mathcal{F}(Q^2, m_V^2)$ is a priori unknown and can be obtained by fitting to the ZEUS data and

$$\Lambda(s) = 2\left(b_0 + \alpha' \log(\frac{s}{s_0})\right). \tag{6.31}$$

Here, $\Delta(Q^2)$ is written as

$$\Delta(Q^2) = \Delta(0)\left(1 + d_0 \frac{Q^2}{Q^2 + d_1}\right), \tag{6.32}$$

where the parameters d_0, d_1 and $\Delta(0)$ have to be fitted to the data. For s_0 is chosen $s_0 = m_\rho^2 + Q^2$ which is allowed because the function $\mathcal{F}(Q^2, m_V^2)$ is fitted to the data for each Q^2 bin separately.

After integrating Eq. (6.30) over t, one obtains

$$\sigma_{\mathbb{P}} \sim \frac{1}{\Lambda(s)}\left(\frac{s}{s_0}\right)^{2\Delta_{\mathbb{P}}(Q^2)}. \tag{6.33}$$

The dependence of the Pomeron intercept $\alpha_{\mathbb{P}}$ on Q^2 is explained by the amount of Pomerons which are exchanged. At higher Q^2, multiple Pomeron exchange has to be taken into account. Whereas at lower virtuality these single contributions cannot be distinguished, at higher Q^2 they can. This has its analogy in DIS events, where at higher Q^2 one probes the inner structure of the nucleon with higher resolution.

For the total ρ^0 production cross section, taking both the Reggeon and Pomeron contributions into account, one obtains

$$\sigma_{\gamma^* p \to \rho^0 p} \sim f(Q^2, s)\frac{1}{\Lambda(s)}\left(A_{\mathbb{R}}\left(\frac{s}{s_0}\right)^{\Delta_{\mathbb{R}}} + A_{\mathbb{P}}\left(\frac{s}{s_0}\right)^{\Delta_{\mathbb{P}}}\right)^2. \tag{6.34}$$

In Fig. 6.25 the predictions for the W and Q^2 dependence of the shapes of the curves are compared with the HERMES and extrapolated E665 data for the four different Q^2 bins.

For all Q^2 bins, the curves were normalised to the data separately. Here, the additional Q^2 dependent term $(m_\rho^2/(Q^2+m_\rho^2))^2$ was used, taken from the VMD model. This term $(m_\rho^2/(Q^2+m_\rho^2))^2$ does not account for all Q^2 dependent effects. The ratios of the normalisation factors for the higher Q^2 bins to the normalisation factor for the lowest Q^2 bin, were $0.6, 0.4$ and 0.4 for $< Q^2 >= 1.33,\ 2.33$ and 4.3 GeV^2 respectively.

For all data, the systematic uncertainties were included in the fit. Systematic uncertainties of 10 %, 25 % and 5 % were taken for the DESY data (see Ref. [80]), the Cornell data (see Ref. [39]) and the E665 data (see Ref. [8]), respectively.

A Naive Parametrisation

Inspired by the above, a naive fitting function was used to fit the data versus W for the lowest Q^2 bin,

$$\sigma(Q^2, W) = \left(\frac{m_\rho^2}{Q^2 + m_\rho^2}\right)^2 \left(A_1\left(\frac{s}{s_0}\right)^{\Delta_1} + A_2\left(\frac{s}{s_0}\right)^{\Delta_2}\right)^2. \tag{6.35}$$

The result of the fit to the data obtained at $Q^2 = 0.75$ GeV^2 is shown in the top left plot in Fig. 6.26. The results for the fitting parameters are

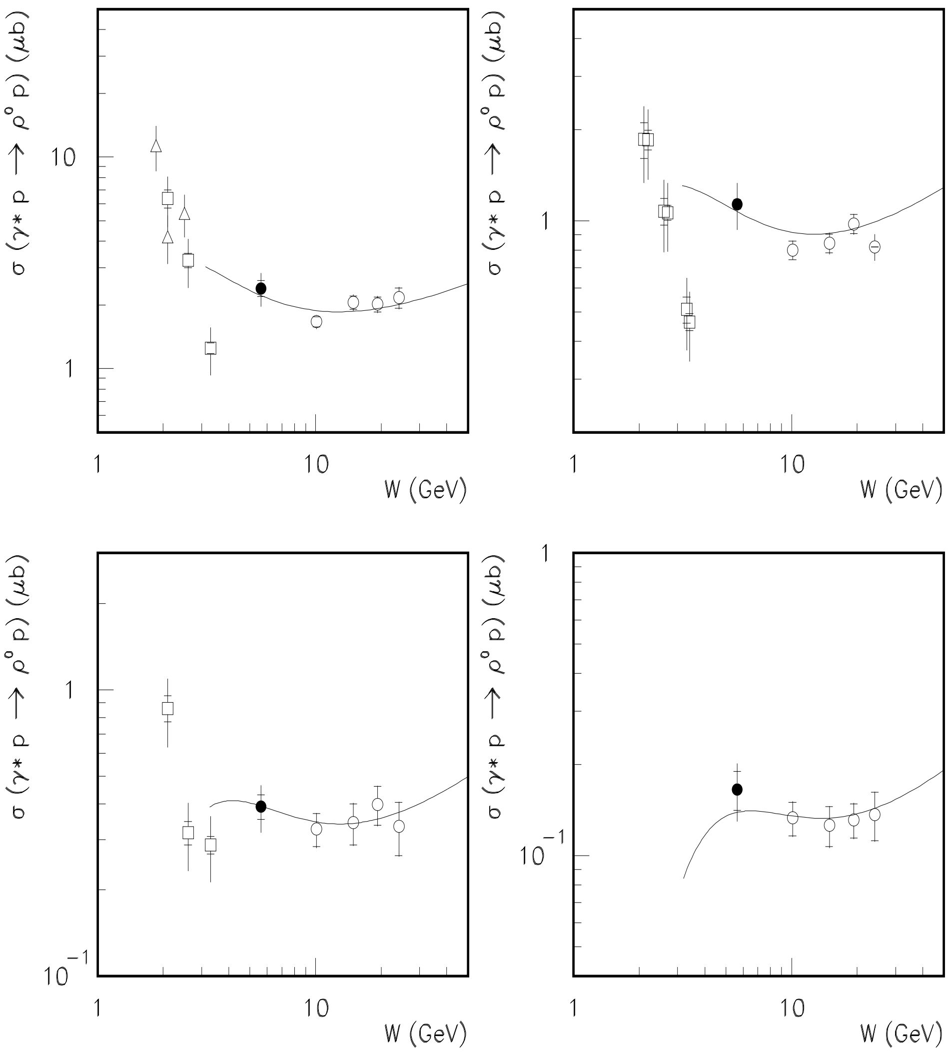

Figure 6.25: *The top left plot shows, with increasing W,* DESY *(open triangles),* Cornell *(open squares),* HERMES *(filled circles) and* E665 *(open circles) data with $Q^2 = 0.75$ GeV^2 for the ρ^0 production cross section versus W. The three other plots show the* Cornell *(open squares),* HERMES *(filled circles) and* E665 *(open circles) data with $Q^2 = 1.33$ (top right), $Q^2 = 2.33$ (bottom left) and $Q^2 = 4.3$ (bottom right) GeV^2. The data are compared to predictions of the parametrisation from Ref. [70, 71].*

$A_1 = 16.4 \pm 2.0$,
$A_2 = 1.3 \pm 0.2$,
$\Delta_1 = -0.90 \pm 0.14$ and
$\Delta_2 = 0.15 \pm 0.08$
with $\chi^2 = 1.7$.

The world data on the intercepts give $\Delta_{\mathbb{P}}(0) = 0.08$ and $\Delta_{\mathbb{R}}(0) = -0.5$. Clearly, this model is too naive to yield reliable results for the intercepts. Nevertheless, it shows how the superposition of two contributions with different intercepts of their Regge trajectories fits the data in the transition region of W. In Fig. 6.26, the top right plot shows the data with $Q^2 = 1.33$ GeV^2, the bottom left plot shows the data with $Q^2 = 2.33$ GeV^2 and the bottom right plot shows the data with $Q^2 = 4.3$ GeV^2. Here, the curves are obtained by using Eq. (6.35) where all parameters are taken from the fit to the data with $Q^2 = 0.75$ GeV^2. Clearly, the $(m_\rho^2/(Q^2 + m_\rho^2))^2$ factor alone cannot account for all Q^2 dependence. When one would fit the curves to the data, keeping all parameters at their fixed values and introducing an additional normalisation constant C to account for additional Q^2 dependent effects, one obtains
$C = 0.95 \pm 0.05$ for $Q^2 = 1.33$ GeV^2 ($\chi^2 = 0.6$),
$C = 0.78 \pm 0.07$ for $Q^2 = 2.33$ GeV^2 ($\chi^2 = 1.7$) and
$C = 0.67 \pm 0.05$ for $Q^2 = 4.3$ GeV^2 ($\chi^2 = 6.2$).

A pQCD Based Model from Ref. [120]

In Ref. [120] results of calculations have been presented using a pQCD based model to describe the longitudinal part of the ρ^0 production cross section. In this model, so-called off-forward parton distributions are derived which were assumed to be a product of DIS parton distributions and an elastic form factor [119]. In Refs. [41, 107] these distributions are referred to as off-diagonal parton distributions and non-forward parton distributions. Off-forward parton distributions can be interpreted as generalised standard parton distributions. The basic difference is in the treatment of the momenta of the incoming and outcoming parton.

The calculations for this model can only be done for the longitudinal part of the ρ^0 production cross section. The transverse part of the ρ^0 production cross section cannot be calculated due to additional terms in its amplitude which do not converge [41]. To extract the longitudinal part of the cross section we use the results of the analysis of the angular distributions for $R_\rho(Q^2)$ since we have seen that a fit to the Q^2 dependence of the cross section as predicted by the VMD model does not give a physical result for R_ρ. This theoretical model can only be used for high Q^2 values, with $Q^2 > 4$ GeV^2.

The analysis of the angular distributions is explained in detail on the following pages. On page 155 we find the expression $R_\rho = c_0 \cdot (Q^2/m_\rho^2)^{c_1}$ with $c_0 = 0.33$ and $c_1 = 0.62$ leading to $R_\rho(Q^2 = 4.3\,\mathrm{GeV}^2) = 1.127$. Hence, we can extract σ_L from our data using

$$\sigma_L = \frac{R_\rho}{1 + \epsilon R_\rho} \sigma_{tot}, \tag{6.36}$$

with $\epsilon = 0.78$ for our highest Q^2 bin. Also for the four E665 data points, extrapolated to $Q^2 = 4.3$ GeV^2, σ_L can be extracted using the same value for R_ρ and an average ϵ retrieved

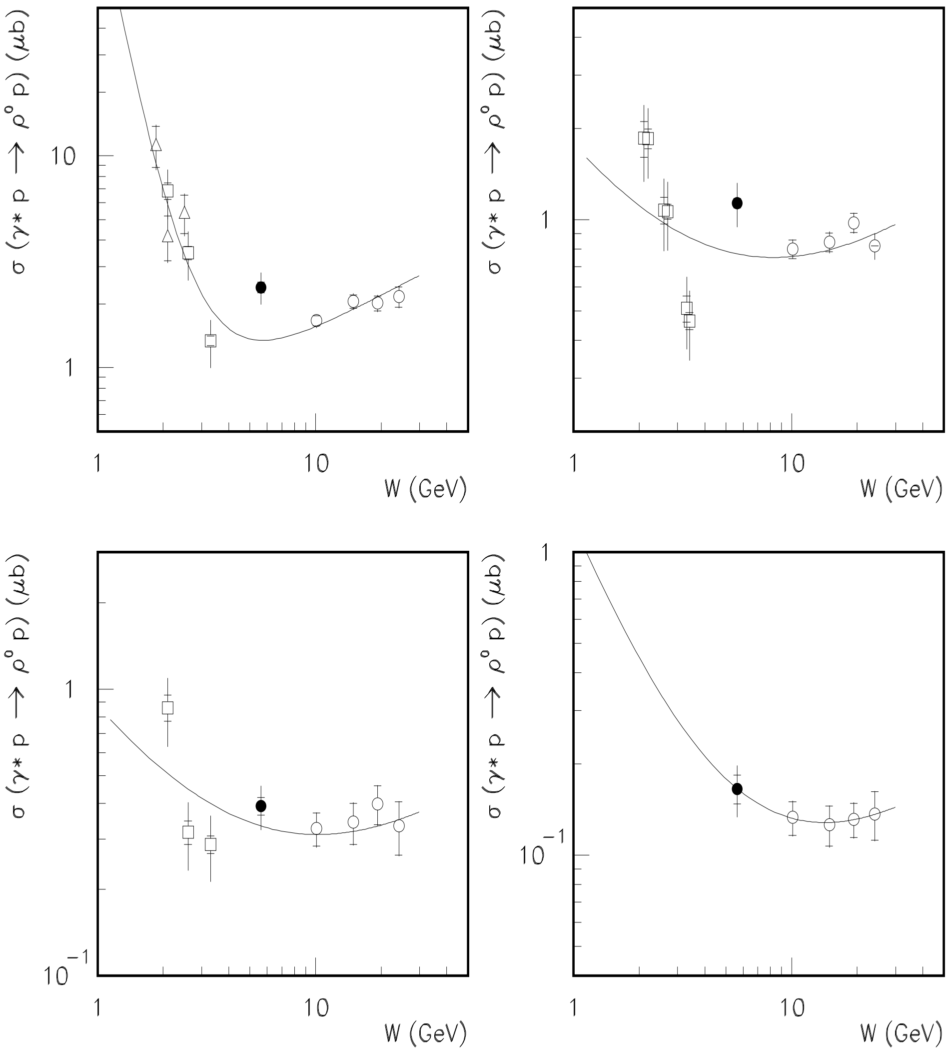

Figure 6.26: *The top left plot shows, with increasing W,* DESY *(open triangles),* Cornell *(open squares),* HERMES *(filled circles) and* E665 *(open circles) data with $Q^2 = 0.75$ GeV^2 for the ρ^0 production cross section versus W compared to the fitting function given by Eq. (6.35). The three other plots show the* Cornell *(open squares),* HERMES *(filled circles) and* E665 *(open circles) data with $Q^2 = 1.33$ (top right), $Q^2 = 2.33$ (bottom left) and $Q^2 = 4.3$ (bottom right) GeV^2. Here, for the curves the fitting results for the data with $Q^2 = 0.75$ GeV^2 are used and the curves are corrected for Q^2 dependent effects using the usual $(m_\rho^2/(Q^2 + m_\rho^2))^2$ propagator.*

from Ref. [8]. Fig. 6.27 shows the prediction and the (extrapolated) data of HERMES and E665 for $Q^2 = 4.3$ GeV^2 versus W.

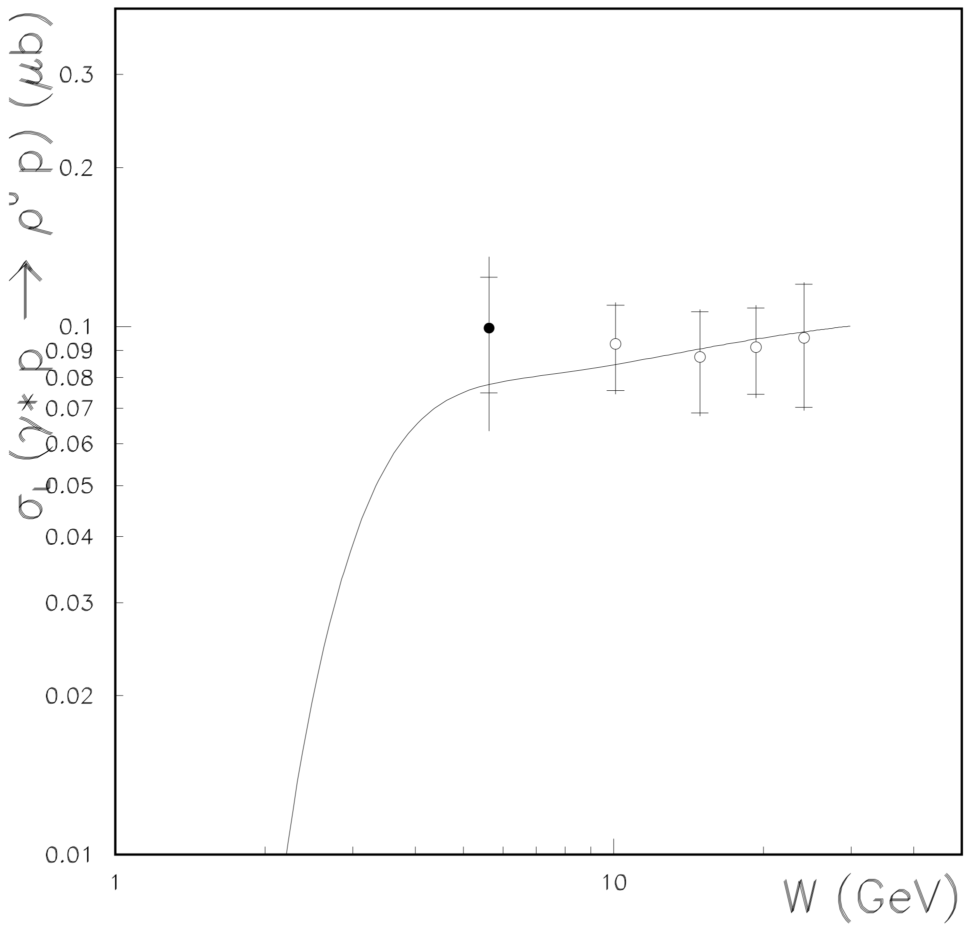

Figure 6.27: HERMES *(solid circles) and* E665 *(open circles) data for the longitudinal part of the ρ^0 production cross section versus W for $Q^2 = 4.3$ GeV^2, compared to a prediction of the pQCD based model from Ref. [120]. Low W data (see Fig. 6.23) shows that the model clearly fails for $W < 4$ GeV.*

6.3 Angular Distributions

6.3.1 Data Selection

Significant effort was devoted to the extraction of angular distributions, of which the main results are presented in Ref. [27]. The kinematical cuts for this analysis were as follows

$$\begin{aligned}
&W > 3.8\,\mathrm{GeV}, \\
&Q^2 > 0.5\,\mathrm{GeV}^2, \\
&y > 0.85, \\
&\theta_e > 40\,\mathrm{mrad}, \\
&p_h > 1\,\mathrm{GeV}, \\
&-t' < 0.5\,\mathrm{GeV}^2, \\
&|\Delta E| < 0.7\,\mathrm{GeV}/c^2, \text{ and} \\
&0.63 < M_{\pi\pi} < 0.91\,\mathrm{GeV}/c^2.
\end{aligned}$$

Subsequently, from this set of data, the azimuthal angle Φ_{ee}, which is the angle between the scattering plane and the production plane in the γ-nucleon center-of-mass system, and the polar decay angles $\theta_{\pi\pi}$ and $\phi_{\pi\pi}$ in the ρ^0 rest frame, with the azimuthal angle defined relative to the electron scattering plane, can be extracted. Under the assumption of s-channel helicity conservation, the angle $\Psi = \phi_{\pi\pi} - \Phi_{ee}$ can be defined. After background subtraction, the data were fitted with the functions given in Eqs. (2.117) and (2.121).

6.3.2 Acceptance Correction

Since the HERMES spectrometer has a limited acceptance, the measured angular distributions have to be corrected for this. During the analysis of the angular distributions, three different methods were examined to correct for the limited acceptance. For the angular distributions, the acceptance correction is more complicated than for the extraction of the cross section, because of the correlations between the angles.

1. Divide By Acceptance

A model is used for the cross section in order to generate the shapes for the various angular distributions in the Monte Carlo sample. The distribution for the angle α (i.e. $\theta_{\pi\pi}, \phi_{\pi\pi}, \Phi_{ee}$ or Ψ) is extracted from the data using

$$W(\alpha) = \frac{\int_{\mathrm{HERMES}} \mathrm{Yield}(\alpha, \beta, \gamma, ...)\, d\beta\, d\gamma\, d....}{A(\alpha)}, \tag{6.37}$$

with

$$A(\alpha) = \frac{\int_{\mathrm{HERMES}} N_{\mathrm{acc}}(\alpha, \beta, \gamma, ...)\, d\beta\, d\gamma\, d....}{\int_{4\pi} N_{\mathrm{gen}}(\alpha, \beta, \gamma, ...)\, d\beta\, d\gamma\, d....}, \tag{6.38}$$

where N_{acc} and N_{gen} are the number of events of the accepted and generated Monte Carlo sample, respectively. Here, $A(\alpha)$ denotes the acceptance correction, which is needed to correct for the integration of the total cross section over all angles except the one of interest over the limited HERMES acceptance. The difficulty is that one integrates over a finite phase space (i.e. the HERMES acceptance) a function in which various angles are correlated. The end result for $A(\alpha)$ may be biased and model dependent. Hence, this method can only be used when the spectra of accepted Monte Carlo events are in good agreement with the spectra of the data.

2. Weighted Projection

Another method is to assign multidimensional weights. Instead of obtaining an average acceptance correction $A(\alpha)$ for each angle separately, one can estimate an overall multidimensional acceptance correction matrix $A(\alpha, \beta, \gamma)$ with

$$A(\alpha, \beta, \gamma, ...) = \frac{N_{\mathrm{acc}}(\alpha, \beta, \gamma, ...)}{N_{gen}(\alpha, \beta, \gamma, ...)}. \tag{6.39}$$

However, this method is hampered by the fact that as soon as one uses HMC to estimate $A(\alpha, \beta, \gamma)$, one rapidly runs out of disk space and running time before sufficient statistics to obtain a meaningful weight for each bin is obtained.

3. Iterative Weighing

Both methods presented above cannot be used in the analysis because they would lead to an unacceptable increase of the systematic uncertainties. The third and most successful method proved to be the following. Monte Carlo events are generated isotropically in both the production angle Φ_{ee} and the decay angles $\phi_{\pi\pi}$ and $\theta_{\pi\pi}$.

Afterwards weights w_i are applied for each event in a certain bin i, where $w_i = W(\theta_i, \phi_i, \Phi_i)$ given in Eqs. (2.114), (2.116) and (2.115). The various matrix elements $r^{\alpha}_{\lambda\lambda'}$ are subsequentially varied until the spectra of the various angles describe the data best, using a least χ^2 fit. The free parameters in this χ^2 fit are r^{04}_{00}, r^{04}_{1-1}, r^{1}_{1-1}, r^{3}_{1-1}, $\mathrm{Tr}(r^1) = 2r^1_{11} + r^1_{00}$, $\mathrm{Tr}(r^5) = 2r^5_{11} + r^5_{00}$, $\mathrm{Tr}(r^8) = 2r^8_{11} + r^8_{00}$ and r^5_{10}. The first seven matrix elements appear also in the individual one-dimensional angular distribution functions $W(\cos(\theta_{\pi\pi}))$, $W(\phi_{\pi\pi})$ and $W(\Phi_{ee})$. The last matrix element r^5_{10} is due to longitudinal-transverse interference and is observable in angular correlations.

When the assumption of SCHC is valid, all spin-flip amplitudes in the ρ^0 density matrix are zero and only T_{-1-1}, T_{00} and T_{11} remain in

$$\rho^{\alpha} = T_{\lambda_\rho,\gamma} \Sigma^{\alpha}_{\gamma\gamma'} T_{\lambda'_\rho,\gamma'}. \tag{6.40}$$

If the exchange particle has natural parity, $\mathcal{P} = (-1)^J$, then

$$T_{-\lambda_\rho,-\gamma} = (-1)^{\lambda_\rho - \gamma} T_{\lambda_\rho,\gamma}. \tag{6.41}$$

This, combined with the standard representation of Σ^α, as given in Ref. [111] constrains the following additional matrix elements appearing in Eq. (2.114), as

$$\mathrm{Im}(r^2_{1-1}) = -r^1_{1-1}, \tag{6.42}$$

$$\mathrm{Im}(r^6_{10}) = -\mathrm{Re}r^5_{10} \equiv \frac{1}{2}\sqrt{R/2}\cos\delta/(1+\epsilon R), \tag{6.43}$$

$$\mathrm{Im}(r^7_{10}) = +\mathrm{Re}r^8_{10} \equiv \frac{1}{2}\sqrt{R/2}\sin\delta/(1+\epsilon R), \tag{6.44}$$

$$r^{5,6,7,8}_{1-1} = 0, \tag{6.45}$$

$$r^{1,2,3,04}_{10} = 0, \tag{6.46}$$

where δ is the phase difference between the transverse and the longitudinal amplitudes (see also Eq. (2.126)). Additionally, the following relationships hold,

$$r^{1,5,8}_{00} = \mathrm{Tr}(r^{1,5,8}) \times r^{04}_{00}, \tag{6.47}$$

$$r^{1,5,8}_{11} = \mathrm{Tr}(r^{1,5,8}) \times \frac{1}{2}(1 - r^{04}_{00}). \tag{6.48}$$

The eight aforementioned free parameters are adjusted until the total χ^2 of the angular distribution $W(\cos(\theta_{\pi\pi}, \phi_{\pi\pi}, \Phi_{ee})$ between the data and the accepted Monte Carlo events is minimised.

6.3.3 Discussion of Systematic Uncertainties

A number of different sources of possible systematic uncertainties were studied for all matrix elements separately. A full description of the study of systematic uncertainties on the measurement of the ρ^0 density matrix elements can be found in Ref. [27].

The systematic uncertainty due to the method of non-diffractive background subtraction was studied by varying the ΔE cut and checking the stability of the end result.

Possible radiative corrections effects were studied by comparing matrix elements derived using a Monte Carlo with or without hard brehmstrahlung included. The $\cos\theta_{\pi\pi}$ distribution only depends on hadronic momenta so that its radiative effects should be small. The angles ϕ and Φ require knowledge of the photon momentum. However, to first order radiative corrections cancel. The measurement of Ψ is not strongly affected by radiative effects.

As for the cross section analysis, the effect of the 1.8 mrad uncertainty in the alignment of the bottom half of the spectrometer was studied by running HRC with geometry files in which the bottom detector was shifted by ± 1.8 mrad.

By varying the assumptions of Eqs. (6.46), (6.47), (6.48) the systematic uncertainty due to model dependent assumptions was evaluated.

The effect of the uncertainty in the double dissociative background is expected to be small since no contribution to the helicity transfer amplitudes is expected to originate from these events [27].

The total systematic uncertainties, given in Tables 6.11 to 6.14 were obtained by quadratically adding all contributions discussed above.

6.3.4 Results

After subtracting the background and applying the acceptance correction as explained above, the measured angular distributions are compared to the distributions of the Monte Carlo events. Figs. 6.28 to 6.31 show the distributions for $\cos\theta_{\pi\pi}$, ϕ, Φ and ψ as a function of Q^2. Data were obtained for the whole range in $\cos\theta_{\pi\pi}$, ϕ, Φ and ψ. Sufficient statistics were obtained to bin the data in small bins and observe clear shapes for the angular distributions. A clear Q^2 dependence of the angular distributions is observed.

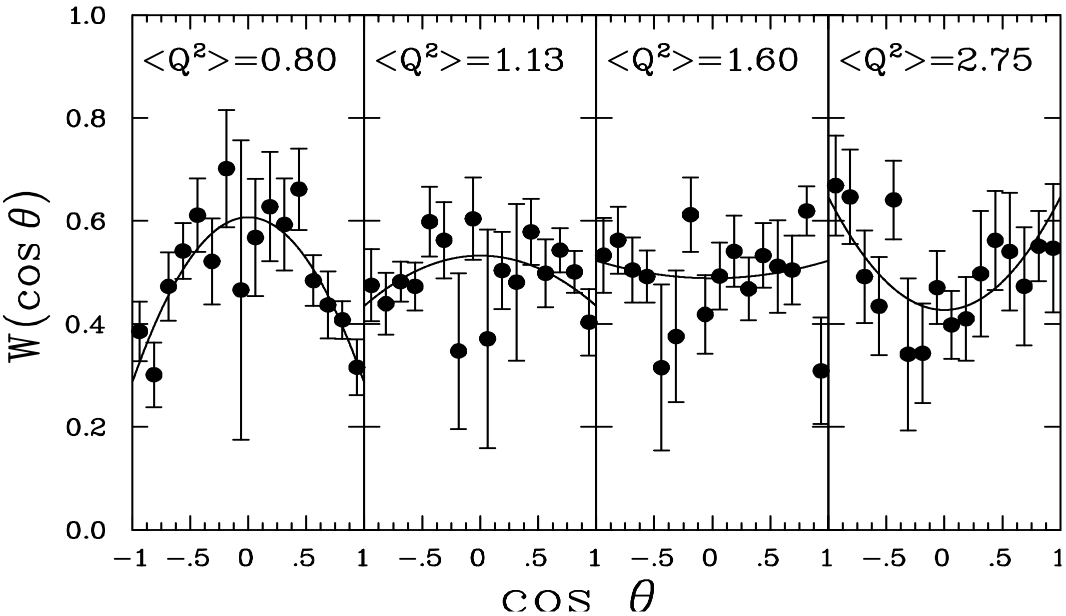

Figure 6.28: *The angular distribution $W(\cos\theta_{\pi\pi})$ for different Q^2 bins. The solid curves represent the results for the fit function given by Eq. (2.117). The average values for each Q^2 bin are given in GeV^2.*

By varying the matrix elements appearing in the expression for the cross section, the Monte Carlo events can be weighed such that the description of the data is maximal, i.e. for which the χ^2 is minimised. The extracted matrix elements are shown in Figs. 6.32, 6.33 and 6.34. while the results are given numerically in Tables 6.11, 6.12 and 6.13 together with the statistical and systematic uncertainties. A fair agreement with results from other experiments can be observed.

Fig. 6.35 shows the correlation between the angle Ψ and $\cos\theta$. As can be seen in Eq. (2.126), the angular distribution function $W(\cos\theta, \Psi)$ has maximum values for $\cos\theta < 0$, $\Psi = 0$ and $\cos\theta > 0$, $\Psi = \pm\pi$ when $\cos\delta = 1$. Hence, it can be concluded that $\cos\delta$ is approximately equal to unity.

If SCHC is valid and the t-channel exchange particle in the $\gamma N \to \rho^0 N$ reaction has natural parity (i.e. $l^P = 0^+, 1^-, 2^+, ...$), then the transverse ρ^0 particles are completely linearly polarised

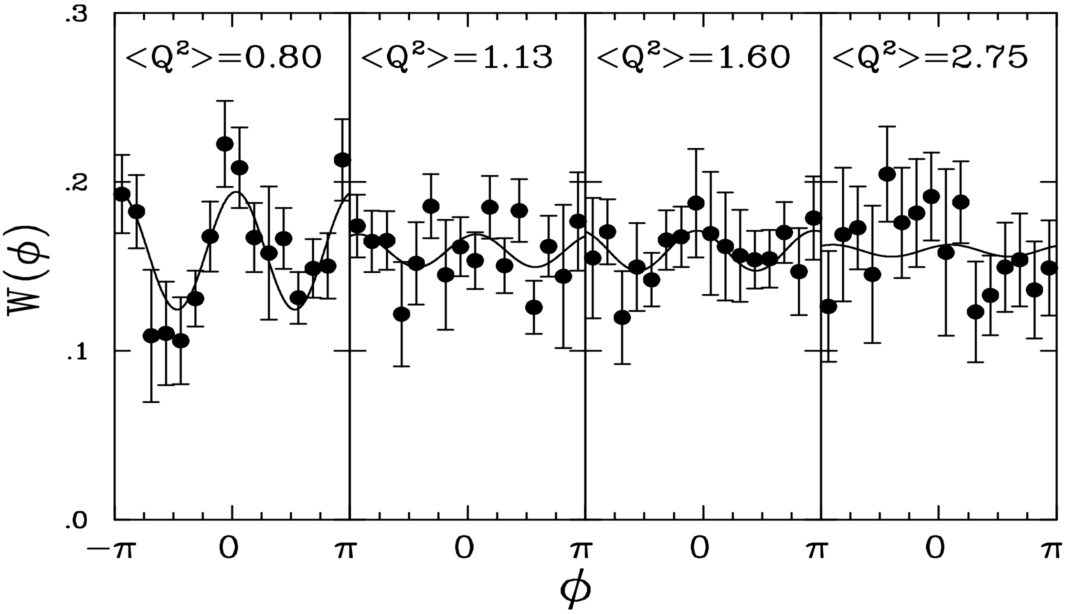

Figure 6.29: *The angular distribution $W(\phi_{\pi\pi})$) for different Q^2 bins. The solid curves represent the fit function given by Eq. (2.118). The average values for each Q^2 bin are given in GeV^2.*

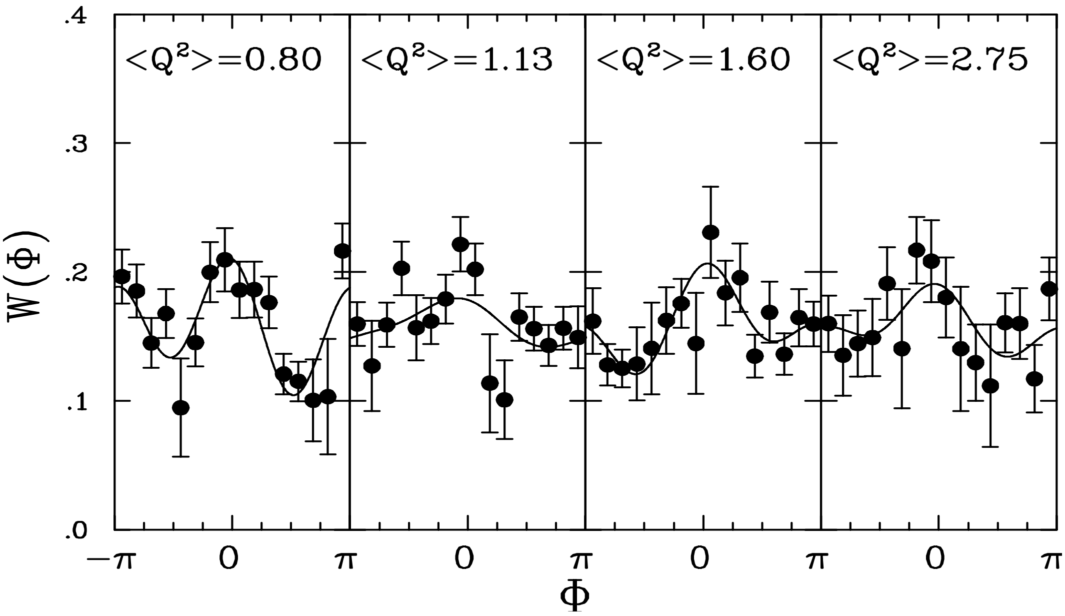

Figure 6.30: *The angular distribution $W(\Phi)$ for different Q^2 bins. The solid curves represent the fit function given by Eq. (2.119). The average values for each Q^2 bin are given in GeV^2.*

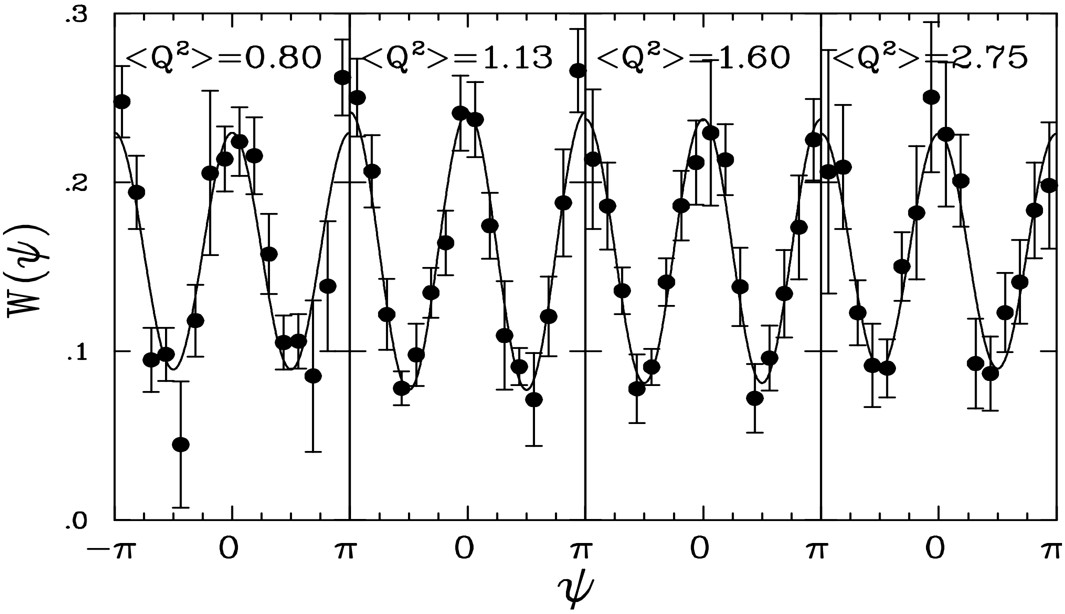

Figure 6.31: *The angular distribution $W(\Psi)$ for different Q^2 bins. The solid curves represent the fit function given by Eq. (2.121). The average values for each Q^2 bin are given in GeV^2.*

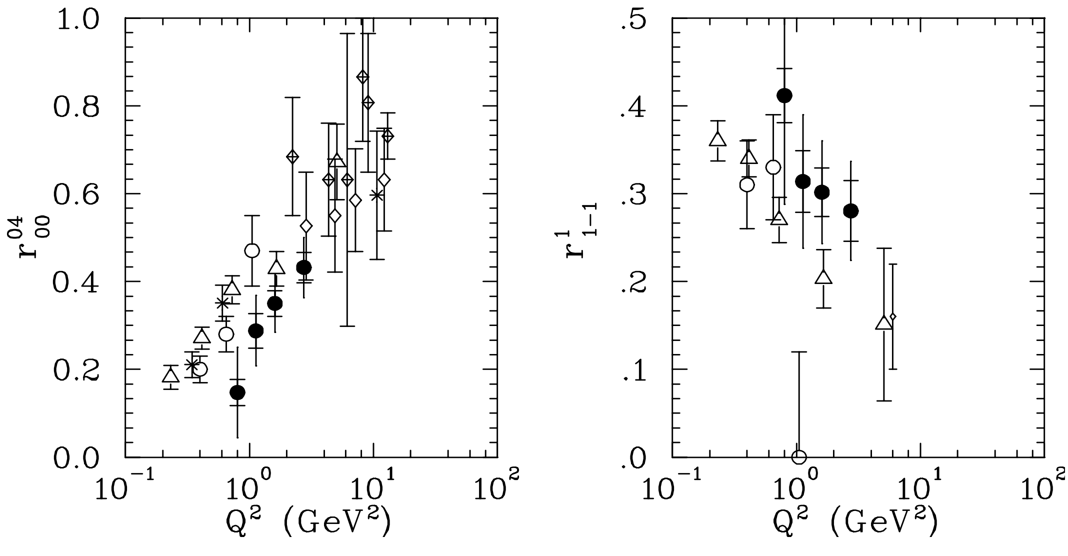

Figure 6.32: *Data for the spin density matrix elements r^{04}_{00} and r^{1}_{1-1} are shown (filled circles) in the left and right figure, respectively. The inner error bar represents the statistical uncertainty. The outer error bar includes the systematic uncertainty added linearly. Results from other experiments are shown for comparison (see Refs. [17], [20], [44], [68] and [80]).*

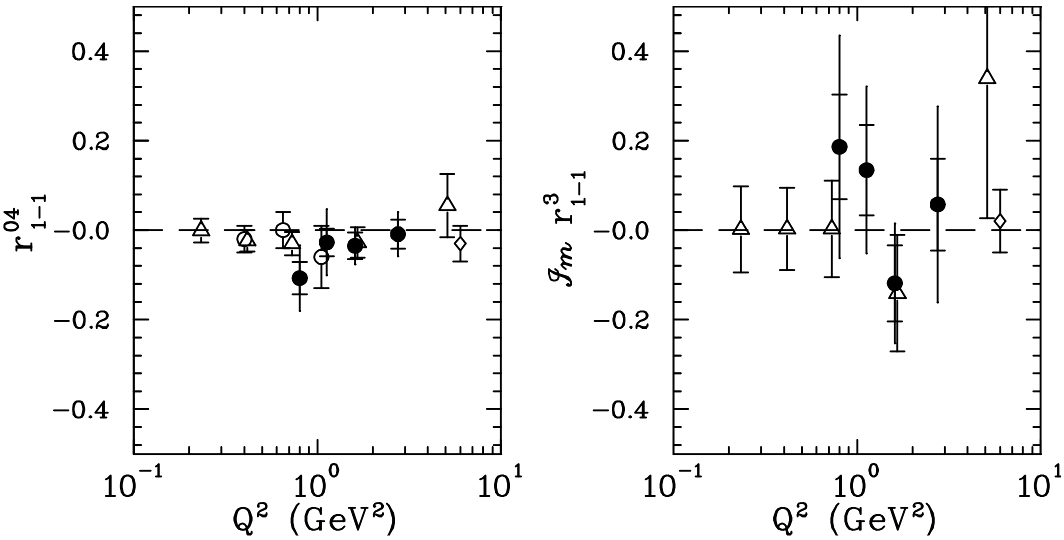

Figure 6.33: *Data for the spin density matrix elements r^{04}_{1-1} and $\mathrm{Im}(r^{3}_{1-1})$ are shown (filled circles) in the left and right figure, respectively. The inner error bar represents the statistical uncertainty. The outer error bar includes the systematic uncertainty added linearly. Results from other experiments are shown for comparison (see Refs. [17], [44] and [80]).*

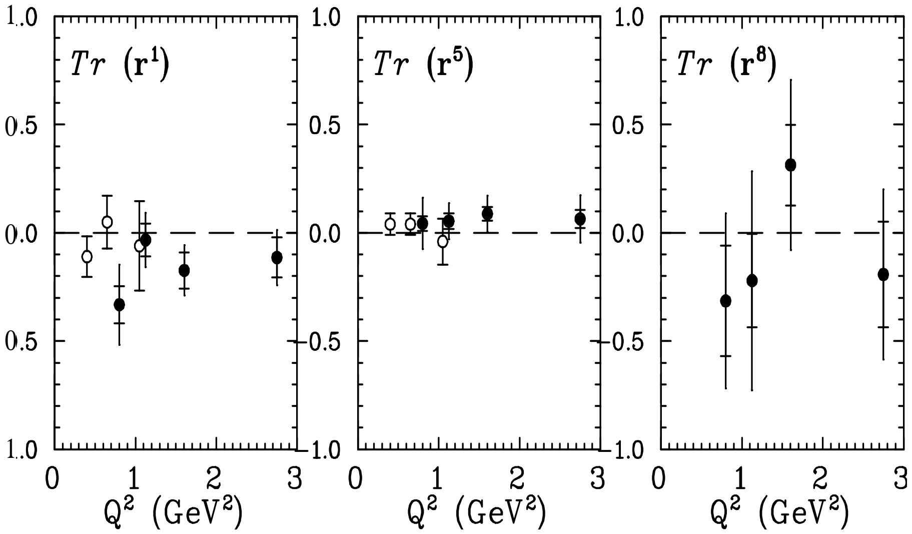

Figure 6.34: *Data for the spin density matrix elements $Tr(r^1)$ (left), $Tr(r^5)$ (middle), and $Tr(r^8)$ (right) are shown (filled circles) as a function of Q^2. The inner error bar represents the statistical uncertainty. The outer error bar includes the systematic uncertainty added linearly. Results from other experiments are shown for comparison (see Ref. [80]).*

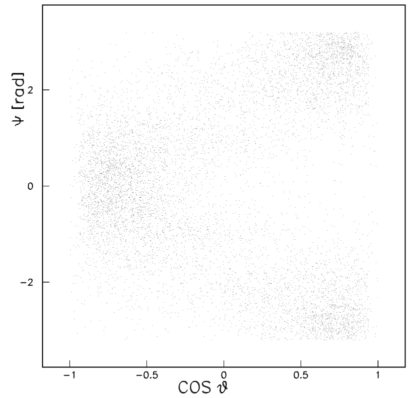

Figure 6.35: *The angle Ψ plotted versus $\cos\theta$, showing the interference between the transverse and the longitudinal part of the angular distribution function $W(\cos\theta, \Psi)$.*

along the normal to the electron scattering plane, as represented by r^1_{1-1} and Eq. (2.122), $r^1_{1-1} = 1/2(1 - r^{04}_{00})$, has to hold. Table 6.13 shows the values for r^1_{1-1} either from direct measurement or derived from the measurement of r^{04}_{00} assuming SCHC and natural parity exchange in the t-channel. The table confirms both assumptions.

Also, assuming SCHC, i.e. Eq. (2.120) holds, the ratio of photoproduced longitudinally over transversely polarised ρ^0 particles, R_ρ, is directly related to the ratio of longitudinally over transversely polarised photon fluxes (ϵ) and the ratio of the total number of electroproduced longitudinally polarised ρ^0 particles (r^{04}_{00}) and transversely polarised ρ^0 particles ($1 - r^{04}_{00}$). Hence, using $R_\rho = (r^{04}_{00})/(\epsilon(1 - r^{04}_{00}))$, the ratio R_ρ is shown as a function of Q^2 in Fig. 6.36. Here, our result agrees fairly well with results for the measurement of R_ρ derived from r^{04}_{00} by other experiments.

The world data are fitted to the function

$$R_\rho(Q^2) = c_0(W) \cdot \left(Q^2/m_\rho^2\right)^{c_1} . \tag{6.49}$$

This fit is done for the data with $W > 10$ GeV (E665, EMC, H1, NMC and ZEUS) and for the data with $W < 10$ GeV (DESY and HERMES), yielding $c_0(W < 10\,\mathrm{GeV}) = 0.33 \pm 0.03$, $c_0(W > 10\,\mathrm{GeV}) = 0.47 \pm 0.03$ and $c_1 = 0.62 \pm 0.04$ which is in disagreement with the VMD model which predicts $c_1 = 1$.

6.3.5 Conclusions

The out-of-plane angles and decay angles for elastic and quasi-elastic production of ρ^0 mesons on ^{3}He have been measured for momentum transfers in the range $0.5 < Q^2 < 4$ GeV^2 and center-of-mass energy between $3.8 < W < 6.5$ GeV. The spin-density matrix elements r^{04}_{00} and r^1_{1-1} are consistent with the assumption of both SCHC and natural parity exchange in the

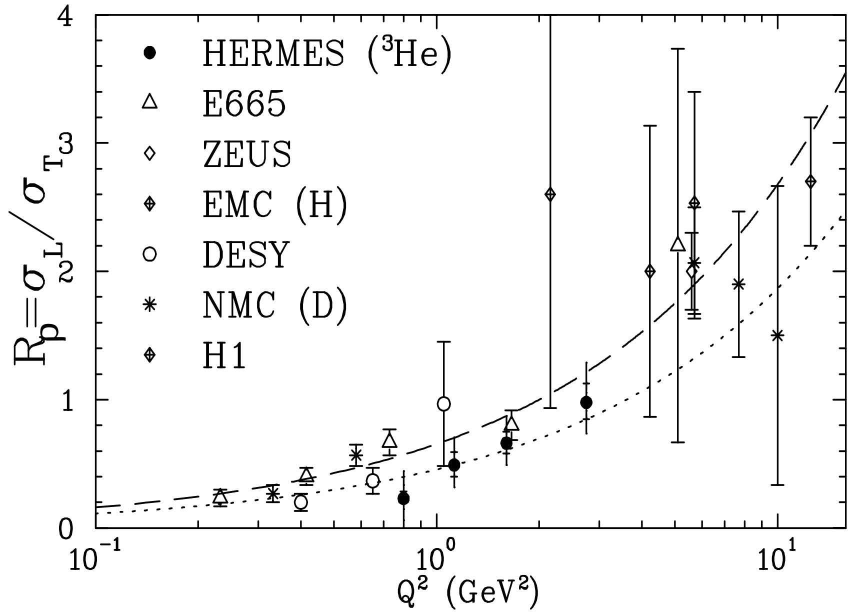

Figure 6.36: *The ratio R_ρ determined from the measured values of r^{04}_{00} using Eq. (2.120) (filled circles). The inner error bar represents the statistical uncertainty. The outer error bar includes the systematic uncertainty added linearly. Results from other experiments are shown for comparison. The curves represent fits with a shape given by Eq. (6.49) for world data with $W < 10$ GeV (dotted curve) and $W > 10$ GeV (dashed curve).*

Table 6.11: *Spin density matrix elements determined from the polar decay angle distributions $W(cos\theta)$ and $W(\phi)$.*

$\langle Q^2\rangle$ GeV^2	r^{04}_{00}	r^{04}_{1-1}	Im(r^{3}_{1-1})
0.80	$0.147 \pm 0.030 \pm 0.073$	$-0.107 \pm 0.036 \pm 0.073$	$0.186 \pm 0.117 \pm 0.132$
1.13	$0.288 \pm 0.040 \pm 0.041$	$-0.027 \pm 0.031 \pm 0.041$	$0.134 \pm 0.101 \pm 0.086$
1.60	$0.350 \pm 0.029 \pm 0.036$	$-0.035 \pm 0.030 \pm 0.036$	$-0.119 \pm 0.085 \pm 0.049$
2.75	$0.432 \pm 0.035 \pm 0.034$	$-0.009 \pm 0.033 \pm 0.034$	$0.057 \pm 0.103 \pm 0.116$

Table 6.12: *Spin density matrix elements determined from the production angle distribution $W(\Phi)$.*

$\langle Q^2 \rangle$ GeV^2	Tr(r^1)	Tr(r^5)	Tr(r^8)
0.80	$-0.332 \pm 0.085 \pm 0.100$	$0.043 \pm 0.034 \pm 0.085$	$-0.314 \pm 0.256 \pm 0.148$
1.13	$-0.033 \pm 0.075 \pm 0.049$	$0.054 \pm 0.036 \pm 0.048$	$-0.221 \pm 0.215 \pm 0.291$
1.60	$-0.174 \pm 0.083 \pm 0.033$	$0.088 \pm 0.032 \pm 0.052$	$0.314 \pm 0.186 \pm 0.206$
2.75	$-0.114 \pm 0.092 \pm 0.035$	$0.064 \pm 0.041 \pm 0.069$	$-0.192 \pm 0.243 \pm 0.150$

Table 6.13: *Spin density matrix element r^1_{1-1} determined from our measurement of r^{04}_{00} (assuming SCHC and natural parity exchange in the t-channel) compared to the measured r^1_{1-1}.*

$\langle Q^2 \rangle$ GeV^2	$r^1_{1-1}(SCHC)$ from r^{04}_{00}	r^1_{1-1} measured
0.80	0.426 ± 0.030	$0.412 \pm 0.031 \pm 0.093$
1.13	0.356 ± 0.033	$0.314 \pm 0.035 \pm 0.041$
1.60	0.325 ± 0.026	$0.302 \pm 0.028 \pm 0.031$
2.75	0.284 ± 0.034	$0.280 \pm 0.034 \pm 0.022$

Table 6.14: *Values for $< \epsilon >$ and R_ρ as determined from r^{04}_{00} assuming SCHC and natural parity exchange in the t–channel. Also the χ^2 values for each Q^2 bin are given.*

$\langle Q^2 \rangle$ GeV^2	$< \epsilon >$	R_ρ (SCHC) from r^{04}_{00}	χ^2/ν
0.80	0.76	$0.23^{+0.06+0.15}_{-0.05-0.12}$	$48/42$
1.13	0.82	$0.49^{+0.10+0.10}_{-0.09-0.09}$	$42/42$
1.60	0.81	$0.66^{+0.09+0.11}_{-0.08-0.10}$	$29/42$
2.75	0.78	$0.98^{+0.15+0.14}_{-0.13-0.13}$	$37/42$

t-channel. Also, the other fitted parameters, r^{04}_{1-1}, r^{3}_{1-1}, $\mathrm{Tr}(r^1)$, $\mathrm{Tr}(r^5)$, $\mathrm{Tr}(r^8)$ are all consistent with zero, as expected from SCHC and natural-parity exchange in the t-channel. The ratio of the cross sections for longitudinal and transversely polarised ρ^0 particles is determined from r^{04}_{00} assuming SCHC. It is found that this ratio rises with Q^2, while our results agree fairly well with the data from other experiments.

A suggestion of a W dependence of R_ρ is found.

Study of the target spin and beam polarisation dependence of ρ^0 production, which will enable the extraction of more helicity transfer amplitudes, is in progress.

6.4 Conclusions

From the cross section analysis and the analysis of the angular distributions, a number of conclusions and observations can be drawn, which are itemised below.

- Data taken in 1995, the first data taking year at HERMES, were analysed and about thousand ρ^0 candidates were extracted.
- The virtual photoproduction for ρ^0 production has a strong Q^2 dependence which is accurately described by the VMD model.
- R_ρ (see Eq. (6.24)) is determined to be slightly negative from the fit to the data and hence cannot be interpreted as the ratio of the cross sections for longitudinal and transversely polarised ρ^0 mesons.
- The HERMES data show a strong W dependence of the cross section. The data in the lower W bins, for all four Q^2 bins, do not agree with the data from the measurement performed at Cornell [39]. The data in the higher W bins, for all four Q^2 bins, agree well with the data of the E665 measurement [8].
- The Q^2 dependence of the slope of the W dependence can be described by a parametrisation presented in Ref [70]. This parametrisation assumes that at higher Q^2, multiple Pomeron exchange has to be taken into account.
- The longitudinal part of the cross section can be described by the pQCD based model from Ref. [120].
- The assumptions of SCHC and natural parity exchange in the t channel are valid in the HERMES kinematic region.
- There is an indication that R_ρ, extracted from the angular distributions by assuming SCHC, is W dependent which would be in contradiction with predictions of the VMD model (see Eqs. (2.61) and (2.62)).
- Future results of the ρ^0 analysis will have smaller systematic uncertainties. The main improvement will be achieved by more thorough Monte Carlo studies of the background.

Bibliography

[1] K. Ackerstaff. *First Results from the* HERMES *Experiment Using Unpolarized Targets.* Ph.D. thesis, 1996. HERMES internal note: 96-030.

[2] K. Ackerstaff et al. The HERMES collaboration. *The* HERMES *Spectrometer.* To be published.

[3] K. Ackerstaff et al. The HERMES collaboration. *Measurement of the Neutron Spin Structure Function* $\mathrm{g}_1^{\mathrm{n}}$ *with a Polarized* ^3He *Internal Target.* Phys. Lett. **B 404**, (1997), 383-389.

[4] K. Ackerstaff et al. The HERMES collaboration. *Coherence Length Effects in Exclusive* ρ^0 *Electroproduction.* To be published.

[5] K. Ackerstaff and M. Funk. *The PinK Documentation Page.* (`http://www-hermes.desy.de/pink/`)

[6] D. Adams et al. (SMC collaboration), Phys. Lett. **B 357**, (1995) 248–254.

[7] M.R. Adams et al. (E665 collaboration), Phys. Rev. Lett., **74**, (1995) 1525.

[8] M.R. Adams et al. (E665 collaboration), Z. Phys., **C 74**, (1997) 237.

[9] G. D'Agostini. *A multidimensional unfolding method based on Bayes' theorem.* Nucl. Instr. and Methods **A 362** (1995) 487-498.

[10] I. Akushevich *Radiative Correction to Cross Section of Exclusive* ρ *Electroproduction* HERMES internal note: 97-059.

[11] G. Altarelli et al., CERN-TH **96-345** (1996).

[12] G. Altarelli, G. Parisi, Nucl. Phys. **B 126**, (1997), 298.

[13] P. L. Anthony et al., Phys. Rev., **D54**, (1996), 6620–6650.

[14] M. Arneodo, Private communications.

[15] M. Arneodo, *Diffraction (at* HERA*) - An Introduction.*
Proceedings of the Photon'97 conference
(May 10-15, 1997)

Photon '97, (Incorporating the XIth International Workshop on Gamma–Gamma Collisions), World Scientific, (1997).
http://www.fys.ruu.nl/ buijs/proceedings/program.html

[16] M. Arneodo et al., *Reevaluation of the Gottfried sum*, Phys. Rev. **D 50** (1994) 1.

[17] M. Arneodo et al., Nucl. Phys. **B 429** (1995).

[18] M. Arneodo et al., Nucl. Phys. **B 487**, (1997), 3.

[19] J. Ashman et al. (EMC collaboration), Nucl. Phys. **B 328**, (1989) 1.

[20] J. J. Aubert et al., Phys. Lett. **B 161**, (1985).

[21] H. Avakian et al., *Performance of F101 Radiation Resistant Lead Glass Shower Counters.* Nucl. Instr. and Methods **A378** (1996), 155.

[22] R.M. Barnett et al., Phys. Rev., **D 54**, (1996), 1.

[23] T.H. Bauer et al., Rev. Mod. Phys., **50**, (1978) 261.

[24] H.J. Behrend et al., Phys. Rev. Lett. 27 (1971), 61.

[25] J.E. Belz. Adaption of Monte Carlo code for exclusive, diffractive ρ^0 production.

[26] J.E. Belz. *Rho Polarization in Exclusive* $A(e, e'\rho^0)$. HERMES internal note: 96-052.

[27] J.E. Belz. *Measurement of Decay Angle Distributions in Diffractive Electroproduction of* ρ^0 *Mesons and an extraction of* $R(Q^2)$. To be published.

[28] S. Bernreuther et al. *Design and performance of the large* HERMES *drift chambers*, Nucl. Instr. Meth. **A 367** (1995), 96.

[29] P.J. Biggs et al., Phys. Rev. Lett. **24** (1970), 1201.

[30] J.D. Bjørken, Phys. Rev. **148** (1966) 1457; Phys. Rev. **D 1** (1970) 1367.

[31] J. Blouw. Private communications.

[32] J. Blouw. *Spin dependent deep-inelastic positron scattering from polarized* ^{3}*He*, Ph.D. thesis, Vrije Universiteit Amsterdam (1998).

[33] S.J. Brodsky and A.H. Müller, Phys. Lett. **B 206**, (1988) 685.

[34] S.J. Brodsky et al., Phys. Rev. **D 50**, (1994) 3134.

[35] S. Brons, Private communications.

[36] K.A. Brownlee, *Statistical Theory and Methodology in Science and Engineering*, John Wiley & Sons, Inc.

[37] W. Brückner, Private communications.

[38] A. Brüll, Private communications.

[39] D.G. Cassel et al, Phys. Rev. **D 24**, (1981) 2787.

[40] CERN `http://wwwcn.cern.ch/asdoc/Welcome.html`

[41] J.C. Collins, L. Frankfurt, M. Strikman, Phys. Rev. **D 56**, (1997), 2982.

[42] P.D.B. Collins, *Regge Theory and High Energy Physics*, Cambridge University Press, Cambridge. (1977).

[43] F.S. Crawford, Jr. *Waves, berkeley physics course - volume 3*, McGraw-Hill Book Company.

[44] M. Derrick et al., Phys. Lett. **B 356**, (1995), 601.

[45] M. Dueren. Private communications.

[46] M. Dueren. *The* HERMES *Experiment: From the Design to the First Results.* Habilitation, 1995. HERMES internal note: 95-002.

[47] M. Dueren, P. Geiger, N. Makins, E. Volk, P. Welch. The HERMES Monte Carlo. `http://www.mpi-hd.mpg.de/ herprod/`

[48] A. Donnachie and P.V. Landshoff, Phys. Lett. **B 296**, (1992) 227.

[49] J. Ellis and R.L. Jaffe, Phys. Rev. **D 9** (1974) 1444;

[50] J. Ellis and R.L. Jaffe, Phys. Rev. **D 10** (1974) 1669.

[51] J. Ellis and M. Karliner, Phys. Lett. **B 341**, (1995) 397–406.

[52] J. V. Emerson, Private communications (1995).

[53] J. V. Emerson. *Modeling of the* HERMES *Transition Radiation Detector.* Masters thesis, (1995). HERMES internal note: 96-038.

[54] A. Fantoni *Costruzione del calorimetro a contatori di vetro al piombo dell'esperimento HERMES per la misura delle funzioni di struttura di spin dei nucleoni.* Ph.D. thesis, (1996). HERMES internal note: 96-015

[55] A. Fantoni Proceedings of the VI International Conference in high energy Physics. (June 8-14, 1996 - LNF) Frascaty Physics Series vol. VI, 659-668

[56] M. Ferstl. Private communications.

[57] K. Fiedler. *Studien zum protoninduzierten Untergrund am* HERMES *- experiment.*, Diploma thesis, Phys. Institute II, University of Erlangen-Nürnberg, 1995.

[58] S.M. Fisher and P. Palazzi. *The* ADAMO *Data System. Programmers Manual - Version 3.2* CERN, 1993. (`http://www1.cern.ch:80/Adamo/ADAMO_ENTRY.html`)

[59] L. Frankfurt et al., Phys. Rev. **D 54**, (1996) 3194.

[60] M. Funk., Private communications.

[61] M. Funk. *Hanna: A C-based HERMES Analysis Tool.* `http://www-hermes.desy.de/hanna/`

[62] S. Gasiorowicz, *Quantum Physics.* John Wiley & Sons, Inc. (1974).

[63] T. Gehrmann and W.J. Stirling. *Present status of polarized parton distributions.* hep-ph/9510243, (1995).

[64] W. Greiner, A. Schäfer. *Quantum Chromodynamics.* Springer-Verlag. (1994).

[65] V.N. Gribov, L.N. Lipatov, Sov. J. Nucl. Phys. **15**, (1972), 78.

[66] K. Goulianos, Phys. Reports **101** (1983), 169.

[67] M. Guidal, Private communications.

[68] The H1 Collaboration, DESY 96-023.

[69] L.P.A. Haakman, Private communications.

[70] L.P.A. Haakman, A. Kaidalov, J.H. Koch Phys. Lett. **B 365**, (1996), 411-417.

[71] L.P.A. Haakman, *QCD aspects of the Pomeron: from soft to hard scales*, Ph. D. thesis, Universiteit van Amsterdam.

[72] E. Hecht and A. Zajac. *OPTICS*, Addison-Wesley, fifth edition, (1980).

[73] The HERMES Collaboration, Technical Design Report (1993).

[74] R. Hofstadter, *Nuclear Physics and Technology*, Vol 2, Springer–Verlag, Berlin, (1967).

[75] H. Holtmann, N.N. Nikolaev, A. Szczurek, J. Speth, B.G. Zakharov *On the determination of double diffraction dissociation cross section at* HERA Z. Phys. **C 69** (1996), 297.

[76] J. Hüfner and B.Z. Kopeliovich, *Towards Study of Color Transparency with Medium Energy Electron Beams.* Proceedings of '95-'96 workshop "Future Physics At HERA".

[77] J.D. Jackson, Il Nuovo Cimento **34** (1964), 1644.

[78] J.D. Jackson, Reviews of Modern Physics, **48** (1976), 417.

[79] M. Jacob and G.C. Wick, Ann. of Phys. **7** (1959) 404.

[80] P. Joos et al., Nucl. Phys. **B 113**, (1976), 53.

[81] M. de Kamps, *Diffractive Vector Meson Production in Deep Inelastic Scattering* Ph. D. thesis, Universiteit van Amsterdam.

[82] A. Kisselev. *Decoder Documentation Page.* `http://www-hermes.desy.de/ kisselev/decmain.html`

[83] P. Kitching. Private communications.

[84] Y.G. Kolomensky et al., *Precision measurement of the neutron spin structure function* $g_1^n(x)$. Proceedings of the 12th international symposium on high-energy spin physics., number 12 in International Symposium on HIGH-ENERGY SPIN PHYSICS, p. 396, Signapore, September 1996. World Scientific.

[85] M. Kolstein. *ACE Manual, Efficiencies.* (`http://www-hermes.desy.de/ machiel/ACEmanu/ACEmanu.html`)

[86] B.Z. Kopeliovich et al., Phys. Lett. **B 324**, (1994), 469.

[87] W. Lachnit. Private communications.

[88] H.L. Lai et al. Phys. Rev. **D 51**, (1995), 4763.

[89] M. R. Lasarev. Private communications (by newsgroups `sci.stat.math` and `sci.stat.edu`). Oregon Health Sciences University, 3181 S.W. Sam Jackson Park Rd., L606, Portland, OR.

[90] W. Lorenzon et al. Phys. Rev. **A 47** (1993), 468.

[91] J. van der Marel, PhD thesis, Universiteit Delft, (1997).

[92] E. Merzbacher, *Quantum Mechanics*, John Wiley & Sons, Inc. (1970).

[93] W.J. Metzger, *Statistical Methods in Data Analysis*, HEN **343**.

[94] J. Nemchik et al., DFTT71/95, KFA-IKP (TH)-24-95, hep-ph/9605231

[95] T.G. O'Neill. Private communications.

[96] T.G. O'Neill. *Preliminary Measurement of Nuclear Transparency in* ^{3}*He(e,e'*ρ^0 *).* HERMES internal usage.

[97] T.G. O'Neill. Monte Carlo code for exclusive, diffractive ρ^0 production (no documentation available as of yet).

[98] Particle Data Group, Phys. Rev. **D 50**, (1994), 1173.

[99] S.F. Pate et al. *Cryogenic Polarised Internal ^{3}He Gas Target for* HERMES
Proc. of the Int. Workshop on Polarized Beams and Polarized Gas Targets, Cologne, Germany, June 6-9, 1995, eds. H.Paetz gen. Schieck and L. Sydow (World Scientific, Singapore, 1996) p. 39.
HERMES internal note 95-017.

[100] C. del Papa et al., Phys. Rev. **D 19**, (1979), 1303.

[101] M.A. Pichowksi and T.-S.H. Lee, Phys. Lett. **B 379**, (1996), 1.

[102] M.A. Pichowksi and T.-S.H. Lee, ANL-PHYS-8529-TH-96, nucl-th/9612049

[103] M.L. Pitt et al. *TOM: A Target Optical Monitor of Polarization and Luminosity for Polarized Internal Gas Targets*
Proc. of the Int. Workshop on Polarized Beams and Polarized Gas Targets, Cologne, Germany, June 6-9, 1995, eds. H.Paetz gen. Schieck and L. Sydow (World Scientific, Singapore, 1996) p. 413.
HERMES internal note 95-018.

[104] J.H. Pollard. *A Handbook of Numerical and Statistical Techniques.* Cambridge University Press, 1977. (page 138)

[105] H.R. Poolman. *Quasi-Free Spin-Dependent Electron Scattering from a Polarized ^{3}He Internal Target*, Ph.D. thesis, Vrije Universiteit Amsterdam (1998)

[106] B. Povh and J. Hüfner, Phys. Rev. Lett. **58**, (1987), 1612.

[107] A.V. Radyushkin, Phys. Lett. **B 380**, (1996), 417-425.

[108] M. Ross and L. Stodolsky, Phys. Rev. **149**, (1966), 1172.

[109] Lothar Sachs. *Statistische Methoden: Planung und Auswertung.*, Springer, 1993.

[110] L.D. Schearer, F.D. Colegrove and G.K. Walters. *Polarization of ^{3}He gas by optical pumping.* Phys. Rev. **132**, (1963), p. 2561.

[111] K. Schilling and G. Wolf, Nucl. Phys. **B 61**, (1973), 381.

[112] K. Schilling and G. Wolf, *"Many-Body Processes"*, Contribution to *Electromagnetic Interactions of Hadrons, Volume 2*, edited by A. Donnachie and G. Shaw, Plenum Press, 1978.

[113] M. H. Schmitt Ph.D. thesis, Harvard University, (1991).

[114] P. Schüler, Private communications.

[115] W.D. Shambroom et al., Phys. Rev. **D 26**, (1982), 1.

[116] A. A. Sokolov and I.M. Ternov, *On Polarisation and Spin Effects in the Theory of Synchrotron Radiation.* Soviet Physics Dokladi 8, (1203), 1964.

[117] P. Söding, Phys. Lett. **19**, (1966), 702.

[118] University of Texas M. D. Anderson Cancer Center, Department of Biomathematics. *The Stattab package, version 1.2*
Source from anonymous ftp: `ftp://odin.mdacc.tmc.edu/pub/source/`
More information at: `http://odin.mdacc.tmc.edu/`

[119] M. Vanderhaeghen, Private communications.

[120] M. Vanderhaeghen, P.A.M. Guichon and M. Guidal. *Hard electroproduction of photons and mesons on the nucleon.*

[121] M. Vincter. *A determination of F_2^n/F_2^p, $d_v(x)/u_v(x)$, and the light quark sea flavour asymmetry using the 1995* HERMES *unpolarised data.* HERMES internal note: 97-013.

[122] E. Volk. Private communications.

[123] H. de Vries et al., At. Data Nucl. Data Tables **36**, (1987), 495.

[124] W. Wander. *DAD Documentation Page.* (`http://www-hermes.desy.de/dad/`)

[125] W. Wander. *Rekonstruktion hochenergetischer Streuereignisse im HERMES Experiment.* PhD Thesis, 1996. HERMES internal note: 96-023.

[126] W. Wander. *HRC: The HERMES reconstruction program.*
`http://www-hermes.desy.de/documentation/swtutorial/swtutorial.html#hrc`

[127] W. Wittek, Private communications.

Summary

HERMES is designed to study the contribution of quarks to the spin of the nucleon (proton or neutron). This can be measured by scattering polarised leptons (in case of HERMES these are electrons) from polarised targets. At high enough energies ($Q^2 > 1$ GeV^2 and $W > 2$ GeV), the nucleon will break up and effectively the lepton will scatter from the quarks. This is referred to as Deep Inelastic Scattering (DIS). Extensive particle identification capabilities at HERMES allow to perform flavour decomposition of the quark spin distributions. In 1995, a polarised ^{3}He target, which effectively can be considered as a polarised neutron target, was used to measure the quark contribution to the neutron spin. Also quark flavour spin distributions were measured. Other theses and publications discuss these results in more detail (e.g. Ref. [3], [32]).

In parallel with these measurements, various other physics topics can be addressed at HERMES. One of these is the subject of exclusive ρ^0 production. Most hadrons in DIS experiments are produced by means of fragmentation processes, where constituents of the target (quarks) are knocked out by the scattering lepton and form new hadrons. In exclusive ρ^0 production, however, the ρ^0 mesons are predominantly produced by the fluctuation of a virtual photon into a quark–antiquark pair. This hadronic object can scatter pseudo elastically (i.e. diffractively) from the target and maintain sufficient energy to evolve into one of the vector mesons: e.g. the ρ^0 , ω, ϕ or J/Ψ. The Vector Meson Dominance (VMD) model describes the Q^2 dependence of the cross section of vector meson production in this kinematic region more accurately than perturbative Quantum Chromo Dynamics (pQCD) is able to.

Moreover, there are certain predictions about the helicity transfer in ρ^0 production. Since the ρ^0 meson is a spin-1 particle (it has to have the same quantum numbers as the photon) which decays rapidly into two pions with zero spin, the angular distributions of the two pions reflect the helicity state of the ρ^0 meson. Together with the distribution of the angle between the ρ^0 decay plane and the ρ^0 production plane, these angular distributions completely define the helicity transfer in the ρ^0 production process.

This thesis reports about the cross section and the angular distributions associated with ρ^0 meson production. It was found that in the kinematical region covered by HERMES, there is a strong dependence of the cross section on W. At low W, the cross section is much higher than at higher W for a fixed value of Q^2. At the highest value for W obtainable at HERMES, the cross section agrees with the data from a measurement done by the E665 collaboration.

Both a parametrisation as a pQCD based model describe the W dependence of the HERMES data reasonably well. Results from the pQCD model are only available for $Q^2 > 4$ GeV^2.

The HERMES data on the angular distributions indicate that the assumption of s-channel helicity conservation (SCHC) and natural parity exchange in the t-channel are both valid. SCHC means that the helicity of the photon is directly and completely transferred to that of the ρ^0. Natural parity exchange in the t-channel means that no quantum numbers are exchanged between the target and the ρ^0 meson. There is an indication that R_ρ, extracted from the angular distributions by assuming SCHC, is W dependent.

At HERMES, study of the target spin and beam polarisation dependence of the ρ^0 production process will enable the extraction of more helicity transfer amplitudes. Such studies are in progress. Future results of the ρ^0 analysis will have smaller systematic uncertainties. The main improvement will be achieved by more thorough Monte Carlo studies of the background.

Samenvatting

Het HERMES experiment is ontworpen om de bijdrage van quarks tot de spin van het nucleon (proton of neutron) te meten. De manier waarop dit gemeten wordt is door gepolariseerde leptonen (in het geval van HERMES zijn dit elektronen) te verstrooien aan gepolariseerde botsingsobjecten. Bij hoge energieëen ($Q^2 > 1$ GeV^2 en $W > 2$ GeV), breekt het nucleon op en verstrooit men effectief aan de quarks. Dit wordt in het Engels 'Deep Inelastic Scattering' (DIS) genoemd. Dankzij de mogelijkheden bij HERMES tot deeltjesidentificatie kunnen spinverdelingsfuncties voor de verschillende quarksoorten apart bepaald worden. In 1995 werd bij HERMES gepolariseerd ^{3}He, wat beschouwd kan worden als een gepolariseerd neutron, als botsingsobject gebruikt om de quarkbijdrage tot de spin van het neutron te meten. Hierbij zijn ook de spinverdelingsfuncties voor de afzonderlijke quarksoorten bepaald. De resultaten van deze metingen worden uitvoeriger behandeld in andere proefschriften en publicaties.

Naast deze metingen kunnen verscheidene andere onderwerpen bestudeerd worden, waaronder dat van exclusieve ρ^0 produktie. De meeste hadronen in DIS experimenten zijn afkomstig van fragmentatieprocessen, waar fragmenten (quarks) uit het nucleon geschoten worden door het verstrooide lepton om vervolgens nieuwe hadronen te vormen. In exclusieve ρ^0 produktie, echter, worden de ρ^0 mesonen voornamelijk gemaakt door middel van de fluctuatie van een virtueel foton in een quark–antiquark paar. Dit hadronische object verstrooit dan pseudo-elastisch (i.e. diffractief) aan het botsingsobject en verkrijgt zodoende voldoende energie om de identiteit van één van de vector mesonen aan te nemen, zoals de ρ^0 , ω, ϕ of J/Ψ. Het VMD model beschrijft de Q^2 afhankelijkheid van de werkzame doorsnede van het vector meson, geproduceerd op deze wijze, met grotere precisie dan pQCD dat kan.

Daarnaast bestaan er een aantal voorspellingen wat betreft de overdracht van heliciteit bij ρ^0 produktie. Omdat het ρ^0 meson een spin-1 deeltje is (het moet immers dezelfde quantumgetallen bezitten als het foton) dat in korte tijd vervalt in twee pionen met een intrinsiek impulsmoment gelijk aan nul, zijn de hoekverdelingen van de twee pionen een maat voor de heliciteitstoestand van het oorspronkelijke ρ^0 meson.

Dit proefschrift brengt verslag uit over de werkzame doorsnede en de hoekverdelingen die geassocieerd kunnen worden met ρ^0 produktie. Gevonden is dat in het kinematische bereik van HERMES, de werkzame doorsnede sterk afhankelijk is van W. Bij lage W is de werkzame doorsnede groter dan bij hoge W voor een vaste waarde van Q^2. Voor de hoogste waarde van W die voor HERMES nog toegankelijk is komt de bij HERMES gemeten werkzame doorsnede overeen met die bepaald door de E665 collaboratie.

Voorspellingen van zowel een parametrisatie als van een model dat gebaseerd is op pQCD, beschrijven de W afhankelijkheid van de data redelijk goed. Het pQCD model kan alleen voorspellingen doen voor $Q^2 > 4$ GeV^2.

De HERMES data voor de hoekverdelingen laten zien dat de aannamen van s-kanaal heliciteitsbehoud (SCHC) en 'natuurlijke pariteitsuitwisseling in het t kanaal' beide gerechtvaardigd zijn. SCHC betekent dat de heliciteit van het foton en van het ρ^0 meson direct aan elkaar gelijk gesteld mogen worden. Natuurlijke pariteitsuitwisseling in het t kanaal betekent dat er geen quantumgetallen uitgewisseld worden tussen het botsingsobject en het ρ^0 meson. Er is een indicatie dat R_ρ, verworven uit de data met behulp van de SCHC aanname, afhangt van W.

Bij HERMES bieden het gepolariseerde botsingsobject en de gepolariseerde verstrooiingsbundel de gelegenheid om de polarisatieafhankelijkheid van de heliciteitsoverdracht te meten. Met deze analyse is reeds begonnen. Toekomstige resultaten van de ρ^0 analyse zullen kleinere systematische onzekerheden hebben. Deze verbetering zal voornamelijk bereikt worden door gedegen studies van de achtergrondscorrectie met behulp van het Monte Carlo programma.

Acknowledgements

This thesis could not have been written without the help of a number of people. I am indebted to my promoter Jo van den Brand for offering me a Ph.D. position and introducing me to the HERMES experiment. I am also grateful for his careful reading of this manuscript and his advice during my four years of research. He ensured that I remained focussed on the main objectives of the HERMES experiment, while giving me the freedom to pursue my own preferences.

I want to thank Gerard van der Steenhoven, who was the HERMES group leader during the last two years of my research. Innumerable times he was available to give me helpful advice to keep my analysis on its way. His enthusiasm often encouraged me and helped me make progress with my analysis.

I thank Thomas Henkes who, during the first two years of my research, introduced me to the HERMES experiment, Hamburg, hardware issues and an original attitude towards life.

In 1995, the first data taking year of HERMES had started and it was thrilling to be part of a team helping to make this experiment work. A large part of my time was spent developing new software, with an inspiring group of people, which was excellently co–ordinated by Michael Düren. For his advice when I had just started developing ACE and for his trust to give me the freedom to do it my own way, I am grateful.

Tom O'Neill and Eric Belz introduced me to the analysis of ρ^0 production, and encouraged me throughout. Tom O'Neill, who co–ordinated the ρ^0 –ϕ analysis group, often helped me understand various issues of the analysis. Even when he was in the USA and I was in Amsterdam, he often managed to help me either by exchanging email messages or by phone. I appreciate his patience and his inventiveness in solving problems.

Numerous discussions with Eric Belz helped me gain insight in the theoretical interpretations of the angular distributions of the ρ^0 particle and the meaning of its polarisation density matrix elements. I am grateful for his contribution to the results presented in this thesis.

I would like to thank Marc Vanderhaeghen for his theoretical contribution.

Also, the theoretical contributions of Leonard Haakman and Justus Koch are highly appreciated, as are their patience and talent to explain their results to an experimental physicist.